Determination and prediction of the mechanical behaviour of architectural fabrics

A thesis submitted for the degree Doctor of Philosophy

in the School of Civil Engineering and Geosciences, Newcastle University

by

Alex George Colman

August 2015

Abstract

This thesis concerns the material behaviour of architectural fabrics for use in the construction of tensile fabric structures, particularly the determination and prediction of biaxial and shear behaviour. Original contributions to knowledge include a novel shear test frame design, an understanding of the influence of biaxial stress on shear behaviour and an improved predictive unit cell model.

While tensile fabric structures are subject to a combination of biaxial tensile stress and shear stress, there is no accepted test methodology for accurately determining shear behaviour of architectural fabrics. Shear behaviour is absent from some analysis methodologies used by industry and broad assumptions must be made by design engineers. A novel picture frame shear test design and associated test protocol is presented that aims to provide a practicable solution for the accurate determination of the shear stiffness of architectural fabrics. Strains are shown to be homogeneous across the test specimen during shear testing. The influence of biaxial stress on fabric shear behaviour is explored through tests conducted on polyvinyl chloride (PVC) coated polyester fabrics, PVC coated glass fabrics and polytetrafluoroethylene (PTFE) coated glass fabrics. Results of the tests, conducted at increasing levels of biaxial prestress, and the implications for analysis are presented.

Existing predictive fabric models based on constituent material properties are unable to predict fabric behaviour with a level of accuracy which is sufficient for their use in design. An improved predictive fabric model is proposed using a sinusoidal description of yarn geometry. A system of compatibility and equilibrium equations is derived which aims to realistically simulate principal deformation mechanisms within real fabrics. The improved model predicts non-linear yarn behaviour and hysteresis using input parameters obtained using non-specialist test equipment, i.e. test equipment which is available in typical material testing laboratories. The model is validated by comparing predicted data with experimentally obtained data for a range of PVC coated polyester fabrics, PTFE coated glass fabrics and silicone coated glass fabrics.

Safer and more efficient structural solutions will be possible if accurate material tests are available to characterise material behaviour. Reliable predictive models will make accurate design parameters easily accessible to designers.

Acknowledgements

I thank my supervisors Peter Gosling and Ben Bridgens for their guidance, encouragement and patience throughout the project. I also thank Lance Rowell, Alex Heslop (Architen Landrell), Matthew Birchall, Jo Renold-Smith (Buro Happold), Françoise Fournier, Farid Sahnoune (Serge Ferrari) and David Wakefield (Tensys) for their insight and for generously giving their time to support the work.

I am grateful to Architen Landrell, Buro Happold, Serge Ferrari, Tensys and the Engineering and Physical Sciences Research Council for funding the project and to Serge Ferrari, Verseidag Indutex and the Taiwan Textile Research Institute for contributing material for testing.

I thank those at the University who provided practical assistance in the laboratory and who fabricated the test frame, particularly Billy Cragie and Dave Innis. I thank Nicola Smithies for her help with the shear testing and for her friendship during our studies. Finally, I thank Cat for her love and support during the write up, without which this thesis may never have been finished.

Outline contents

Detailed contents with lists of figures and tables are included at the start of each chapter

Chapter 1: Introduction

"Our times demand lighter, more energy-saving, more mobile and more adaptable, in short more natural buildings, without disregarding safety and security"

Otto (2004)

Contents

Figures

Tables

1.1 Context

1.1.1 Background

Figure 1.1 The Moses Mabhida Stadium, Durban, 2010 FIFA World Cup. © SBP/Kurt Knopler

Architectural fabrics are used in the construction of tensile fabric structures, enabling the creation of striking structural engineering projects around the world. Projects range in size from small awnings to large span structures, for example sports stadia (Figure 1.1). While simple fabric coverings have been used throughout history, a desire to minimise our impact on the natural environment by reducing our consumption of energy and materials means that fabric structures have modern day relevance. Architectural fabrics are lightweight, translucent to light and require minimal support, thus modern fabric structures embody state-of-the–art, structurally efficient building solutions. New technologies also allows some architectural fabrics to be recycled (Fournier, 2013).

Architectural fabrics comprise a woven base cloth encased in a polymeric coating (Figure 1.2). These composite materials resist all applied loads through tension in the plane of the material, as they have negligible bending and compression stiffnesses (Bridgens *et al.*, 2004a; Bridgens *et al.*, 2004b; Bridgens and Birchall, 2012). This differs from conventional forms of construction which resist applied loads by arch action or by stiffness in bending. The shape of a fabric canopy is fundamental to a structure's ability to resist loads in the plane of the fabric. Anticlastic (doubly curved) forms make possible load resistance through tension, enabling resistance against both uplift (wind) and down-force (snow + wind). Prestress must also be applied to ensure that, under all anticipated loading conditions, the structure remains in tension.

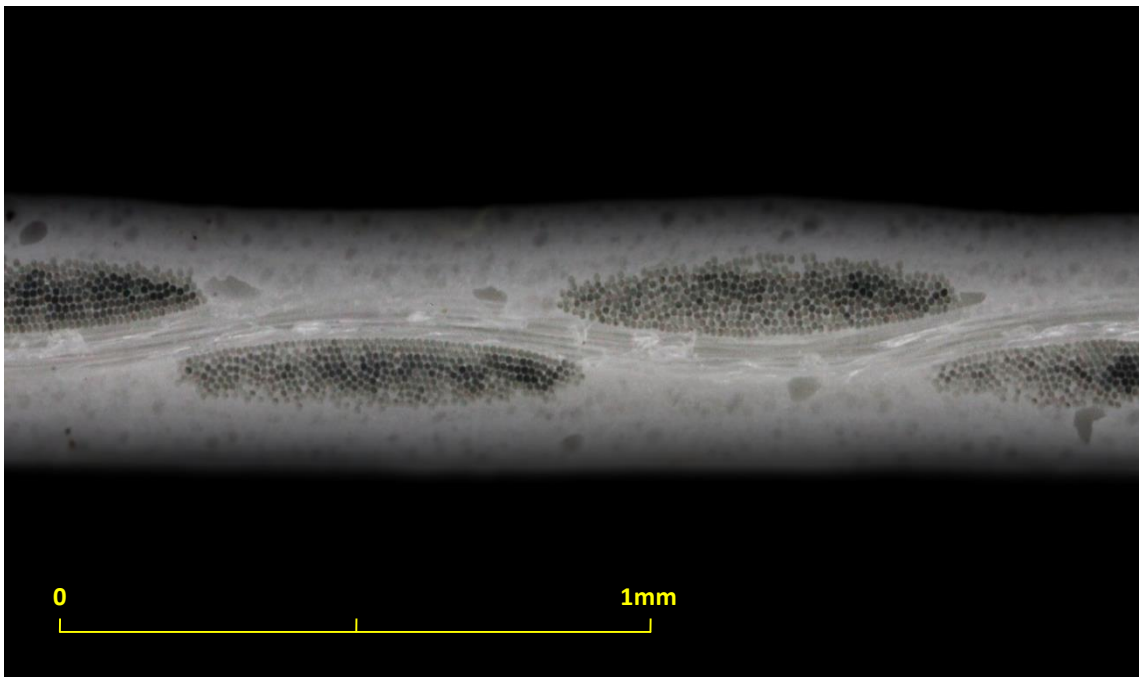

Figure 1.2 Image of an architectural fabric's cross section, illustrating a fill cross section of Ferrari 1202 PVC/PES fabric

Three basic structural forms are the basis of all tensile fabric structures: conics, saddles and hypars. More elaborate designs are then possible by combining these fundamental shapes. The necessary anticlastic surfaces are achieved by virtue of shear deformation, i.e. flat panels of fabric are sheared as prestress is applied during installation. Shearing of the fabric also occurs from deflections due to changes in a structure's surface geometry in response to applied loads. Therefore, understanding and quantifying the biaxial and shear behaviour of architectural fabrics is important to design engineers. Further, woven materials have a limiting shear deformation after which wrinkling will occur (Grosberg and Park, 1966).

An alternative to *tensile* fabric structures are *pneumatic* fabric structures. Pneumatic structures are either air supported or air inflated, or a hybrid of both. Air supported structures have a pressurised envelope, inhabited by the structure's occupants, which supports a fabric covering and applied loads. Air inflated structures (Figure 1.3) have pressurised elements, i.e. beams, that support a covering. Advantages of these structures are possible further weight reductions and temporary or demountable applications (Birchall, 2013). An increased understanding of architectural fabric material behaviour and improved modelling capabilities will also benefit the analysis and design of pneumatic fabric structures.

Figure 1.3 Sports Canopy, National Tennis Centre, London. © George Stowell

1.1.2 Design practices

Designing a tensile fabric structure is complicated as both form and function must be considered simultaneously as a structure's shape and stress distribution are interdependent. Further, it is desirable that the applied prestress is uniform over the fabric's surface. Achieving this requires that the fabric forms a minimal surface in which all the boundary points are connected with the minimal possible area of material. Determination of a tensile fabric structure's surface shape is through a process of 'form-finding' using numerical or, traditionally, physical models.

Traditionally, physical soap film models (Figure 1.4) were used to explore possible minimal surface shapes for tensile structures (Otto, 1967). These models produce minimal surfaces with inherent uniform tensile stresses. Modern numerical modelling approaches have allowed the creation of 'pseudo minimal surfaces' which reduce limitations of possible shapes. A smoothly varied distribution of prestress will exist over a pseudo minimal surface.

Different designers employ different numerical modelling approaches in the form-finding process, as specialist numerical form-finding processes for tensioned fabric structures sit outside the capabilities of standard structural analysis software packages. Further, British or European standards do not yet exist for the design and analysis of tensile fabric structures and limited guidance is available, although the CEN TC250 Working Group has been established to write a standard for membrane structures for inclusion in Eurocode 10. The most notable available guidance to date is the TensiNet European Design Guide (Mollaert and Foster, 2004) which recommends best practice based on the shared knowledge of the tensile fabric structures industry.

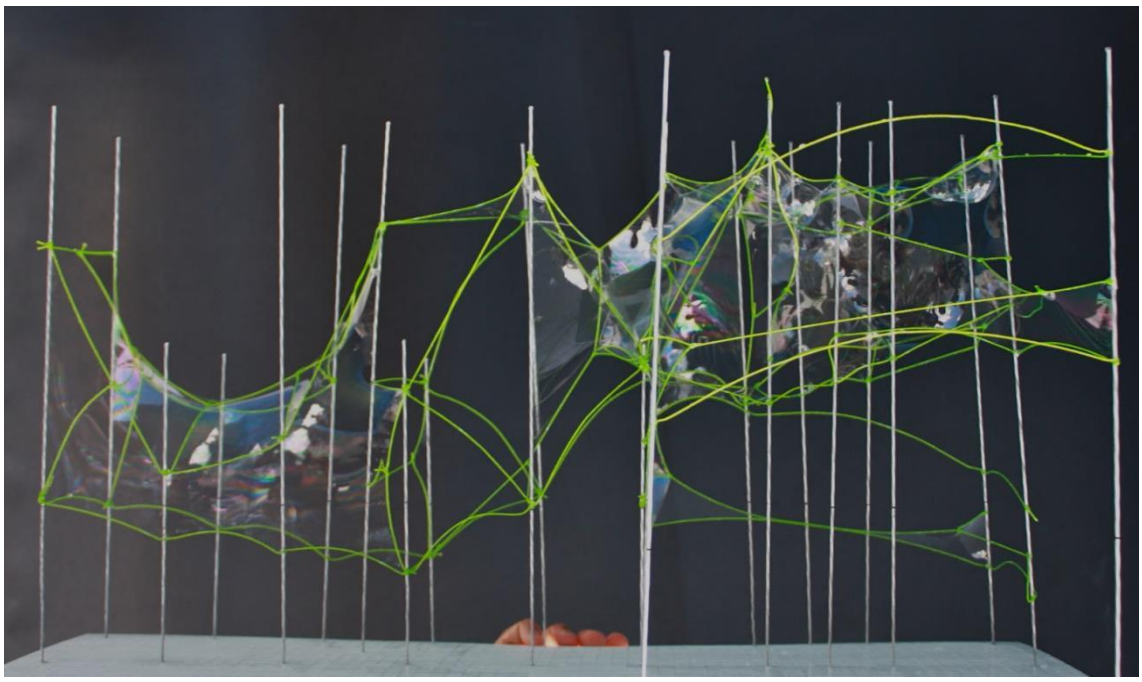

Figure 1.4 Example of a soap film model. © Net Constructions

Designers have developed a range of software which is used across the fabric structures industry with different analysis methodologies (Table 1.1). The results of an international round robin exercise demonstrate the dissimilarity of results for simple analysis problems when designers utilise different approaches (Gosling *et al.*, 2013a). Some analysis software will treat the fabric as a mesh of disparate elements, or cables, neglecting shear and Poisson's effects. Some finite element based approaches rely on assumptions of plane stress, requiring a linear representation of material behaviour. A high level of uncertainty must exist if results are considered to be correct for all the methodologies/software used.

Design is further complicated by the combination of an architectural fabric's constituent materials, as the woven yarn structure of the base cloths and the interaction of the yarns with the coatings results in complex in-plane tensile and shear behaviour. Elastic moduli, Poisson's ratios and shear stiffnesses are not constrained by the same relationships as for homogeneous, isotropic materials and are arguably inappropriate for describing this complex behaviour (Gosling and Bridgens, 2008). Crimp interchange (the interaction between the woven yarns) results in non-linear stress-strain behaviour that is hysteretic and anisotropic (Bridgens *et al.*, 2004a; Bridgens, 2005). Failure to accurately identify the material properties and accurately characterise behaviour of architectural fabrics results in uncertainty in design and analysis. Other sources of uncertainty exist, including degradation of the material in service and tear propagation. Consequently, designers use high factors of safety (Table 1.2), typically using values of 3 to 8 (Barnes *et al.*, 2004a; Gosling *et al.*, 2013b).

Table 1.1 Analysis codes used by participants in round robin exercise, reproduced from Gosling et al. (2013a)

Analysis code	Analysis methodology (details as provided by recipients)	Shear stiffness used	Poisson's ratio used	Poisson's ratio modified in Exercise 4?
3D3S 10.1	Non-linear Finite Element Methods, Equations solved using the Newton-Raphson method; Cable element and Trimesh Element.	NDP	NDP	Yes: V_{wf} = 0.457 (Note 2)
Carat++ (carat.st.bv.tum.de)	Form finding using updated Reference Strategy; analysis using geometrical nonlinear membrane elements (large deformations, small strains)	Yes	Yes	Yes: 0.4
EASY 9.2 (www.technet-gmbh.de)	Force density	No	No	NDP
Easy (www.technet-gmbh.de)	Force density	No	No	NDP
GSA 8.5 (www.oasys.com)	Form finding: soap-film with geodesic / ratio spacers to control mesh	Yes	Yes	NDP
GSA 8.5 (www.oasys.com)	Form finding using Dynamic Relaxation; large displacement, small-strain tension only membrane analysis.	Yes	Yes	V_{fw} = 0.457 (Note 2)
In house code	No details provided	NDP	NDP	NDP
inTENS v5i	Dynamic relaxation. Triangular constant strain membrane elements	Yes	Yes	NDP
ixForten 4000 release 4.3.6	Force density	No	No	NDP
Mpanel FEA	Geometrically nonlinear solver	NDP	NDP	Yes: V_{fw}=0.8 V_{fw}=0.457 (Note 2)
Not specified	Form finding using force density cable net. Large displacement, small strain analysis.	Yes	Yes	To suit reciprocal rule
PRISM. VERSION 1.00-03.	3 noded linear stress-strain triangle. Equations are solved using the conjugate gradient method.	NDP	NDP	Yes: V_{wf} = 0.457 (Note 2)
Research code	6 node, large strain, linear strain triangle	Yes	Yes	No
Rhino-Membrane 1.2.7 (www.ixcube.com)	Rhino-Membrane uses an algorithm based on the update reference strategy. Form finding was run for 200 iterations.	N/A	N/A	N/A
Sofistik 2010	4-node quad-elements with membrane characteristics (only tension, simplified linear-elastic orthotropic material law	Yes	V_{fw} not used	Yes: 0.49
Sofistik Version 2010 (11.10-25)	FE-Analysis : Direct Skyline Solver (Gauss/Cholesky)	Yes	Yes	Yes: 0.4999
Sofistik Version: 11.17-25	No details provided	Yes	Yes	NDP
Strand7	Non-linear analysis, direct sparse matrix	Yes	Yes	Yes: 0.5
TENSYL	Dynamic Relaxation	Yes	Yes	Yes: 0.3
TL_Form & TL_Load	Dynamic Relaxation using simplex elements	Yes	Yes	NDP
TL_Form & TL_Load	Dynamic Relaxation using simplex elements	Yes	Yes	NDP
WinFabric Version 7.2	Force density, Newton Raphson	No	No	NDP

Notes: (1) E = elastic modulus, v = Poisson's ratio, w = warp direction, f = fill direction, N/A = not applicable, NDP = no details provided

(2) A value of v_{fw} = 0.457 complies with the reciprocal rule for the specified values of E_w, E_f and E_{wf}. The specified value of v_{fw} intentionally did not comply.

Table 1.2 Stress reduction factors of safety for tensile fabric structure design according to different organisations and countries, reproduced from Gosling et al (2013b)

Source	Stress factors	Stated uncertainty incorporated within the stress factor
International Association of Shell and Spatial Structures Working Group 7 recommendation for pneumatic structures	4.2 – 6.0 (warp) 5.0 – 7.0 (fill)	Fabric and testing consistency; calculation accuracy; loading, fabrication and installation uncertainty; environmental degradation; unforeseen factors
American Society of Civil Engineers	4.0 – 7.8	Life cycle factor; strength reduction factor; load combination factor
French Design Guide	4.5 – 7.0	Fabric and seam quality; structure scale (probability of defects); pollution & environmental degradation (including quality of finite element analysis)
German standard (DIN 4134) with reduction factors according to Minte	Fabric 4.9 – 6.4 permanent load 2.9 – 3.2wind load 4.4 – 5.1 snow load Seams 6.7 – 9.5 permanent load 3.5 wind load 4.9 snow load	Uniaxial strength, modified depending on whether structure is loaded biaxially or uniaxially; load factor; material factor, accounting for seams and connections; load duration; pollution and degradation; temperature
Draft Italian Code	4.5 wind 3.75 snow	No details provided
Chinese Technical Standard	5	Factor of 2.5 for simultaneous wind and snow loading
Membrane Structures Association of Japan guide for 'Specific Membrane Structures'	8 for sustained loads 4 for temporary loads	No details provided

Uncertainties can be classified as aleatoric or epistemic. Aleatoric uncertainty is the statistical variation of the materials and conditions applied to a structure, such as varying strength across a roll or between batches of a fabric. It is not possible to suppress such uncertainty, but it can be quantified in design and analysis. Epistemic uncertainty is the systematic uncertainty arising from factors of the design and analysis that are neglected or inaccurate, such as the shear stiffness in some approaches of analysis. Epistemic uncertainties can be eliminated or reduced. In the context of tensile fabric structures, epistemic uncertainty can be reduced by achieving a better understanding of material behaviour and improving how material properties are represented in analysis.

1.1.3 Testing practices

Standardised uniaxial tensile testing (ISO 1421:1998) is carried out by material manufacturers to determine tensile strength in the yarn directions of architectural fabric products. Standard uniaxial test machines are used with commercially available clamping attachments and capstans for fabric

specimens. However, the results of this uniaxial testing do not quantify the biaxial or shear behaviour of architectural fabrics and it is not possible to infer these behaviours from uniaxial test data. Other testing methodologies are required to provide more useful information for design and analysis.

Biaxial tensile testing is specified by design engineers and fabricators in order to understand and quantify the in-plane biaxial behaviour of woven materials. These tests are used to establish material properties for analysis or compensation values for fabrication. The results of biaxial testing explain material behaviour including the effects of crimp interchange. This is vitally important as architectural fabrics behave as a mechanism and not as a continuum, a product of the interaction between the woven yarns. Biaxial testing of architectural fabrics is a specialist laboratory service and is provided by only a few laboratories globally. Testing is time consuming and expensive, prohibitively so for smaller tensile fabric structure projects.

Shear testing of architectural fabrics is rarely specified by engineers or fabricators. Rule of thumb methods are suggested instead, such as taking 1/20 of the direct strength (Barnes *et al.*, 2004b). Shear test methodologies for architectural fabrics should be capable of simultaneously applying shear deformations biaxial tensile load to a specimen. Ensuring the homogenous deformation is difficult and subsequently complex interpretation of the results can be required in order to infer shear stress and quantify shear stiffness (Colman *et al.*, 2014).

As with the design and analysis, there exists limited available guidance regarding the testing of architectural fabrics. The Membrane Structures Association of Japan has produced standards for determining the elastic constants of membrane materials (MSAJ, 1995) and in-plane shear stiffness (MSAJ, 1993). The American Society of Civil Engineers has also produced a short standard which states biaxial testing should be carried out by material manufactures, but does not detail how to conduct the testing (ASCE/SEI, 2010). Test methodologies (both for shear and biaxial behaviour) must be appropriate to capture the complex material behaviour of architectural fabrics so as to provide accurate values for design.

1.2 Aim and objectives

The aim of this research project is to develop an analytical/numerical tool to enable the accurate prediction of the non-linear stiffness characteristics of architectural fabrics for analysis of tensile fabric structures.

The key **hypothesis** is that the non-linear stiffness characteristics of coated woven fabrics can be predicted from information which is easily obtainable, i.e. using typical material testing equipment, from a small sample of the material in question.

Achieving the aim has been divided into two parts. The first part is the development of a novel test apparatus and associated test protocol to accurately quantify shear behaviour of biaxially tensioned architectural fabrics. Existing knowledge drawn from methodologies in related fields of work will be used. The second part is the formulation of an analytical predictive model that can characterise architectural fabric material behaviour without the need for specialist experimental testing. This will extend the work in this area by Bridgens (2005) by advancing a unit cell predictive model to be more representative of the woven geometries of architectural fabrics and their complex material behaviour.

Making accurate representation of fabric behaviour readily available to design engineers reduces the uncertainty in design. Reduced uncertainty improves the accuracy of structural analysis, making possible safer and more efficient solutions and allows designers to explore more innovative structural forms.

Specific **objectives** are to:

1. Design and fabricate a shear test apparatus suitable for architectural fabrics;
2. Investigate the in-plane shear behaviour of architectural fabrics, including the effect of different levels of biaxial tension;
3. Improve the accuracy of the predictive model unit cell model proposed by Bridgens (2005) to determine biaxial stress-strain behaviour. Improvement to be made by incorporating non-linear, inelastic load response and hysteresis;
4. Develop the model to include shear response;
5. Develop suitable testing to provide the improved predictive model with input parameters; and
6. Demonstrate the accuracy of the predictive model developed through a series of comparative biaxial and shear tests.

1.3 Structure of the thesis

Chapter 2 provides a literature review. After a brief overview of architectural fabrics and the biaxial behaviour of coated woven materials, a detailed appraisal of shear behaviour is presented. This is followed by an evaluation of available test apparatuses and associated methodologies, which involves a review of work concerning both biaxial and shear testing. A review of fabric modelling is also provided with a focus on unit cell models and shear modelling approaches. The review identifies limitations and benefits of previous work and presents the rational for the testing and modelling approaches adopted in the current study.

Chapter 3 describes the design of a novel picture frame test apparatus suitable for characterising shear behaviour of architectural fabrics (objective 1). A picture frame test apparatus has been developed following a comparison of shear testing methodologies presented in Chapter 2. Chapter 3 also presents an investigation of the influence of biaxial tensile stress on the shear response of architectural fabrics through a series of experimental tests performed on PVC coated polyester fabrics, PVC coated glass fabrics and PTFE coated glass fabrics (objective 2). Linear approximations are calculated and their appropriateness for use in design and analysis is discussed. A comparison of the linear approximations with current rule-of-thumb methods used in industry is also made.

Chapter 4 presents the development of an analytical unit cell model for predicting the biaxial stiffness characteristics of architectural fabrics (objective 3). First, a description of the woven yarn geometry is established and a quantitative assessment of the accuracy of the description is made. Subsequently, a novel system of non-linear equilibrium and compatibility equations is derived which modifies the yarn description when it is subject to imposed biaxial load. Further, a novel look-up function is described which replicates a fabric's non-linear, inelastic load response and hysteresis. A revised set of equations, based on existing approaches identified in Chapter 2, is presented for modelling shear of woven fabrics with asymmetric orthogonal yarns (objective 4).

Chapter 5 establishes suitable methods for obtaining input parameters for the model developed in Chapter 4 (objective 5). Methods of determining material properties using standard testing equipment are described, as is a macro photography methodology for making measurements of a fabric's yarn geometry. Subsequently, validation of the predictive model is presented which involves comparison of different model formulations against biaxial test data. A series of experimental tests on PVC coated polyester fabrics, PTFE coated glass fabrics and Silicone coated glass fabrics are described for generating comparative test data performed (objective 6).

Chapter 6 presents a brief research summary and the main conclusions of the project. Suggestions for future work are also made.

References are listed alphabetically by first author at the end of the thesis using the Harvard reference system.

1.4 Publications

Journal papers

Colman, A.G., Bridgens, B.N., Gosling, P.D., Jou, G.T. and Hsu, X.Y. (2014) 'Shear behaviour of architectural fabrics subjected to biaxial tensile loads', *Composites Part A: Applied Science and Manufacturing*, 66(0), pp. 163-174.

DOI: http://dx.doi.org/10.1016/j.compositesa.2014.07.015.

A copy of the journal paper is included in the appendices.

Conference papers/presentations

Colman, A.G., Bridgens, B.N. and Gosling, P.D. (2013) 'A predictive biaxial meso-mechanical model for characterising architectural fabrics', Structural Membranes. 9-11 October 2013, Munich, Germany.

Colman, A.G., Bridgens, B.N. and Gosling, P.D. (2013) 'A picture frame shear test methodology to determine accurate shear properties of architectural fabrics', *TensiNet Symposium: [Re]Thinking lightweight structures*. 8-10 May 2013, Istanbul, Turkey.

Chapter 2:
Literature review

Contents

Figures

Tables

2.1 Architectural fabrics

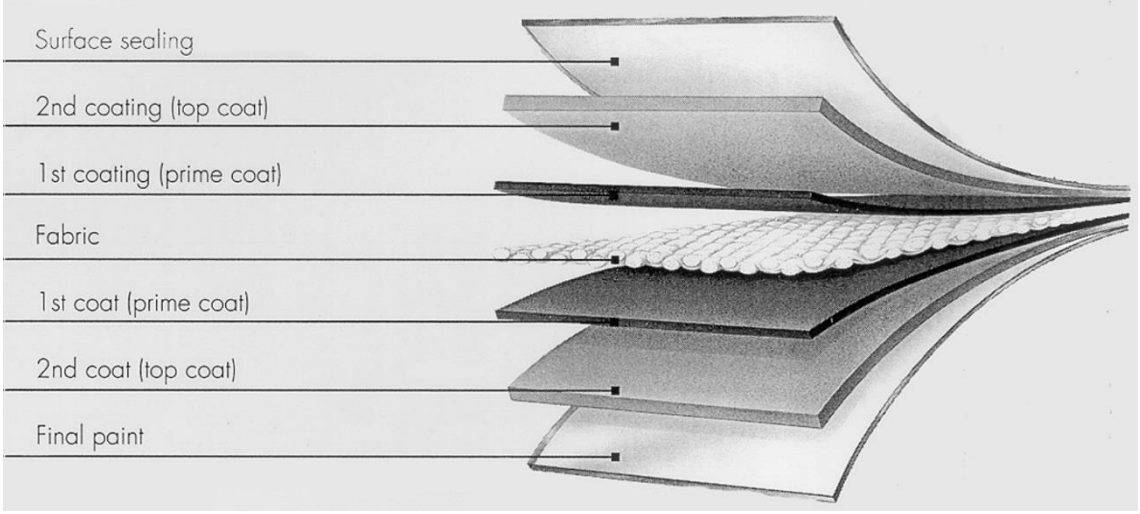

Figure 2.1 Typical composition of an architectural fabric, reproduced from Blum *et al.* (2004a)

Architectural fabrics are composite materials which generally comprise a base cloth of woven yarns encased in a polymeric coating (Figure 2.1). Yarns are made from twisted bundles of fibres and the mechanical properties of the fibres influence the behaviour of a single yarn and the fabric as whole (Hearle *et al.*, 1972; Blum *et al.*, 2004a). Architectural fabrics are normally plain woven (Figure 2.2a), i.e. the yarns are woven in a one-over-one-under fashion, although other weave types are possible, for example satin weave (Figure 2.2b) and twill weave (Figure 2.2c).

Typically, polyester (PES) or glass fibres are used in the manufacture of base cloths for architectural fabrics, although cotton, nylon, aramid and polytetrafluoroethylene (PTFE) fibres are also used. These alternatives are used less extensively owing to drawbacks which are highlighted by Bridgens (2005): cotton and nylon are limited by their short lifespans, as cotton is prone to moisture damage and fungal attack and nylon has poor resistance to ultraviolet light; the use of aramid fibres can also be problematic as they exhibit very low levels of elastic strain; and PTFE fibres have low tensile strength.

Polyester base cloths are generally paired with polyvinyl chloride (PVC) coatings and glass fibre fabrics typically have PTFE coatings. Increasingly, silicone coatings are also used in combination with glass fibre cloths. PVC coated polyester (PVC/PES) fabrics may be classified as one of five distinct types in view of their tensile strength and material composition (Table 2.1). Similarly PTFE coated glass fibre (PTFE/glass) fabrics may be classified as one of seven different types (Table 2.2).

The extreme low weight of these materials and their smaller amount of embodied energy compared to conventional materials, for example steel or glass, makes them desirable to building designers (Berger, 1999; Bridgens *et al.*, 2004b). Architectural fabrics with different constituent materials have different material properties (Table 2.3) to suit different applications and budgets.

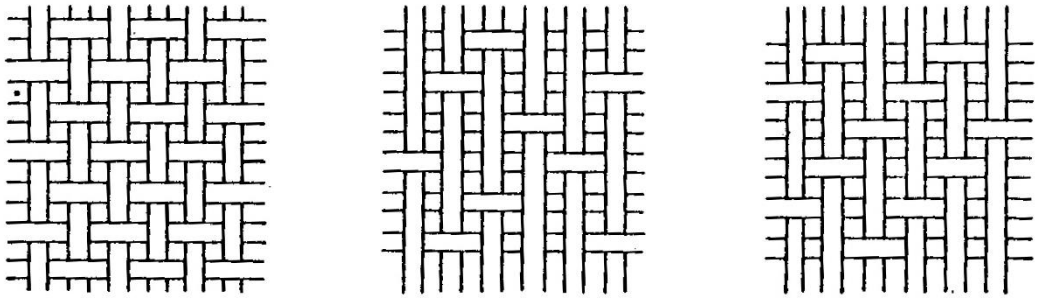

(a) (b) (c)

Figure 2.2 Basic weave patterns: (a) plain weave; (b) satin weave; and (c) twill weave, reproduced from MSAJ (1995)

Table 2.1 Classification of PVC/PES fabrics, reproduced from Blum *et al.* (2004a)

	Type 1	Type 2	Type 3	Type 4	Type 5
Surface weight (g/m²)					
French design guide	720	1 000	1 200	1 400	2 000
WG Messe Frankfurt	800	900	1 050	1 300	1 450
Yarn linear density (dtex)					
French design guide					
WG Messe Frankfurt	1 100	1 100	1 670	1 670	2 200
Tensile strength warp/weft (kN/m)					
French design guide	60/60	84/80	110/104	120/130	160/170
WG Messe Frankfurt	60/60	88/79	115/102	149/128	196/166
Trapezoidal tear test (N)					
French design guide					
WG Messe Frankfurt	310/350	520/580	800/950	1 100/1 400	1 600/1 800
Yarn number per cm warp/weft					
French design guide					
WG Messe Frankfurt	9/9	12/12	10.5/10.5	14/14	14/14

Table 2.2 Classification of PTFE/glass fabrics, reproduced from Blum *et al.* (2004a)

Type	G1	G2	G3	G4	G5	G6	G7
Tensile strength warp/weft (kN/m)	26/22	43/28	70/70	90/72	124/100	140/120	170/158
Filament diameter (micrometer)	9	6	3	6	3	3 or 6	3
Surface weight (g/m²)	500	420	800	1 00	1 200	1 500	1 600
Trapezoidal tear test (N)			300/300	300/300	400/400	500/500	450/450

Table 2.3 General comparative properties of materials for architectural fabrics, reproduced from Blum *et al.* (2004a)

	PVC coated polyester fabrics	PTFE coated glass fabrics	Silicone coated glass fabric	PTFE coated PTFE fabrics
Tensile strength warp/weft (kN/m)	115/102	124/100	107/105	84/80
Fabric weight (g/m²)	1 200 (type 3)	1 200 (G5)	1 100	830
Trapezoidal tear test (N)	800/950	400/400	960/700	925/925
Visible light transmission (%)	10-15	10-20	< 80	19-38
Flexibility/crease recovery	high	low	high	high
Fire reaction	M2 (NFP 92 503) B1 (DIN 4102)	M1 (NFP 92 503) B1/A1 (DIN 4102)	A (ASTM E-108) no toxic smokes	
Cleaning	easier with top coats	self cleaning	self cleaning	self cleaning
How to make the seams	by high frequency	thermally	vulcanisation	stitching
Life span	> 15-25	> 25	> 25	
Cost	low	high	high	

2.1.1 Biaxial behaviour

Woven fabrics are well known to be anisotropic materials with complex non-linear stress-strain behaviour (Peirce, 1937; Menges and Meffert, 1976; Schock, 1991). Testa *et al.* (1978) identified that biaxial behaviour is governed by crimp interchange and elongation of the yarns. Crimp interchange can result in negative strains under applied biaxial load (Schock, 1991) and bending stiffnesses are negligible and neglected in design as it is very low compared to the tensile stiffness (Testa *et al.*, 1978; Boisse *et al.*, 2001). Bridgens (2005) presents a comprehensive review of biaxial behaviour and other investigators also detail the phenomena (Nguyen *et al.*, 1999; Mohammed *et al.*, 2000; Page and Wang, 2000; Potter, 2002; Boisse *et al.*, 2005; Pargana *et al.*, 2007; Zhu *et al.*, 2007; Hivet and Duong, 2011; Nguyen *et al.*, 2013).

Coatings set the yarns in place and limit the relative movement of the yarns and yarn interactions (Skelton and Freeston, 1971; Testa *et al.*, 1978). In this way, the coatings can greatly reduce the deformability of the fabric and tear propagation as they impregnate effecting yarn behaviour the yarns and binds the yarn fibres together and prevent yarns from sliding relatively to one another (Naik and Madhavan, 2000; Farboodmanesh *et al.*, 2005). The coatings will also reduce tear propagation.

2.1.2 Shear behaviour

Shearing occurs in the plane of a flat panel of fabric when it is bent into double curvature (Mack and Taylor, 1956; Cusick, 1965). Shearing of architectural fabrics is thus a necessary and fundamental deformation mechanism to form the anticlastic forms required when building tensile fabric structures. However, it is asserted that woven materials have a limiting shear deformation after which wrinkling will occur (Grosberg and Park, 1966; Skelton, 1976). Wrinkling is unacceptable both aesthetically if it occurs during installation and as a potential cause of failure if it occurs under imposed loading, but neither the shear deformations that occur in membrane structures, nor the values of limiting shear angle for *coated* fabrics, have been quantified. To avoid wrinkling, fabric structures are discretised into multiple panels (Figure 2.3).

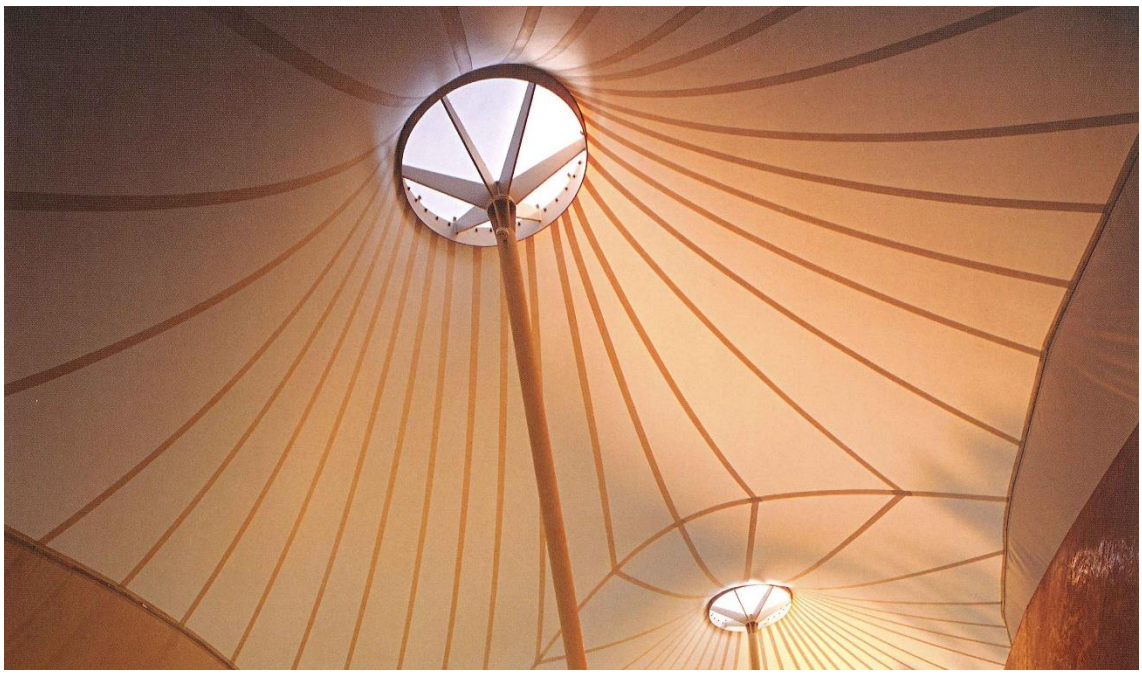

Figure 2.3 Longitude 131°, Ulurur-Kata Tjuta National Park, Australia, underside of a double conic tensile fabric structure in which multiple fabric panels which are required to achieve the desired curvature are visible, reproduced from Drew (2008)

It is important to distinguish between shear of fabrics with and without yarn rotation. Typically, shear of woven fabrics refers to a change in angle between perpendicular yarn directions (Figure 2.4a). However, shear can be measured with respect to any perpendicular axis in the plane of the fabric (§2.3.3) and can occur with no change in angle between perpendicular yarn directions (Figure 2.4b). The latter circumstance is observed when strain occurs in the perpendicular yarn directions and the strain in one direction does not equal that in the other. This project is concerned with shear with yarn rotation.

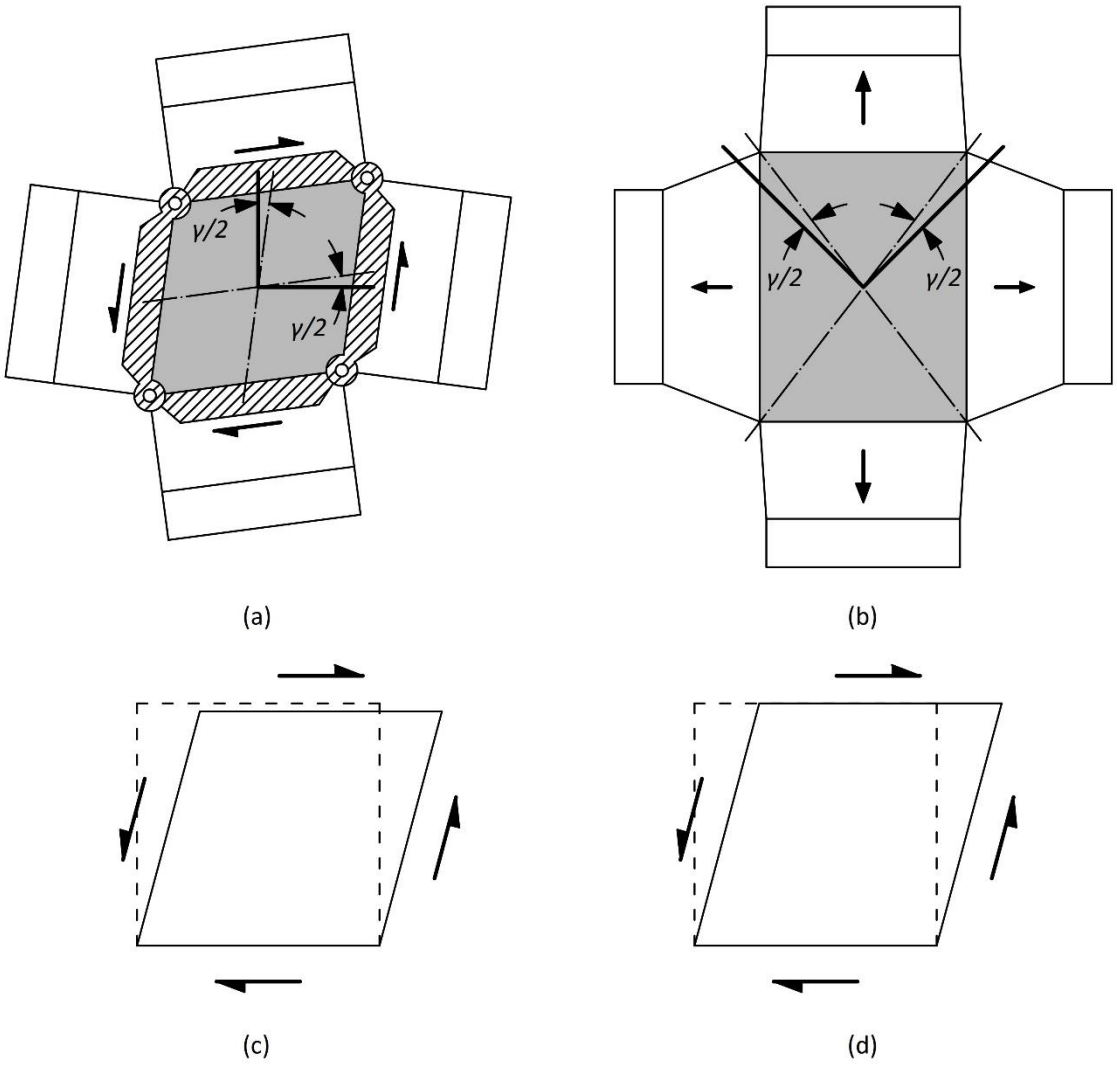

Figure 2.4 Shear of architectural fabrics. (a) Shear of biaxial specimen with yarn rotation; (b) shear of biaxial specimen without yarn rotation, (c) pure shear, where area reduces but yarn length stays constant; and (d) simple shear, where constant area but yarns extend

Further, shear of woven fabrics is pure shear (Figure 2.4c) and not simple shear (Figure 2.4d) (Spivak and Treloar, 1968; Leaf and Sheta, 1984); deformation occurs with constant side lengths and not with constant areas. Therefore, shear of fabric test specimen or a panel of fabric will cause a reduction in the fabric's area.

Shear stiffness of coated fabrics is predominantly governed by the protective polymeric coating with the contribution of the yarns being relatively insignificant (Skelton and Freeston, 1971; Testa *et al.*, 1978). To date, the shear stiffness of *coated* fabrics is routinely assumed to be linear (Pargana et al., 2007; Bridgens and Birchall, 2012; Gosling et al., 2013a). This is despite it being long known that shear behaviour of coated fabrics is in fact highly non-linear (Skelton and Freeston, 1971) (Figure 2.5). The relatively lower values of shear stiffness observed in *uncoated* fabrics arise from the gaps between the individual woven yarns, and this also accounts for hysteresis of shear force (Culpin, 1979; Matsudaira *et al.*, 1985)

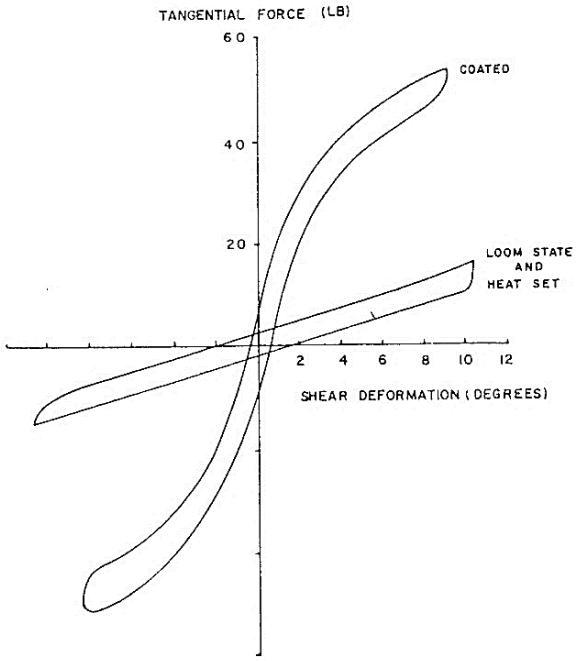

Figure 2.5 Comparison of shear stress-strain curves for a woven fabric having no coating against the same fabric with a polythene coating, reproduced from Skelton and Freeston (1971)

Grosberg and Park (1966) established three distinct stages of shear deformation through studies on uncoated fabrics. The first is characterised by lateral bending of the yarns, which occurs as the result of rigid yarn intersections (Figure 2.6a). Grosberg and Park (1966) posit that this is only true for very small angles of shear when shear force is large enough to overcome static friction at the yarn intersections due to a normal force acting at the cross over. This is supported by later works (Grosberg *et al.*, 1968; Page and Wang, 2000; Sun and Pan, 2005). For example, Page and Wang (2000) calculate that for a range of fabrics shear deformation without rotation of the yarns is negligible and will occur at angles of less than 0.05°. However, the latter study concerned fabrics for composite forming, so normal forces at the yarn intersections will be lower than compared to those of architectural fabrics where there will tension in the yarns. Consequently, lateral bending of the yarns may occur at higher angles when shearing tensioned fabrics, although the coating is likely to interact with this mechanism.

During the second stage, slippage at the yarn intersections occurs, i.e. the yarns rotate, and the yarns undergo elastic deformation. There exists space between the yarns that permits relative rotation of the warp and fill yarns until the free space is taken up (Grosberg and Park, 1966; Culpin, 1979). Grosberg and Park (1966) observed this stage up to approximately 10° of shear. (Mack and Taylor (1956) proposed an early simplification of this shear deformation mechanism which assumes that yarns rotate about pin jointed constraints at the yarn intersections, thus idealising the yarns as inextensible ridged beam elements with no slippage occurring at the yarn intersections (Figure 2.6b).

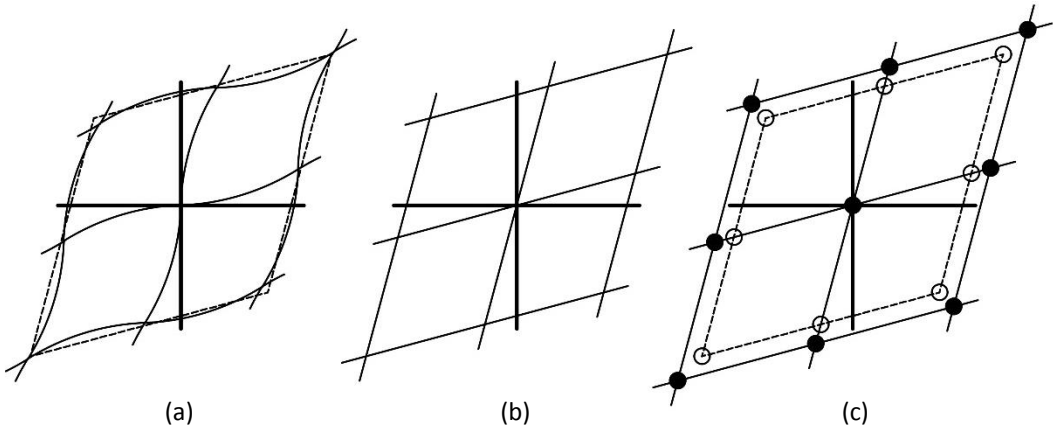

Figure 2.6 Shear deformation mechanisms: (a) yarn bending due to rigid intersection; (b) trellis shear, i.e. rotation at the intersection; and (c) translation at the yarn intersections

Later work concerning woven fabrics routinely assumes this simplification of shear deformation (Skelton and Freeston, 1971; Potter, 1979; Nguyen *et al.*, 1999; Mohammed *et al.*, 2000; Page and Wang, 2000; Liu *et al.*, 2004; Liu *et al.*, 2005; Sun and Pan, 2005). Slippage of the yarns is observed during deformation of *uncoated* fabrics (Figure 2.6c) (Page and Wang, 2000; Harrison *et al.*, 2004). However, in a uniform shear condition, slippage at the yarn intersections will hardly occur owing to the symmetry of the weave (Page and Wang, 2000). However, slippage of coated architectural fabrics is unlikely to occur as coating penetration has been shown to inhibit the base cloth will no longer be a freely rotating material and act as a rigid embedded reinforcement (Farboodmanesh *et al.*, 2005).

Finally, the third stage is defined by jamming of the woven yarns, which is also termed lock up. Lock up occurs as adjacent yarns come into contact with one another as the gaps between the individual yarns reduce with increasing shear angle (Figure 2.7). This results in the build-up of in-plane compressive forces which cause wrinkling in the fabric (Grosberg and Park, 1966).

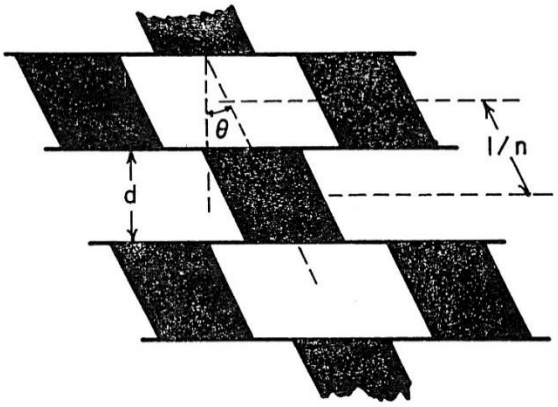

Figure 2.7 Shear deformation of woven fabric approaching the shearing limit where adjacent yarns will come into contact and cause buckling of the material , reproduced from Skelton (1980)

The shear resistance of uncoated fabrics may be considered negligible until lock up occurs (Boisse *et al.*, 2001). Shear strain is observed increase significantly thereafter (Boisse *et al.*, 2005; Cao *et al.*, 2008; Launay *et al.*, 2008).

However, the concept of lock up, as it is applied to uncoated fabrics, cannot apply to *coated* fabrics as the coating will "jam" the weave structure. Further, lock up will not occur instantaneously upon side-by-side contact of the yarns. Rather, the three-dimensional woven yarns must gradually deform and compress for the fabric to undergo shear deformation. A reduction in stiffness when observing stress strain test data for uncoated fabric indicates the onset of buckling (Leaf and Sheta, 1984). This observation may equally apply to coated fabrics and would be expected at lower angles of shear due to the presence of the coating.

As mentioned above, early work suggests that yarn behaviour does not significantly impact the shear behaviour of coated fabrics (Skelton and Freeston, 1971; Testa *et al.*, 1978). Further, modern analysis of fabric structures may neglect the influence of tensile behaviour on shear behaviour, i.e. the two behaviours are considered to be uncoupled (Xue *et al.*, 2003; Bögner-Balz and Blum, 2008). However, picture frame tests (§2.2.2) performed on *uncoated* woven reinforcements have indicated an increase in shear stiffness with increasing pre-tension (Harrison *et al.*, 2002; Willems *et al.*, 2007). While Harrison *et al.* (2012) noted problems with these studies, namely large variability in test data making assessment of the interaction between shear and tensile behaviour difficult, tension in the yarns will increase the normal force acting at the cross overs which will in turn increase frictional resistance. Sharma *et al.* (2003) also investigated shear-tension coupling. Results indicated only minor coupling and it was suggested that biaxial tension does not need to be included when modelling shear. However, these studies concern uncoated fabrics for use in draping processes for composite forms, so no low tensile loads are applied in the plane of the fabric.

There is at least coupling between in-plane tension and the onset of wrinkling when a woven fabric is subject to shear deformation (Launay *et al.*, 2008; Willems *et al.*, 2008; Harrison *et al.*, 2012). This is reasonable to expect with uncoated fabrics as tension applied in one yarn direction will increase the spacing between adjacent yarns in the orthogonal direction. However, the effect of tensile loads applied to architectural fabrics on the materials' shear behaviour has not been quantified. This is necessary to determine the limits of shear deformation, i.e. double curvature, that can be achieved in design and to fully quantify fabric behaviour.

2.2 Fabric testing

2.2.1 Biaxial testing

Biaxial tensile testing is necessary to characterise the biaxial behaviour of structural fabrics. Early biaxial testing was conducted by Haas and Dietzius (1917), whose work involved specimens that were either flat or cylindrical. Biaxial testing on cylinders of fabric (Figure 2.8) uses inflation pressure to apply load in the circumferential direction and displacement of the end of the cylinder to apply load in the axial direction. Other investigators have adopted similar cylinder test methodologies (Eeg-Olofsson, 1955; MacRory and McNamara, 1967; Skelton and Freeston, 1971; Mott *et al.*, 1985). When testing permeable fabrics, a bladder may be inserted inside the fabric cylinder and inflated (Cusick, 1965; Mott *et al.*, 1985), but in such arrangements it may be possible that the material properties of the bladder could influence the results of the tests. While biaxial tensile behaviour and shear behaviour are normally investigated separately (Bassett *et al.*, 1999; Bögner-Balz and Blum, 2008), the fabric permits application of shear stress to the cylinder by the application of torsional force to the end of cylinder (Turner *et al.*, 2008).

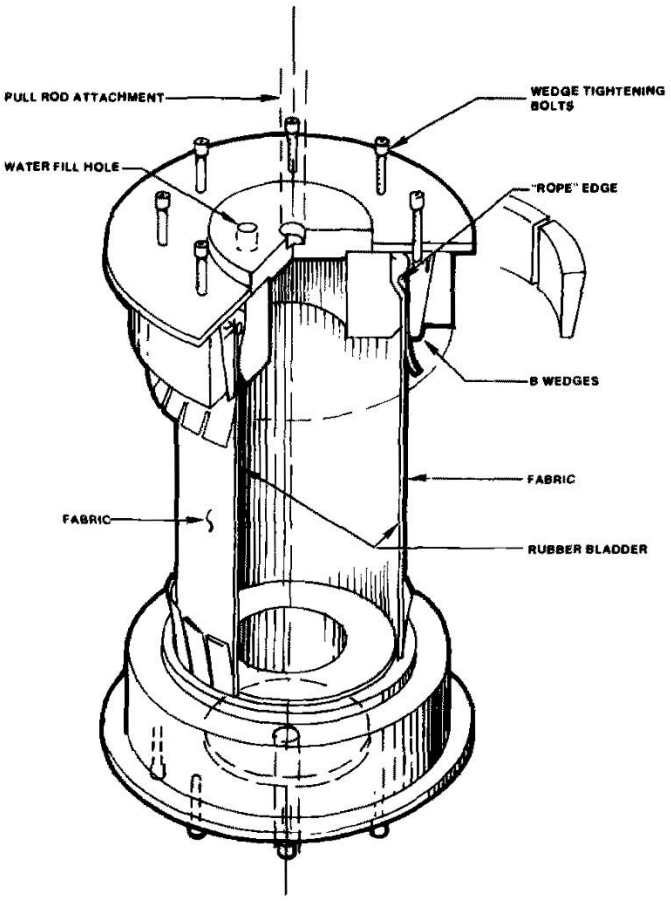

Figure 2.8 Example biaxial tensile test set up using a cylindrical test specimen, N.B the set up illustrated shows a rubber bladder inside the fabric cylinder, reproduced from Mott *et al.* (1985)

However, the specimen would require a seam in order to construct the cylinder. While it is possible to weave a complete cylinder, it would not be possible to coat the woven cylinder as coating is applied to an architectural fabric. Therefore, the influence of the seam must be accounted for.

The only international standard concerning the biaxial testing of architectural fabrics is produced by the Membrane Structures Association of Japan (1995) and prescribes a cruciform test specimen with slits cut in the arms of the specimen (Figure 2.9). The specimen can be restrained at the ends of the arms by a single clamp plate or with the slits separated and fixed separately. According to standard, stress developed in the centre of the specimen is approximately 92.1% of the applied load (MSAJ, 1995). With a specimen made to the dimension used in the project the stress developing in the centre of the specimen is 95.3% (Bridgens, 2005; Bridgens *et al.*, 2011). The difference in the two results may be attributed to the different dimensions of the specimens.

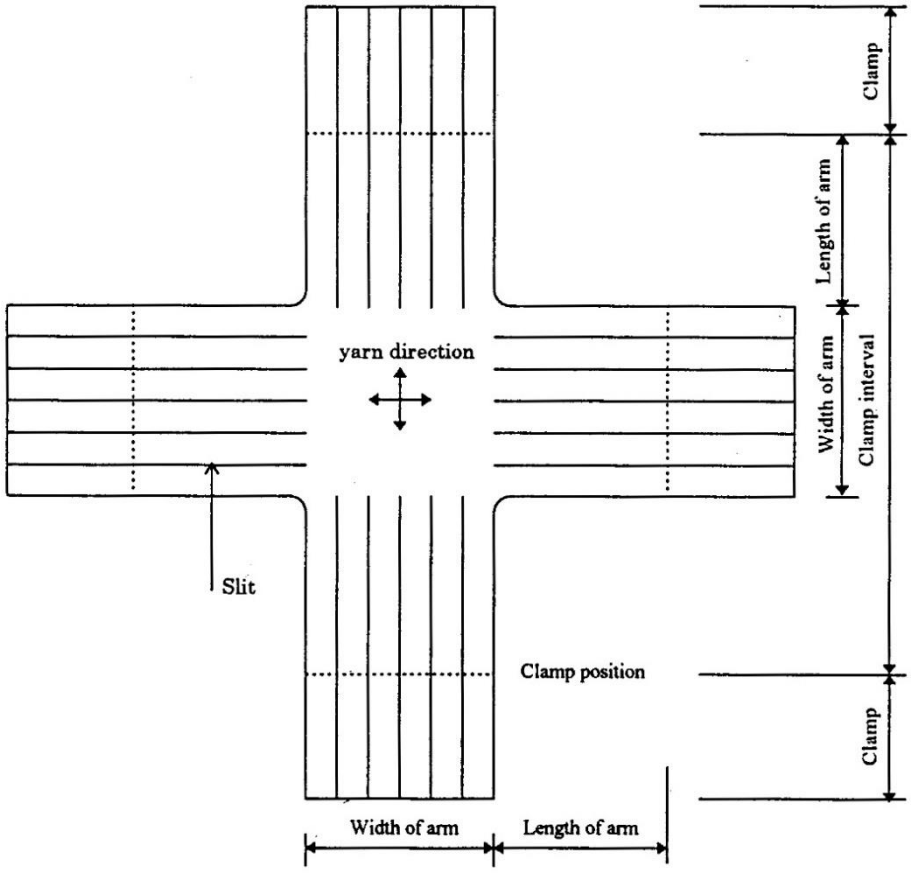

Figure 2.9 Cruciform biaxial specimen with slits cut in arms of the specimen, reproduced from MSAJ (1995) N.B. width and length of arms ≥ 16cm and distance between clamps ≥ 48cm

Other types of biaxial test specimen have been used and Bassett *et al.* (1999) reviewed available biaxial test methods and the different specimens employed therein (Figure 2.10). While squares of fabric have been used (Reichardt *et al.*, 1953), such specimens have given way to the typical cruciform specimens which are used in early work by Klein (1959) and Clulow and Taylor (1963).

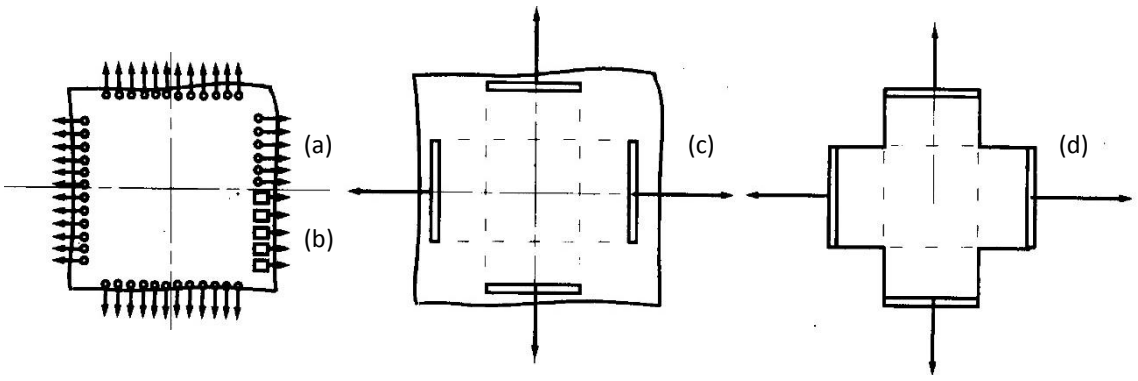

Figure 2.10 Different kinds of fabric gripping in biaxial fabric test rigs: (a) point gripping, (b) grab test, (c) cruciform test, and (d) segmented clamps, reproduced after Bassett *et al.* (1999)

Slits were introduced to allow for large strains without distorting the specimen along the clamped edge (Reinhardt, 1976). The use of slits increases stress in the centre of the specimen, as without slits, stresses in the aforementioned studies were found to be between 72.1% and 90.3% of the applied loads (MSAJ, 1995; Bridgens, 2005). Biaxial cruciform tests have become the industry standard (Barnes et al., 2004b; Blum et al., 2004b; Bridgens et al., 2011).

Biaxial testing is to be carried out using the floating biaxial test rig developed by Newcastle University and Bridgens (2005) based on a design by Architen Landrell (Figure 2.11). These rigs have an upper "floating" frame that is free to translate and rotate in the plane of a fabric test specimen. When load is applied to a test specimen, the axis of floating upper frame will translate and rotate to provide balanced loading and alignment relative to the lower frame. Further, this frame design permits application of load using only two actuators.

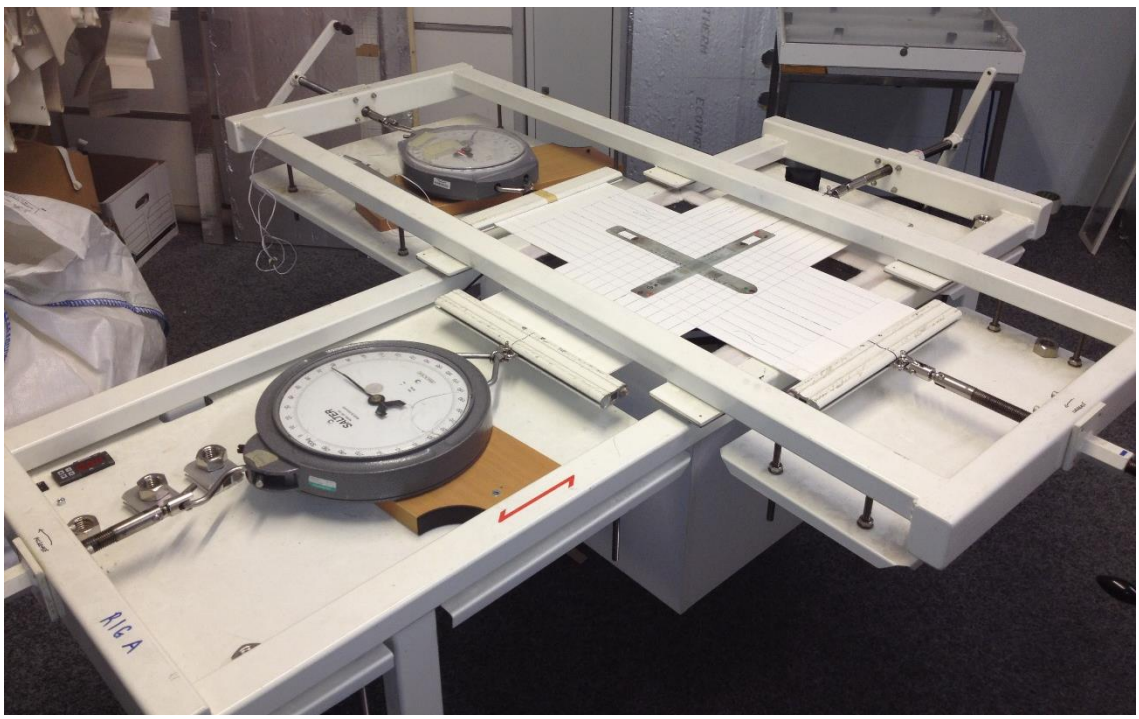

Figure 2.11 Floating biaxial test rig developed by Architen Landrell

2.2.2 Shear testing

The only standardised methodology for the shear characterisation of architectural fabrics has been produced by the Membrane Structures Association of Japan (MSAJ, 1993). Therefore, further development of test equipment and methodologies must look to this standard, previously published experimental work, and industry best practice. Much of the up-to-date literature concerning shear testing relates uncoated fabrics for use in composite forming (Bassett *et al.*, 1999; Mohammed *et al.*, 2000; Page and Wang, 2000; Lebrun *et al.*, 2003; Zhu *et al.*, 2007; Cao *et al.*, 2008; Launay *et al.*, 2008; Lomov *et al.*, 2008). This work is useful in the development of methodologies for the testing of architectural fabrics, but it is important to recognise that differences exist when considering shear of coated fabrics. Uncoated fabrics are typically tested to large angles of shear and have low shear stiffness, compared to architectural fabrics which are tested at small angles and have relatively high shear stiffness (Table 2.4).

Table 2.4 Maximum angles of deformation and approximated linear shear stiffness for uncoated and coated fabrics

	Authors	Test methodology	Max. γ (°)	G (kN/m)
Uncoated studies	Page and Wang (2000)	Bias extension	55	0.005*
	Zhu *et al.* (2007)	Bias extension	50	0.01*†
	Launay *et al.* (2008)	Picture frame and bias extension	50	0.23-1.09*
	Cao *et al.* (2008)	Picture frame and bias extension	55	0.04-0.09*
Coated studies	Vysochina *et al.* (2005)	T-shaped specimen	15	50.4 and 51.5
	Bögner-Balz and Blum (2008)	45° biaxial cruciform	15	1.3-2.4
	Jackson *et al.*(2009)	Picture frame	15	5.0-143.2
	Galliot and Luchsinger (2010b)	Shear Ramp	15	8.9-57.8

* Approximate linear stiffness to 15°
† Calculated with use using the method proposed by (Launay *et al.*, 2008) from crosshead load

To accurately simulate the in situ behaviour of an architectural fabric it is necessary to simultaneously apply predetermined biaxial tension and shear deformation. It is desirable to apply a homogenous strain field to the fabric specimen as this allows simple calculation of the stresses resulting from the applied load.

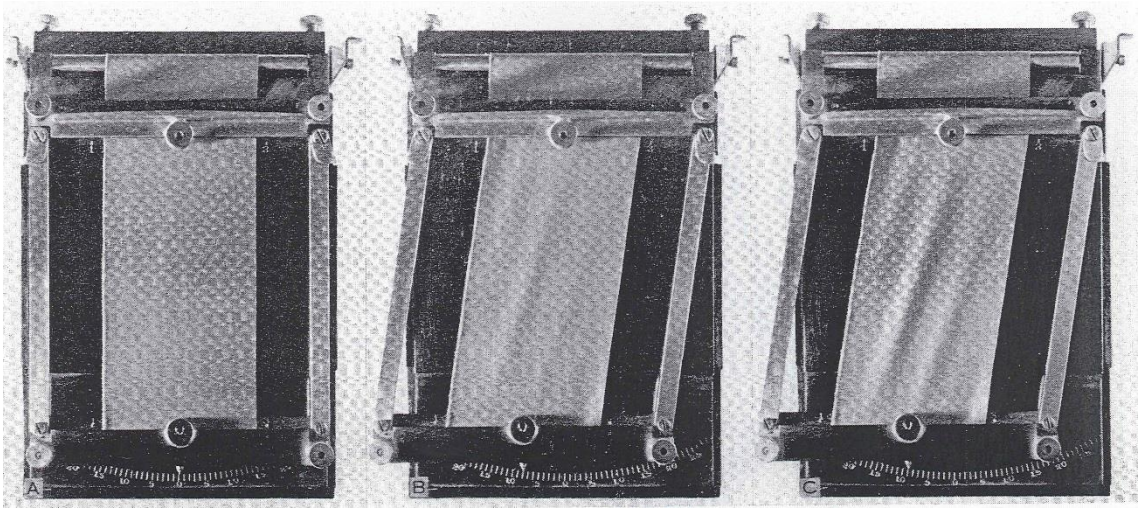

Figure 2.12 Appearance of specimen in the "Planoflex" at three stages during the measurement: (left to right) specimen before deflection; wrinkles and end point; and wrinkles 1 degree beyond end point, reproduced from Dreby (1941)

Dreby (1941) developed an early example of shear test apparatus for measuring the extent to which a fabric can be deformed (Figure 2.12). However, this and other early test apparatus designs did not enable simultaneous application of biaxial tensile and shear stress and failed to produce a homogeneous stress distribution in the plane of the fabric (Kawabata, 1980; Leaf and Sheta, 1984). Thus, early test apparatus are unsuitable for characterising shear behaviour of architectural fabrics.

Galliot and Luchsinger (2010a) highlight some of the more recent methodologies for shear testing of woven materials (Figure 2.13). The KES-F shear test (Kawabata, 1989; Lo and Hu, 2002; Lomov *et al.*, 2003b; Lomov and Verpoest, 2006), the T-shaped specimen test (Vysochina *et al.*, 2005) and the extensively used bias extension test (Mohammed *et al.*, 2000; Zhu *et al.*, 2007; Cao *et al.*, 2008; Launay *et al.*, 2008; Lomov *et al.*, 2008) cannot apply biaxial tension whilst shearing the specimen. A stress analysis of the specimen during a KES-F shear test has also demonstrated that the specimen is not subject to pure shear deformation (Hu and Zhang, 1997).

The biaxial cruciform test with 45° yarns (Blum *et al.*, 2004b; Bögner-Balz and Blum, 2008) applies biaxial tension, but the level of tension varies with shear deformation, and cannot be independently controlled. This method also requires a specimen that is difficult to prepare and can only apply 1:1 biaxial stress ratios. The aforementioned inflated cylinder test used in relation to shear Turner *et al* (2008) does allow independent control of biaxial tension and shear (through axial tension, inflation pressure and torsion, respectively), but no procedure to quantify the influence of the seam is presented.

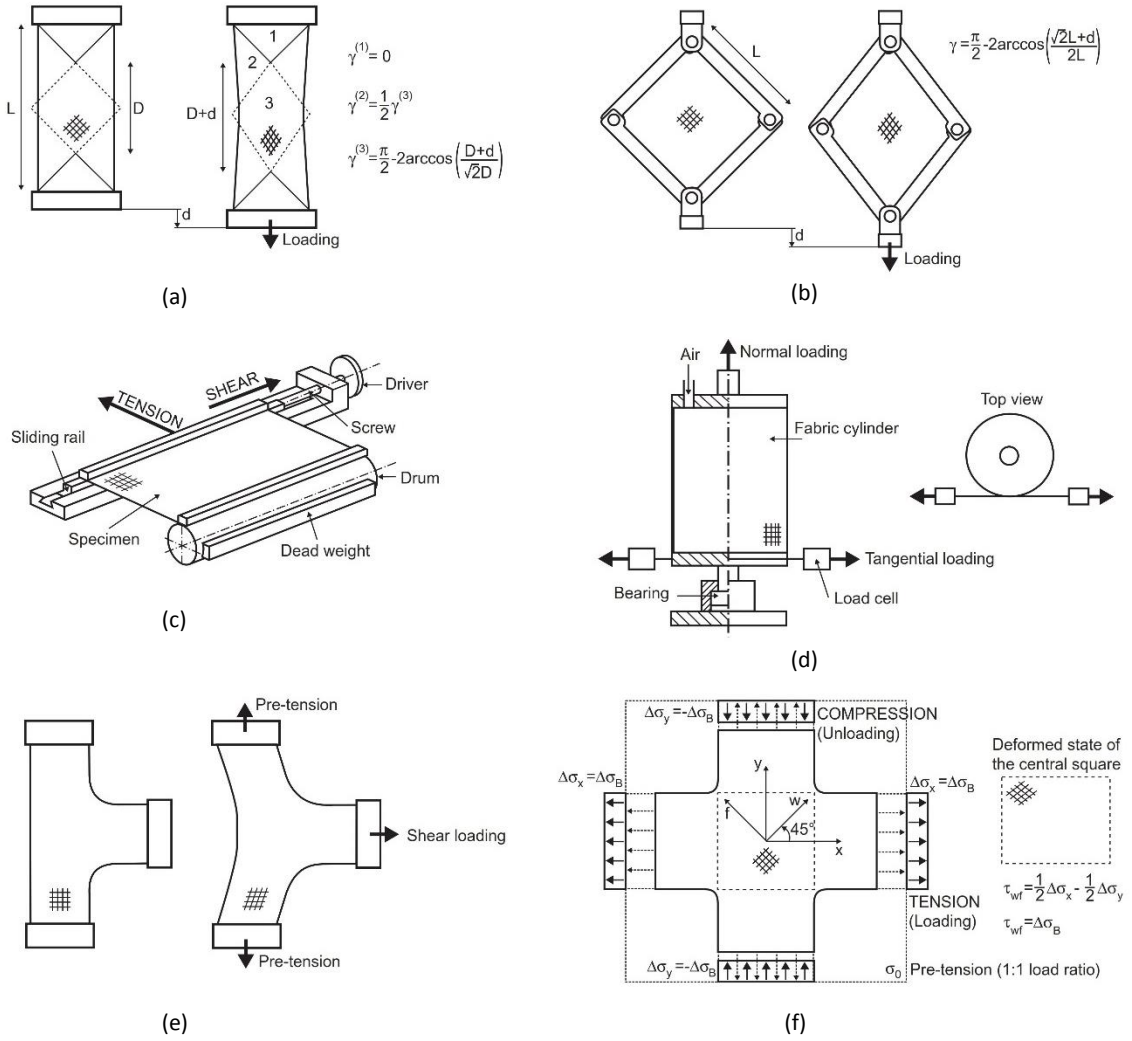

Figure 2.13 Test methods used for the investigation of fabric shear response: (a) bias test; (b) picture frame shear test; (c) KES-F tester; (d) fabric cylinder shear device; (e) T-shaped specimen test; and (f) 45° cruciform test, reproduced from Galliot and Luchsinger (2010a)

An alternative methodology, the 'shear ramp' method, utilises a cruciform specimen in a biaxial test rig (Galliot and Luchsinger, 2010a; Galliot and Luchsinger, 2010b). This approach to shear characterisation produces a non-homogeneous shear strain field and consequently a non-homogeneous shear stress field. Therefore, the complex calculation of a correction factor is required to analyse the test results.

Recently, Harrison *et al.* (2012) developed a biaxially stressed bias test, by applying a load to each side of a bias test specimen by means of an arrangement of clamps and weights. However, in its present form the approach cannot control the load applied by the weights and no assessment of homogeneity of the strain field has been undertaken. A combined test apparatus has also been proposed by Cavallaro *et al.* (2007), but again no demonstration of the homogeneity of the strain field has been presented.

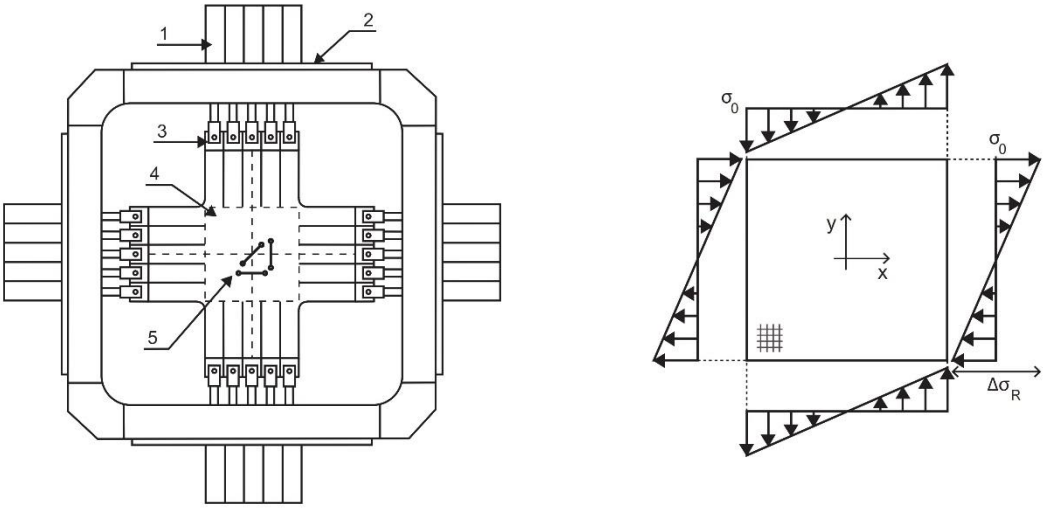

Figure 2.14 Schematic of biaxial test machine used for the shear ramp method and application of shear deformation: (1) actuators; (2) linear bearings; (3) grips; (4) specimen; and (5) extensometers, σ_0 is biaxial pretension and $\Delta\sigma_R$ is variation of tensile stress in the shear ramp, reproduced from Galliot and Luchsinger (2010b)

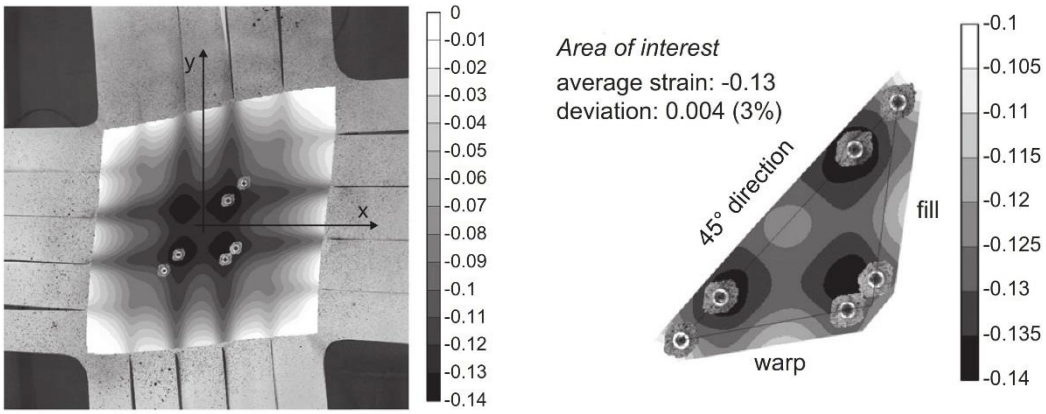

Figure 2.15 Shear strain ε_{xy} in the cruciform specimen obtained with digital image correlation for the shear ramp method (F1002 sample), reproduced from Galliot and Luchsinger (2010b)

It has been suggested that assumptions regarding homogeneity of strain fields during shear deformation should always be validated and optical methods, such as digital image correlation (DIC), may be the only way of assuring homogenous deformation during the testing of woven materials (Lomov *et al.*, 2008). DIC has become a frequently used technique to observe the in-plane deformation of test specimens (Blum and Bögner, 2001; Boisse *et al.*, 2005; Zhu *et al.*, 2007; Cao *et al.*, 2008; Lomov *et al.*, 2008).

Galliot and Luchsinger (2010b) use a DIC technique to assess the homogeneity of the shear strain field in a shear ramp test (Figure 2.15). The investigators consider the strain to be homogenous

over a central area of interest where the deviation in strain is less than 4% of the average strain (of the area). Therefore the stress in this area is also assumed to be homogenous.

The picture frame shear test (Figure 2.13b) (Culpin, 1979; Nguyen *et al.*, 1999; Lebrun *et al.*, 2003; Peng *et al.*, 2004; Farboodmanesh *et al.*, 2005; Cao *et al.*, 2008; Launay *et al.*, 2008; Jackson *et al.*, 2009) allows application of biaxial prestress, which, subject to stress relaxation, can be maintained during a subsequent shear test by clamping the shear specimen along its edges. The frame is intended to subject the specimen to a uniform deformation that should result in a homogenous state of pure shear. Homogenous deformation allows for calculation of the shear stress-strain relationship and definition of the shear stiffness. A further benefit of this method is that the fabric can be biaxially mechanically conditioned (Bridgens *et al.* 2004a) prior to shear testing, to enable medium to long term fabric behaviour to be explored.

Assuming homogenous shear deformation, shear force may be calculated from the kinematics of the frame (Equation 2.1). The shear force is typically normalised with respect to the side length of the specimen (Harrison *et al.*, 2002; Harrison *et al.*, 2004; Peng *et al.*, 2004; Cao *et al.*, 2008). Peng *et al.* (2004) propose a normalisation method based upon an energy method, which for test set ups where the specimen fully fits the frame reduces to the method proposed by Harrison *et al.* (2004) (Equation 2.2).

$$F_s = \frac{P}{2cos\theta}$$ **Equation 2.1**

$$F_s = \frac{P}{2Lcos\theta}$$ **Equation 2.2 (Harrison *et al.*, 2004)**

A number of different picture frame designs currently exist and frame and specimen dimensions vary between laboratories (Cao *et al.*, 2008). All designs have common features, including pinned corner connections and clamping mechanisms to secure the specimens. Typical practice is to mount specimens such that the material is clear of a frame's corners (Figure 2.16a). This prevents localised buckling of the specimen and disruption to the stress field. However, removing the corners is undesirable as it requires the arms and fingers of the sample (which are only subject to uniaxial stress) to transfer shear from the frame to the centre of the specimen (Lebrun *et al.*, 2003). This can result in a high degree of 'lag' between the shear angle of the frame and the shear deformation of the test specimen and deformation may not be homogenous (Figure 2.16b).

Alternatively, the specimen can be fitted such that it fills the frame, though with material removed around the hinged corner connections (Figure 2.16c). Lebrun *et al.* (2003) demonstrated that in this configuration the bending of the yarns near to the clamped edge impacts on the shear angle transferred from the frame into the specimen.

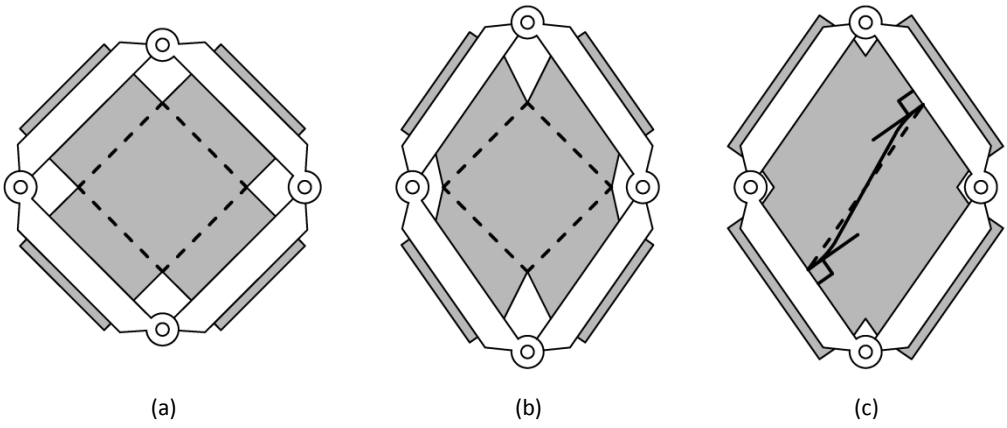

Figure 2.16 Picture frame set-up options: (a) undeformed picture frame with fabric cut away from the corners; (b) deformed picture frame showing retarded biaxial shear deformation; and (c) deformed picture frame with specimen more tightly fitted in frame, illustrations after test photographs by Launay *et al.* (2008)

Bending of the yarns could generate additional tension in the yarns and Hivet and Duong (2011) observed that results of the picture frame test are not repeatable when such tension is induced. However, these tests were for uncoated non-tensioned fabrics and shear testing of architectural fabric is performed with applied pretension on materials with typically higher shear stiffnesses. Consequently, it is anticipated that this effect will be negligible, though nevertheless deformation will be examined for this possible occurrence.

Lebrun *et al.* (2003) propose a modified picture frame test specimen in which tensile loads are applied over a reduced portion of the shearing surface (Figure 2.17). The purpose it to reduce tension in the fibres during shear, i.e. to allow yarn slip (§2.1.2). In the case of architectural fabrics it is necessary to maintain tension. Further, shear force is not transferred from the frame into the specimen along the length of the specimen and no assessment of the homogeneity of the strain field is presented.

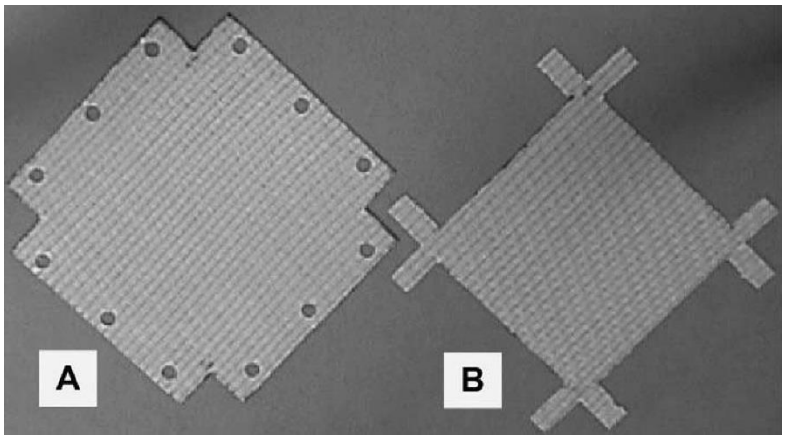

Figure 2.17 Comparison of a typical and a modified picture frame test specimen, reproduced from Lebrun *et al.* (2003)

Two previous studies have used picture frames that allowed for specimen to be fitted such that they completely fill the frame, with no material removed in the corners (Culpin, 1979; Jackson *et al.*, 2009). However, these frame designs which intend the specimen to be fully fitted fail to correctly consider the kinematics of the frame. The centre of the pinned corner connections (about which the frame hinges) are not aligned with the clamped edges of the specimen. This causes a 'scissor effect' resulting in loss of biaxial stress across the specimen and local buckling or crushing of the fabric in the corners of the frame.

To achieve the desired homogenous shear strain, and therefore allow accurate calculation of shear stress, the centre of the pinned connections must align with the clamped edges of the specimen, as described by Bassett *et al.* (1999) (Figure 2.19). However, no practical implementation of a frame design capable of fully fitting a specimen with correct alignment of the hinges has been proposed.

Mohammed *et al.* (2000) investigated the effects of cross-head speed on shear stress strain response and found no dependence. Further, shear behaviour has been shown to be independent of the size of picture frame test used (Liu *et al.*, 2005). However, these are for uncoated materials and do not consider the effect of coating.

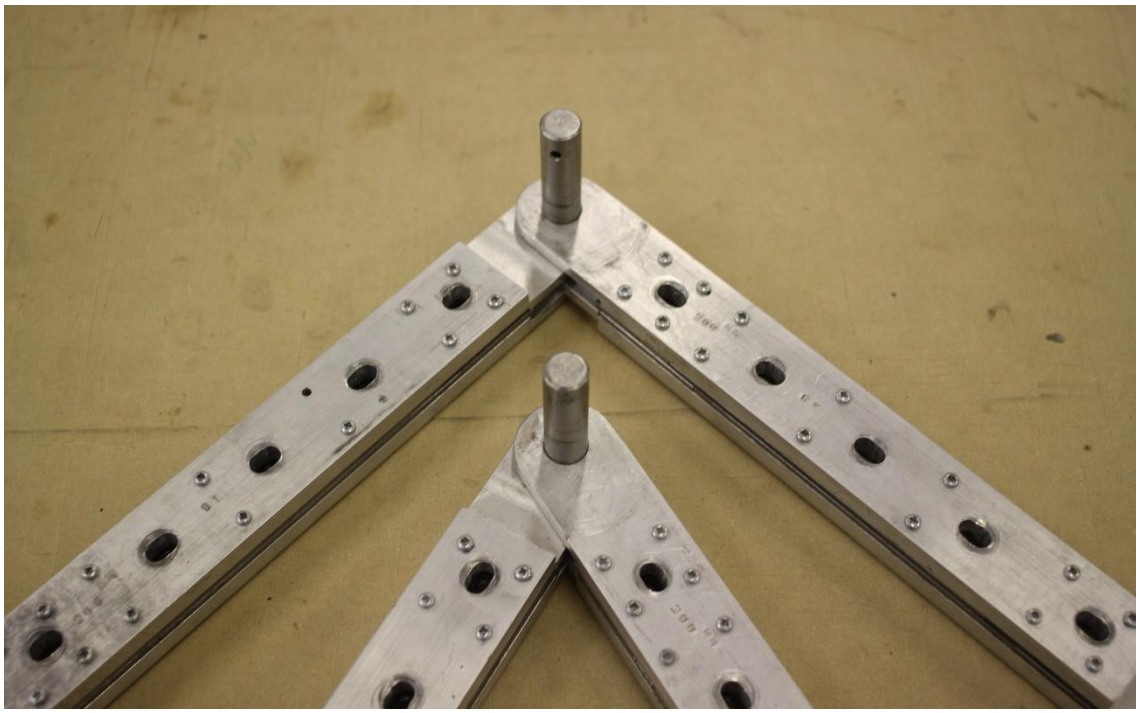

Figure 2.18 Partial view of the frame used by Jackson *et al.* (2009) illustrating the scissoring of the frame with increasing shear angle resulting in a reduction in area bound by the frame and a reduction is clamped edge.

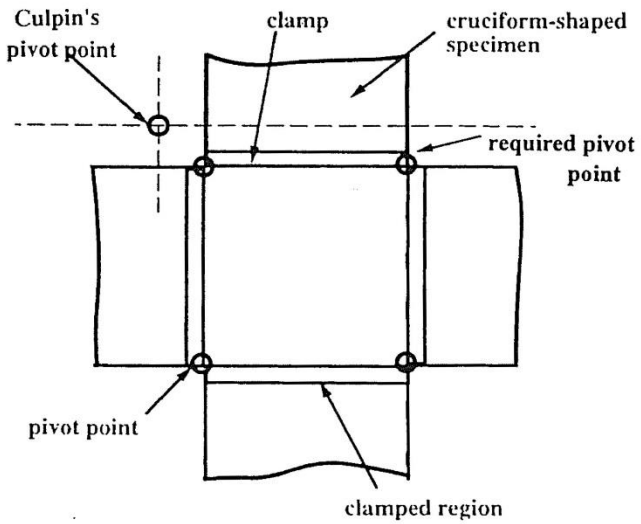

Figure 2.19 Principles of picture frame shear test apparatus proposed, which also illustrates the location of pivot in the design by Culpin (1979), reproduced from Bassett *et al.* (1999)

As mentioned above, the bias extension test cannot apply biaxial tension while shearing the specimen, though for uncoated fabrics tests it is extensively used for investigating shear behaviour (Mohammed *et al.*, 2000; Potter, 2002; Wang, 2002; Zhu *et al.*, 2007; Cao *et al.*, 2008; Launay *et al.*, 2008; Lomov *et al.*, 2008; Hivet and Duong, 2011). Further, several studies considering uncoated fabrics have compared results of bias and shear tests (Boisse *et al.*, 2001; Lebrun *et al.*, 2003; Sharma *et al.*, 2003; Cao *et al.*, 2008).

A comparative study performed by Cao *et al.* (2008) suggests that deformation mechanisms are more accurately reproduced in the picture frame test, but that bias testing is an adequate methodology for determining locking angles. The investigators performed a bench mark study of shear test set ups and bias test set ups at different institutions and observed similar shear behaviours for the different test methods for uncoated fabrics. However, the methodologies impose different loading conditions of the test specimens and biaxial load has been shown to influence the locking angles. Further, the concept of lock up is not expected to be the same with coated materials (§2.1.2).

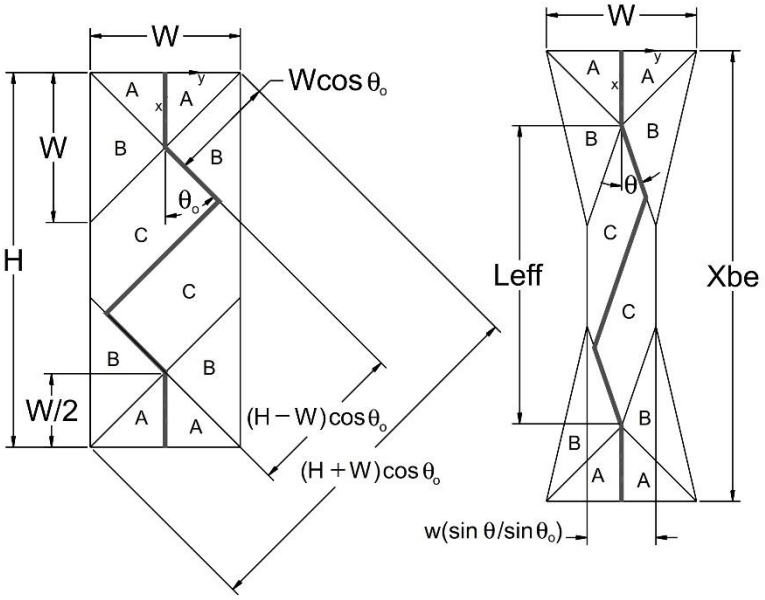

Figure 2.20 Schematics showing the underformed (left) and deformed (right) shapes of the specimen in the bias extension test, reproduced from Lebrun *et al.* (2003)

Lebrun *et al.* (2003) identified distinct regions of deformation in the plane of the bias test specimen (Figure 2.20). The shear angle in region C is assumed to be double that in region B and no shear occurs in region A.

An expression for the shear angle can be derived from the height and width of the test specimen, *H*, *W*, and the displacement applied by the test rig during a test, δ (Equation 2.3). Launay *et al.* (2008) propose an iterative approach to calculate the shear force as a function of changing shear angle, γ, from the applied load, *P* (Equation 2.4). This calculation permits comparison of picture frame and bias extension results as it determines normalised shear force per unit length i.e. is the same the normalised picture frame shear force (Equation 2.2). The approach accounts for the different regions of shear. Different aspects of the specimen are used in the bias test (Table 2.5). The groups that performed tests on unbalanced fabrics did so only with 2:1 samples.

$$cos\theta = \frac{(H+\delta)-W}{2(H-W)cos\theta_0}$$

Equation 2.3
(Lebrun et al., 2003)

$$F_s(\gamma) = \frac{1}{2H-3Wcos\gamma}\left(\left(\frac{H}{W}-1\right)\cdot P\cdot\left(cos\frac{\gamma}{2}-sin\frac{\gamma}{2}\right) - W\cdot F_s\left(\frac{\gamma}{2}\right)cos\frac{\gamma}{2}\right)$$

Equation 2.4
(Launay *et al.*, 2008)

Table 2.5 Bias test specimen size, adapted from Cao *et al.* (2008)

Group	Material	Height, H (mm)	Width, W (mm)	W:L
Hong Kong University of Science and Technology	Plain weave	230	115	2:1
INSA-Lyon, France	Plain weave	230	115	2:1
		300	100	3:1
		450	150	3:1
	Balanced twill weave	300	150	2:1
		300	100	3:1
		450	150	3:1
	Unbalanced	400	200	2:1
Northwestern University, USA	Plain weave	230	115	2:1
	Balanced twill	240	120	2:1
University of Nottingham, UK	Plain weave	200	100	2:1
		250	100	2.5:1
		300	100	3:1
	Unbalanced	200	100	2:1
	Twill weave	250	100	2.5:1
		300	100	3:1

2.3 Predictive fabric modelling

Generally, biaxial fabric models are developed to suit one of two purposes. The first purpose is to represent biaxial test data, with predictions made only between experimental data points obtained through biaxial testing. The second purpose is to predict the biaxial fabric behaviour without having biaxial test data available. It is the second of these two types of model that is of interest here, as models which require biaxial test data inherently do not reduce the need for biaxial testing.

2.3.1 The unit cell

Fabric models describe woven materials at one or more hierarchical levels (Table 2.6) (Lomov *et al.*, 2001; Lomov *et al.*, 2003a). Models which establish a description of the woven yarns typically describe a repeatable area of the weave pattern known as the unit cell and will simplify the shape of the yarns and the crimp (Kemp, 1958; Grosberg and Park, 1966; Menges and Meffert, 1976; Testa *et al.*, 1978; Lomov *et al.*, 2003a; Boisse *et al.*, 2005; Bridgens, 2005; Liu *et al.*, 2005; Badel *et al.*, 2007; Pargana *et al.*, 2007; Potluri and Sagar, 2008; Dolatabadi and Kovař, 2009b; Grujicic *et al.*, 2009). Different investigators consider different areas of the weave pattern (Figure 2.21).

Table 2.6 Hierarchy of fabric structure and models, adapted from Lomov *et al.* (2001)

Structure	Elements	Model
Yarn	Fibres	Fibre distribution in the yarn and its change under load/strain Mechanical properties of the yarn
Unit cell	Yarns	Geometry of the yarns and its change under load/strain Mechanical behaviour of the fabric under repeat loading
Fabric	Unit cell	Mechanical properties (stiffness/strength) Permeability tensor

Models which describe the internal woven architecture follow on from an early work by Peirce (1937), who defined the unit cell using measurements of the yarn geometry (Figure 2.22). Peirce (1937) also defined crimp as "*the percentage excess length of the yarn axis over the cloth length*" and identified crimp interchange as a fundamental mechanism governing lateral contraction and elongation of a woven material.

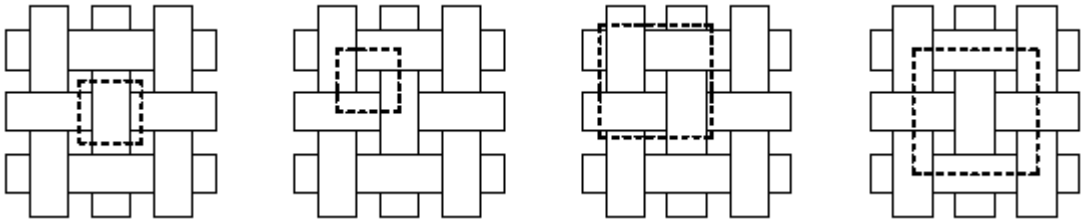

Figure 2.21 Examples of area of weave pattern used in unit cell representations, from (a) Pargana *et al.* (2007), (b) McBride and Chen (1997), (c) Skelton (1980) and (d) Nguyen *et al.* (1999)

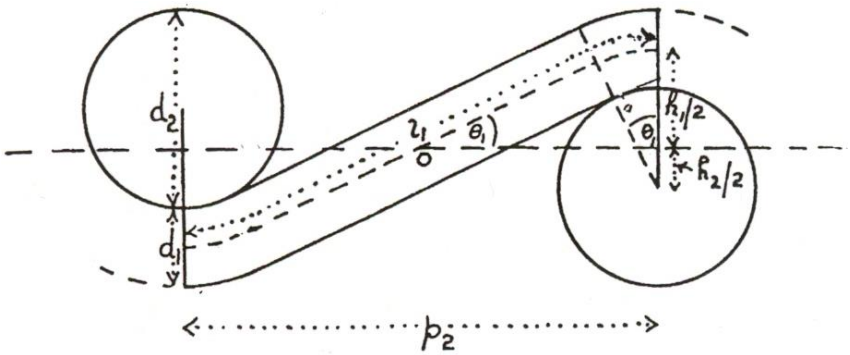

Figure 2.22 Early description of the fabric unit cell with circular yarn cross sections, illustrating the notation for a plain weave fabric, reproduced from Peirce (1937)

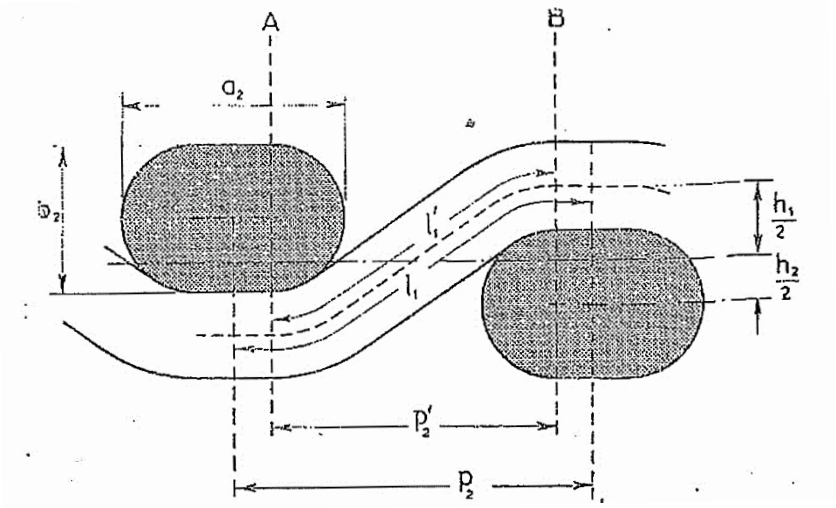

Figure 2.23 Racetrack yarn geometry used as the basis for an extension of the work of Peirce (1937), reproduced from Kemp (1958)

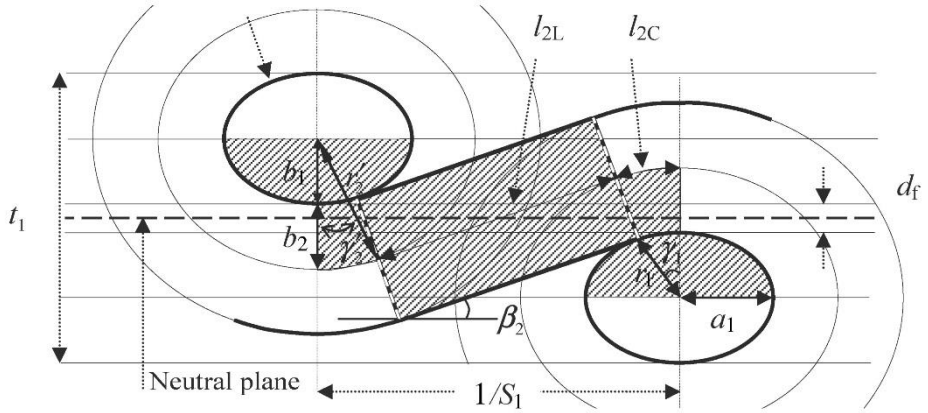

Figure 2.24 Elliptical yarn geometry employed in a model to determine geometry from experimental test data of fabric behaviour, reproduced from Dolatabadi and Kovař (2009a)

The circular yarn cross sections proposed by Peirce (1937) are not a realistic approximation of real yarns, at least for architectural fabrics which are substantially flat (Figure 1.2). Subsequent models have sought to improve the representation of yarn geometry: Kemp (1958) proposes racetrack cross sections (Figure 2.23); Hearle and Shanahan (1978) develop and early lenticular model; Dolatabadi and Kovař (2009a) employ elliptical cross sections (Figure 2.24); and Pargana *et al.* (2000) propose rhomboids (Figure 2.27). However, none of these representations offer the most realistic approximation of the weave structure of typical architectural fabrics, at least by visual inspection. Note that due to gaps between adjacent yarns, sections of the undulating yarn which are not in contact with an orthogonal yarn's cross section are provided within the models of the aforementioned works as straight sections of yarn (Figure 2.22 to Figure 2.24).

Sinusoidal representation (McBride and Chen, 1997; Wang, 2002; Bridgens, 2005) offers the best visual approximation for architectural fabrics. Further, sinusoidal representation permits consistent description of the yarn cross section and the undulating yarn (Figure 2.25 and Equation 2.5 to Equation 2.8). This allows for relationships between yarn geometry and applied forces. However, by using a continuous sine waveform the sections between the yarns are not straight. Straight sections could be included, but this may be unnecessary in the case of architectural fabrics as the yarns are tightly woven and the non-contact lengths are substantially non-existent. Further, where orthogonal yarns are not in contact the curvature of the sine curve is low.

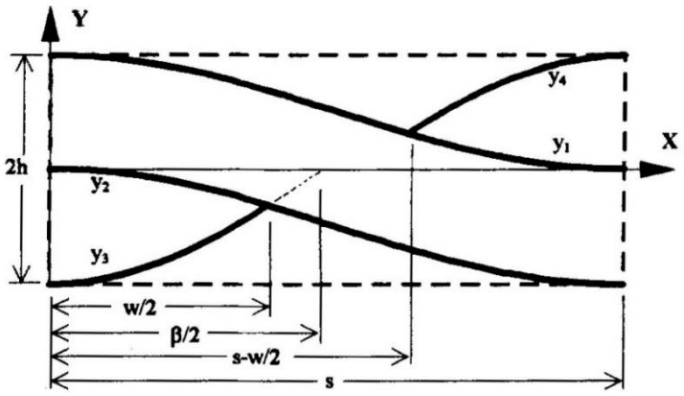

Figure 2.25 Cross sectional view of a sinusoidal unit cell in which four curves are used to describe the yarn cross section and the yarn waveform, reproduced from McBride and Chen (1997)

$$y_{1(x)} = \frac{h}{2}\left[cos\frac{\pi x}{s} + 1\right] \qquad (0 < x < s)$$

Equation 2.5
(McBride and Chen, 1997)

$$y_{2(x)} = \frac{h}{2}\left[cos\frac{\pi x}{s} - 1\right] \qquad (0 < x < s)$$

Equation 2.6
(McBride and Chen, 1997)

$$y_{3(x)} = -h\,cos\left[\frac{\pi x}{\beta}\right] \qquad \left(0 < x < \frac{w}{2}\right)$$

Equation 2.7
(McBride and Chen, 1997)

$$y_{4(x)} = -h\,cos\left[\frac{\pi\left(x - (s-\beta)\right)}{\beta}\right] \qquad \left(s - \frac{w}{2} < x < s\right)$$

Equation 2.8
(McBride and Chen, 1997)

Sawtooth models (Kawabata *et al.*, 1973a; Menges and Meffert, 1976; Stubbs and Fluss, 1980; Bridgens, 2005) offer a simplified representation of the unit cell in which the yarn waveforms are represented as bar linkages (Figure 2.27). Geometric parameters which define sawtooth models can be easily defined, but these models cannot realistically describe the yarn extension and change in geometry of a continuously undulating yarn.

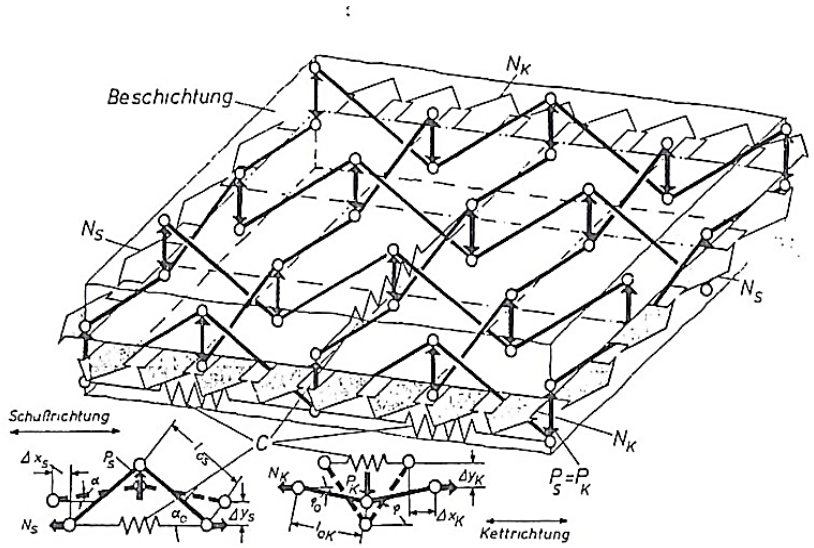

Figure 2.26 Sawtooth model for PVC coated polyester fabrics under biaxial stress, the model comprises bars connected by flexible joints, reproduced from Menges and Meffert (1976)

2.3.2 Modelling biaxial behaviour

Methods to carry out the analsysis of woven fabrics fall into two main catergories: analytical models and numical models. Considering first analyitical models, Peirce (1937) developed mathematical expressions to relate changes to the fabric geometry to strains applied in the plane of the fabric with the assumption that the yarns are axially ridged. Models which are built on the work of Peirce (1937) include yarn extension (Olofsson, 1964; Freeston *et al.*, 1967; Menges and Meffert, 1976; Testa *et al.*, 1978) and later models attempt to incorporate further deformation mechanisms (Kawabata *et al.*, 1973a; Kato *et al.*, 1999; Pargana *et al.*, 2000; Lomov *et al.*, 2003a; Pargana *et al.*, 2007; Dolatabadi and Kovař, 2009a). For example, Lomov *et al.* (2003a) develops a mathematical model which incorporates tension, friction, vertical and lateral compression and torsion of the yarns.

It is suggested that yarn crushing stiffness is important to accurately predict real fabric behaviour (Pargana *et al.*, 2000). Despite this, crushing stiffness is considered by only a few models (Kawabata *et al.*, 1973a; Kato *et al.*, 1999; Pargana *et al.*, 2007). By way of example, Pargana *et al.* (2007) incorporate yarn crushing as an elastic link across the thickness of a yarn (Figure 2.27). The models which do include yarn crushing stiffness are calibrated against test data, so the modelling approaches they present are not suitable for this project.

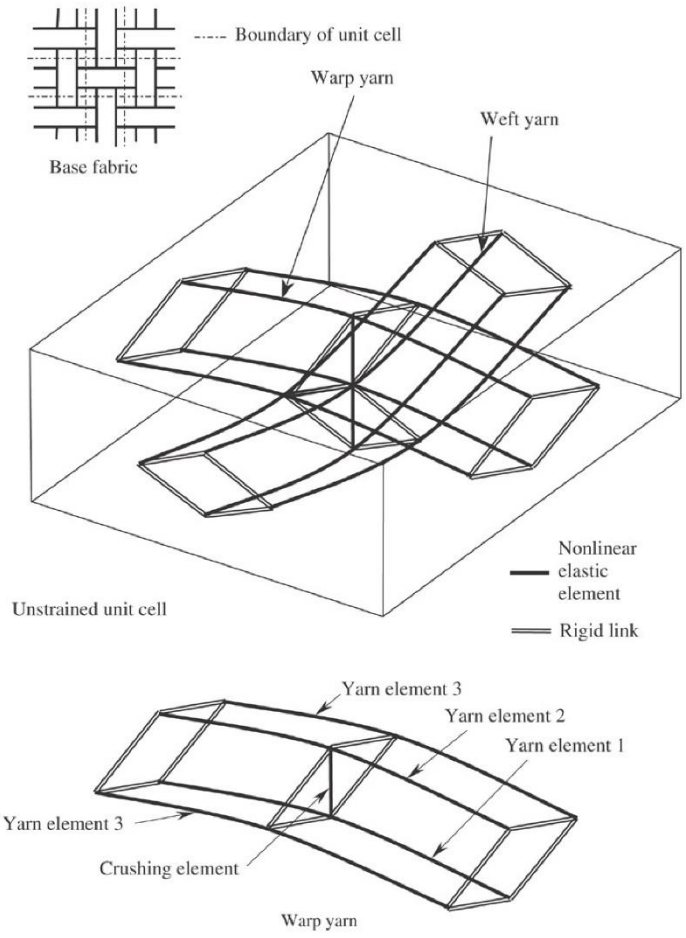

Figure 2.27 Unit cell model incorporating yarn crushing stiffness element, reproduced from Pargana *et al.* (2007)

Additionally, there is no standard method for determining crushing stiffness, which at least in part may explain why it is often negated. However, methods for determining crushing are described by Sasai and Kawabata (1985), so considering *coated* fabrics, such tests could be performed on as-produced yarns or yarns removed from their polymeric coating. This would be problematic, as yarn behaviour is affected by the coating as it impregnates and encapsulates the yarns (§2.1.1), thus the results of tests on yarns without coating would not represent the behaviour of the yarns in situ. Further, yarns are likely to be damaged in the case where the coating is removed. Determination of crushing stiffness for architectural fabrics is unlikely to be easily achieved.

Menges and Meffert (1976) propose a simplified analytical approach to model the relationship between forces and geometry of a woven fabric (Figure 2.26) in which only "principal" deformation mechanisms: crimp interexchange, yarn extension and coating extensions, are modelled. The investigators' sawtooth model represents the deformation of yarns and the coating under biaxial load. Secant moduli are used to model the viscoelastic behaviour of the yarns and a spring constant represents the restraint imposed by the coating. Springs representing the coating are aligned with the warp and fill yarn directions. This model forms the basis of later analytical models (Testa *et al.*,

1978; Bridgens, 2005). Spring constants are not accurately determined for coating stiffness and the models do not predict the non-linear behaviour. As mentioned above, these models cannot realistically describe yarn extension. Further, they also represent the out of plane force at the yarn cross over as a point load act. However, despite their simplification these sawtooth models achieve good correlation with test data.

In an attempt to improve upon the sawtooth approach, Bridgens (2005) proposes a sine curve discretised into straight linkages. A sinusoidal representation of the model having a similar formulation to the sawtooth models is also adopted by Wang (2002). These models also typically neglect bending stiffness of the yarns (Menges and Meffert, 1976; Testa *et al.*, 1978; Bridgens, 2005; Pargana *et al.*, 2007).

Considering numerical models, Blackletter *et al.* (1993) presented an early application of the finite element method to evaluate the mechanical behaviour of woven fabrics. Representing the unit cell as 256 20-noded hexahedral elements, Blackletter *et al.* (1993) developed model which achieved good agreement with comparative test results. This model relied up on a further FE model to determine the behaviour of individual yarns and determination of a single load condition required 30mins of computing time with available 1990's computer hardware. Subsequent numerical models successfully sought to reduce solution times (Chapman and Whitcomb; Woo and Whitcomb, 1996) any many more numerical models have since been developed for woven materials, particularly woven fabrics used in reinforced composite forming (Glaessgen *et al.*, 1996; Gasser and Hivot 2001; Durville 2003; Šejnoha and Zeman, 2008; Ivanov *et al.*, 2011, Green *et al*., 2014).

Ansar *et al.* (2011) recently presented an exceptionally thorough review of the numerical modelling techniques for characterising the geometry, mechanical behaviour and impact behaviour woven composites. An earlier review was also presented by Crookston *et al.* (2005). The principal advantage of these numerical FE models is that they offer realistic representation of the yarn waveforms and the yarn contact, as they do not require the simplifications of the analytical models described above. However, it has been long established that determination of yarn crushing stiffness and the relationship between transverse yarns compress and longitudinal tension is an essential requirement of numerical models (Boisse *et al.*, 2001, Bridgens, 2005).

Bridgens' (2005) review of fabric models identified the means to determine yarn parameters, namely: 1) yarn testing by removal of the yarns from the fabric; 2) test data form as produced yarns; and 3) calibration of the model against test data. However, removal of the yarn from the fabric is time consuming and difficult for a coated fabric, notwithstanding the fact that the in situ behaviour will differ to the behaviour of the yarns once removed from the fabric. Further, as produced yarn behaviour will also differ from that of the yarn once it is incorporated in a matrix of coating and interwoven with other yarns, therefore these two methods of yarn testing cannot easily and reliably

determine the yarn behaviour of the in situ yarns of a woven fabric. Further, calibration is not an option if the purpose of the model is to negate the need for biaxial testing.

Moreover, FE models are constructed having specific geometric descriptions and material inputs for specific fabrics, so they are inherently difficult to modify for different fabrics. Consequently, numerical FE models cannot provide design engineers with a model which requires only easily to obtain input parameters, nor model which is capable of reverse engineering fabric, i.e. enable designers to determine the yarn properties for a fabric with particular biaxial mechanical behaviour. Therefore, an analytic mechanical model will be developed here.

2.3.3 Modelling shear behaviour

A number of meso-scale shear models have been developed to predict the shear properties of *uncoated* woven materials (Mack and Taylor, 1956; Grosberg and Park, 1966; Kawabata *et al.*, 1973b; Skelton, 1976; Leaf and Sheta, 1984; McBride and Chen, 1997; Nguyen *et al.*, 1999; Liu *et al.*, 2004; Liu *et al.*, 2005; Sun and Pan, 2005; Lomov and Verpoest, 2006). Early analytical shear models seek to identity the limit of shear deformation, i.e. the onset of wrinkling, for uncoated fabrics using geometrical parameters (Mack and Taylor, 1956; Grosberg and Park, 1966; Skelton, 1976). The model by Mack and Taylor (1956) allows unlimited rotations of the yarns about the yarn cross overs and later work introduces mechanisms to limit the degree of shear deformation, such as modelling side-by-side yarn contact (Figure 2.28) (Skelton, 1976; Skelton, 1980).

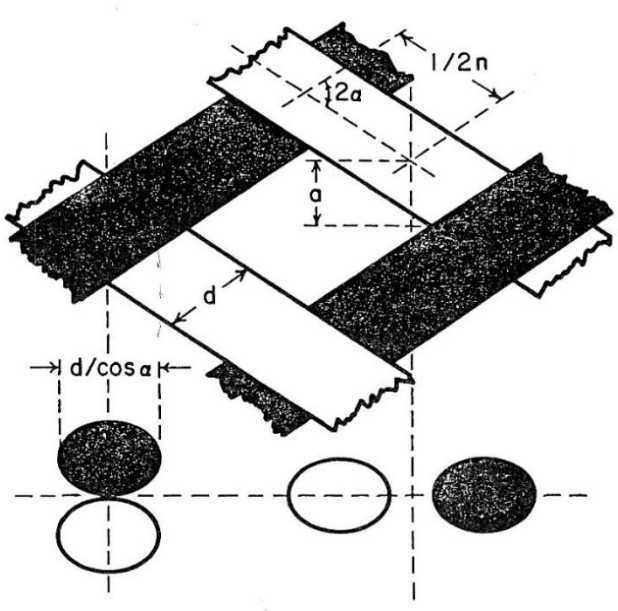

Figure 2.28 Shearing of interwoven incompressible cylinders in which a limiting shear deformation is imposed, reproduced from Skelton (1980)

The modelling of side-by-side contact imposes a simplification which does not consider the out-of-plane dimension. In reality, yarns will contact one another at lower angles of shear than such models will predict. Prodromou and Chen (1997) demonstrate that if yarns are represented in this way, i.e. as rigid beam elements, models may not accurately represent deformation at higher angles of shear or beyond the angle at which the onset of wrinkling will occur. However, this may not be relevant in the context of architectural fabrics were angles of deformation are relatively lower than for rigid composite forming. Further, models which assume rigid beam elements achieve good correlation with test results (Grosberg and Park, 1966; Skelton, 1980; Liu *et al.*, 2004; Liu *et al.*, 2005).

Sun and Pan (2005) developed a shear model based on the deformation modes described by Grosberg and Park (1966), but which incorporates the out-of-plane dimension of the yarns. However, while the model more closely reflects the behaviour of real woven fabrics compared to the model of Grosberg and Park (1966), the later model relies upon a constant for the torsional rigidity of the yarns about their longitudinal axis which is difficult to accurately determine. McBride and Chen (1997) develop a sinusoidal model (Figure 2.24) for predicting elastic properties of woven yarns by calculating changes in the yarn cross sections upon deformation of the unit cell for uncoated fabrics. The calculated deformations are used in a fibre bundle model (Cai and Gutowski, 1992) to determine the elastic properties.

Building on the model proposed by McBride and Chen (1997), Liu *et al.* (2004) and Liu *et al.* (2005) propose analytical shear models for uncoated fabrics that predict lateral compaction (Equation 2.9) and frictional resistance (Equation 2.10), respectively. The models consider moment equilibrium of the forces acting about the centre of each yarn intersection (Figure 2.29). Yarn compaction is also refers to compaction in the out of place direction as if the fabric is compressed between to plates fabric is compressed between two plates (Potluri and Sagar, 2008). The compaction force, F_c, is a function of the width of the yarn, which chances with change in shear angle, and the fibre volume fraction. The width of the yarn changes with the shear angle.

The compaction force is the product of stress in the transverse direction of the yarn is obtained from the inverse of the compliance tensor, calculated after Cai and Gutowski (1992). A coefficient of friction, μ, is required for calculating the moment due to compaction. The limitation of these models is that they have identical warp and fill yarn geometries.

All of the aforementioned analytical models require either calibration against test data or experimental determination of empirical values at the yarn and coating level.

$$M_c = 2\int_{(sin\gamma-1)l/2}^{(1+\sin\gamma)l/2} F_c\, x\, dx$$

$$= [F_c\, x^2]^{(1+\sin\gamma)l/2} - [F_c\, x^2]^{(sin\gamma-1)l/2}$$

$$= F_c\left[\left((1+sin(\gamma))\frac{l}{2}\right)^2 - \left((sin(\gamma)-1)\frac{l}{2}\right)^2\right]$$

$$= F_c\left[\left(\frac{l^2}{4}+\frac{l^2}{2}\sin(\gamma)+\frac{l^2}{4}sin^2(\gamma)\right)-\left(\frac{l^2}{4}-\frac{l^2}{2}\sin(\gamma)+\frac{l^2}{4}sin^2(\gamma)\right)\right]$$

$$= l^2 F_c \sin(\gamma)$$

Equation 2.9

(Liu *et al.*, 2005)

$$M_F = 4\int_0^{\pi/2}\int_0^{w/2\cos(\theta-\varphi)} \frac{F_f}{A} R^2\, dR\, d\varphi$$

$$= 4\int_0^{\pi/2} \frac{F_f}{A}\cdot\left[\frac{R^3}{3}\right]^{w/2\cos(\theta-\varphi)} d\varphi$$

$$= 4\int_0^{\pi/2} \frac{F_f}{A}\cdot\frac{w^3}{3\times 8cos^3(\theta-\varphi)}\, d\varphi$$

$$= \frac{1}{6}\int_0^{\pi/2} \frac{F_f}{w^2}cos(\gamma)\cdot\frac{w^3}{8cos^3(\theta-\varphi)}\, d\varphi$$

$$= \frac{1}{6}\int_0^{\pi/2} \mu\pi f_y \cdot w\cdot cos(\gamma)\cdot\frac{d\varphi}{cos^3(\theta-\varphi)}$$

$$= \frac{1}{6}\mu\pi w f_y cos(\gamma)\int_0^{\pi/2}\frac{d\varphi}{cos^3(\theta-\varphi)}$$

$$= \frac{1}{6}\mu\pi w f_y I cos(\gamma)$$

Equation 2.10

(Liu *et al.*, 2004)

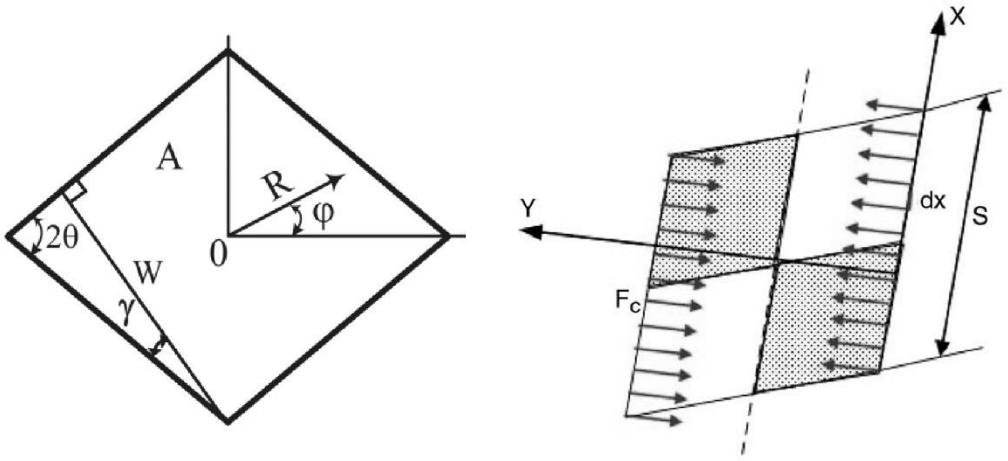

Figure 2.29 Integration over the area of the crossover to calculate the friction shear resistance moment (left), reproduced from Liu *et al.* (2004) and deformed unit cell for plain weave to calculate shear compaction resistance moment (right), reproduced from Liu *et al.* (2005)

Relatively fewer analytical models consider shear of coated materials (Yu *et al.*, 1994; Nguyen *et al.*, 1999; Pargana *et al.*, 2000; Tanov and Brueggert, 2003; Pargana *et al.*, 2007; Ramgulam *et al.*, 2008). Shear of the coating may be modelled using a spring which acts diagonally between yarn crossovers (Yu *et al.*, 1994; Tanov and Brueggert, 2003). Spring have also been be added at the contact edge (Nguyen *et al.*, 1999). The latter approach is more realistic, though spring constants must be determined experimentally or calibrated against data.

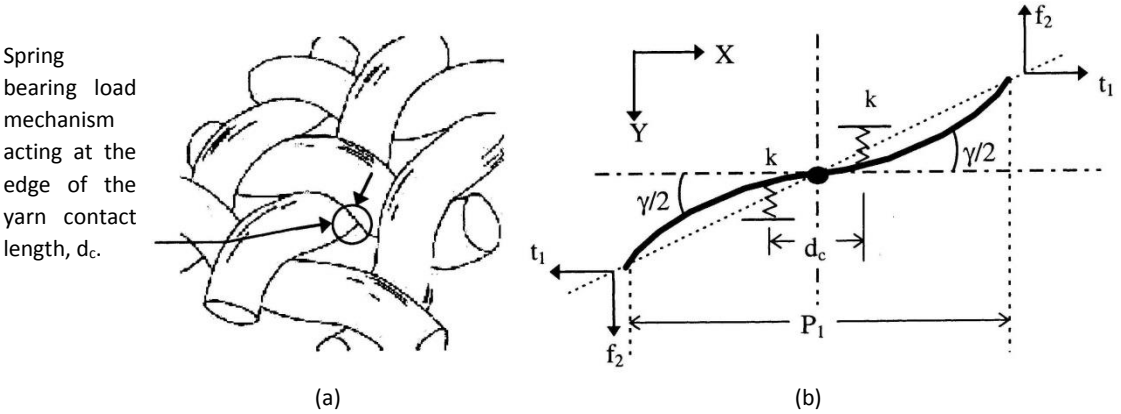

Figure 2.30 Point bearing loads acting at the edge of the cross-over contact length on a unit cell: (a) point shown on fabric; and (b) Representation in the form of a beam deflection, reproduced from Nguyen *et al.* (1999)

Ramgulam *et al.* (2008) developed an coated shear model for balanced fabrics to predict shear beyond the initial region described by Grosberg and Park (1966). However, the formulation (Equation 2.11) requires determination of the bending stiffness of the yarns, E_b. Determining bending stiffness would have the same problems as for crushing stiffness (§2.3.2). Further, the work does not address how to accurately determine the normal force at the yarn crossovers, Fy.

For architectural fabrics, normal forces arising from yarn tension at the crossover and the influence of the coating is likely to be more significant than the influence of yarn bending, which is assumed to be negligible (§2.1.1).

$$F\ sin\theta = E_b sin^2(45-\theta)\cdot p + \frac{1}{3}\mu F_y a$$

Equation 2.11
(Ramgulam *et al.*, 2008)

Macroscopic models have been developed that do not consider the internal woven geometry (Lo and Hu, 2002; King *et al.*, 2005; Peng and Cao, 2005). These models have the advantage as they allow modelling of complex components, i.e. 3D composite moulded parts, while maintaining an adequate level of computational efficiency. Macro models consider the fabric as a continuum, a typical example is proposed by Lo and Hu (2002) in which behaviour is derived from theoretical transformations of compliance in the principal and bias directions of the fabric to give an expression for the shear modulus of the fabric in any axes direction (Equation 2.12). While comparison of the results with experimentally obtained data demonstrate good agreement (Figure 2.31), the model is dependent upon the availability of accurate test data. Thus, though such models may be useful to fill in gaps between test data, they are not capable of truly predicting shear characteristics. For any given fabric of interest, testing is needed.

$$\frac{1}{G_\theta} = \left(\frac{4}{G_{45}}\right) cos^2\theta\ sin^2\theta + \frac{1}{G}(cos^2\theta\ sin^2\theta)^2$$

Equation 2.12
(Lo and Hu, 2002)

where G_θ is the shear modulus in a given axis direction denoted by θ, G45 the shear modulus in the bias direction, G is the shear modulus in the principal axes (defined by the yarn direction) and θ is the angle between the yarn directions and the axes of interest

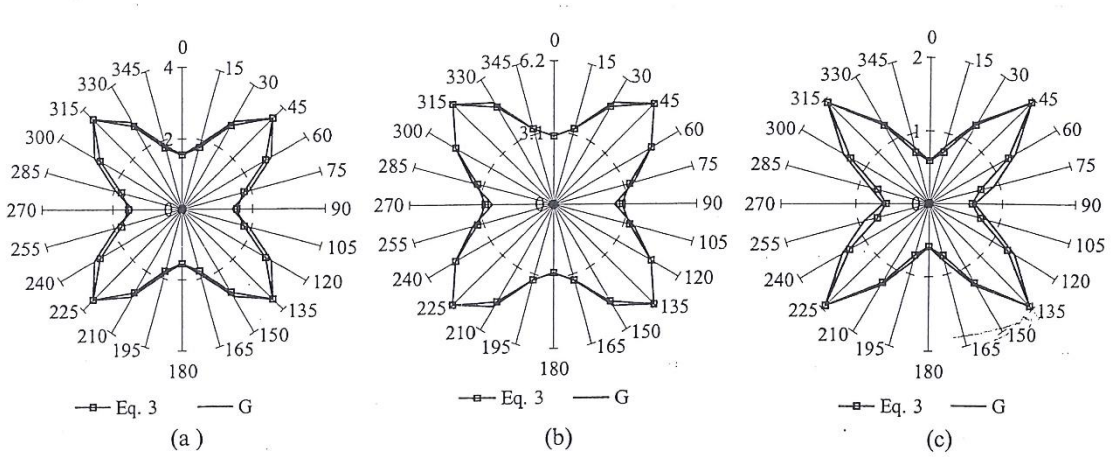

Figure 2.31 Theoretical and experimental results of fabric shear moduli: (a) plain weave, (b) twill weave, and (c) satin weave, Eq. 3 is Equation 2.12, reproduced from Lo and Hu (2002)

A further alternative to analytical approaches is to assume linear approximation accounting for constant torque, T_r, and frictional resistance as a linear function of the shear angle (Kawabata et al., 1973b; Kawabata, 1989). Kawabata *et al.* (1973b) derived formulations for both relaxed fabrics (Equation 2.13) and fabrics where tension is applied to the yarns (Equation 2.14). The obvious drawback is that calibration constants, C_1 to C_4, must be matched against real test data.

$$T_r = T_{r0} \pm C_1 F_c \pm C_2 F_c \pm C_2 F_c \varphi + C_3 \varphi + C_4 \varphi F_c$$

Equation 2.13
(Kawabata *et al.*, 1973b)

$$T_r = T_{r0} \pm (C_1 + C_2 \varphi) F_c + (C_3 + C_4 F_c) \varphi$$

Equation 2.14
(Kawabata *et al.*, 1973b)

Finite element models are also used to simulate the complex yarn interactions (Page and Wang, 2000; Tanov and Brueggert, 2003; Cavallaro *et al.*, 2007; Durville, 2008; Potluri and Sagar, 2008; Grujicic *et al.*, 2009; Nguyen *et al.*, 2013). The advantage of these models is they do not require the necessary simplifications of analytical models, i.e. there is no requirement to assume a description of the yarn waveform or represent the coating as a spring. However, finite element models require accurate determination of the yarn and coating properties and are developed for specific fabrics. Establishing the required yarn tensile and crushing properties is critical, although difficult as described in §2.3.2. Therefore, an analytical model will be developed for ease of use and to be used more generally for many architectural fabrics.

2.4 Summary

Biaxial and shear behaviour of architectural fabrics is non-linear, inelastic and hysteretic due to interactions of the woven yarns and the polymeric coatings. Coatings limit yarn movements causing the behaviour of coated fabrics to be fundamentally different to the behaviour of uncoated fabrics. Much of the work concerning testing and modelling of woven fabrics is directed to uncoated materials, particularly materials used for rigid composites. Uncoated fabrics exhibit lower shear stiffnesses and are tested to higher angles of shear deformation which are required to form complex three-dimensional composite parts.

Accurate and reliable testing methodologies are needed to reduce uncertainty associated with material behaviour in the design and analysis of tensile fabric structures. In-plane biaxial testing is the de facto industry standard for determining biaxial behaviour of architectural fabrics. A biaxial test rig developed by Bridgens (2005) and Newcastle University is to be used for determining biaxial behaviour of materials used in the course of this project. However, there is no British or European standard and little published guidance for characterising shear behaviour of coated woven fabrics. Consequently, shear behaviour is poorly understood and broad assumptions are made regarding shear of these materials. Shear stiffness is routinely assumed to be linear for coated fabrics despite it being know that this not the case. Understanding the limits of shear deformation is required determine the limits of shear deformation, i.e. the double curvature, that can be achieved. Further, while architectural fabrics when in use are subject to biaxial stress and shear deformation, there have been no studies to investigate the effect of the level biaxial pretension on these materials.

Comparing the available shear methodologies demonstrates the suitability of the picture frame test for characterising shear behaviour of architectural fabrics. The picture frame test apparatus enables the simultaneous application of biaxial tension and shear deformation necessary to accurately simulate the in situ behaviour of architectural fabrics. The comparison also highlights tests which designers may wish to avoid, such as the KES-F test, the bias test and T-shaped specimen test, which cannot apply biaxial tension during shearing. Bassett et al. (1999) proposed a conceptual picture frame design of which no practical embodiment has been developed.

Comparative testing of the picture frame test and the bias extension test for uncoated fabrics has shown similar material behaviour despite the methodologies imposing different loading conditions upon test specimens. No such comparison has been perform with coated woven fabrics.

An alternative to using expensive experimental testing to determine the necessary material properties are predictive models. Existing mechanical unit cell models have been used to replicate test data and predict in-plane biaxial and shear behaviour of woven materials. However, data produced using existing predicted models is not currently used in design of tensile fabric structures and many models are not intended to predict the stress-strain behaviours of coated architectural

fabrics. Bridgens (2005) developed a predictive unit cell model for architectural fabrics based on sawtooth model proposed by Menges and Meffert (1976). Although, these models cannot model the yarn waveforms as realistically as finite element models, they enable the development of more general models that do not require against calibration against test data. Models that can sufficiently replicate the results of experimental testing offer time and cost savings to designers.

Chapter 3:
A shear test methodology for architectural fabrics

Contents

Figures

Tables

3.1 Introduction

Figure 3.1 Milk Market, Limerick, a conic fabric structural form showing the anticlastic (doubly curved with opposite curvature in perpendicular directions) shape achieved by shearing the flat fabric panels during installation. © Schlaich Bergermann und Partner 2011

Flat panels of fabric must undergo shear deformation to achieve the curved anticlastic forms required when constructing a tensile fabric structure (Figure 3.1). Understanding and quantifying shear behaviour of architectural fabrics is important to design engineers as large shear deformations are inherent in fabric structures, both during installation and under imposed loading (§2.1.2).

Accurate determination of shear stiffness will allow for the improved simulation (e.g. though finite element analysis) of deflection and formability of tensile fabric structures as well as the avoidance of wrinkling. Therefore, safer and more efficient structural solutions will be possible and designers will be able to explore more innovative architectural forms.

This chapter presents the design of a novel picture frame shear apparatus. The picture frame test is suitable for replicating the in situ behaviour of architectural fabrics as it is capable of applying biaxial stress to a shear test specimen (§2.2.2). The novel frame design applies biaxial stress while aiming to subject the test specimen to homogenous shear deformation and eliminate distortion of the specimen by the frame itself. The chapter also presents a series of tests performed using the novel frame design on a range of fabrics at increasing levels of biaxial stress. These tests explore the interaction between biaxial tension and shear behaviour for the coated materials used in the construction of tensile fabric structures. A further series of tests compare bias test results with picture frame test results for architectural fabrics.

3.2 Novel picture frame design

The proposed design is a practical embodiment of the frame design presented by Bassett *et al.* (1999). The design of Basset has not before been practically realised. The novel frame design does not require the undesirable practice of removing material in the corners of a test specimen (§2.2.2). Further, correct positioning of the pinned connections is maintained while providing optimum transfer of shear force from the frame to the test specimen by a space in the centre of the pinned connection which accommodates the fabric. The novel design achieves this by allowing for free yarn rotation in the corners of the specimen, as the pinned connections do not penetrate the plane of the fabric. The frame (Figure 3.2a) comprises four pairs of aluminium bars with a machined steel grip inlaid into each bar, each pair of bars comprising an upper bar and a lower bar. Yokes formed at the ends of the bars provide the hinges at each corner of the frame when the equipment is assembled. The yokes are centred to align with the perimeter of the area bound by the frame, i.e. the inside edge of the frame, so as the area bound by the frame and the area of test specimen are coterminous at any angle of shear deformation. Further, the yokes of adjacent bars are machined to interlock with one another when the frame is assembled. The steel grips protrude from the bars to achieve an interference fit with a test specimen and are machined to fit around the yokes to provide an area behind the pin, relative to the specimen, which enables the edge of the specimen to be secured along its entire length.

The upper and lower bars are connected by a series of fasteners, provided as Allen bolts and nuts, which pass through elongated slots within the bars. The elongated slots are positioned to coincide with slits cut in a biaxial cruciform fabric specimen, wherein the slits form fingers in the arms of the specimen (Figure 3.7). The elongated slots provide a tolerance to accommodate deviation in the location of the slits in a given fabric specimen. In use, a fabric specimen is positioned between the front and rear bars with the corner of the specimen coincident with the centre of the yokes, i.e. the axis of the rotation of each hinge, (Figure 3.2b). Tightening of the fasteners draws the front and rear bars together, thus clamping the specimen between the front and rear bars.

The pairs of bars are connected at each corner by front and rear pins (or stub shafts) inserted into the yokes of the front and rear bars, respectively. By providing separate front and rear pins, rather than a single pin passing all the bars at each corner of the frame, a gap is created between the front and rear pins which coincides with the plane of a fabric specimen held in the frame at each of the pinned connections (Figure 3.3 and Figure 3.4). This feature of the novel design allows the specimen to be fully restrained, whilst still permitting free yarn rotation at the corners of the frame. The front and rear pins at two of the corners are formed as part of a two-part bracket which ensures that the centres of the all the yokes align when the frame is assembled. Alignment is ensured with two-part brackets provided at only two opposing corners of the frame as, when assembled correctly, the other corners will align by virtue of the frame's geometry (Figure 3.2c). Small lugs (Figure 3.4) are used to pin the connections at the remaining two corners.

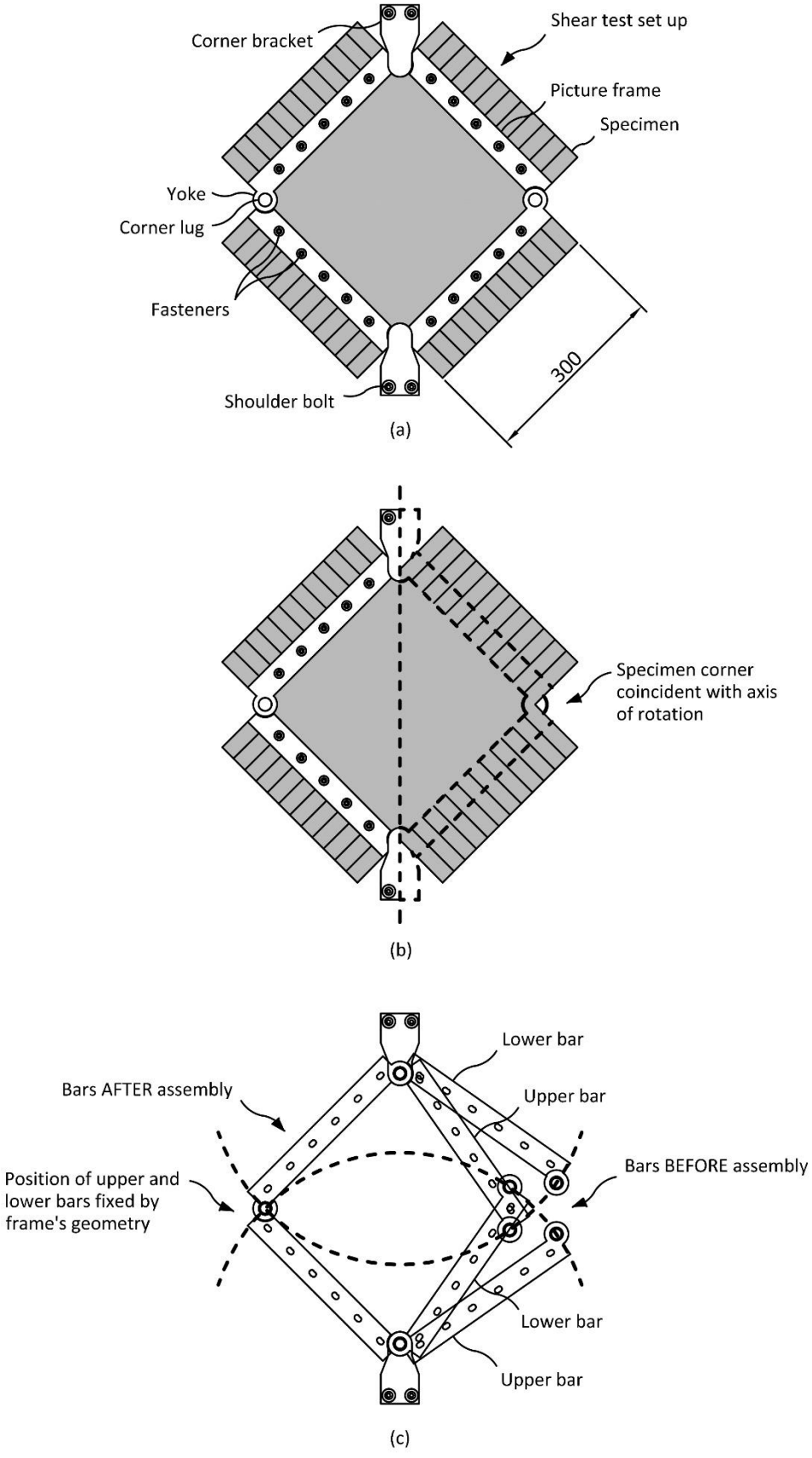

Figure 3.2 The novel picture frame design, showing (a) assembled frame with a fabric test specimen fully restrained; (b) cut-away view illustrating the specimen's position in the frame; and (c) aligning the upper and lower bars during assembly

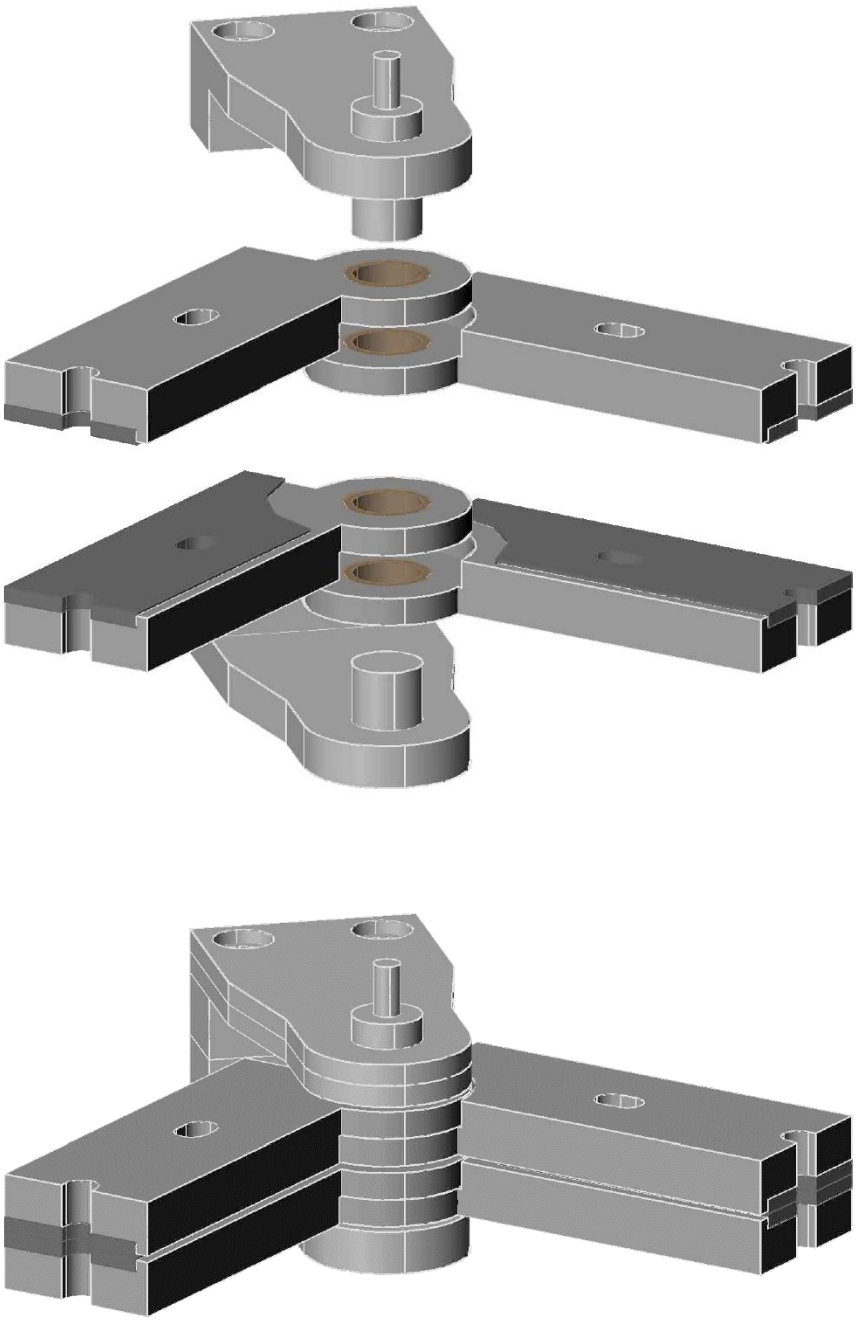

Figure 3.3 Three-dimensional views of the frame's corner detail: (top) an exploded view illustrating, from top to bottom, upper part of corner bracket, adjacent upper bars, corresponding adjacent lower bars and lower part of corner bracket; and (bottom) assembled view, note the gap running through a central horizontal plane of the hinge

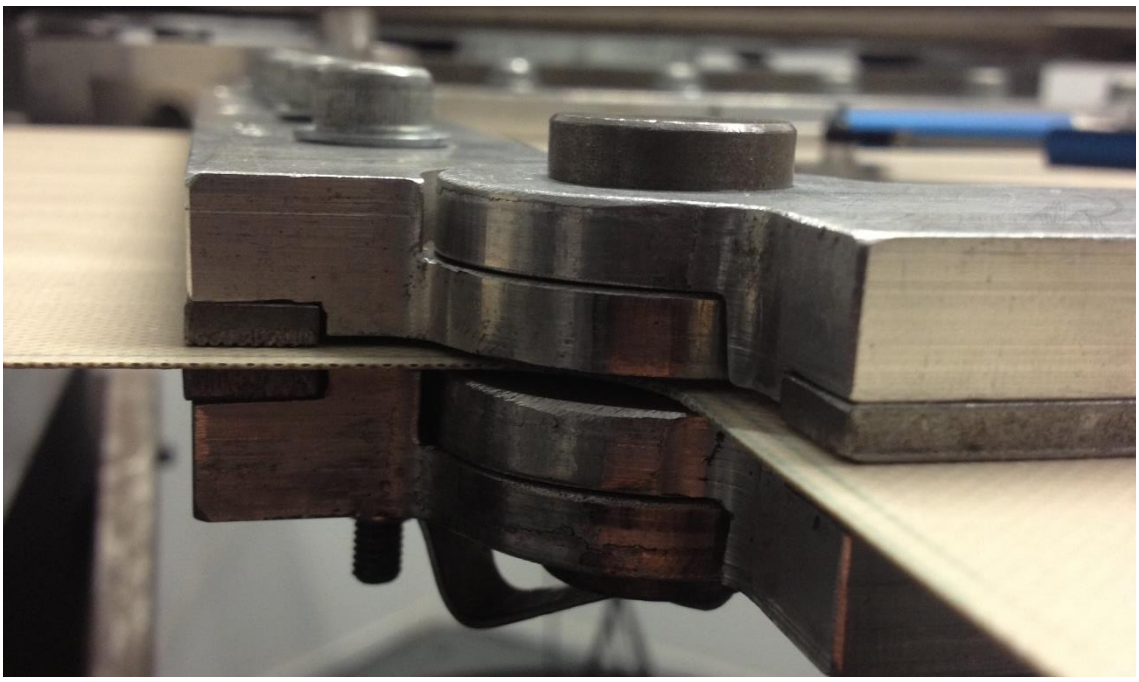

Figure 3.4 Corner detail of the frame shown in use, front and rear pins allow the creation of a gap in the plane of the fabric thus enabling free yarn rotation in the corners of the specimen whilst the specimen is fully restrained by the frame.

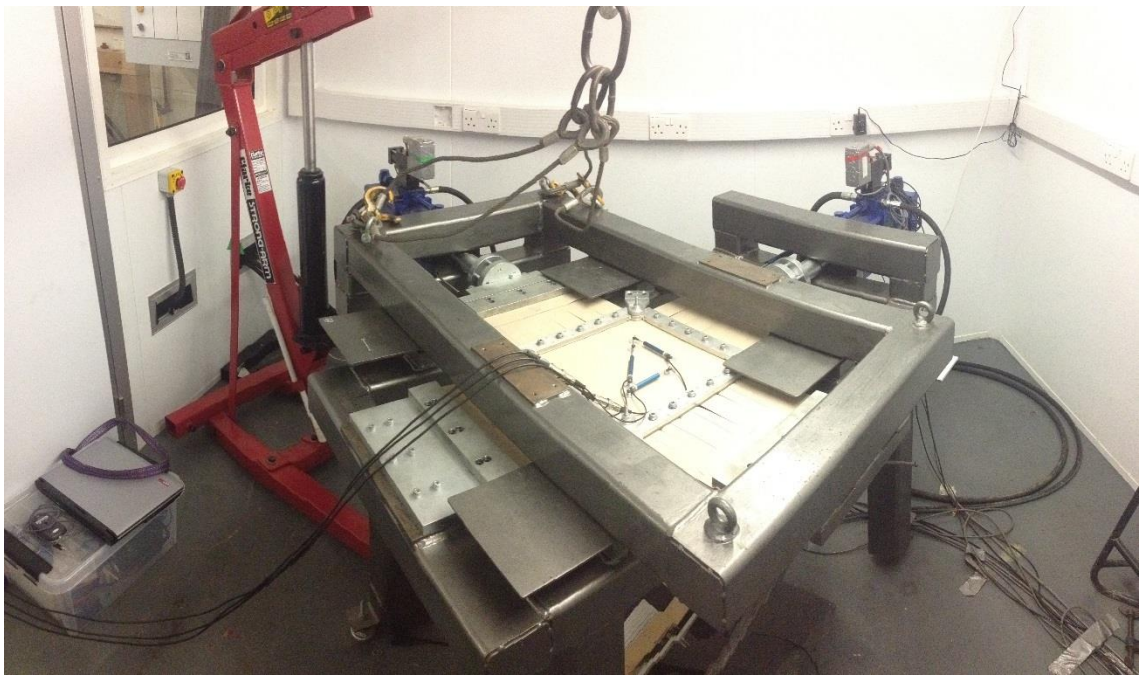

Figure 3.5 Novel shear test picture frame in use, a floating biaxial test rig applies biaxial load to a fabric specimen as the picture frame is installed, linear extensometers are shown affixed to the surface of the specimen for measuring deformation of the fabric surface (§3.3.2)

The frame was constructed from 6082-T5 aluminium alloy. This alloy was chosen for the design as it is readily available, is a high strength alloy, exhibits good resistance to cyclic loading and has good machinability. A 3D model of the proposed design was implemented in Autodesk Inventor to analyse the stresses that would occur in the frame during testing. To prevent failure of the frame, a limit on the allowable level of stress was imposed of 50% of the 0.2% proof stress (referred to as the offset yield point). This condition limits the maximum allowable stress in the frame to 115MPa. The 3D Inventor model predicts that a maximum value of 111.4MPa will occur in the frame at a biaxial stress of 25kN/m. Values of prestress for the strongest PTFE/Glass fibre fabrics are typically around 5kN/m (Balz and Dencher, 2004). Further, as factors of safety used in design are typically between 5 and 8 (§1.1.2) and the typical tensile strength of type 5 PVC/PES and G7 PTFE/glass fabrics is 170kN/m (§2.1), design loads will range between 20 and 35kN/m for the strongest materials. A maximum value of biaxial stress of 25kN/m is therefore suitable for initial investigation of the materials at the loading conditions expected in situ. However, to test at the maximum values of design load a more substantial frame may be needed.

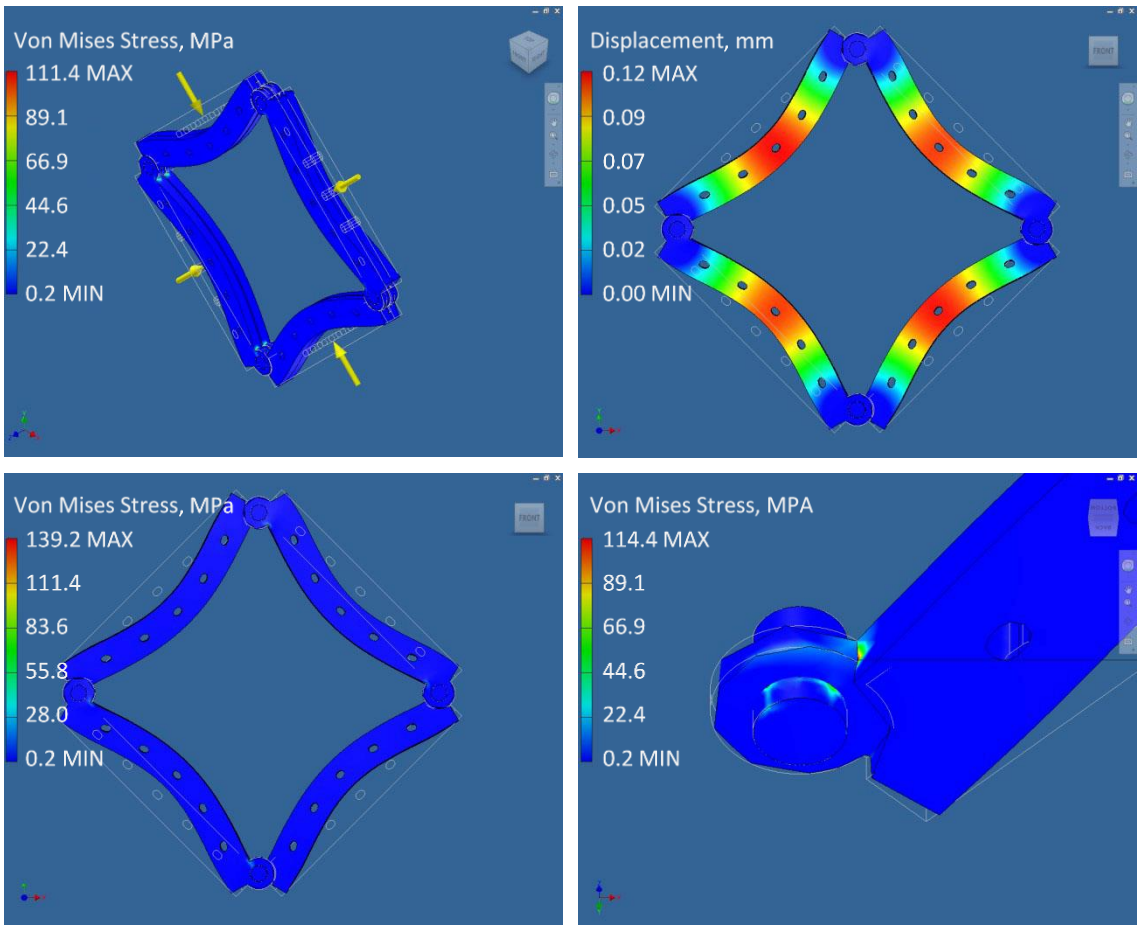

Figure 3.6 Inventor analysis of the proposed frame design; (top left) UDL load applied to each bar represents tensile force in a restrained specimen (Inventor visualises UDLs as a point acting in the centre of the UDL); (top right) displacement; (bottom left) stress in the frame; and (bottom right) stress at corner between the yoke and the bar

The dimensions of the frame accommodate a 300x300mm biaxial cruciform specimen (§3.3.1), though frames of other dimensions could take the same form. The dimensions of the shear test frame allow the frame to be used with Newcastle University's existing biaxial test rig (Figure 3.5). The frame had to be compatible with a test specimen which suited the existing rig and did not clash with any features of the rig when in use. It was also desirable for the bars to be lightweight for ease of handling and to prevent the self-weight of the frame having an adverse effect on the behaviour of a fabric specimen. In addition, the steel grips which are required for an interference fit with a test specimen were found to be a time consuming component to fabricate. Therefore, it was necessary that a set of existing grips were used in the fabrication of the new test frame. This requirement placed a further limitation on the frame's design. The exact frame design is specified in the workshop drawings provided in the Appendices.

3.3 Initial picture frame shear testing

A series of initial shear tests were conducted using the materials detailed in Table 3.1. Three tests were performed on each of the materials in order to assess the repeatability of the method. Biaxial tensile stresses of 5.87kN/m (5.25% of the measured UTS) and 3.55kN/m (2.5% of the measured UTS) were applied to the F1202 and B18089 fabrics respectively. These tensile stresses were chosen as they were of interest to the project's sponsors. The exact values of prestress were unimportant at this stage of the project and the effect of the level of prestress was subsequently investigated (§3.4).

Table 3.1 Fabrics used for initial shear testing

Fabric	Manufacturer	Material		Weight (g/m^2)	Thickness (mm)	Tensile strength* (kN/m)
		Base cloth	Coating			
F1202	Serge Ferrari	PES	PVC	1050	0.78	112/112
B18089	Verseidag	Glass fibre	PTFE	1150	0.70	140/120

*as specified by the manufacturer
PET = Polyethylene terephthalate; PVC = Polyvinylchloride; PTFE = Polytetrafluoroethylene

3.3.1 Specimen preparation

The manufacturing process can cause fill yarns to bow or skew causing warp and fill yarns to intersect with one another at angles other than 90° (Skelton and Freeston, 1971). Consequently, fabric cruciform specimens were prepared with the arms cut parallel to the yarn directions (Bridgens and Gosling, 2004), i.e. not necessarily orthogonal to one another (Figure 3.7). This preparation method enables the biaxial stress to be correctly applied to the yarns, as load is resisted in-line with the yarns without inducing undesired shear deformation. Axis centrelines were carefully drawn onto virgin fabric by tracing a single yarn in each axis direction. All other dimensions of each specimen were then offset from the centrelines, including the fingers of each specimen.

All specimens to be placed in the biaxial test rig used in this research project required elongate sleeves or "pockets" to be formed at the ends of the specimens' arms. During testing, each pocket holds a circular steel bar to enable the specimen to be held in specially designed clamps which allow loading of the specimen up to a fabric's failure load while minimising crushing of the yarns (Bridgens, 2005). The pockets were formed by folding over the specimen at the ends of the arms and bonding the fabric to itself using a means suitable for a given fabric type. PVC coated fabrics were easily bonded using a strong adhesive. PTFE and Silicone coated fabrics required welding at high temperatures, ranging from 150 to 200°C, with the provision of a strip of thermosetting material placed within the weld.

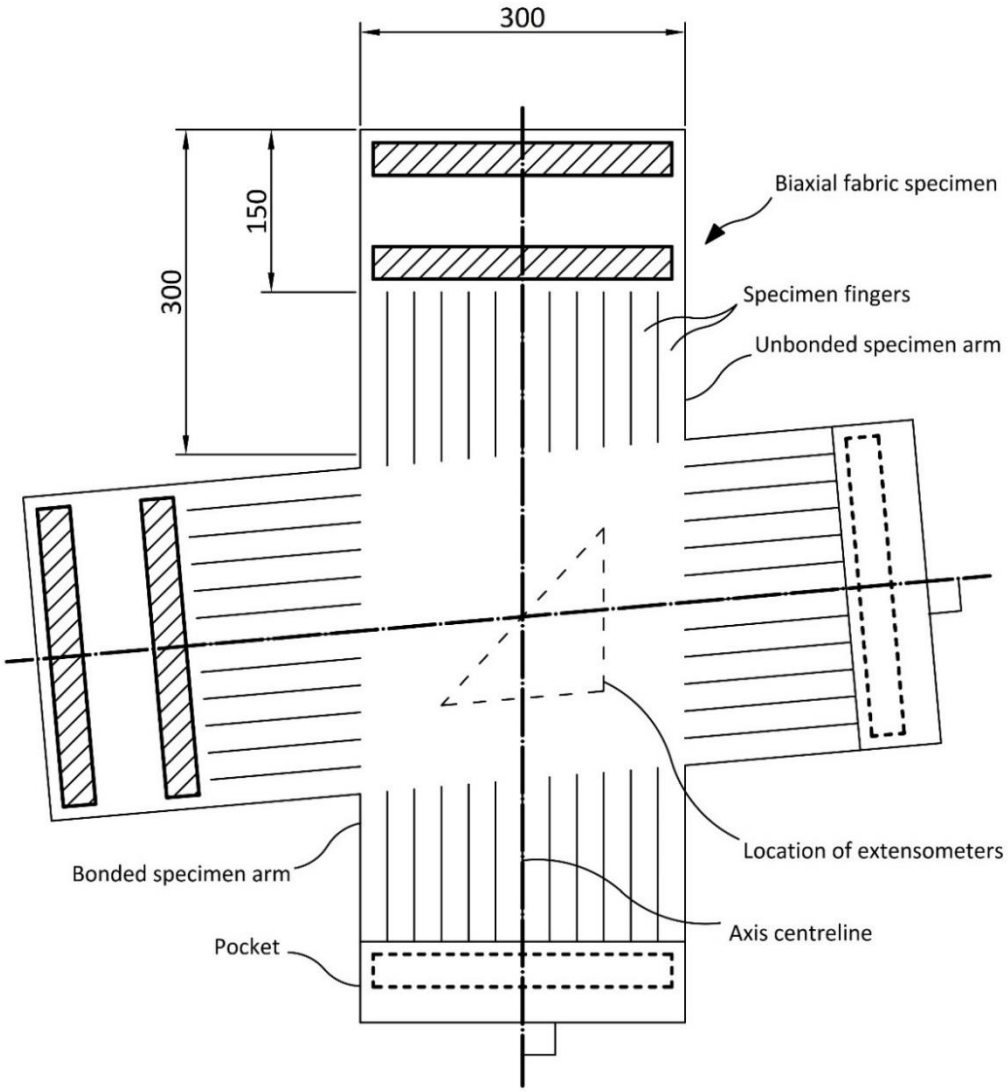

Figure 3.7 Cruciform biaxial specimen prepared with arms parallel to the yarn directions (angle between warp and fill is exaggerated) as described by Bridgens and Gosling (2004). Dimensions are the same for each arm. Top and left arms are un-bonded; bottom and right arms show pockets formed by folding and bonding the specimen to itself

3.3.2 Determination of shear stress and strain

Deformation measurements were obtained during testing from an arrangement of three contact extensometers affixed to the surface of the centre of the cruciform specimens (Figure 3.8). The sensors used were *Penny and Giles* potentiometric linear position sensors (2 x SLS095/40 and 1 x SLS095/50). The measurements obtained were used to calculate an estimate of the strains in the directions of the yarns and the shear strain. The extensometers were affixed to the test specimen by aluminium mounts comprising a 2mm threaded bar which was used penetrate the fabric. The mounts also comprise Ø25mm discs, which hold each mount perpendicular to the plane of the fabric. A similar arrangement of extensometers was used by Galliot and Luchsinger (2010b) who

calculated the shear strain using a formula suitable only for orthogonal starting angles, i.e. samples with orthogonal yarns. As non-orthogonal initial angles were expected to be encountered owing the method of specimen preparation (§3.3.1), a revised formulation for deriving the shear angle was used (Equation 3.1). This approach offers a straightforward means for determining the strain in a specimen which can easily be setup using conventional laboratory equipment.

$$\gamma = cos^{-1}\left(\frac{\left(L_2(1+\varepsilon_2)\right)^2 + \left(L_3(1+\varepsilon_3)\right)^2 - \left(L_1(1+\varepsilon_1)\right)^2}{2\left(L_2 + (1+\varepsilon_2)\right)\left(L_3(1+\varepsilon_3)\right)}\right) \qquad \textbf{Equation 3.1}$$

where γ is the change in angle (shear angle), L is the initial length measured by each linear extensometer and ε is the strain calculated in the direction of each extensometer from measurements obtained during testing. Subscripts 1, 2 denote the extensometers in the warp and fill directions, respectively, and subscript 3 denotes the remaining extensometer affixed to the specimen at approximately 45° to the yarn directions.

An approximation of the shear force, Fs, applied to the fabric was resolved from the crosshead load of the uniaxial test machine (Harrison *et al.*, 2004; Peng *et al.*, 2004).

$$F_s = \frac{P}{2 \times \cos\left(\frac{\alpha - \gamma}{2}\right) \times L} \qquad \textbf{Equation 3.2}$$

where Fs is shear force, P is crosshead load, α is the initial angle of the top/bottom inside corner of the shear frame and γ is the change in angle (shear angle)

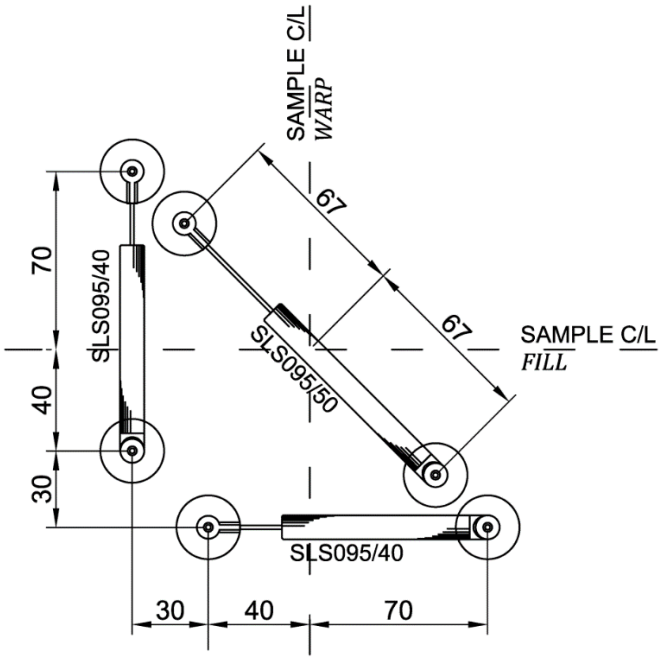

Figure 3.8 Arrangement of linear extensometers on the surface of a fabric test specimen, showing placement of the extensometers in relation to the warp and fill centrelines

3.3.3 Test protocol

A floating biaxial test rig, (Bridgens and Gosling, 2004; Bridgens, 2005) was used to apply and maintain biaxial pretension prior to and during installation of the frame (Figure 3.2). The pretension was held for a period of one hour to minimise loss of prestress in the shear frame due to relaxation. After preloading, the shear frame was then fitted to the specimen being tested while the level of biaxial stress was maintained by the biaxial test rig. The shear frame was fitted around the specimen with the bars of the frame parallel to the yarn directions. The upper bars of the frame are placed on top of the specimen while it is held in the biaxial test rig. The lower bars were then secured beneath the specimen using the fasteners which were placed through the bars and the slits cut in the arms of the specimen. The fasteners were first loosely tightened to allow for final positioning of the shear frame and attachment of the corner brackets and lugs. After fully tightening the fasteners, the test specimens could be removed from the biaxial test rig and placed in a uniaxial test machine for shearing with the frame maintaining the applied pretension in the fabric.

The project's industrial sponsors were interested in shear deformations of approx. 5-6°, as these are the anticipated deformation in situ. However, the profile used to validate the frame was specified to subject the fabric specimen to higher shear angles, so as to observe the ability of the corner connections to allow for yarn rotation. Therefore, the shear test profile used achieved a maximum angle of 15° (Figure 3.9).

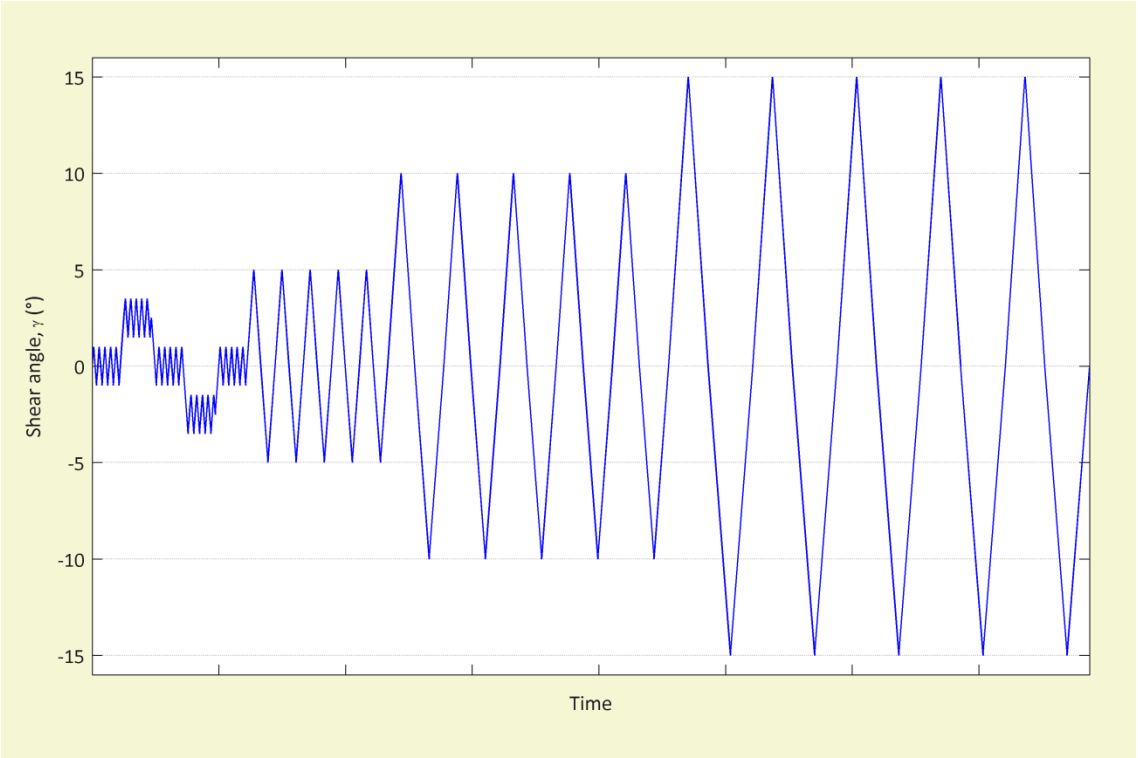

Figure 3.9 Shear test profile for initial shear tests, the profile is based on that of the Membrane Structures Association of Japan shear test standard MSAJ (1993) and discussion with the project's sponsors

The shear test profile comprises a positive and negative half of each shear cycle, where the frame is extended and compressed in the axis of the uniaxial test rig, respectively. The rate of deformation applied was 2mm/min of crosshead displacement. At this rate of displacement, the total test time for the profile was approximately 22 hours. Owing to the kinematics of the frame, a constant rate of crosshead displacement does not result in constant rate of angular change. While it would be preferable to perform the shear tests at a constant rate of angular change, it was not possible with the testing equipment used. However, at the 2mm/min rate of crosshead displacement, the range of rates of angular change is small, ranging from 0.51°/min to 0.58°/min at –'ve 15° and +'ve 15°, respectively.

3.3.4 Results of initial shear testing

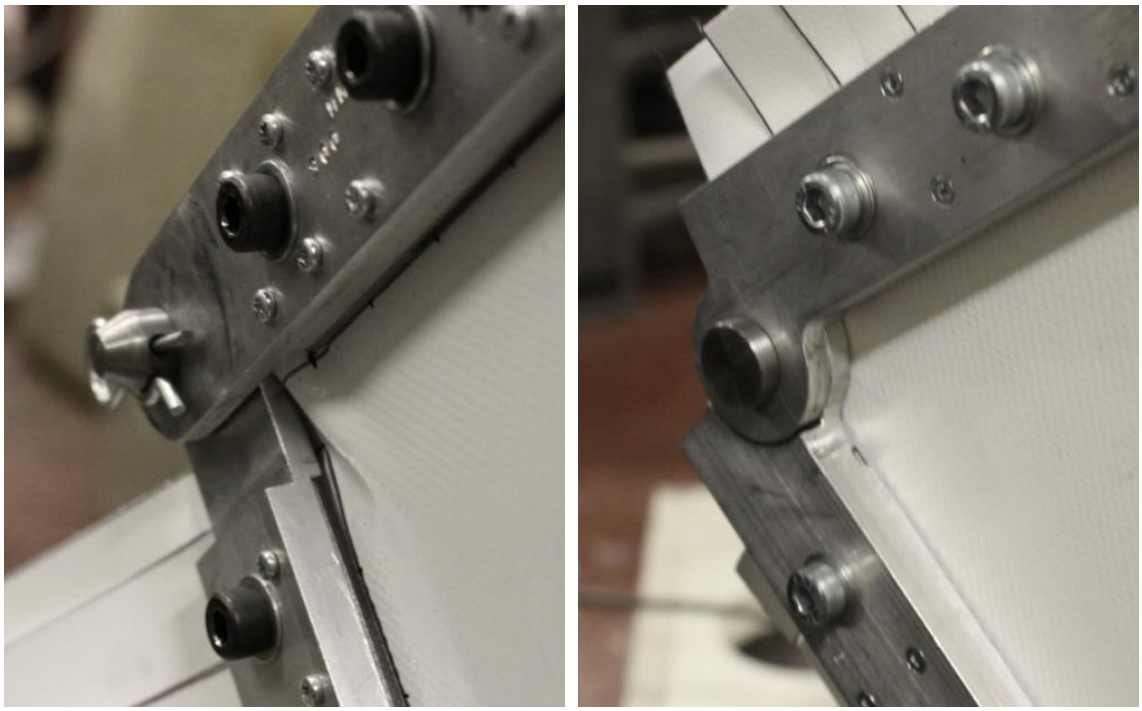

Figure 3.10 Corner details of picture frame test apparatus during shearing at approximately 15° of shear displacement, showing (left) the frame deign of Jackson *et al.* (2009) and (right) the proposed novel frame design

From visual inspection made during the shear testing, no out-of-plane deformation was observed as the result of the frame's design. No pinching or jamming of the specimen occurred as the yarns, indicating that the yarns were free to rotate, thus preventing wrinkling of the specimen in the corners of the frame, as was seen when using an existing frame design (Figure 3.10). The tension in the specimen appeared to be maintained during the shear testing. However, while being able to quantify the level of stress in the specimen during shearing is desirable, there is no apparent way to achieve this in practice. The linear positon sensors can show reduction in strain, but without any means to measure the force along the clamped edges of the frame, it is not possible to quantity the tension in the specimen.

It has been suggested that the picture frame test methodology is non-repeatable when tension is present in yarns (Hivet and Duong, 2011). However, the shear stress-strain plots indicate that the novel frame design and the test methodology, when used in combination, are capable of producing repeatable results (Figure 3.12 and Figure 3.13). The results show increasing non-linearity of the response to shear deformation, though the response does not exhibit a stiffening associated with lock-up (§2.1.2). This is despite wrinkling being visible at high angles of shear for the PTFE/glass fabrics (Figure 3.11). The average shear modulus, *G*, of each cycle set (Table 3.2) is linearly approximated between the uppermost and lowest point of each cycle (tip-to-tip), as described in the Japanese standard (MSAJ, 1993). Further, to compare positive and negative gradients, linear approximations are obtained for the final 1/3 of each loading and unloading curve to compare the gradients. The average values do not include the initial cycles of each set, which are visibly stiffer, although stiffness of the initial curves would be of interest, for example if modelling installation.

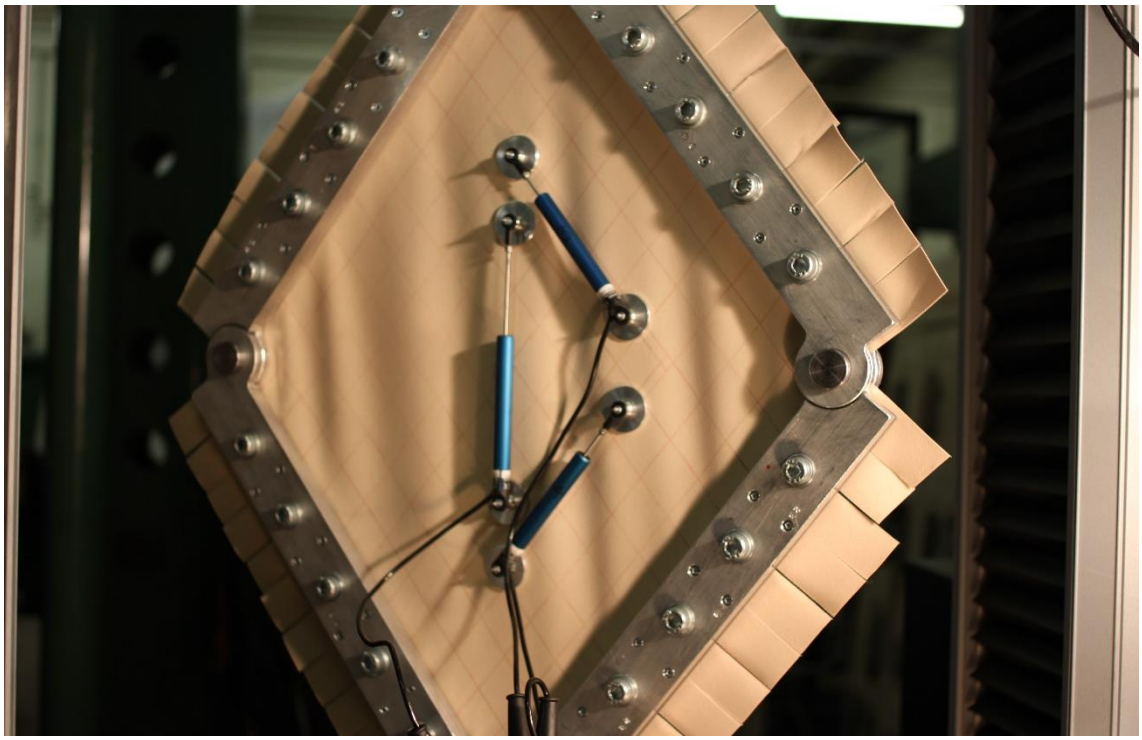

Figure 3.11 Wrinkling at approximately 12° of shear deformation B18089, the appearance of the wrinkles has been exaggerated by illuminating the surface of the specimen at an acute angle

The constant stiffness values show good agreement between the tests performed on the same fabric and corresponding values of stiffness are observed for positive and negative halves of the shear cycles. Shear stiffness is observed to decrease with each set of increasing shear angle. It is not clear which measure of the shear stiffness, i.e. at which angle, best represents the shear behaviour.

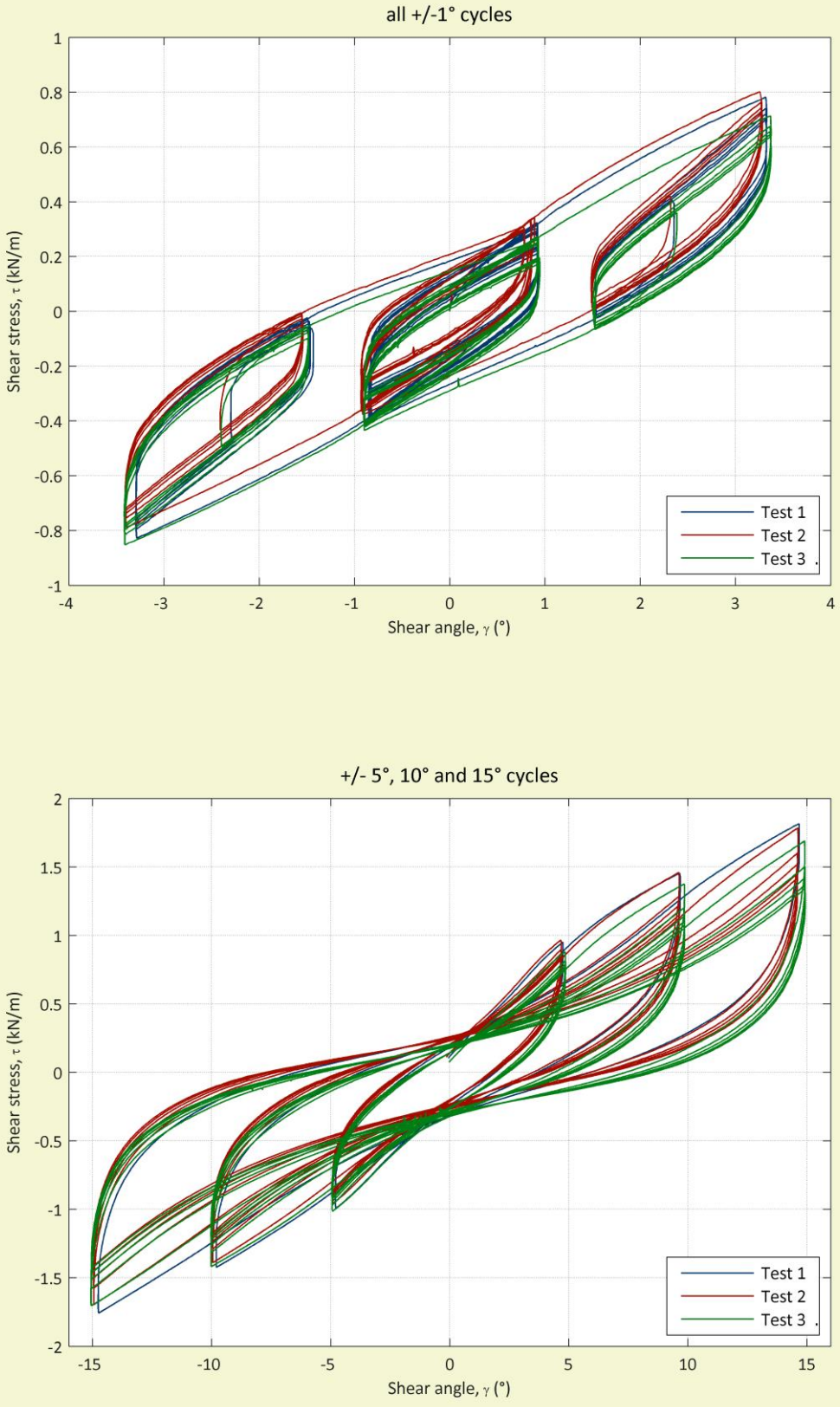

Figure 3.12 Shear test results for Ferrari F1202, with cycles at 1° shown separately for clarity

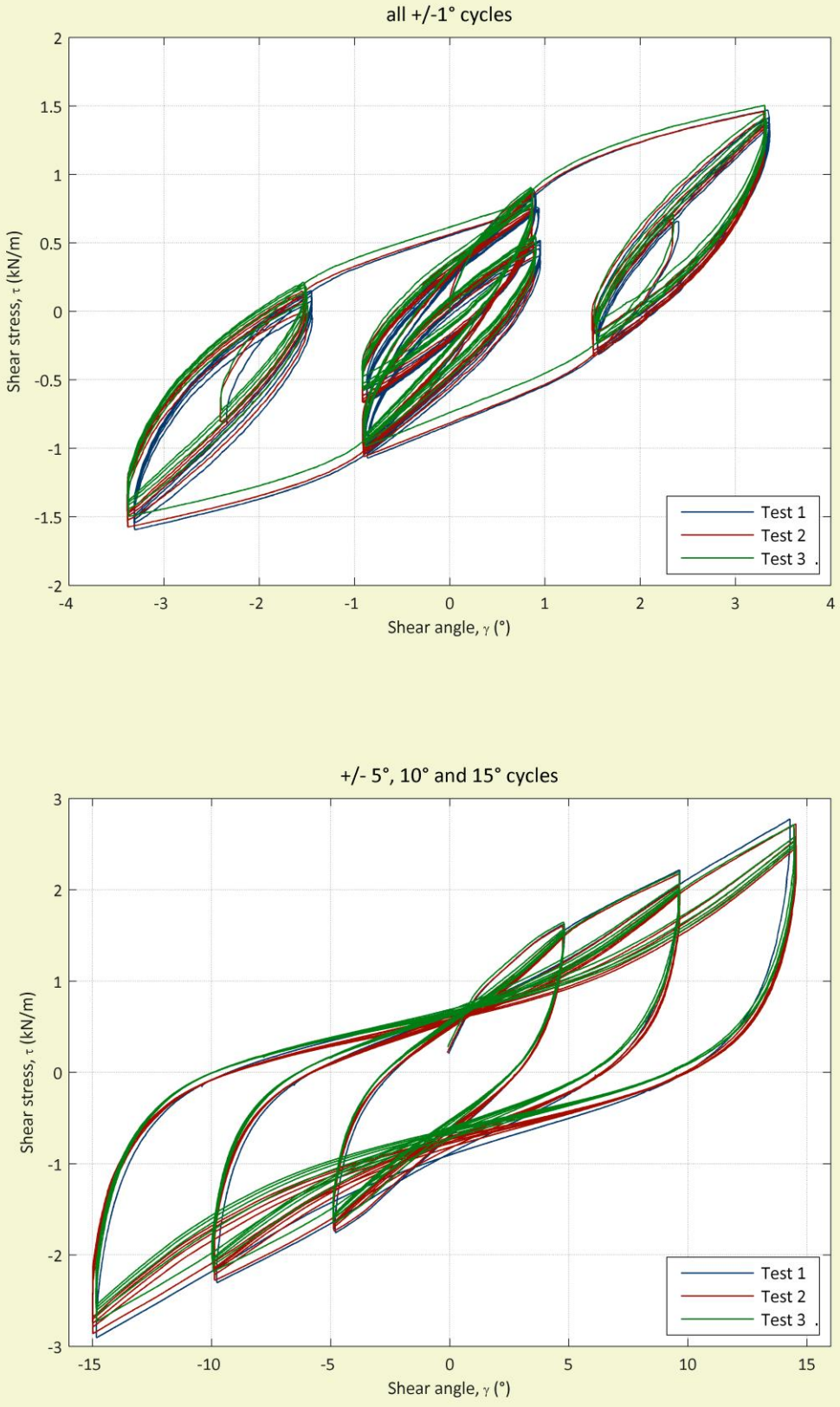

Figure 3.13 Shear test results for Verseidag B19089, with cycles at 1° shown separately for clarity

Table 3.2 Shear stiffness, *G*, for all cycle sets for each test

		Shear Stiffness, *G* (kN/m)								
		Test 1			Test 2			Test 3		
	Cycle set	+'ve curve	-'ve curve	Tip - Tip	+'ve curve	-'ve curve	Tip - Tip	+'ve curve	-'ve curve	Tip - Tip
Ferrari 1202 (PVC/PES)	1 (1°)	14.6	14.9	23.1	14.9	14.4	22.2	13.0	14.3	21.4
	2 (1°)	17.2	11.5	23.8	17.7	11.5	23.7	16.1	10.9	22.2
	3 (1°)	10.3	12.6	20.3	10.5	12.4	19.5	9.9	12.4	19.1
	4 (1°)	10.5	16.3	23.6	10.1	15.7	22.5	10.2	15.8	22.0
	5 (1°)	10.2	10.3	19.1	11.1	10.4	18.8	9.7	9.9	17.9
	6 (5°)	-	-	-	8.8	8.9	10.6	8.3	8.8	10.3
	7 (10°)	-	-	-	6.5	6.7	7.3	6.2	6.5	7.1
	8 (15°)	-	-	-	5.7	6.0	6.0	4.7	5.3	6.0
Verseidag B18089 (PTFE/glass)	1 (1°)	39.5	39.5	59.7	38.7	39.0	59.7	38.9	39.8	58.9
	2 (1°)	35.7	28.1	52.6	35.4	28.4	52.8	35.5	27.8	52.1
	3 (1°)	27.3	33.3	48.3	26.5	32.7	48.3	26.2	33.3	47.5
	4 (1°)	24.7	34.7	50.1	23.2	33.6	49.5	23.7	33.8	48.9
	5 (1°)	28.4	27.0	44.1	27.6	26.4	44.2	27.6	26.4	43.0
	6 (5°)	-	-	-	12.8	12.8	19.1	12.4	12.7	18.7
	7 (10°)	-	-	-	9.4	9.3	12.4	9.1	9.3	12.1
	8 (15°)	-	-	-	8.9	9.3	10.3	8.5	9.4	10.1

The shear stiffness approximations for the F1202 PVC/PES fabric derived through the experimental testing are substantially lower than rule-of-thumb values suggested in the European design guide for use in analysis (Mollaert and Foster, 2004). For the F1202 the rule-of-thumb estimate for the shear stiffnesses is 42kN/m (compared to a maximum value determined from testing of 23.8kN/m and minimum value of 4.7kN/m). The PTFE/glass fabric rule-of-thumb measure is 38kN/m and is similar to the values determined through testing for the initial 1° cycles. However, with increasing shear deformation the values obtained through testing become markedly lower (minimum value is 8.5kN/m). These differences suggest that the rule-of-thumb measures can only provide very approximate measures of shear stiffness and should be used in design and analysis with caution.

The values of elastic moduli used to calculate the rule-of-thumb estimates were obtained through commercial biaxial testing undertaken by Newcastle University based on a biaxial test standard (MSAJ, 1995).

3.4 The influence of biaxial stress on shear behaviour

With a frame design and methodology capable of producing repeatable results established, three plain woven architectural fabrics (SCC200, CMX220 and FGT1000) were used to investigate the influence of biaxial stress on fabric shear behaviour (Table 3.3). These fabrics were chosen to represent a range of strengths, shear stiffnesses and constituent materials. Biaxial stress of 3%, 6% and 9% of each fabric's ultimate tensile strength were applied prior to, and maintained during, shear testing (Table 3.4). 3% of ultimate tensile strength corresponds to a typical prestress value, with 6% and 9% values being used to explore how the shear behaviour varies with increasing biaxial stress. Shear behaviour at other biaxial stress ratios would also be of interest, but was beyond the scope of the project.

Table 3.3 Fabrics shear tested at different values of biaxial stress

Fabric	Manufacturer	Material		Weight (g/m^2)	Thickness (mm)	Tensile strength* (kN/m)
		Base cloth	Coating			
SCC200	Taiyo Kogyo, Japan	PET	PVC	832	0.68	76/81
CMX220	Taiyo Kogyo, Japan	Glass fibre	PVC	813	0.55	115/111
FGT1000	Chukoh, Japan	Glass fibre	PTFE	1700	1.00	207/177

*as specified by the manufacturer (warp direction/fill direction)
PET = Polyethylene terephthalate; PVC = Polyvinylchloride; PTFE = Polytetrafluoroethylene

Table 3.4 Stresses applied to test specimens prior to shearing

Fabric	% UTS	Prestress (kN/m) Warp/FIll
Taiyo Kogyo SCC200 (PVC/PET)	3	2.25 x 2.43
	6	4.50 x 4.86
	9	6.75 x 7.29
Taiyo Kogyo CMX220 (PVC/glass)	3	3.45 x 3.33
	6	6.90 x 6.66
	9	10.32 x 9.99
Chukoh FGT1000 (PTFE/glass)	3	6.18 x 5.31
	6	12.36 x 10.72
	9	18.54 x 15.93

3.4.1 Test protocol

The shear test profile used for the initial shear testing was revised to limit shear deformation to a maximum value of -6° and +6° (Figure 3.14). Given the weight of the materials to be tested, and that wrinkling was only observed at angles greater than 10° for the B18089 during the initial tests, -6° and +6° was assumed to be a suitable maximum value which would avoid inducing wrinkling. The revised profile comprises 13 sets of cycles, each set containing three cycles. Unlike the profile used for conducting the initial tests (Figure 3.9), the revised profile applies shear deformation to a specimen in sets of increasing shear deformation followed by sets in which the shear deformation is reduced. This was to observe the effect of shear stress at large angles of deformation on the shear stiffness at relatively lower angles of deformation. Cycles are repeat to condition the specimen such that the behaviour measured is representative of the fabric in situ, as this is the behaviour required to model tensile fabric structure designs.

At crosshead displacement of 2mm/min, the duration of the revised shear test profile is approximately 17 hours. The range of rate of angular change is reduced, ranging from 0.53°/min to 0.55°/min at –'ve 6° and +'ve 6°, respectively.

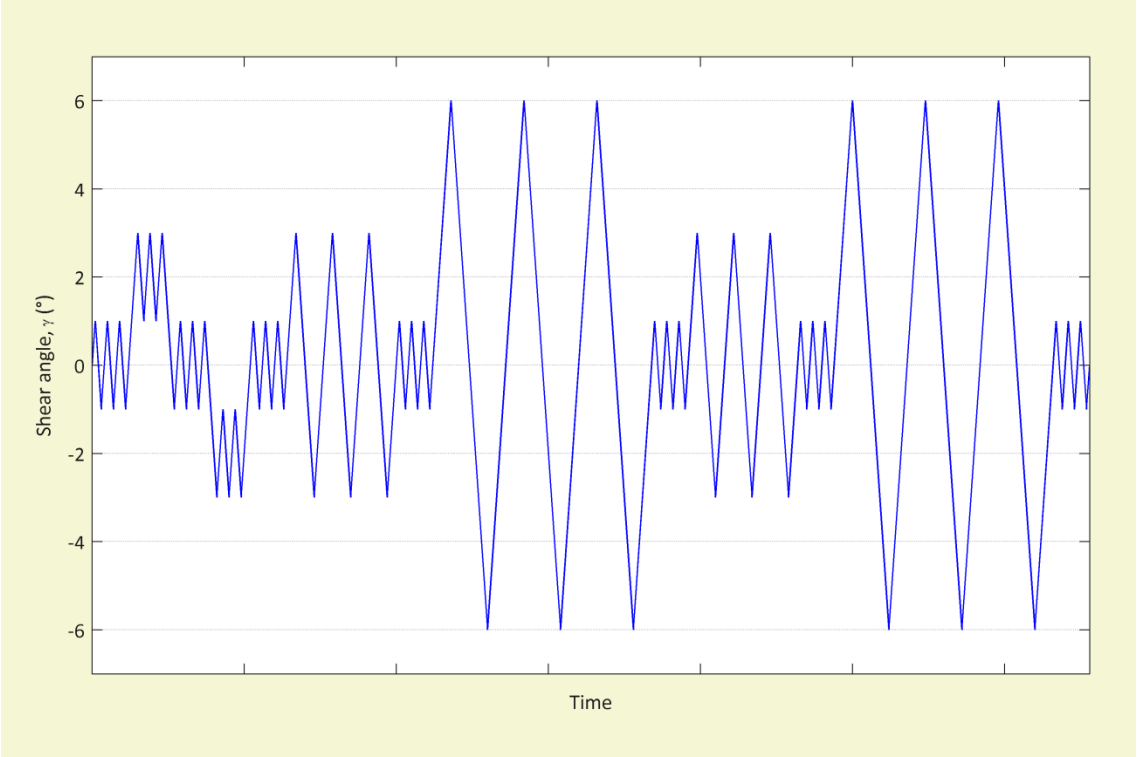

Figure 3.14 Revised shear test profile, with maximum shear deformation at 6°

3.4.2 Digital Image Correlation

To assess the suitability of the use of linear extensometers and the overall suitability of the picture frame design and the test method employed, a Digital Image Correlation (DIC) technique was used during one of the shear tests performed on a specimen of CMX220 fabric. DIC is an optical technique for measuring deformation of an object's surface. DIC has been used to assess the homogeneity of strain fields in previous textile deformability studies (Zhu et al., 2007; Lomov et al., 2008; Galliot and Luchsinger, 2010b) and enables the full-field strain measurement of the entire specimen. DIC is a non-contact measurement solution and does not impact the stiffness of a material under inspection. Strains are calculated from images of the deformed specimen, which is covered in a stochastic pattern (Figure 3.15). Commercially available software (*Correlated Solutions*' *Vic-Snap* and *Vic-3D*) is used to capture and process images from stereo camera set-up (Figure 3.16) to provide a three-dimensional field deformation, from which a two-dimensional strain field may by derived. The grey value pattern in small areas of the sample is tracked using DIC software. Images taken during the DIC test were recorded every 30 seconds and a modified profile was used which includes higher shear angles to assess the limitations of the shear frame. Higher angles of shear deformation were added to the end of the revised test profile (§3.4.1).

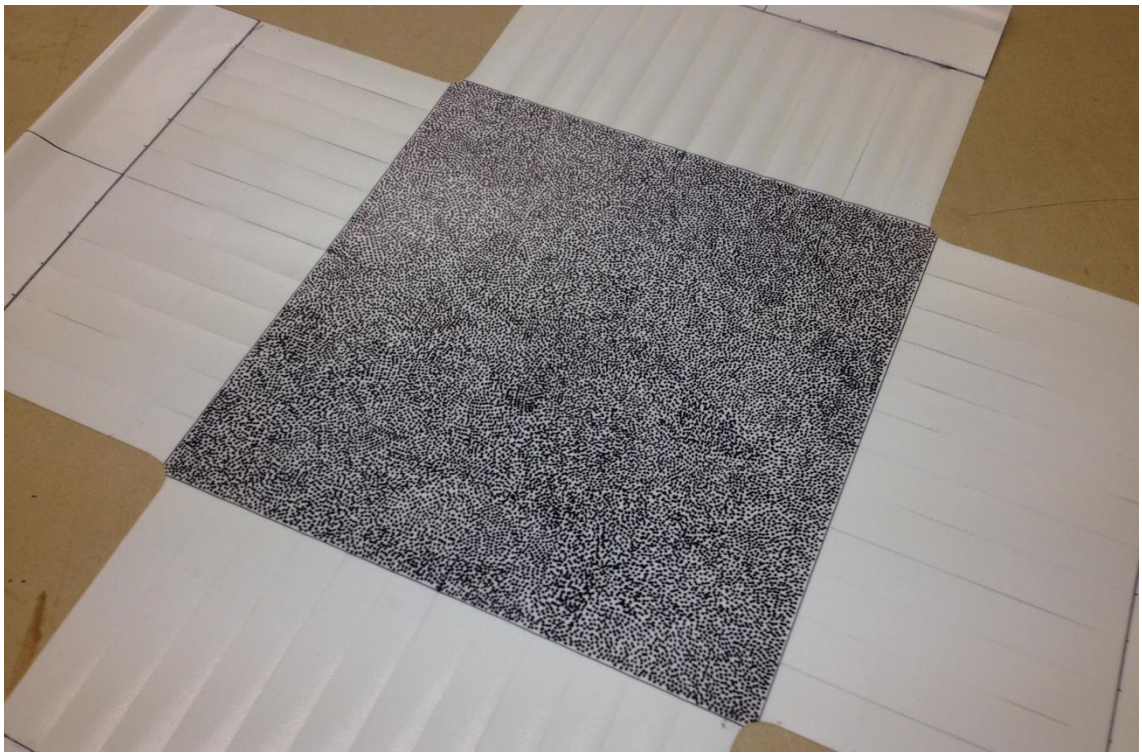

Figure 3.15 Biaxial cruciform specimen (CMX220) prepared for shear test with stochastic speckle pattern for Digital Image Correlation (DIC) analysis. The pattern has been applied to the specimen with a permanent marker pen. While more rapid methods of applying the pattern are available, e.g. spray paint, the pen method reduces the risk of scrapping the specimen.

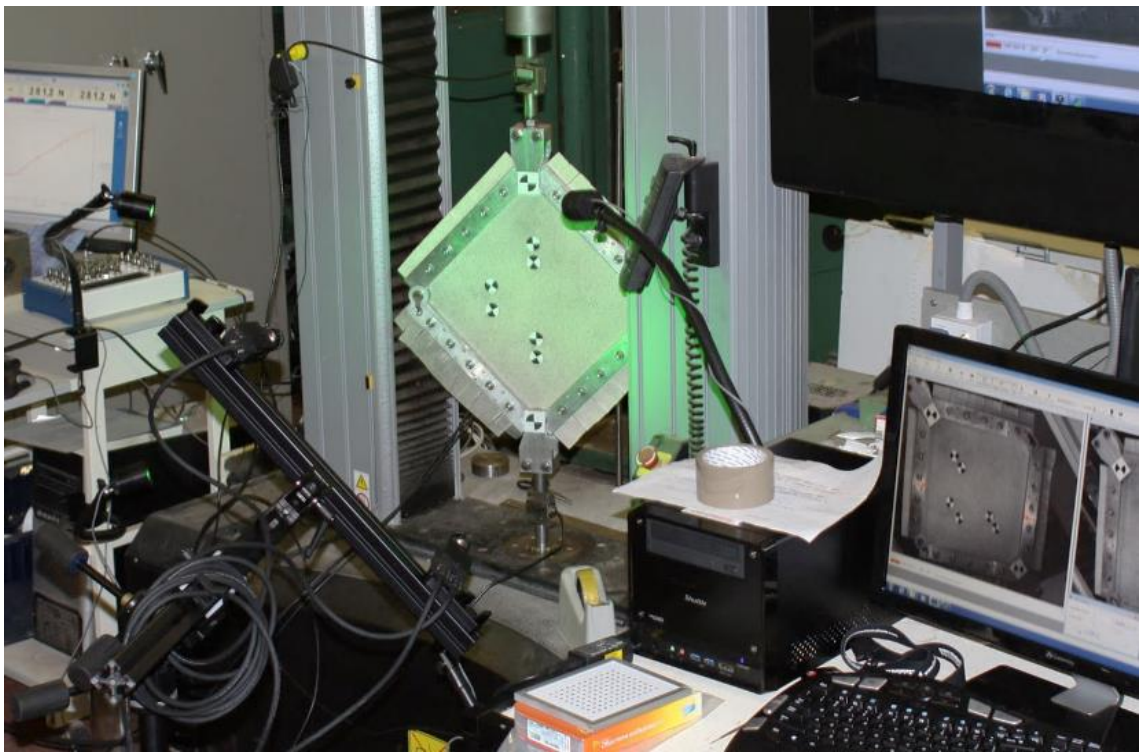

Figure 3.16 Digital image correlation set up, green light is used to illuminate the specimen as this improves the contrast of the stochastic pattern as view by the DIC system's cameras

3.4.3 Strain field homogeneity

The shear strain results obtained from DIC analysis show that that the shear deformation is not absolutely uniform across the sample (Figure 3.17 and Figure 3.18). However, the variation is small, as standard deviations of the shear strain across the entire sample do not exceed 5% of the average shear strain (Table 3.5). This 5% criterion is passed on a previous study by Galliot and Luchsinger (2010b) in which it was only valid for a small central area of the specimen and was only demonstrated for large angles, i.e. 15°, where the deviation is divided over a larger average strain. Here it is true across the entire specimen for each of the angles prescribed up to the maximum shear deformation applied: $\gamma = 15°$. The variation is likely to be the result of bending of the yarns near to the clamped edge. The DIC results also show agreement with the shear angles calculated from extensometer readings (Figure 3.19) and thus the extensometers provided a suitable means to obtain the shear deformation of the specimen during testing. While the shear strain can be considered to be homogeneous across the specimen, the shear strain induced in the specimen is less than the shear angle of the frame (due to yarn rotation at the clamps). This is not problematic if the shear strain is calculated from extensometer readings, but it does mean that crosshead movement cannot be used as an accurate measure of shear strain.

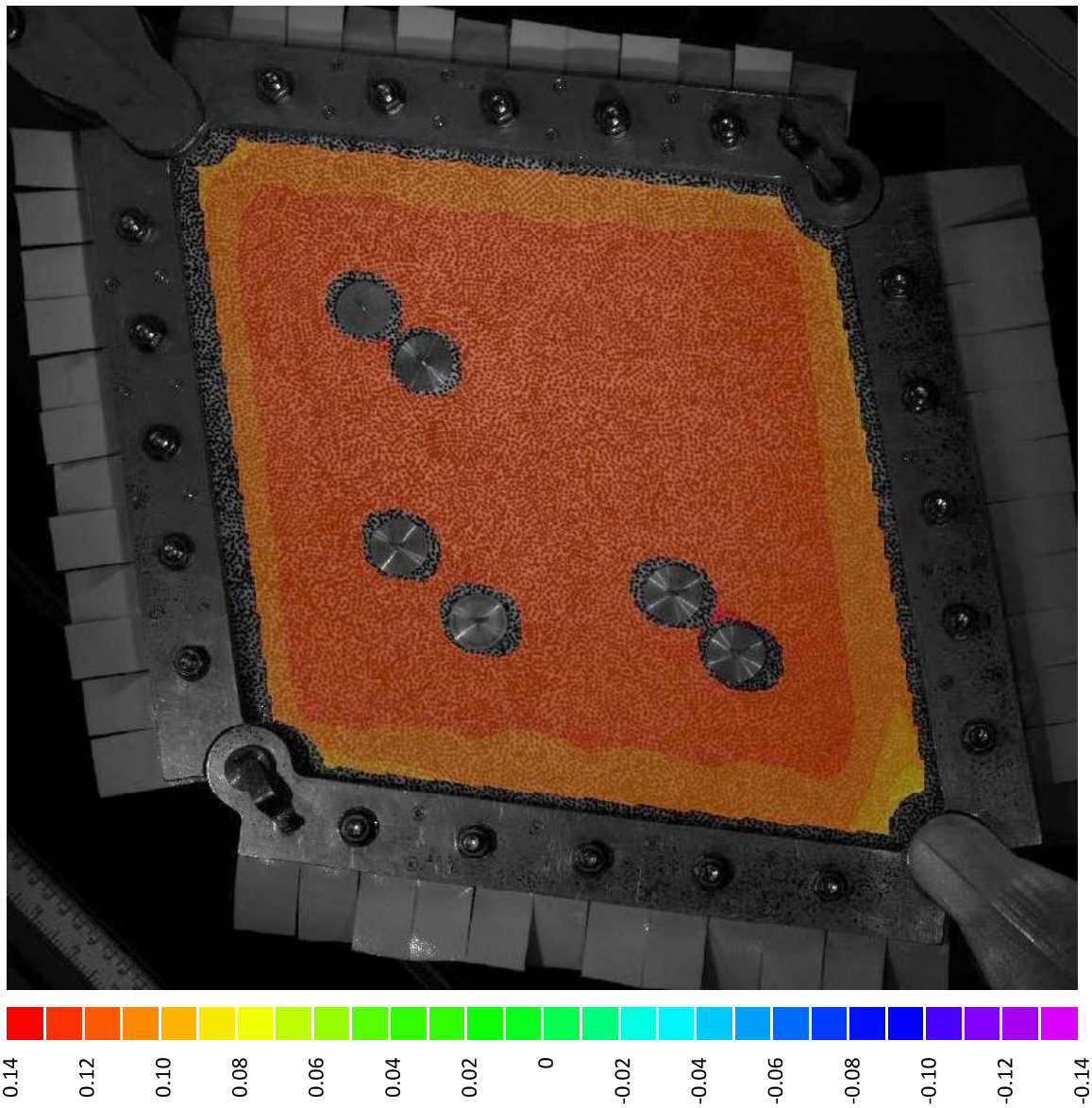

Figure 3.17 Shear strain ε_{xy} for CMX220 at 3% UTS at +15° of shear, strains obtained with Digital Image Correlation (DIC). Contours match DIC images for the shear ramp method published by Galliot and Luchsinger (2010b). Each colour boundary indicates a difference in shear angle of 1.1°

Table 3.5 Standard deviation of shear strains

Mean ε_{xy}	Mean γ	Standard deviation ε_{xy}	% deviation
0.008	0.9	0.0004	5.0
0.024	2.8	0.0011	4.6
0.049	5.7	0.0023	4.7
0.073	8.4	0.0035	4.7
0.098	11.4	0.0047	4.8
0.123	14.2	0.0058	4.7

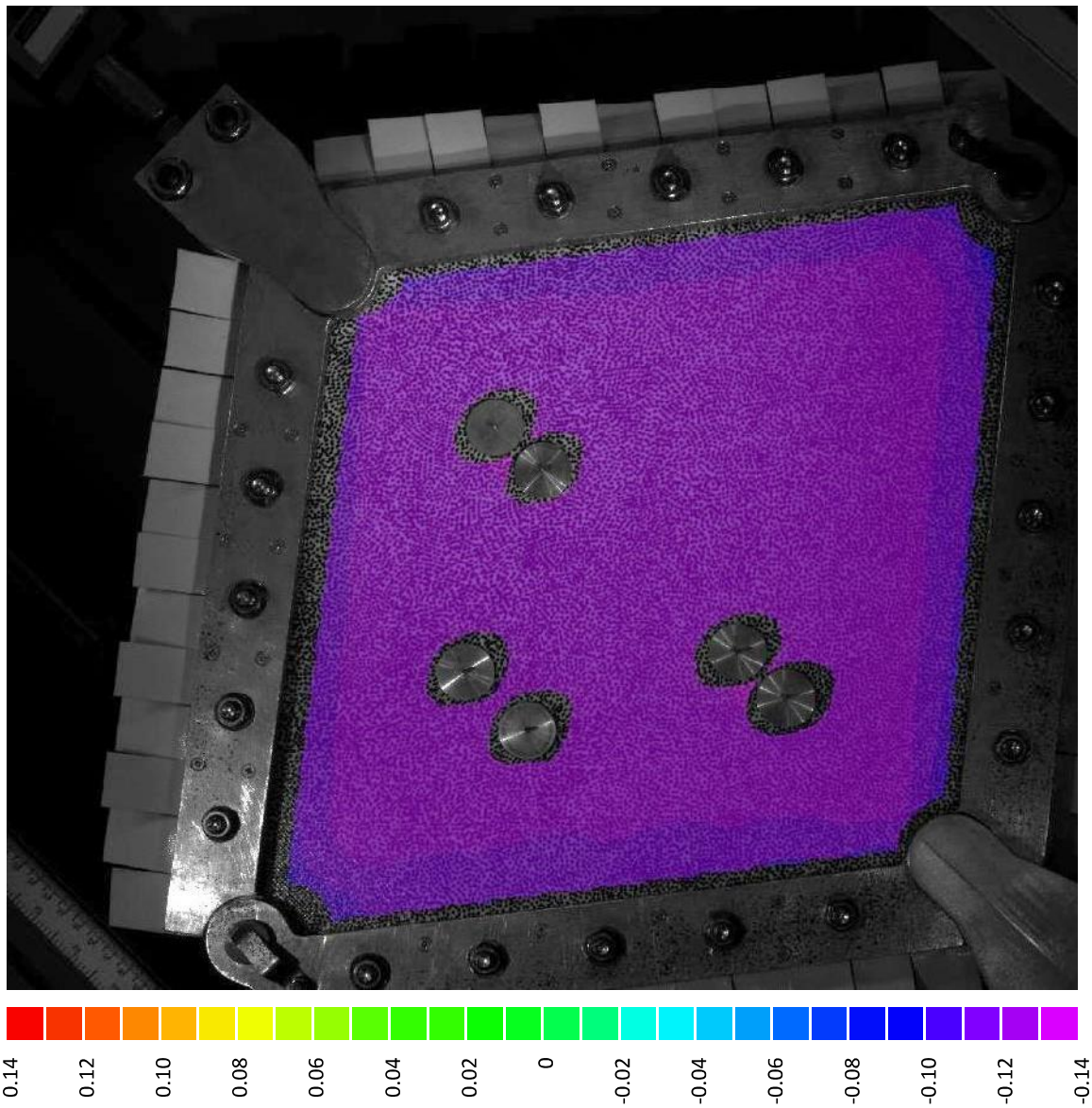

Figure 3.18 Shear strain ε_{xy} for CMX220 at 3% UTS at -15° of shear, strains obtained with Digital Image Correlation (DIC). Contours match DIC images for the shear ramp method published by Galliot and Luchsinger (2010b). Each colour boundary indicates a difference in shear angle of 1.1°

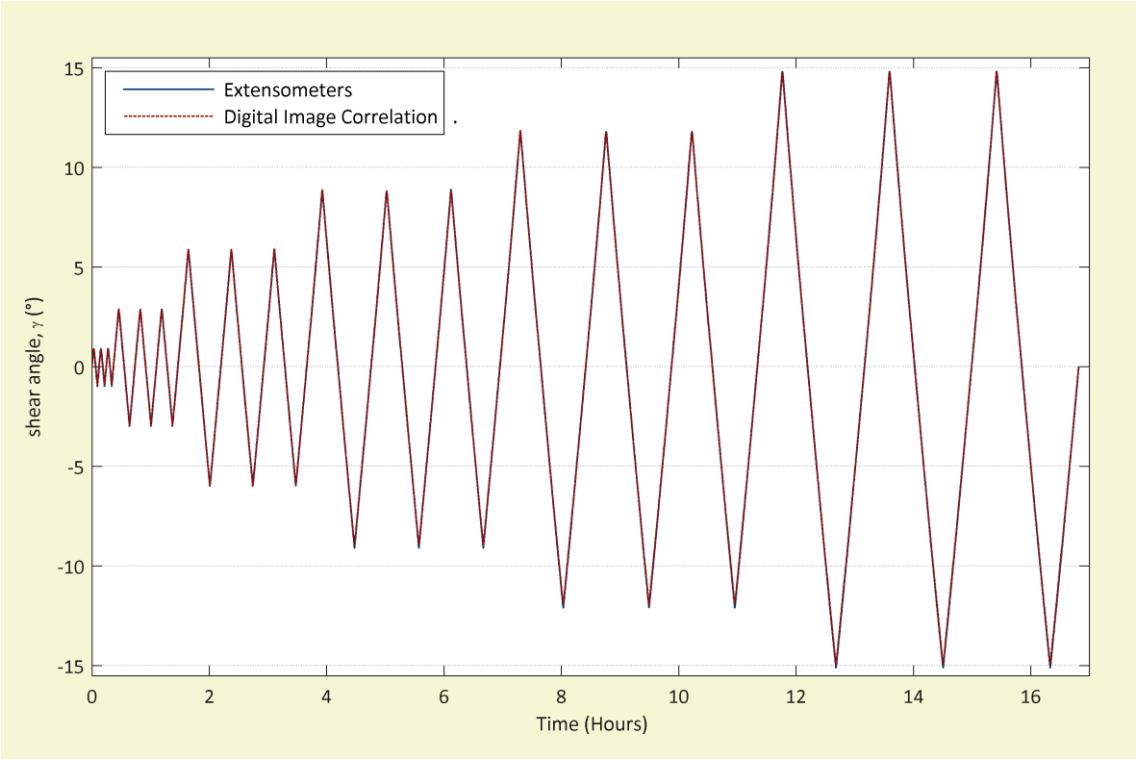

Figure 3.19 Comparison of the shear angle derived from linear extensometers and DIC images (over the area of the extensometers). CMX220 at 3% UTS with modified shear profile shown.

3.4.4 Shear stress-strain cycles and calculation of the shear modulus

Plots of the test results (Figure 3.20 to Figure 3.23) separate sets of shear cycles by angle of shear deformation and fabric type and allow for a visual comparison of the shear behaviour between tests at different biaxial stresses. Each cycle can be seen to consist of a positive and negative half, with each half having a portion of loading (increasing absolute shear stress) and unloading (decreasing absolute shear stress). The cycles in Figure 3.20 to Figure 3.23 progress in the clockwise direction and each cycle set consists of 3 cycles (as previously shown in Figure 3.14). Initially, values of shear stiffness were calculated as described in the MSAJ standard (MSAJ, 1993) (Figure 3.20 and Table 3.6) – currently the only available test standard. The standard describes tip-to-tip measures of stiffness at ± 1° of shear and is an average of the stiffnesses derived for the second and third cycles. Installation behaviour is captured in the initial cycle. Tip-to-tip stiffness is determined from the gradient of a line that connects the point of maximum shear stress-strain (the tip) of the positive half of a shear cycle with the point of maximum absolute shear stress-strain (the tip) of the negative half. Results show increasing shear stiffness with increased biaxial stress across the three fabrics tested. Accounting for shear at different biaxial stress states should be considered for accurate prediction of material behaviour, as differences of these magnitudes in shear stiffness have been shown to significantly impact the results of fabric structure analysis (Bridgens and Birchall, 2012).

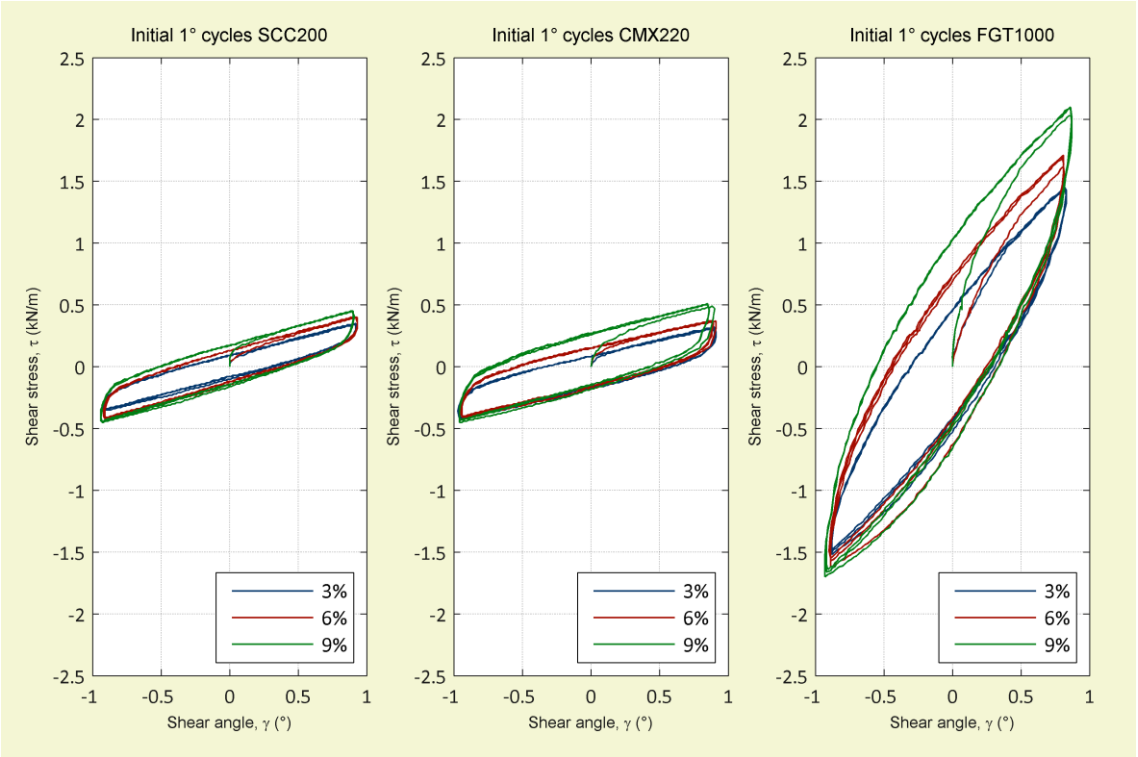

Figure 3.20 Shear stress-strain plots for initial +/- 1° cycles. Results show increasing shear required to achieve 1° of deformation with increasing biaxial stress

Table 3.6 Shear moduli at initial +/-1° of shear deformation

Fabric	Material	Shear moduli, G (kN/m)		
		3% UTS	6% UTS	9% UTS
SCC200	PVC/PET	21.8	25.7	28.0
CMX220	PVC/glass	22.6	24.3	29.6
FGT1000	PTFE/glass	99.2	109.9	120.3

Elastic constants have been determined for SCC200 and CMX220 by Bridgens *et al.* (2011) and can be compared with rule-of-thumb measures. Using the rule-of-thumb method that the states shear modulus is typically elastic modulus/20 (Barnes et al., 2004b), the shear modulus would be 15-17kN/m for SCC200 and 43-58kN/m for CMX220 (the range of values reflects a measure derived from either of the unequal warp and fill stiffness). It is immediately apparent that the rule-of-thumb stiffness measures and the stiffness measures determined through experimental testing are not similar in magnitude. At 3% UTS (typical prestress) the rule-of-thumb measure for the SCC200 fabric is 22-31% less, and for the CMX220 fabric is 90-157% higher than that obtained through testing. It would be interesting to quantify the influence or significance of these differences, say, through comparative structural analysis, but this is beyond the scope of this research project. As in the previous section, these differences suggest that the rule-of-thumb measures can only provide very approximate measures of shear stiffness and should be used in design and analysis with caution.

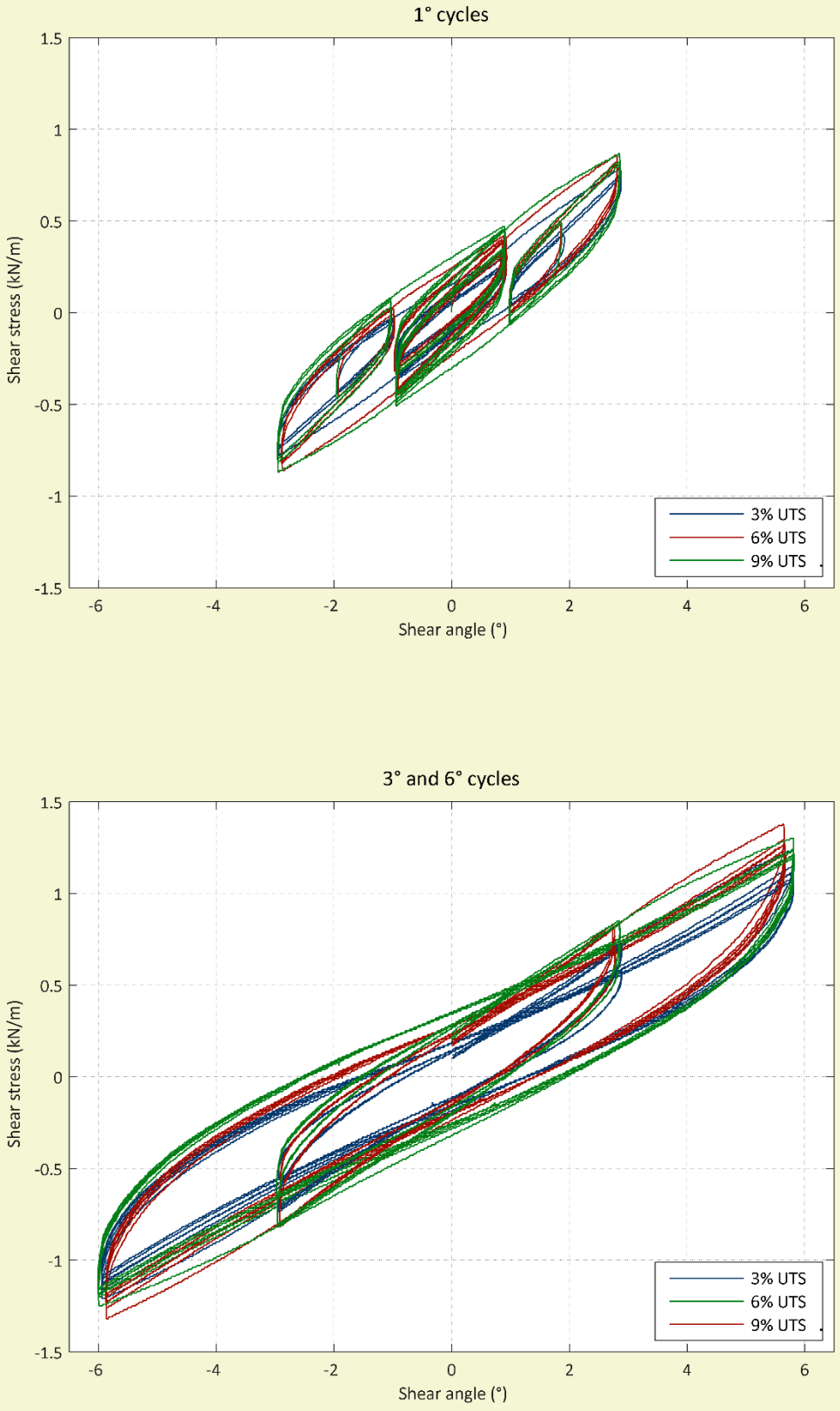

Figure 3.21 Picture frame shear test results for SCC200 (PVC/PET)

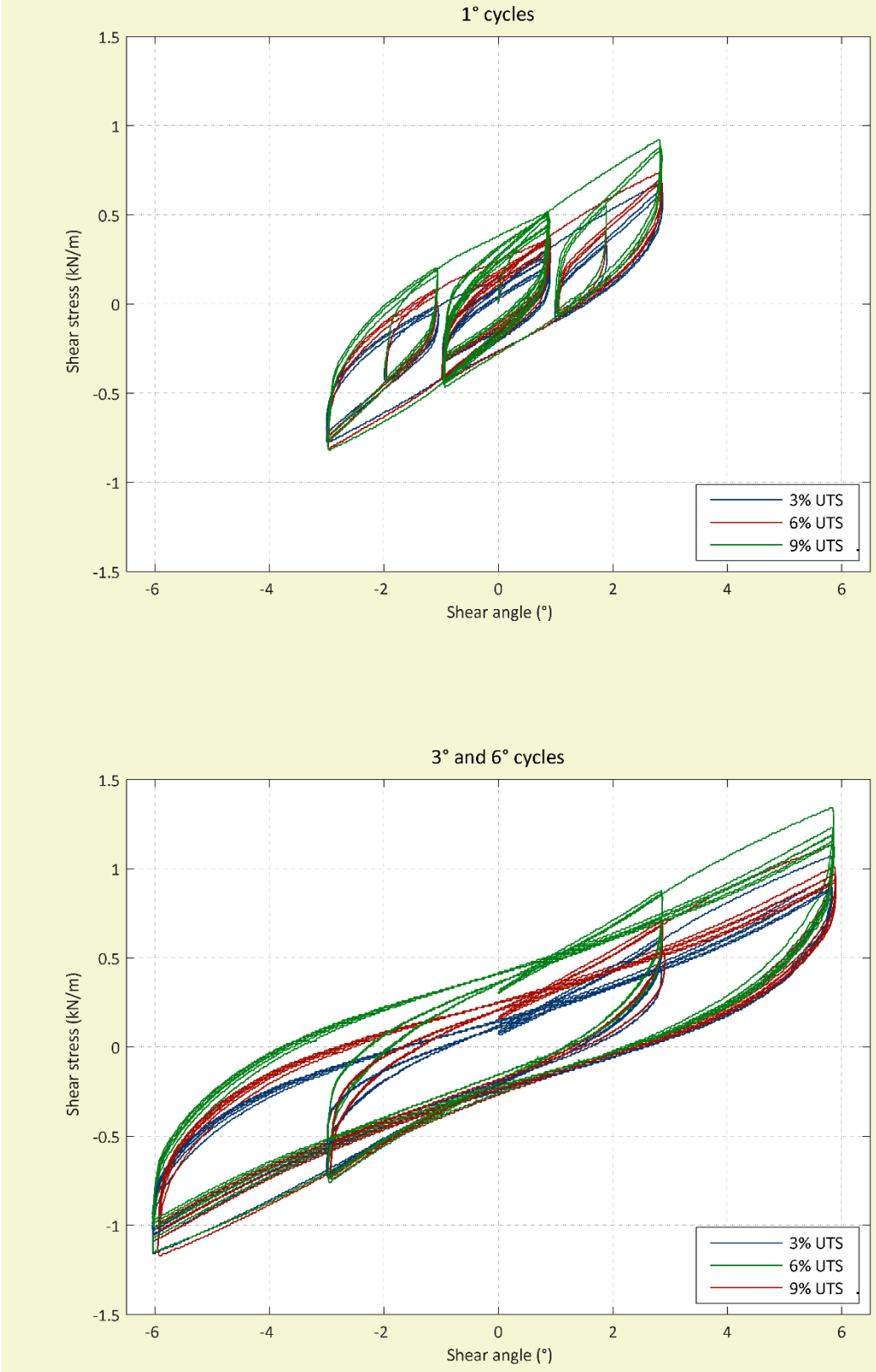

Figure 3.22 Picture frame shear test results for CMX220 (PVC/glass)

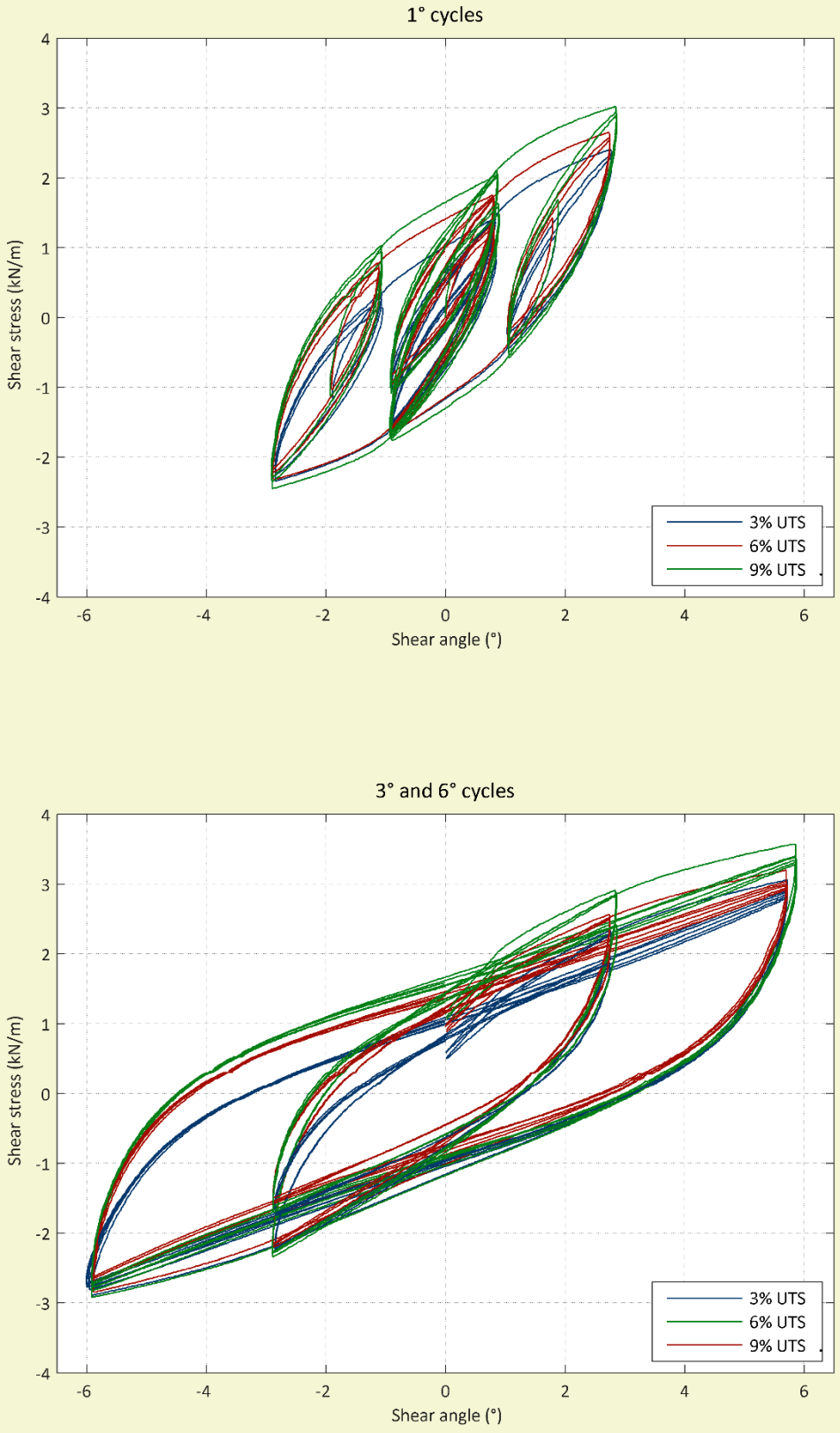

Figure 3.23 Picture frame shear test results for FGT1000 (PTFE/glass)

There are several ways to make a linear approximation. While tip-to-tip measures of stiffness effectively ignore the gradient of any part of the shear cycle, they provide an approximation of overall behaviour. However, it is observed that a portion of each half of a cycle is approximately linear after an initial period of shear deformation that occurs either 1) after a change in the direction of shearing; or 2) when shear deformation occurs at an angle that has not yet been prescribed by the test profile. The latter observation is apparent only in the positive half of any cycle and that the linear parts of the positive and negative halves of all cycles are substantially parallel to one another. For the second and third cycles within each cycle set, the approximately linear part is seen to extend for the loading portion of each half of the cycle. A linear approximation of this linear part of the data is proposed as an alternative constant measure of the non-linear shear stress-strain behaviour.

Approximations of shear stiffness were calculated from the second and third cycles (Table 3.7). All tip-to-tip measures show increasing shear stiffness for all angles of shear deformation with increasing biaxial stress. However, the alternative linear approximations show no consistent discernible increase in shear stiffness with increasing biaxial stress for the parts of the cycles considered. The measures of shear stiffness are similar for both the positive and negative halves of the shear stress-strain cycles. The rule-of-thumb measures compared to the approximations for the positive loading portion of the shear cycles (again for the initial 1° cycles) are as follows: for the SCC200 fabric the rule-of-thumb measure is between 8.5% less and 3.7% more than the approximation of the test data; and for the CMX220 fabric the rule-of-thumb measure is 196-300% more than the approximation of the test result. Whilst the rule-of-thumb measures for the SCC200 fabric is comparable to the approximate measure, such closely matched results were not achieved from the CMX220 fabric.

Shear deformation observed in coated woven fabrics is resisted by rotation at yarn intersections, yarn bending, shear of the coating and coating compaction (§2.1.2). The observed increase in shear stiffness is likely to be the result of increased rotational friction at the yarn intersections, which is caused by an increase in out-of-plane contact forces. This is the only shear deformation mechanism that is likely to be affected by increasing levels of tension in the yarns. The differences observed between the cycles at increasing biaxial stress can be seen to arise during the initial shear deformation. The phenomenon is best seen in the plots of the initial shear stress-strain behaviour to 1° (Figure 3.20).

Table 3.7 Shear stiffnesses, *G*, for all cycle sets for all fabrics tested

Cycles	% UTS	Shear Stiffness, *G* (kN/m)								
		SCC200			CMX220			FGT1000		
		+'ve curve	-'ve curve	Tip - Tip	+'ve curve	-'ve curve	Tip - Tip	+'ve curve	-'ve curve	Tip - Tip
1 (1°)	*3%*	16.4	16.4	21.8	14.5	14.5	22.6	66.8	63.2	99.2
	6%	16.8	18.0	25.7	14.2	14.5	24.3	67.0	62.6	109.9
	9%	17.6	18.0	28.0	16.1	16.2	29.6	67.3	63.7	120.5
2 (1°)	*3%*	18.1	12.9	21.8	16.6	11.2	22.7	56.2	51.4	89.6
	6%	18.3	15.3	26.0	16.3	11.2	24.6	55.2	57.6	98.3
	9%	17.0	15.1	27.0	18.0	12.9	30.1	58.0	57.4	109.4
3 (1°)	*3%*	13.0	14.8	19.2	10.9	12.6	19.5	52.7	56.0	85.6
	6%	14.7	16.7	23.9	11.5	14.1	23.0	53.2	58.4	98.0
	9%	15.2	16.7	26.1	12.9	15.1	27.9	53.8	58.6	106.2
4 (1°)	*3%*	12.2	16.4	21.0	10.0	15.5	21.6	42.9	51.4	82.0
	6%	13.9	19.1	25.8	11.2	16.5	25.4	46.3	53.8	95.2
	9%	13.5	16.7	26.4	13.1	17.4	29.1	48.8	55.1	102.9
5 (1°)	*3%*	12.5	12.8	17.8	10.6	10.3	18.0	51.7	49.4	79.3
	6%	13.8	14.9	22.3	10.7	10.9	20.7	48.8	50.0	88.1
	9%	14.4	14.8	24.5	12.0	11.9	25.3	51.2	51.0	97.4
6 (3°)	*3%*	12.1	12.3	14.2	10.3	10.6	13.1	29.4	28.3	46.3
	6%	13.0	13.4	16.5	10.2	11.1	14.2	26.2	29.4	47.8
	9%	11.5	11.9	16.3	10.6	11.2	15.8	27.9	29.0	51.6
7 (1°)	*3%*	11.9	12.1	17.1	10.0	10.1	17.2	47.4	46.6	74.3
	6%	13.2	14.4	21.7	10.0	10.6	20.0	44.9	46.9	82.5
	9%	14.2	14.3	23.8	11.3	11.5	24.4	47.3	48.5	91.6
8 (6°)	*3%*	10.1	10.2	11.4	8.6	9.0	10.1	18.7	16.5	28.3
	6%	10.8	10.8	12.8	8.0	8.9	10.4	16.2	17.9	28.8
	9%	8.9	8.9	11.9	8.5	8.7	11.3	17.5	17.1	30.6
9 (1°)	*3%*	9.9	10.1	15.1	8.4	8.1	14.6	38.8	36.2	62.8
	6%	11.1	12.6	19.2	7.9	8.1	17.2	37.3	36.3	69.5
	9%	11.8	12.2	21.2	9.3	8.9	21.5	39.1	37.0	77.6
10 (3°)	*3%*	8.8	8.9	11.2	6.9	6.9	9.7	22.3	21.0	36.5
	6%	9.8	9.9	13.4	6.7	7.1	10.6	20.0	21.3	37.4
	9%	9.1	9.2	13.7	7.4	7.2	12.3	21.3	20.8	40.6
11 (1°)	*3%*	10.1	10.3	15.2	8.5	8.6	14.6	39.5	37.2	62.4
	6%	11.4	12.2	19.4	8.1	8.5	17.4	37.5	37.9	69.1
	9%	12.5	12.6	21.6	9.6	9.2	21.7	38.9	38.3	76.8
12 (6°)	*3%*	9.6	9.9	10.7	8.2	8.5	9.3	19.3	17.6	27.3
	6%	10.4	10.6	12.2	7.3	8.3	9.4	16.6	19.7	27.8
	9%	8.9	9.2	11.6	7.9	8.2	10.4	18.2	18.8	29.5
13 (1°)	*3%*	9.5	9.6	14.6	8.2	7.6	14.1	37.5	34.3	60.6
	6%	10.7	11.6	18.7	7.6	7.9	16.8	35.8	35.0	67.1
	9%	11.5	11.9	20.8	9.0	8.6	21.2	37.6	35.2	74.2

Additional energy is required to overcome the frictional resistance in order to deform the fabric. The correlation between strain energy and biaxial stress is seen from the increasing area within the stress-strain curves (Figure 3.20 to Figure 3.23). The results indicate that biaxial tension and shear behaviour are linked for architectural fabrics.

Increasing biaxial stress in the fabric will increase contact forces at the pins in the corners of the frame, with a corresponding increase in rotational friction of the hinges. The effect of frame friction with applied biaxial loading is difficult to isolate from the overall response of the frame plus the fabric, and has not been considered in previous studies using picture frame shear testers. To investigate the effects, biaxial load must be applied to the frame to simulate a shear test in a manner that does not introduce any shear resistance. Preliminary testing involved clamping two perpendicular strips of individual yarn bundles into the shear test frame (Figure 3.24), the yarn bundles having been first subjected to uniaxial loading in the biaxial test rig (Figure 3.25). The applied biaxial loading corresponds to the 3%, 6% and 9% biaxial load ratios considered in this study (Table 3.4). A shear test was then conducted in the normal manner and the results compared to the results of the actual tests.

This preliminary testing indicated that friction in the hinges of the frame accounts for approximately 10% of the total shear resistance recorded for any level of biaxial pretension. This means that the fabric is subjected to 90% of the expected level of shear stress. Further testing is required to accurately determine a 'stress reduction factor' that could be used in the calculation of shear moduli.

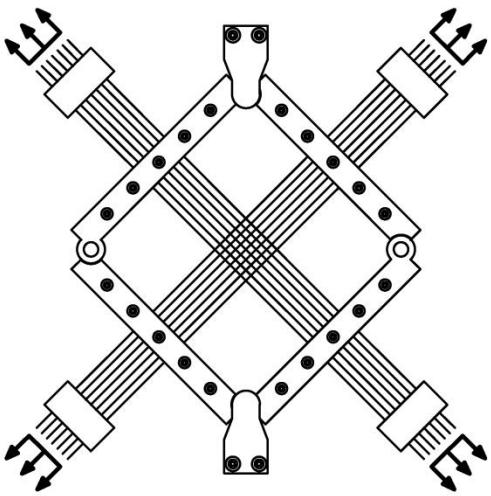

Figure 3.24 Strips of yarn bundles clamped in the picture frame as part of preliminary testing to establish the influence of biaxial tension on the frictional resistance of the hinged shear frame

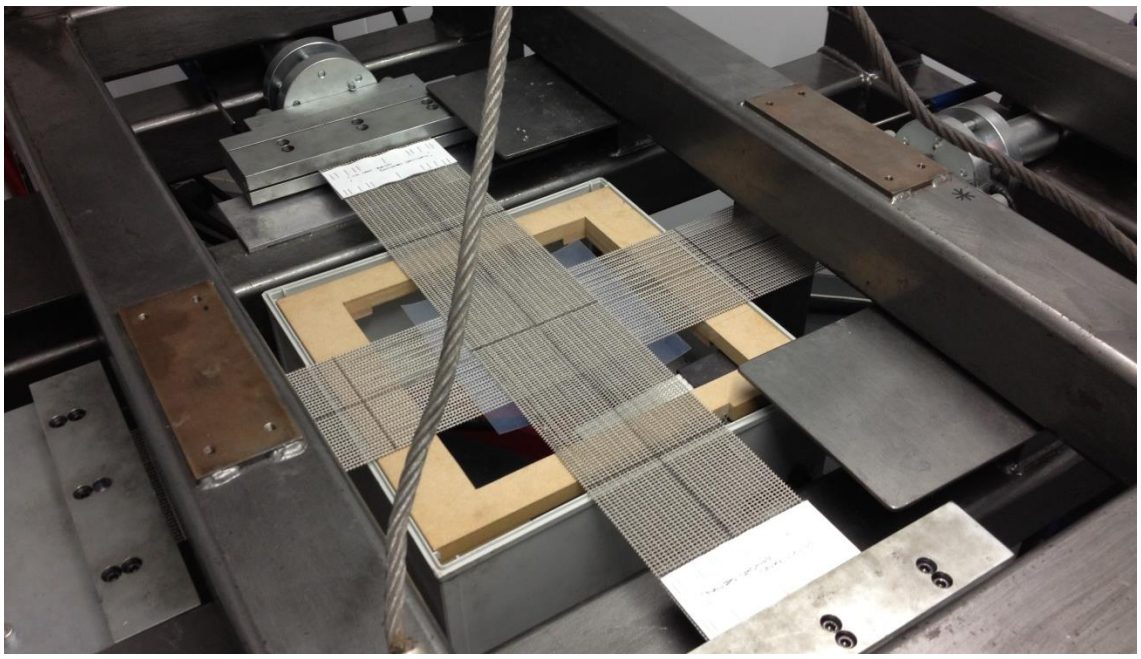

Figure 3.25 Strips of yarn bundles in held in the biaxial test rig having, the perpendicular strips subject to uniaxial loading

3.4.5 Modelling shear stiffness

Any increase in shear stiffness with increasing biaxial stress has implications for the analysis methodology used for tensile fabric structures. Material properties used for analysis of tensile fabric structures are typically defined within a plane stress orthotropic framework, using elastic moduli and interaction terms (Barnes *et al.*, 2004b) (Equation 3.3).

$$\begin{Bmatrix} \varepsilon_w \\ \varepsilon_f \\ \varepsilon_{wf} \end{Bmatrix} = \begin{bmatrix} \frac{1}{E_w} & \frac{-v_{fw}}{E_f} & 0 \\ \frac{-v_{wf}}{E_w} & \frac{1}{E_f} & 0 \\ 0 & 0 & \frac{1}{G} \end{bmatrix} \cdot \begin{Bmatrix} \sigma_w \\ \sigma_f \\ \sigma_{wf} \end{Bmatrix} \qquad \textbf{Equation 3.3}$$

where, ε = strain, σ = stress, E = direct stiffness G = shear stiffness and subscripts w and f denote warp and fill directions, respectively.

The plane stress framework is used to approximate complex non-linear behaviour with linear parameters. This approach has the benefit of making fabric material behaviour compatible with commercial analysis software. The zero terms in the stiffness matrix indicate an assumed non-interdependence between biaxial and shear behaviour. However, the results of shear tests suggest that non-zero terms may be required to account for the influence of biaxial tension on shear behaviour when designer engineers use the assumption of plane stress behaviour in analysis. Due to the non-linear, hysteretic nature of the test results a different analysis framework may be more appropriate, as previously demonstrated for biaxial behaviour (Gosling and Bridgens, 2008).

3.5 Bias shear testing

A series of tests were proposed in which bias shear test data would be compared to picture frame test data obtained using the novel frame design. A comparative bench mark study identified similar behaviours for uncoated fabrics without the application of biaxial tension (Cao *et al.*, 2008). If the behaviour of *coated* fabric exhibited by the two tests was observed to be similar, it was posited that the bias test data could be used as input data for a predictive shear model. Advantages of the bias shear test (§2.2.2) include that it is simple and fast to implement and there is no requirement for large and complex to prepare test specimens.

It is important to consider how the specimen is held during bias testing. Clamps used for uniaxial testing of architectural fabrics may have coarse teeth (Figure 3.26), which are intended to grip the specimen without crushing the yarns (as this may reduce the tensile strength of the specimen and cause failure during a test). However, the fabric may slip through the clamp. The situation is not a problem in uniaxial testing performed in the yarn direction, as deformation may be measured using instrumentation attached to a specimen between the clamps. As bias test methodologies require a fixed gauge length between clamps, a set of bias testing clamps suitable for testing of architectural fabrics were design and fabricated. The bias clamps (Figure 3.27) were designed around the same fine teeth used in the picture frame design. The exact clamp design is specified in the workshop drawings provided in Appendix B.

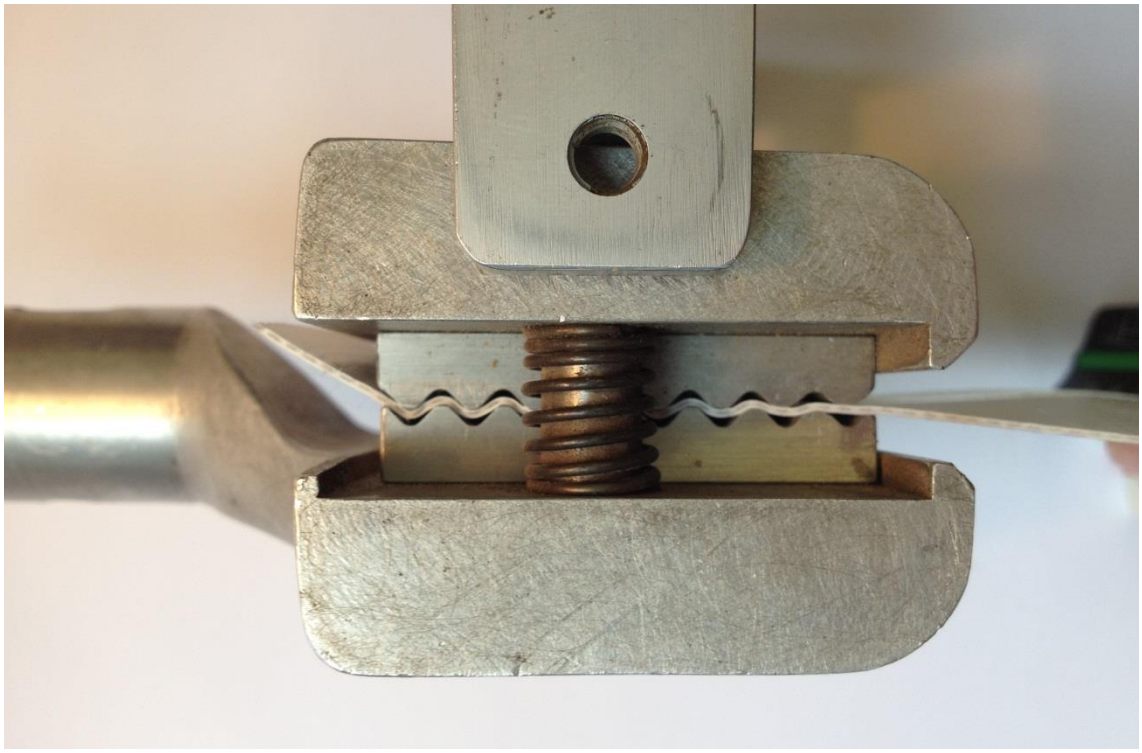

Figure 3.26 Existing clamp design with coarse teeth, in which test specimens are observed to slip though clamp during testing

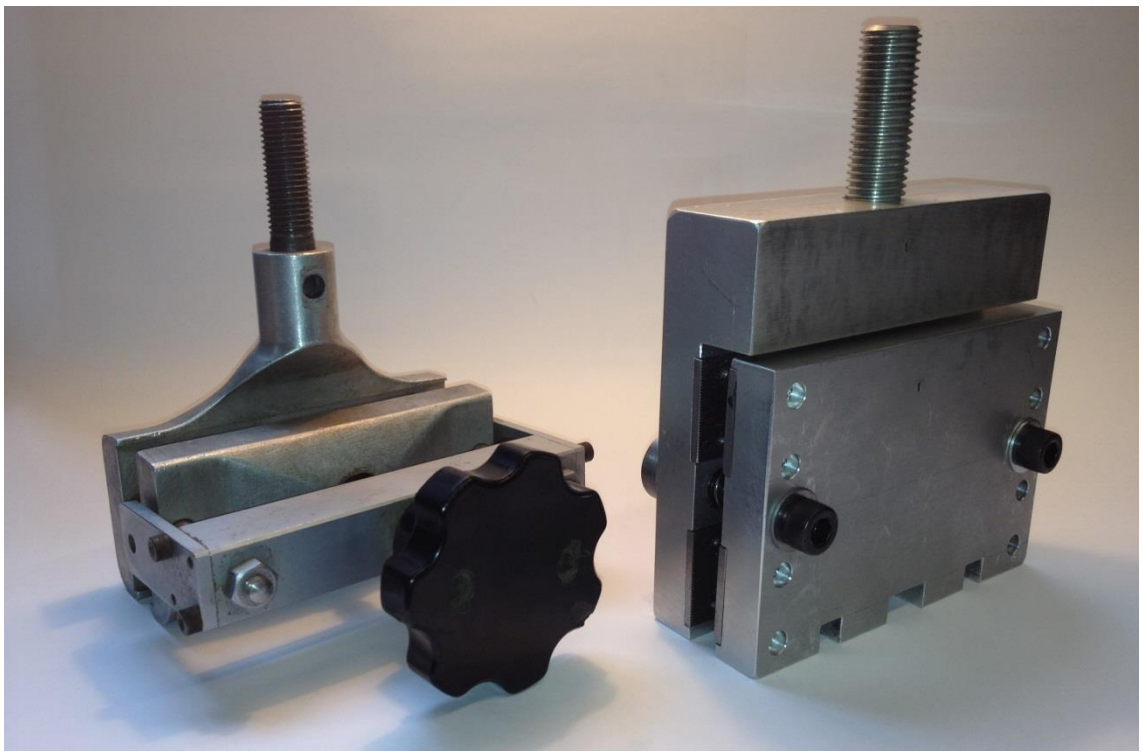

Figure 3.27 Existing clamp design (left) and revised design (right) suitable for bias testing

The results of the comparative testing (Figure 3.28 to Figure 3.33) indicted that the shear stress-strain behaviour between the two test methods is not similar for the fabrics tested. The bias test fails to capture the initial stiffnesses observed in the picture frame results. Further, the stiffnesses according to bias test are lower throughout the deformation of the specimen, which is to be expected. There appears to be no relationship between stress-strain response obtained when using the picture frame test and the bias test methodologies. Therefore, normalisation methods used when testing uncoated fabrics (Lebrun *et al.*, 2003; Cao *et al.*, 2008; Launay *et al.*, 2008) should be used with caution by investigators using the bias test to explore behaviour of coated and architectural fabrics.

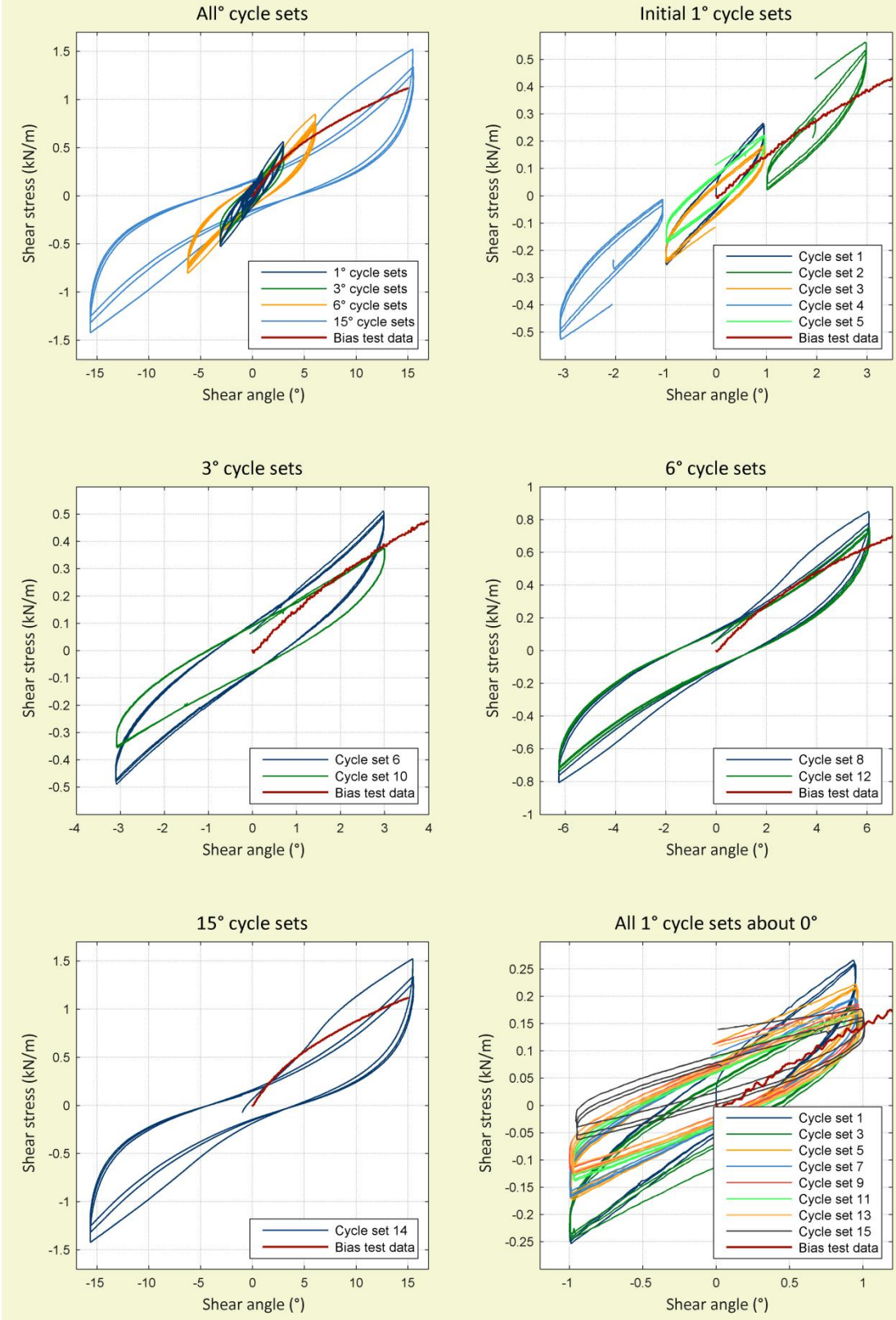

Figure 3.28 Picture frame and bias shear test results for Ferrari 702 (PVC/PES)

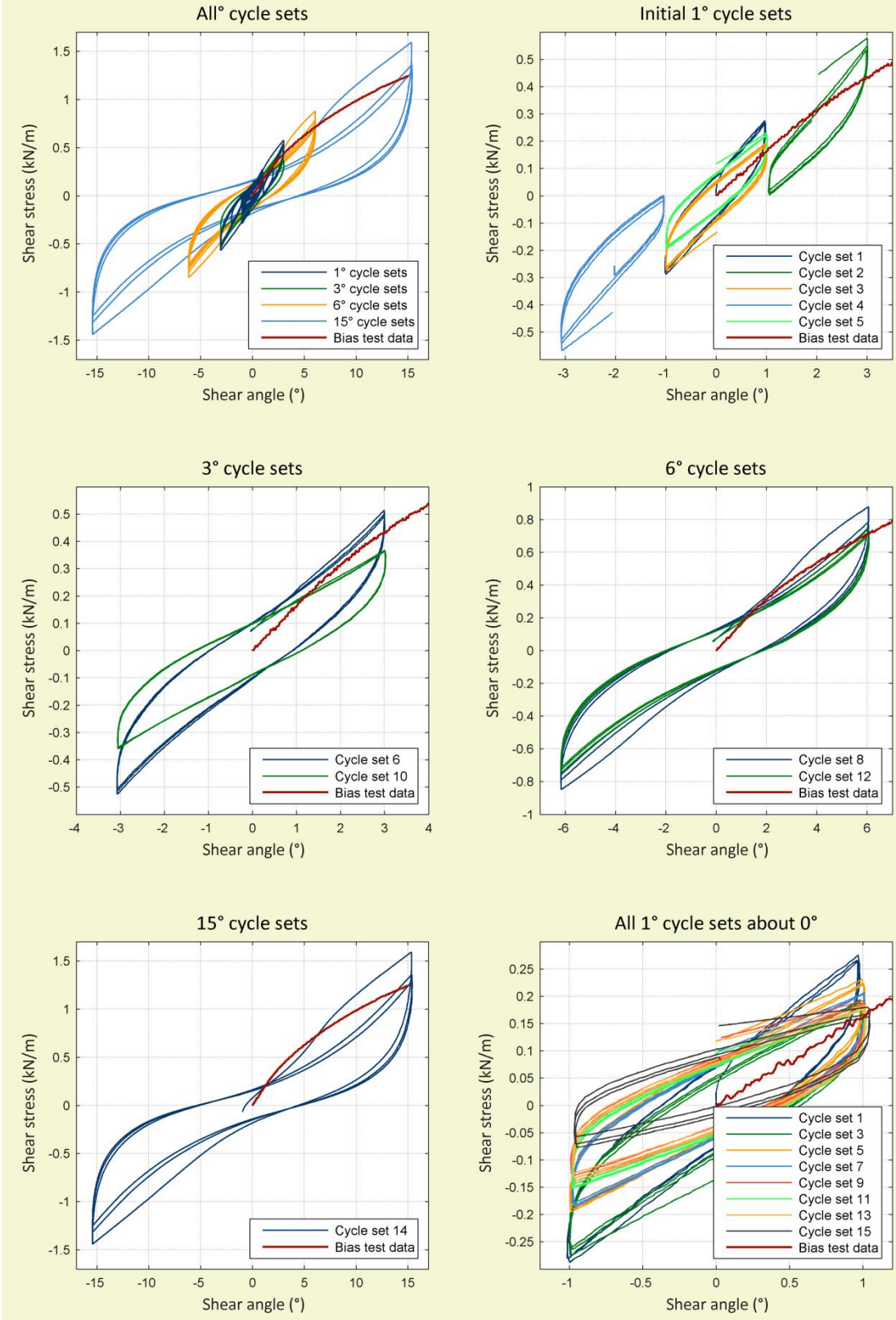

Figure 3.29 Picture frame and bias shear test results for Ferrari 1202 (PVC/PES)

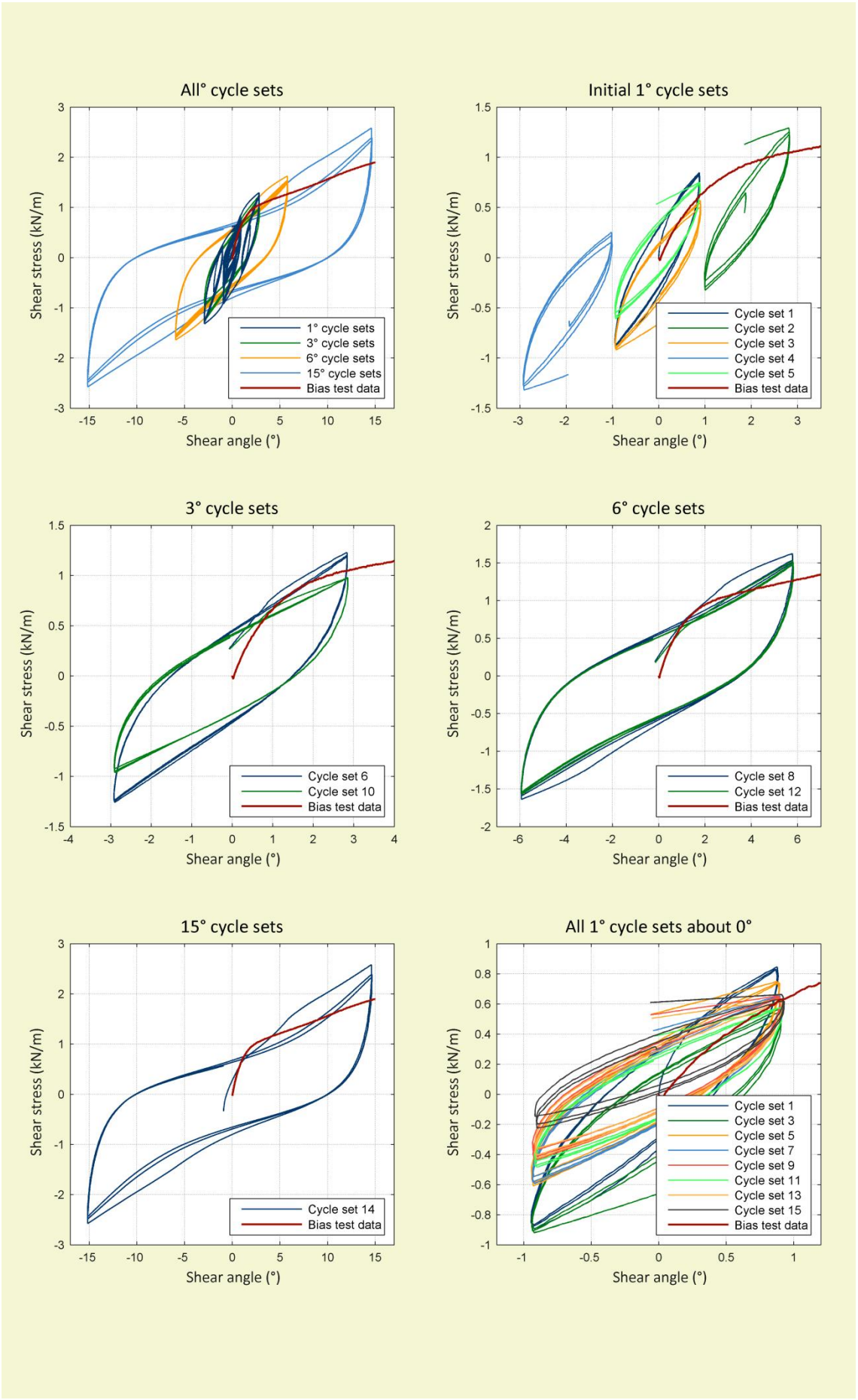

Figure 3.30 Picture frame and bias shear test results for Verseidag B10089 (PTFE/glass)

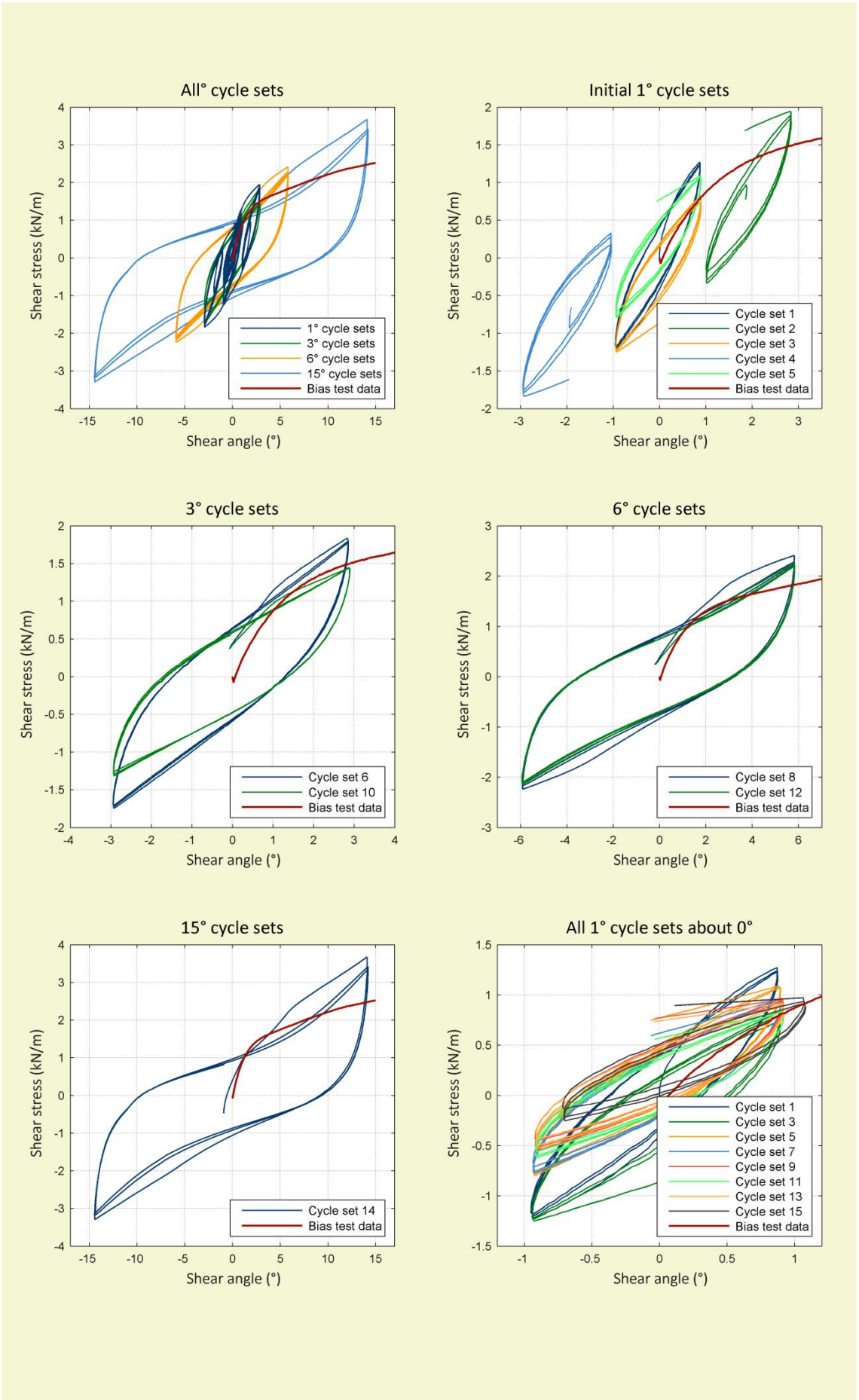

Figure 3.31 Picture frame and bias shear test results for Verseidag B18059 (PTFE/glass)

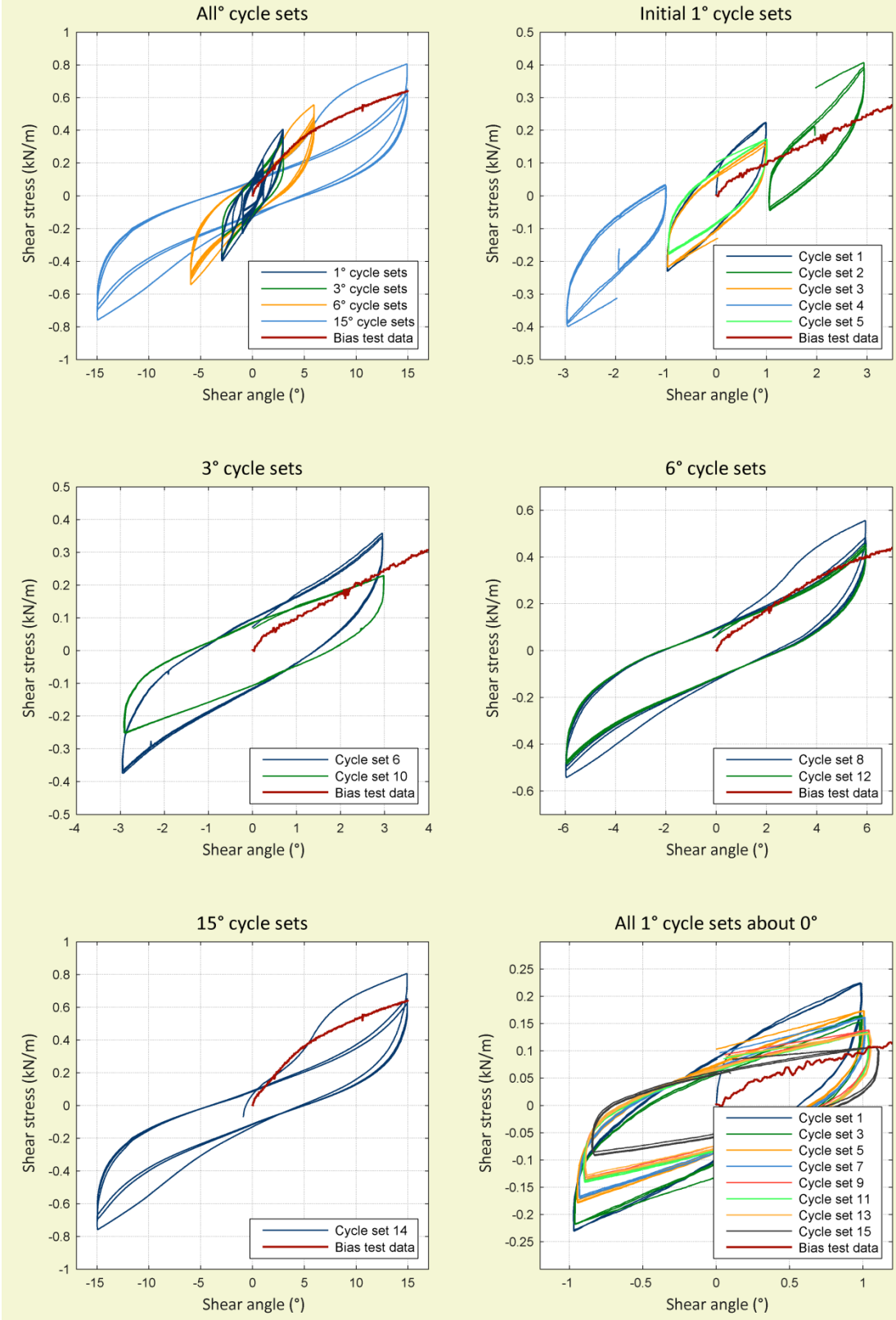

Figure 3.32 Picture frame and bias shear test results for PD Interglas ATEX3000 (silicone/glass)

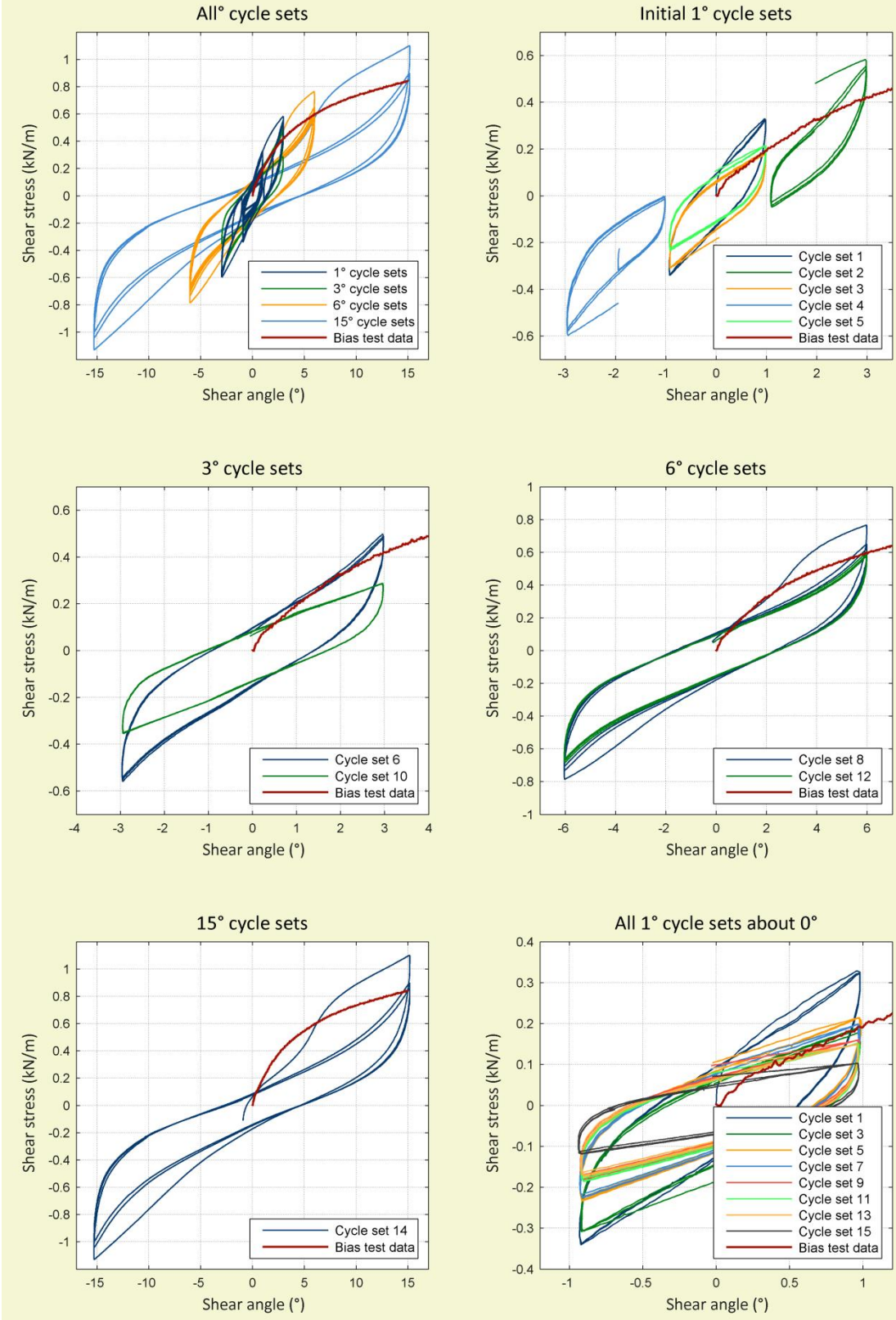

Figure 3.33 Picture frame and bias shear test results for PD Interglas ATEX5000 (silicone/glass)

3.6 Summary

There are no British or European standards for shear testing of architectural fabrics and there is little available guidance. However, development of European standards for fabric testing and fabric structures design are underway, with the CEN TC250 Working Group established to write a standard for membrane structures for inclusion in Eurocode 10. Therefore, identifying accurate methods for characterising shear behaviour is important.

A methodology based on a novel picture frame design has been proposed which allows determination of the shear stress-strain relationship. Achieving a homogenous strain field during testing allows for accurate determination of an architectural fabric's response to shear deformation. There is no requirement for correction factors to account for non–homogeneity of the strain field.

Methods for shear characterisation are important but interpretation of the results must also be addressed. The use of linear approximations of the stiffness values may be problematic for the design and construction of tensile surface structures. From the results of the test performed on PVC coated polyester fabrics, PVC coated glass fabrics and PTFE coated glass fabrics, short and medium term behaviour is different and materials are softer at higher angles of deformation (further testing would be required to investigate other materials). However, uncertainty over a choice of a single stiffness value could be dealt with, with the use of a statistical approach that considers variability of all parameters, such as described by Gosling *et al.* (2013). It would be useful to extend recent comparative biaxial testing studies by Bridgens *et al.* (2011) to include shear test methods and protocols in multiple locations.

The novel picture frame has been employed to subject a test specimen to a known biaxial stress state, which is maintained whilst a homogenous shear deformation is applied. The homogeneity of the shear strain across the specimen makes determination of the shear stress in the fabric straightforward, however friction in the frame hinges does mean that a reduction factor is required to determine the shear force from the applied load. Given the difficulty of accurately determining the hinge friction with applied biaxial load, a pragmatic approach would be to minimise the friction in the frame to avoid the need for a reduction factor. For the frame presented here, replacement of the self-lubricating bushes with needle roller bearings could provide a significant reduction in friction.

Shear *behaviour* is shown to change with increasing biaxial stress, with greater strain energy required to mobilise shear deformation in a highly tensioned fabric. Whether biaxial pretension affects constant values of the shear *stiffness* of the fabric depends on how the stiffness is evaluated from the non-linear, hysteretic shear response. The tip-to-tip value of shear stiffness varies with biaxial stress, but the effect on the gradient of an approximately 'linear' part of the curve is minimal.

To include interaction of biaxial and shear stresses in the plane stress framework requires non-zero interaction terms, but further testing, and a consensus on how the shear stiffness should be calculated, would be required before values could be proposed. Given that the validity of using the plane stress framework to describe fabric behaviour is limited, it is proposed that further development should focus on methods that can fully capture the complex tensile and shear response of coated woven fabrics. One option currently being developed uses neural networks to relate stresses to strains with no assumptions about the form of the material response, with potential to incorporate stress history to capture hysteretic, visco-elastic behaviour (Bartle *et al.*, 2013).

Chapter 4:
A predictive model for architectural fabrics

Contents

Figures

Tables

4.1 Introduction

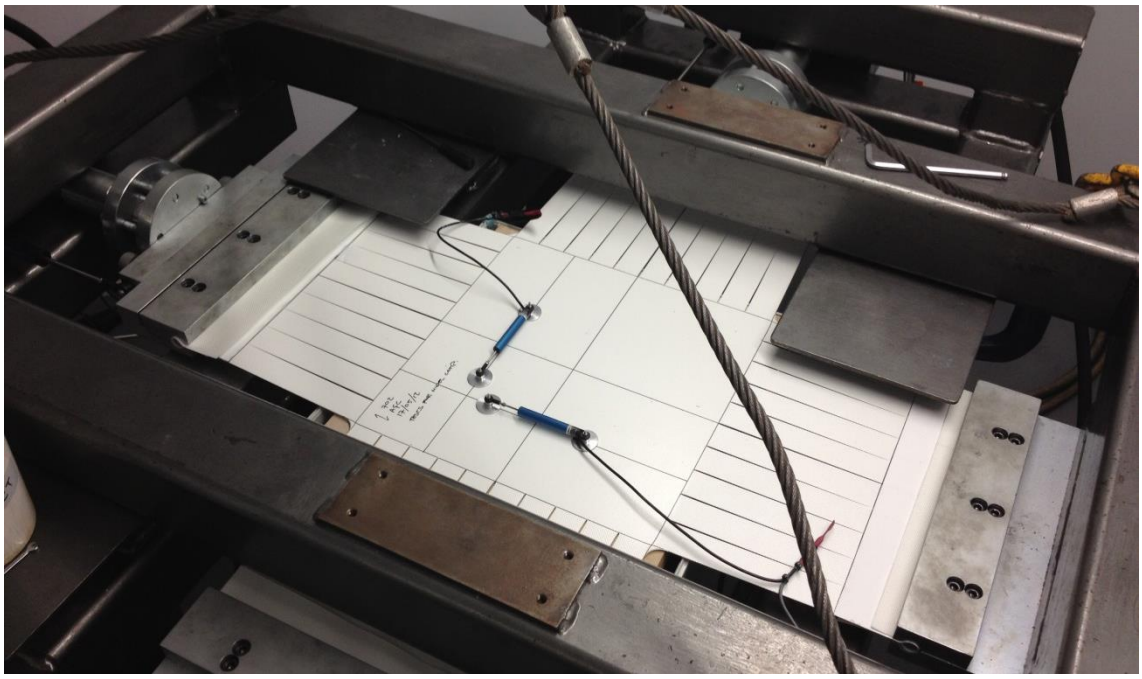

Figure 4.1 Biaxial test apparatus with cruciform sample

To reduce uncertainty in the analysis and design of tensile fabric structures, design engineers require accurate material properties for modelling and calculations. While complex specialist testing methodologies, such as biaxial testing (Figure 4.1), can supply the required properties, the testing is time consuming and expensive. Specialist testing can be prohibitively expensive for small tensile fabric structure projects. An alternative to experimental testing is analytical predictive modelling, whereby a model is used to accurately predict the results of experimental tests. Such models benefit designers by reducing the time and cost associated with obtaining material properties through testing. Easy and rapid determination of fabric properties would allow for many possible fabrics to be compared for a project and to evaluate their performance for a given design. Currently, results generated by predictive fabric models are not used in tensile fabric structure design.

Much of the existing body of work focuses on predicting the mechanical response of a given fabric used for rigid composite forming (2.2.2). However, these models are typically for a specified uncoated fabric. Designers of tensile fabric structures utilise a wide range of different architectural fabrics, fabricated from different constituent materials and with disparate material behaviour and properties. This is due to varying material performance, design requirements and financial constraints. While material properties and a material's response to load will differ between fabrics and fabric types, basic underlying mechanisms of deformation are the same. Therefore, it is desirable that in developing a predictive fabric model it should be suitable for a wide range of architectural fabrics.

This chapter describes the further development of the sawtooth model of Bridgens (2005) which was based upon early work by Menges and Meffert (1976). Bridgens (2005) developed a model comprising a unit cell and models crimp interchange and the interaction between the yarns and the coating for a plain weave fabric.

4.1.1 Model requirements

The model shall:

- Predict the in-plane biaxial and shear behaviour of coated woven fabrics used in the design and construction of tensile fabric structures;
- Be suitable for a range of fabrics;
- Require no calibration against a data set;
- Rely only on easily obtainable input parameters, using standard equipment and test methods available to designers and fabricators;
- Produce repeatable results by removing subjective interpretation of input data; and
- Be demonstrated as valid through comparison with experimentally obtained test data.

4.1.2 Model nomenclature

Similar nomenclature has been adopted to that used by Bridgens (2005). Units used throughout the predictive model are specified against the definitions below.

Subscripts 1 and 2 denote warp and fill yarn directions, respectively. When a relationship between variables is the same in both yarn directions, the respective formulae are combined and presented as a single formula, with the subscripts denoting the yarn direction of each variable within the formulation, for example:

$$y_1 = A_1 cos\left(\frac{\pi x_1}{l_1}\right)$$ **Example 1**

$$y_2 = A_2 cos\left(\frac{\pi x_2}{l_2}\right)$$ **Example 2**

$$y_{1,2} = A_{1,2} cos\left(\frac{\pi x_{1,2}}{l_{1,2}}\right)$$ **Example 1 and Example 2 expressed as a single formula**

’	Modified value with applied load, e.g. A = crimp amplitude, A’ = modified crimp amplitude
$_0$	Initial value, e.g. A_0 = initial crimp amplitude
a	Amplitude of the surface defining the cross section (mm)
c	Contact length between intersection yarns (mm)
f	Total force applied to the unit cell (N)
fy	Out of plane force (N)
l	Unit cell length, half yarn wavelength (mm)
s	Yarn length (mm)
t	Yarn thickness (mm)
v	Poisson’s ratio
w	Yarn width (mm)
x	In plane direction, cross section coordinates
y	Out of plane direction, cross section coordinates
A	Crimp amplitude (mm)
AREA	Yarn cross sectional area (mm^2)
E	Young’s modulus (N/mm)
F	Applied load (N/mm)
Fc	Compressive force (N/mm^2)
Ff	Frictional force (N)
Fk	Force acting on coating (N/mm width), $Fk_{1,2}$ acts over $l_{2,1}$
RATIO	Ratio between yarn width and unit cell length, $w_{1,2}$ with respect to $l_{2,1}$
ε	Strain

4.2 Summary of the predictive model

The chapter presents the development of a novel predictive fabric model. A system of compatibility and equilibrium equations (Equation 4.1 – Equation 4.10) is derived which aims to realistically simulate principal deformation mechanisms within a range fabrics used in the construction of tensile fabric structures. These equation make up the model's objective function. Each equation is present below with reference to the subsequent pages in which the derivation of the respective equation is described. The model has been formulated to predict non-linear yarn behaviour and hysteresis using input parameters obtained using non-specialist test equipment, i.e. test equipment which is available in typical material testing laboratories.

The principal advantages of implementing the above model over existing models is 1) providing design engineers with a model which does not require difficult to obtain input parameters, i.e. input which can only be obtain from time consuming/expensive testing and 2) providing a model which is capable of reverse engineering fabric, i.e. enable designers to determine the yarn properties for a fabric with particular biaxial mechanical behaviour.

A sinusoidal description of the yarn geometry is first developed (§4.3.1, 103). Subsequently, the interdependent relationships which govern how the model predicts fabric behaviour are combined sequentially, starting with ensuring equilibrium of the crimp interchange by maintaining the sum of the out of plane forces, $fy_{1,2}$, equal to zero (Equation 4.1) and the sum of the amplitudes, $a_{1,2}$, equal to the sum of the half yarn thicknesses, $t_{1,2}$ (Equation 4.2) (§4.3.2, 113).

$$0 = f_1\left[\frac{2A_1\pi\ sin\left(\frac{\pi w_2}{2l_1}\right)}{l_{1,2}\sqrt{\left(1+\left(\frac{A_1\pi}{l_1}\ sin\left(\frac{\pi w_2}{2l_1}\right)^2\right)\right)}}\right] - f_2\left[\frac{2A_2\pi\ sin\left(\frac{\pi w_1}{2l_2}\right)}{l_{1,2}\sqrt{\left(1+\left(\frac{A_2\pi}{l_2}\ sin\left(\frac{\pi w_1}{2l_2}\right)^2\right)\right)}}\right] \qquad \textbf{Equation 4.1}$$

$$0 = A_1 + A_2 - \frac{t_1 + t_2}{2} \qquad \textbf{Equation 4.2 (adapted after Peirce (1987))}$$

It is also necessary to constrain the relationships between the lengths of the unit cell, $l_{1,2}$, the yarn lengths, $s_{1,2}$, and the crimp amplitudes, $A_{1,2}$ (Equation 4.3 and Equation 4.4) (§4.3.2, 113).

$$0 = l_{1,2} - \frac{s_{1,2} + \sqrt{{s_{1,2}}^2 - {A_{1,2}}^2\pi^2}}{2} \qquad \textbf{Equation 4.3}$$

$$0 = l_{1,2} - \frac{s_{1,2} + \sqrt{{s_{1,2}}^2 - {A_{1,2}}^2\pi^2}}{2} \qquad \textbf{Equation 4.4}$$

Further constraints are required by the model's formulation to maintain constant cross sectional area (Equation 4.5 and Equation 4.6) and the ratio of yarn width to the length of the unit cell in the orthogonal yarn direction (Equation 4.7 and Equation 4.8) (§4.3.2, 113).

$$0 = AREA_1 - \frac{-A_2 w_1(\pi - 2)cos\left(\frac{\pi w_1}{2l_2}\right) + 2A_2 l_2 sin\left(\frac{\pi w_1}{2l_2}\right) - 2w_1(A_2 - t_1)}{\pi} \quad \textbf{Equation 4.5}$$

$$0 = AREA_2 - \frac{-A_1 w_2(\pi - 2)cos\left(\frac{\pi w_2}{2l_1}\right) + 2A_1 l_1 sin\left(\frac{\pi w_2}{2l_1}\right) - 2w_2(A_1 - t_2)}{\pi} \quad \textbf{Equation 4.6}$$

$$0 = \frac{w_{0\,1}}{l_{0\,2}} - \frac{w_1}{l_2} \quad \textbf{Equation 4.7}$$

$$0 = \frac{w_{0\,2}}{l_{0\,1}} - \frac{w_2}{l_1} \quad \textbf{Equation 4.8}$$

Finally, the model must calculate yarn elongation due to force in the yarn (Equation 4.9 and Equation 4.10) (§4.3.2, 119).

$$0 = s_1 - s_{0\,1}\left[1 + wfun\left(\frac{f_1}{l_2} - stressAdjustment_1\right) + strainAdjustment_1\right] \quad \textbf{Equation 4.9}$$

$$0 = s_2 - s_{0\,2}\left[1 + ffun\left(\frac{f_2}{l_1} - stressAdjustment_2\right) + strainAdjustment_2\right] \quad \textbf{Equation 4.10}$$

This system of equations is solved for given force applied to the unit cell in each yarn direction, $f_{1,2}$, to predict the deformation, and thus the stain, of the unit cell. The model is implemented in MATLAB and uses MATLAB's built in solver, *fsolve*, to evaluate the system of equations.

4.3 Model formulation

4.3.1 Yarn geometry

Existing fabric models have proposed different approaches to describing the shape of yarn cross sections and crimp (§2.2). These approaches achieve different levels of accuracy in representing yarn geometry and will also vary in complexity for implementation within a numerical model. Of the aforementioned studies, only Gong *et al.* (2009) quantitatively assessed the appropriateness of the choice of representation, but only for the yarn cross sections.

A description of the yarn cross section which is consistent with the waveform of the interlacing orthogonal yarn will make for simpler implementation within a mechanical model. Circular, elliptical, racetrack and sawtooth representations offer an inaccurate representation of the continuously undulating woven yarns, and polynomial and surface functions are too complex for initial development of a mechanical analytical model. The appropriateness of sinusoidal waveforms has been suggested by Bridgens (2005). An assessment of the accuracy of using sinusoidal yarn descriptions was the first step in the development of the improved predictive model.

A series of curve fits were used to compare sine waves against the yarn waveforms of architectural fabrics. Images of fabric cross sections for three fabrics (Table 4.1) with differing crimp characteristics and production methods have been obtained using a macro lens with a digital SLR camera (using the methodology described in §5.2.2). Images in each of the warp and fill directions were obtained for each fabric which were then processed in MATLAB using a custom processing tool (Figure 4.2). Multiple images were captured to ensure that the fits obtained were repeatable. A series of 13 points (*x, y* coordinates) were determined along the yarn's centreline to define a single yarn wavelength by first selecting the start and the end of the yarn waveform. The processing tool would then add 11 divisions which enabled the subsequent selection of points along the top and bottom of a yarn's profile from which the yarn centreline was determined. MATLAB's built-in curve fitting toolbox was then used to fit one and two term sine waveforms to the selected points allowing for the calculation of measures of goodness of fit (Table 4.2 and Table 4.3). These measures allow for a quantitative assessment of the representation of the yarns.

Table 4.1 Architectural fabrics used for fitting sine waves

Fabric	Manufacturer	Material		Weight (g/m^2)	Thickness (mm)
		Base cloth	Coating		
702†	Serge Ferrari, France	PES	PVC	750	0.56
B18059	Verseidag, Germany	Glass fibre	PTFE	1550	1.00
ATEX5000	PD Interglas, UK	Glass fibre	Silicone	685	0.90

† Précontraint®
PES = Polyester, PVC = Polyvinylchloride, PTFE = Polytetrafluoroethylene

The measures of goodness of fit show good correlation between the selected points and the approximating sinusoidal curves when using only a single sine term. Normalised root mean square error (NRMSE) values (root mean square error (RMSE) values normalised over the yarn amplitudes) are less than 5% for every curve measured. The highest average and single values are only 3.6% and 4.6%, respectively. These numbers amount to very small differences between the fitted sine curves and the collected data points. All of the average R^2 values exceed 0.99, i.e. 99% of the variance is explained by the points which define the centrelines of the yarns.

The sum of squared error (SSE) values show small discrepancies between the data points and sine waveforms. These small differences are to be expected, as random variations, for example from yarns bedding into one another, would produce deviation from a mathematical description. It is also possible that yarns are disturbed when the samples are cut and/or discrepancies are introduced as the result of inaccuracies when selecting the data points.

Improvements in the measured values are observed when two sine terms are used to fit the data points. Average NRMSE values all fall below 3% and adjusted R^2 values show that improvement is made in accounting for the variance of the data points, when compared to the fit using a single sine term. However, in developing the model, the use of additional sine terms in formulating the predictive model must be considered against the need to determine an increased number of coefficients from measurements of the yarn cross section, which would also make the model more mathematically complex. Curve fits using only a single sine term are determined from only the amplitude and wavelength. This can be done quickly and easily from the images of the fabric cross sections. With the measures of goodness of fit reported using a single sine term, additional terms were not used in the initial formulation. Additional terms could be included subsequently to improve accuracy following the development of a working predictive model. Plotting the results (Figure 4.3 and Figure 4.4) demonstrates the strong similarity between the yarns and sinusoidal waveforms.

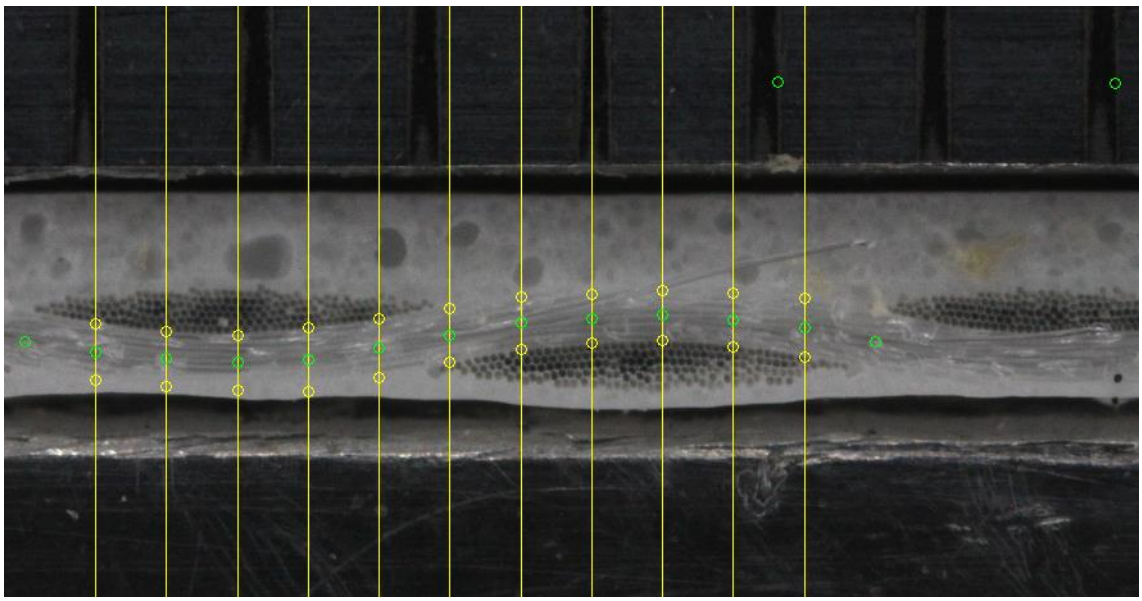

Figure 4.2 Ferrari 702 warp yarn cross section showing selection of the top and bottom yarn edges, and the subsequently determined centreline, points in the top right of the image allow calculation of the image scale

Table 4.2 Summary of measures of goodness of fit when using one sine term (mean values)

		SSE *(μm)*	R^2	Adj. R^2	RMSE *(μm)*	Range *(mm)*	NRMSE *(%)*
Ferrari 702 (PVC/PES)	Warp	0.05	0.997	0.997	2.32	0.117	2.0
	Fill	0.33	0.991	0.989	5.64	0.158	3.6
Verseidag B18059 (PTFE/Glass)	Warp	0.86	0.995	0.995	8.85	0.350	2.5
	Fill	1.59	0.994	0.993	12.49	0.408	3.1
Interglas ATEX5000 (Silicone/Glass)	Warp	0.70	0.997	0.996	9.07	0.408	2.2
	Fill	0.32	0.996	0.995	5.84	0.240	2.4

Table 4.3 Summary of measures of goodness of fit when using two sine terms (mean values)

		SSE *(μm)*	R^2	Adj. R^2	RMSE *(μm)*	Range *(mm)*	NRMSE *(%)*
Ferrari 702 (PVC/PES)	Warp	0.02	0.999	0.998	1.66	0.117	1.4
	Fill	0.14	0.996	0.993	4.42	0.158	2.8
Verseidag B18059 (PTFE/Glass)	Warp	0.33	0.998	0.997	6.59	0.350	1.9
	Fill	0.40	0.999	0.998	7.14	0.408	1.7
Interglas ATEX5000 (Silicone/Glass)	Warp	0.74	0.996	0.996	7.95	0.367	2.2
	Fill	0.21	0.998	0.996	5.42	0.240	2.3

Where yarns are not in contact with the orthogonal yarns, the yarn will be straight (Peirce, 1937; Kemp, 1958). Straight sections could be inserted into a sinusoidal profile, but this was deemed to be unnecessary owing to the goodness-of-fit achieved. This finding could result from small or non-existent lengths of the yarn where there is no contact between orthogonal yarns and/or the low curvature of the sine waveforms midway between the yarn intersections.

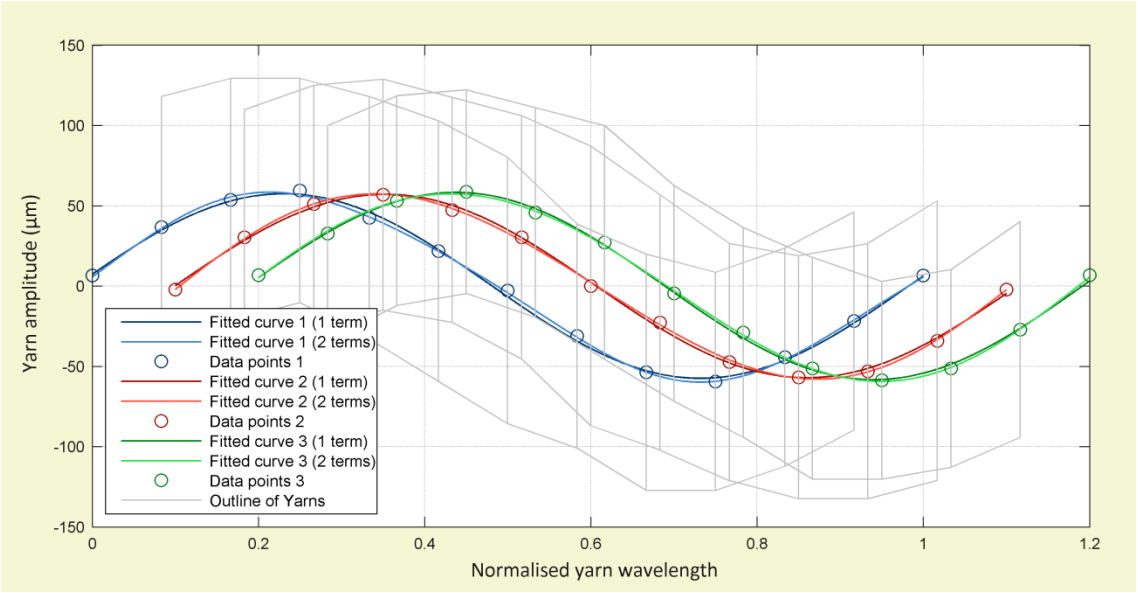

Figure 4.3 Sine fits for Ferrari 702 warp yarn (chosen as 702 warp samples exhibited best fit), curves are offset for clarity

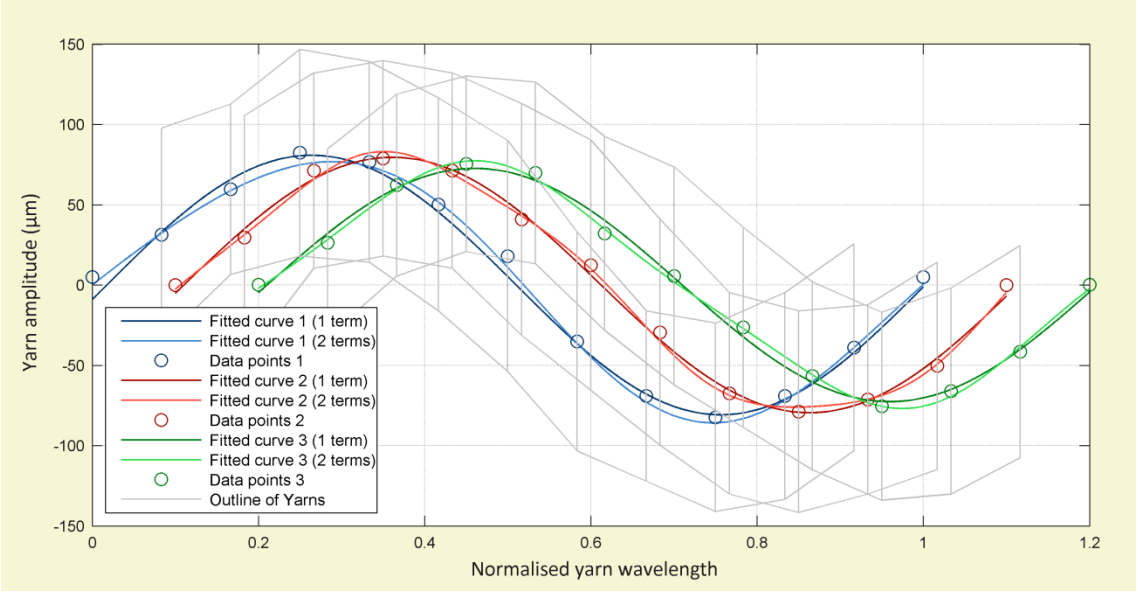

Figure 4.4 Sine fits for Ferrari 702 fill yarn (chosen as 702 fill samples exhibited worst fit), curves are offset for clarity

For a sine waveform to be implemented within a predictive unit cell model, the sinusoidal description must be capable of being incorporated within a system of equilibrium and compatibility equations. The work of Liu *et al.* (2004), which proposes an analytical model with elliptical yarn cross sections that calculates the normal force at the yarn intersections, forms the basis of a suitable approach. By defining a function to describe the surface of an elliptical yarn (Equation 4.11) and considering the equilibrium of an infinitesimal length yarn (Figure 4.5) subjected to force in the yarn, Liu *et al.* (2004) derived an expression for normal force acting over the yarn intersection (Equation 4.12 - Equation 4.14).

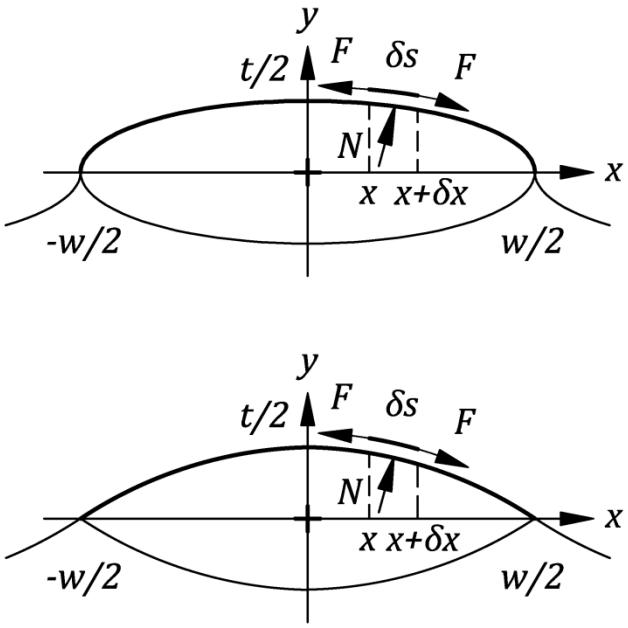

Figure 4.5 An infinitesimal length of warp yarn over a fill yarn or vice versa for an elliptical yarn, from Liu *et al.* (2004) (top), and a sinusoidal yarn (bottom)

If this approach could be implemented within a model using a sinusoidal description, it was posited that is may be possible to adapt the formulation to provide the out-of-place force required to model crimp interchange. The normal force acting over the yarn intersection for a sinusoidal yarn waveform was similarly calculated by defining a sine function to describe the yarn surface (Equation 4.15) and considering the equilibrium of an infinitesimal length yarn subjected to force in the yarn. The expression for the normal force can be shown to be unchanged by altering the yarn description (Equation 4.16 - Equation 4.23).

$$y(x) = t\sqrt{0.25 - \frac{x^2}{w^2}}$$

Equation 4.11 (Liu *et al.*, 2004)

$$N(x) = \frac{-F}{w}\frac{y''}{\sqrt{(1+y'(x)^2)^3}}$$

Equation 4.12 (Liu *et al.*, 2004)

where,

$$y'(x) = -\frac{tx}{\sqrt{0.25 - \frac{x^2}{w^2}}\,w^2}$$

Equation 4.13

$$y''(x) = -\frac{tx^2}{\left(0.25 - \frac{x^2}{w^2}\right)^{\frac{3}{2}}\,w^4} - \frac{t}{\sqrt{0.25 - \frac{x^2}{w^2}}\,w^2}$$

Equation 4.14

$$y(x) = \frac{t}{2} cos\left(\frac{\pi x}{w}\right)$$ **Equation 4.15**

$$y'(x) = -\frac{t\pi}{2w} sin\left(\frac{\pi x}{w}\right)$$ **Equation 4.16**

$$y''(x) = -\frac{t\pi^2}{2w^2} cos\left(\frac{\pi x}{w}\right)$$ **Equation 4.17**

The equilibrium equations of the infinitesimal yarn length are,

$$\sum F_x = F\frac{1}{\sqrt{1+y'(x+\delta x)^2}} - N(x)w\delta s\frac{y'(x)}{\sqrt{1+y'(x)^2}} - F\frac{1}{\sqrt{1+y'(x)^2}} = 0$$ **Equation 4.18 (Liu *et al.*, 2004)**

$$\sum F_y = F\frac{y'(x+\delta x)}{\sqrt{1+y'(x+\delta x)^2}} + N(x)w\delta s\frac{1}{\sqrt{1+y'(x)^2}} - F\frac{y'(x)}{\sqrt{1+y'(x)^2}} = 0$$ **Equation 4.19 (Liu *et al.*, 2004)**

where,

$$ds = \sqrt{1+y'(x)^2}\, dx$$ **Equation 4.20 (Liu *et al.*, 2004)**

Substituting the expression for *ds* (Equation 4.20) into either of the equilibrium equations (Equation 4.18 or Equation 4.19) and solving for *N* gives,

$$N(x) = \frac{F}{y'(x)w}\frac{\left(1/\sqrt{1+y'(x+\delta x)^2}\right) - \left(1/\sqrt{1+y'(x)^2}\right)}{\delta x}$$
$$= \frac{F}{y'(x)w} g'(x)$$ **Equation 4.21 (Liu *et al.*, 2004)**

where,

$$g(x) = \frac{1}{\sqrt{1+y'(x)^2}}$$ **Equation 4.22 (Liu *et al.*, 2004)**

Substituting the first order differential of the sinusoidal yarn description, *y* (Equation 4.16), into the expression for *g* (Equation 4.22) and differentiating allows the subsequent substitution into the expression for *N* (Equation 4.21) which can then be simplified (Equation 4.23). Removing the expressions for the first and second order differentials of *y* (Equation 4.16 and Equation 4.17) results in the original expression for the normal force, *N*, as required (Equation 4.12). By substituting arbitrary values into the expression for the normal force, the shape of the force distributions were compared (Figure 4.6) (10N yarn force, *F*, was applied to yarn cross sections with a thickness, *t*, of 2mm and a width, *w*, of 7mm).

$$N(x) = \frac{F}{-\frac{t\pi}{2w}\sin\left(\frac{\pi x}{w}\right)w} \cdot - \frac{2t^2\pi^3 \sin\left(\frac{\pi x}{w}\right)\cos\left(\frac{\pi x}{w}\right)}{w^3\left(4 + \frac{t^2\pi^2\sin^2\left(\frac{\pi x}{w}\right)}{w^2}\right)^{\frac{3}{2}}}$$

$$= \frac{4F\ t\ \pi^2 \cos\left(\frac{\pi x}{w}\right)}{w^3\left(4 + \frac{t^2\pi^2\sin^2\left(\frac{\pi x}{w}\right)}{w^2}\right)^{\frac{3}{2}}}$$

$$= \frac{F\ t\ \pi^2 \cos\left(\frac{\pi x}{w}\right)}{2w^3\left(1 + \frac{t^2\pi^2\sin^2\left(\frac{\pi x}{w}\right)}{4w^2}\right)^{\frac{3}{2}}}$$

$$= \frac{F}{w} \cdot \frac{t\ \pi^2 \cos\left(\frac{\pi x}{w}\right)}{2w^2\sqrt{\left(1 + \left(\pm\frac{t\pi}{2w}\sin\left(\frac{\pi x}{w}\right)\right)^2\right)^3}}$$

Equation 4.23

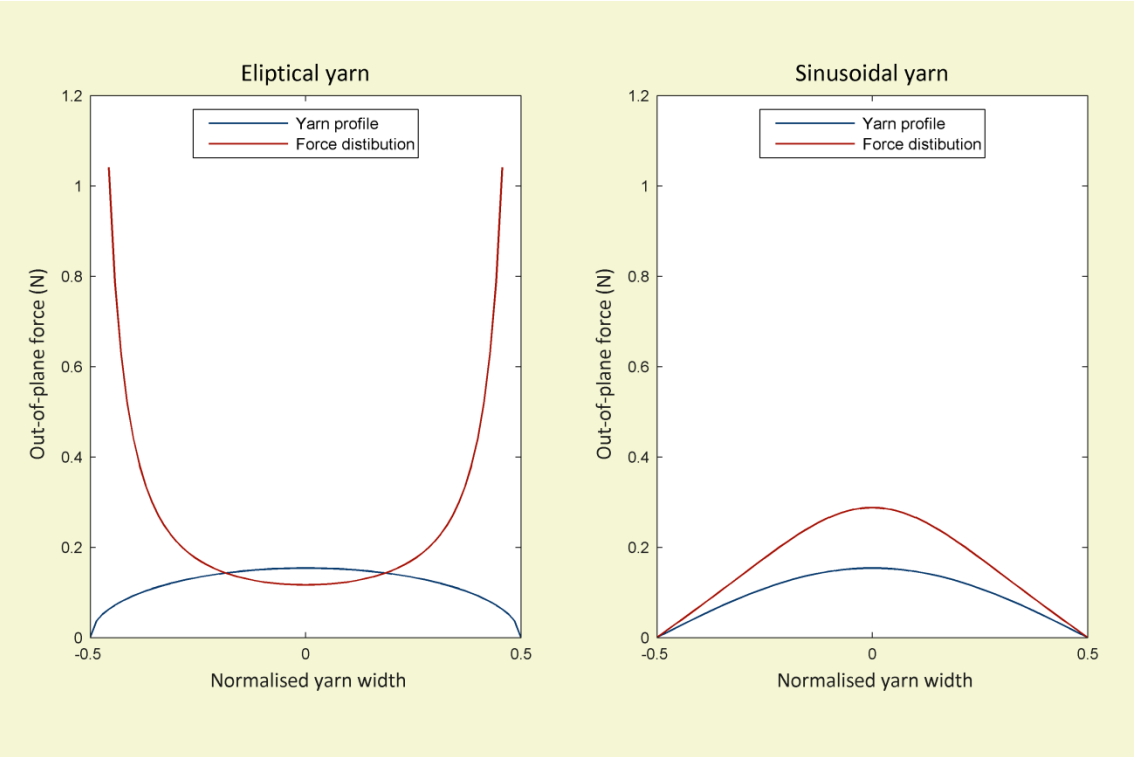

Figure 4.6 Distribution of the normal force over the yarn cross section for (left) an elliptical yarn and (right) a sinusoidal yarn, using the same yarn width, yarn thickness force in the yarn

As the gradient of the curve defining the elliptical cross section approaches infinity, so does the value of the normal force. The maximum normal forces are at the edges of the yarn cross section with the minimum values over the yarn centreline. This distribution is counterintuitive, as the distribution represents a situation where a stiff, bar-type intersecting yarn is being bent over the surface of the yarn cross section. In contrast, the sinusoidal representation of the yarn cross section results in a far more intuitive distribution of the forces. The maximum normal force is over the yarn centreline and tends toward zero at the yarn edges, which is to be expected where the interwoven yarn is being pulled parallel to horizontal axis of the yarn cross section.

A unit cell model was proposed in which the shape of the yarn cross section was consistent with the shape of the interwoven yarn (Figure 4.7). The yarn waveform and contact surface with the cross section of the intersecting yarn are defined by a single sinusoidal curve. The analytical predictive model describes this unit cell as two orthogonal cross sections, considering the yarn properties, geometries and applied forces independently for each of the yarn directions. A second sinusoidal curve was used to describe the surface of the yarn cross section which is not in contact with the intersecting yarn. Both of the sinusoidal waveforms can be defined in terms of the crimp amplitudes, unit cell lengths (half yarn wavelengths), yarn widths and thicknesses of real fabrics (Figure 4.8 and Equation 4.24 to Equation 4.27). Unlike the sinusoidal model proposed by Wang (2002) the normal force is calculated over the orthogonal yarn cross section. Yarn properties are held constant along the length of the yarns, as varying the properties would introduce a level of complexity too great and is beyond the scope of this research project. However, further work could incorporate the capability to vary the yarn properties if required.

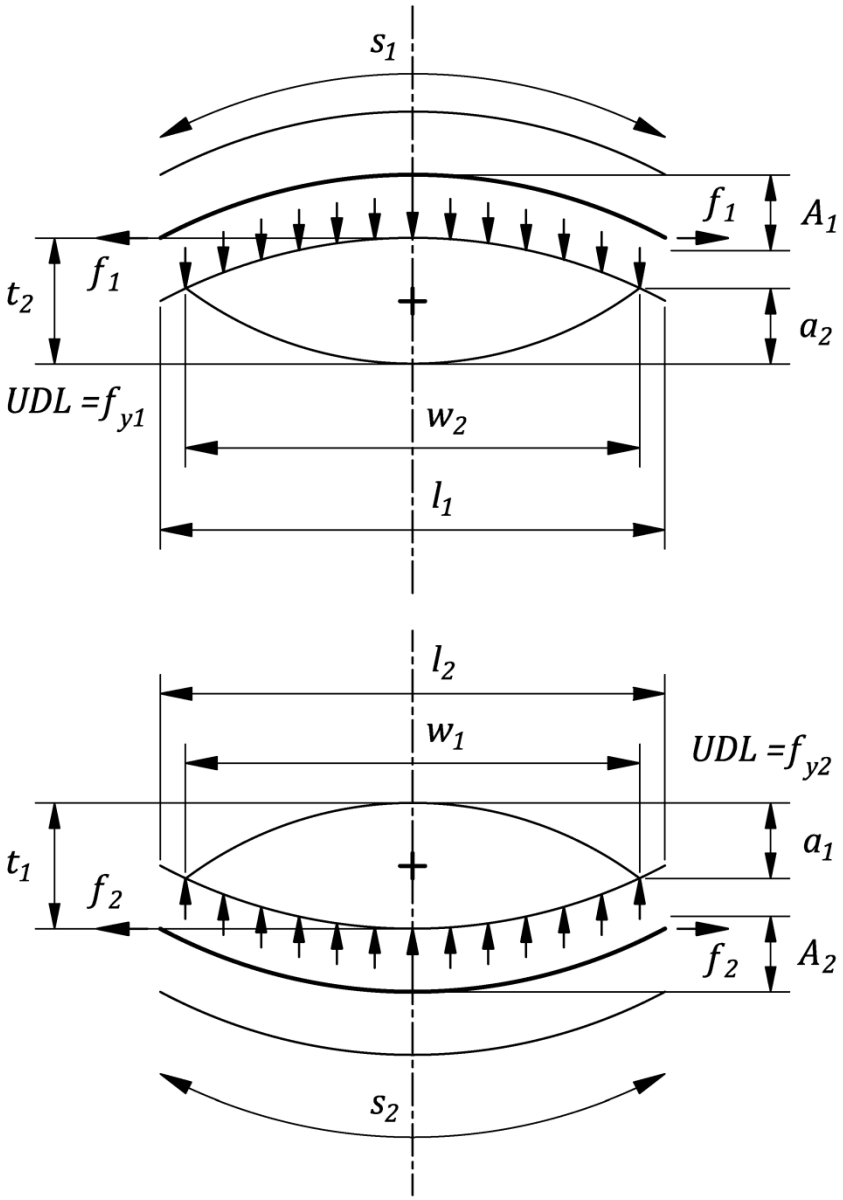

Figure 4.7 Sinusoidal representation of the fabric unit cell model, cross sections are orthogonal to each other about their centrelines

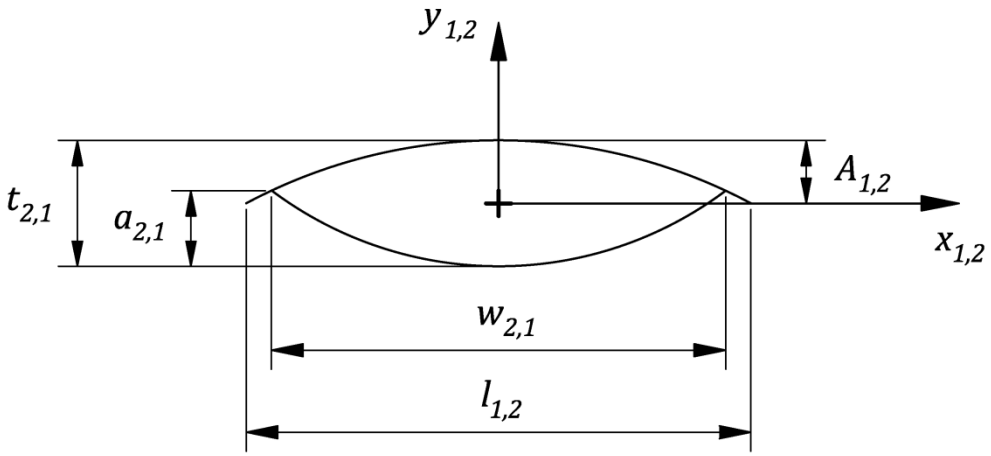

Figure 4.8 Simplified view of the unit cell geometry showing the dimensions required to define sinusoidal waveforms

The first curve, which defines the shape of waveform over the length of the unit cell, was derived as a function of the unit cell length, $l_{1,2}$, and is expressed in terms of values which can be obtained from real fabrics (Equation 4.24), namely unit cell length, yarn widths and yarn amplitudes. The second curve, which defines the surface of the orthogonal yarn not in contact with the undulating yarn, was then derived as a function of the width of the orthogonal yarn cross section (Equation 4.25). The second term in Equation 4.25 translates the curve in the y direction such that the ends of second curve are coterminous with the first curve where $x_{1,2} = \pm w_{2,1}/2$.

$$y_{1,2} = A_{1,2}cos\left(\frac{\pi x_{1,2}}{l_{1,2}}\right) \text{ for } \left(-\frac{l_{1,2}}{2} < x_{1,2} < \frac{l_{1,2}}{2}\right) \quad \textbf{Equation 4.24}$$

$$y_{1,2} = -a_{2,1}cos\left(\frac{\pi x_{1,2}}{w_{2,1}}\right) + A_{1,2}cos\left(\frac{\pi w_{2,1}}{2l_{1,2}}\right) \text{ for } \left(-\frac{w_{2,1}}{2} < x_{1,2} < \frac{w_{2,1}}{2}\right) \quad \textbf{Equation 4.25}$$

The amplitude $a_{1,2}$ can be expressed in terms of yarn thickness $t_{2,1}$ (Equation 4.26) and can be substituted into the expression of the second curve to provide an expression which is also in terms of values which can be obtained from real fabrics (Equation 4.27).

$$a_{2,1} = t_{2,1} - A_{1,2}\left(1 - cos\left(\frac{\pi w_{2,1}}{2l_{1,2}}\right)\right) \quad \textbf{Equation 4.26}$$

$$y_{1,2} = -\left(t_{2,1} - A_{1,2}\left(1 - cos\left(\frac{\pi w_{2,1}}{2l_{1,2}}\right)\right)\right)cos\left(\frac{\pi x_{1,2}}{w_{2,1}}\right) + A_{1,2}cos\left(\frac{\pi w_{2,1}}{2l_{1,2}}\right) \text{ for } \left(-\frac{w_{2,1}}{2} < x_{1,2} < \frac{w_{2,1}}{2}\right) \quad \textbf{Equation 4.27}$$

4.3.2 Crimp interchange

The application of in-plane biaxial load to a fabric will result in crimp interchange. Changes to the measurements taken from real fabrics that define the yarn geometry will occur as force equilibrium within the weave is maintained. This complex interaction between the orthogonal sets of yarns is responsible for a fabric behaving as a mechanism, rather than as a continuum, and is the fundamental deformation mechanism that is considered by the predictive model. The changing yarn lengths, yarn widths, and crimp amplitudes are constrained within the model by two fundamental geometrical relationships. Firstly, assuming negligible yarn bending stiffnesses (Peirce, 1937), the sum of out-of-plane forces (a product of the yarn geometry and applied load) must equal zero (Equation 4.28). Secondly, in order that the yarns remain in contact and that applied loads act in a single plane, the sum of the amplitudes must equal the sum of half of each yarn thickness (Equation 4.29).

$$fy_1 = fy_2$$ **Equation 4.28**

$$A_1 + A_2 = \frac{t_1 + t_2}{2}$$ **Equation 4.29 (adapted after (Peirce, 1937))**

The crimp amplitudes and thicknesses are determined directly from measurements of a fabric's cross section. As in the calculation of normal forces presented by Liu *et al.* (2004), out-of-plane forces may be calculated by considering equilibrium of an infinitesimal length of yarn cross section (Figure 4.9). However, the required expression was obtained by resolving the previously revised calculation of the normal force (Section 4.3.1) and subsequently integrating over the width of the yarn cross sections (Equation 4.30).

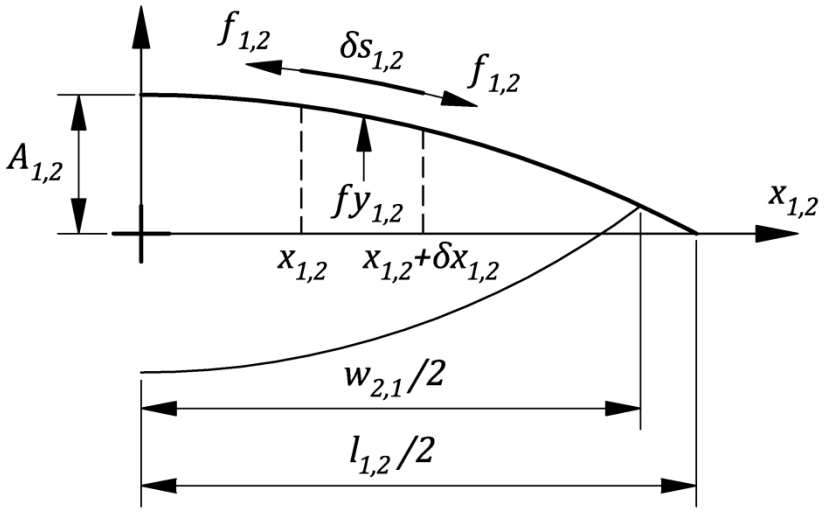

Figure 4.9 Out-of-plane forces acting on an infinitesimal length of warp/fill yarn over a fill/warp yarn cross section

$$fy_{1,2} = \int_{-\frac{s_{1,2}}{2}}^{\frac{s_{1,2}}{2}} N_{1,2} \frac{1}{\sqrt{1 + {y'_{1,2}}^2}} w_{1,2}\, ds$$

$$= \int_{-\frac{w_{2,1}}{2}}^{\frac{w_{2,1}}{2}} \frac{-f_{1,2} y''_{1,2}}{w_{1,2}\sqrt{\left(1 + {y'_{1,2}}^2\right)^3}} \frac{1}{\sqrt{1 + {y'_{1,2}}^2}} w_{1,2} \sqrt{1 + {y'_{1,2}}^2}\, dx$$

$$= -f_{1,2} \int_{y'_{1,2}\left(-\frac{w_{2,1}}{2}\right)}^{y'_{1,2}\left(\frac{w_{2,1}}{2}\right)} \frac{d\left(y'_{1,2}\right)}{\sqrt{\left(1 + {y'_{1,2}}^2\right)^3}}$$

$$= -f_{1,2} \left[\frac{\left(1 + {y'_{1,2}}^2\right) y'_{1,2}}{\sqrt{\left(1 + {y'_{1,2}}^2\right)^3}} \right]_{y'_{1,2}\left(-\frac{w_{2,1}}{2}\right)}^{y'_{1,2}\left(\frac{w_{2,1}}{2}\right)}$$

$$= -f_{1,2} \left[\frac{y'_{1,2}}{\sqrt{1 + {y'_{1,2}}^2}} \right]_{y'_{1,2}\left(-\frac{w_{2,1}}{2}\right)}^{y'_{1,2}\left(\frac{w_{2,1}}{2}\right)}$$

$$= -f_{1,2} \left[-\frac{A_{1,2}\pi\, sin\left(\frac{\pi w_{2,1}}{2l_{1,2}}\right)}{l_{1,2}\sqrt{1 + \left(\frac{A_{1,2}\pi}{l_{1,2}}\, sin\left(\frac{\pi w_{2,1}}{2l_{1,2}}\right)\right)^2}} + \frac{A_{1,2}\pi\, sin\left(-\frac{\pi w_{2,1}}{2l_{1,2}}\right)}{l_{1,2}\sqrt{1 + \left(\frac{A_{1,2}\pi}{l_{1,2}}\, sin\left(-\frac{\pi w_{2,1}}{2l_{1,2}}\right)\right)^2}} \right]$$

$$= f_{1,2} \left[\frac{2A_{1,2}\pi\, sin\left(\frac{\pi w_{2,1}}{2l_{1,2}}\right)}{l_{1,2}\sqrt{\left(1 + \left(\frac{A_{1,2}\pi}{l_{1,2}}\, sin\left(\frac{\pi w_{2,1}}{2l_{1,2}}\right)^2\right)\right)}} \right] \quad \textbf{Equation 4.30}$$

where,

$$y_{1,2} = A_{1,2} cos\left(\frac{\pi x_{1,2}}{l_{1,2}}\right) \text{ for } \left(-\frac{w_{2,1}}{2} < x_{1,2} < \frac{w_{2,1}}{2}\right) \quad \textbf{Equation 4.31}$$

$$y'_{1,2} = -\frac{A_{1,2}\pi}{l_{1,2}} sin\left(\frac{\pi x_{1,2}}{l_{1,2}}\right) \quad \textbf{Equation 4.32}$$

$$y''_{1,2} = -\frac{{A_{1,2}}^2 \pi}{{l_{1,2}}^2} cos\left(\frac{\pi x_{1,2}}{l_{1,2}}\right) \quad \textbf{Equation 4.33}$$

It is also necessary to establish a relationship between the length of the unit cell, the yarn lengths and the crimp amplitudes, as these parameters are interdependent. Therefore, an expression to calculate the length of the intersecting yarns within the unit cell from the measured values of crimp amplitude and cell length was required. An elliptical integral (Equation 4.34) by Stroud (1996) may be used to define the length of a sinusoidal curve. However, the solution of an elliptical integral is not straightforward. Instead, a Taylor series expansion by Stroud (2011) was used which allows for an approximation for the sinusoidal length to be more easily calculated (Equation 4.35) (McBride and Chen, 1997). Before considering yarn extension, yarn lengths can be determined and held constant whilst the unit cell lengths and crimp amplitudes are varied to satisfy the fundamental geometric relationships (Equation 4.28 and Equation 4.29) when load is applied to the model. Rearranging the approximating expression (Equation 4.36) permits the calculation of the unit cell lengths from the yarn lengths and crimp amplitudes (Equation 4.27) by means of the quadratic equation. This approach makes possible the later inclusion of an update for the yarn lengths, thus enabling the incorporation of yarn extension into the model (§4.2.3).

$$s_{1,2} = \int_{-\frac{l_{1,2}}{2}}^{\frac{l_{1,2}}{2}} \sqrt{1 + \left(y'_{1,2}\right)^2}\, dx \qquad \textbf{Equation 4.34}$$

$$\approx \int_{-\frac{l_{1,2}}{2}}^{\frac{l_{1,2}}{2}} 1 + \frac{1}{2}\left(y'_{1,2}\right)^2 dx$$

$$\approx \int_{-\frac{l_{1,2}}{2}}^{\frac{l_{1,2}}{2}} 1 + \frac{1}{2}\left(-\frac{A_{1,2}\pi}{l_{1,2}} sin\left(\frac{\pi x_{1,2}}{l_{1,2}}\right)\right)^2 dx$$

$$\approx l_{1,2} + \frac{{A_{1,2}}^2\pi^2}{4l_{1,2}} \qquad \textbf{Equation 4.35}$$

$$0 \approx 4{l_{1,2}}^2 - 4s_{1,2}l_{1,2} + {A_{1,2}}^2\pi^2 \qquad \textbf{Equation 4.36}$$

$$l_{1,2} \approx \frac{s_{1,2} + \sqrt{{s_{1,2}}^2 - {A_{1,2}}^2\pi^2}}{2} \qquad \textbf{Equation 4.37}$$

As load is applied to the model, the shape of the yarn cross sections will remain consistent with the shape of the orthogonal interwoven yarns (Section 4.3.1). Therefore, changes in the yarn cross sections occur simultaneously with changes in the crimp and elongation of the unit cell in the orthogonal yarn directions. The model requires constraints to govern the interdependent changes in geometry. While it is possible to constrain the deformation of the cross sectional areas, the yarn widths and the yarn thicknesses, the imposed constraints needed to be compatible with one another or the model will be over constrained.

In addition to crimp interchange, Poisson's ratios and crushing stiffnesses of the yarns will influence changes in the yarn cross section (§2.1). However, fibre bundle models may be needed to predict changes resulting from such effects (Cai and Gutowski, 1992). This extra modelling would require experimental data from as spun yarns, tested prior to weaving and coating, and would need to be subsequently modified to account for the weaving and coating processes. It is possible that yarns could be removed from the coating for testing, although removing yarns from a fabric for testing would be problematic and it would be likely to cause damage to the yarns (§2.3.2). A need to determine Poisson's ratio values and yarn crushing stiffnesses through experimental testing would not be compatible with the requirements of the predictive model (Section 4.1.1). Furthermore, any testing of individual yarns removed from the weave and coating may not be representative of the yarns in situ (§2.3.2). Consequently, an attempt to accurately attribute a proportion of the changes in the yarn cross sections to yarn crushing would be prohibitively complex. Therefore, for the modelled to be developed, compressive deformation and Poisson's effects of the yarns have been not be considered, although the model could be extended later to include these effects.

The adopted approach assumes that changes in yarn cross section (i.e. area and waveform) arise from rearrangement of the fibres comprising the yarns only. This was modelled by allowing the yarn to vary in cross sectional shape while maintaining constant area (Glaessgen *et al.*, 1996; Bridgens, 2005). The approach also maintains the proportion of the yarn width with respect to the cell length (Equation 4.38). The combination of these two constraints causes the yarn to crush with increasing load in the perpendicular yarn direction (Figure 4.10). By having consistent yarn geometry, the elongation of yarns and changing crimp amplitudes are implicitly linked with transverse yarn widths and thicknesses which negates a requirement to determine a crushing stiffness value.

$$\frac{w_1}{l_2} = \frac{w_2}{l_1}$$ **Equation 4.38**

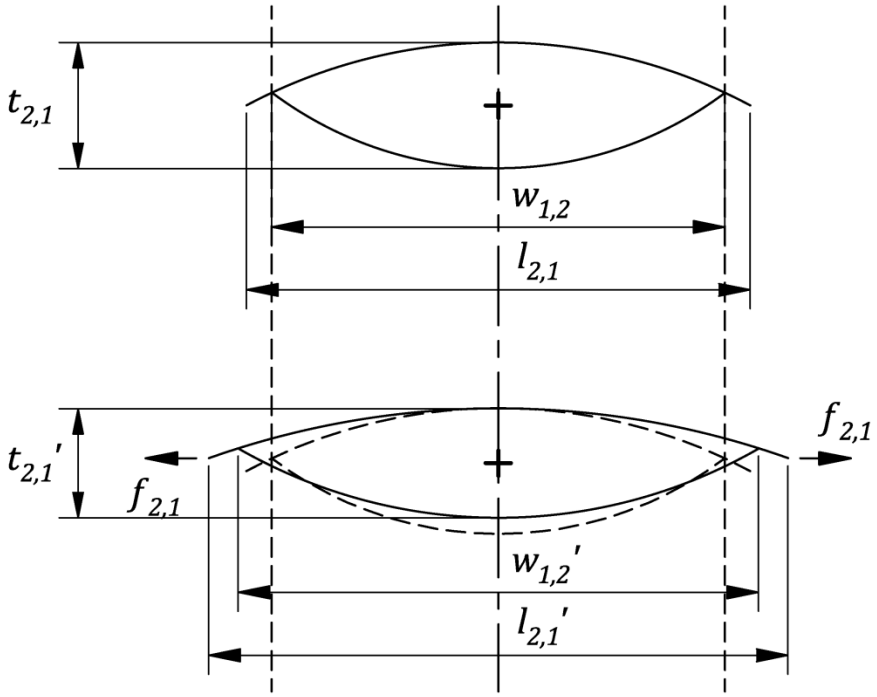

Figure 4.10 Deformation of the yarn cross section due to applied load, showing the undeformed cross section (top), and deformation of the cross section with constant area (bottom)

To define the yarn cross sectional areas, integrals of the bounding sinusoidal curves can be calculated and added together. However, any part of the integrals that overlap (Figure 4.11) must be subtracted from the result. The final expression is in terms of parameters which can be obtained from real fabrics (Equation 4.39) by substituting in the expression for $a_{1,2}$ (Equation 4.16).

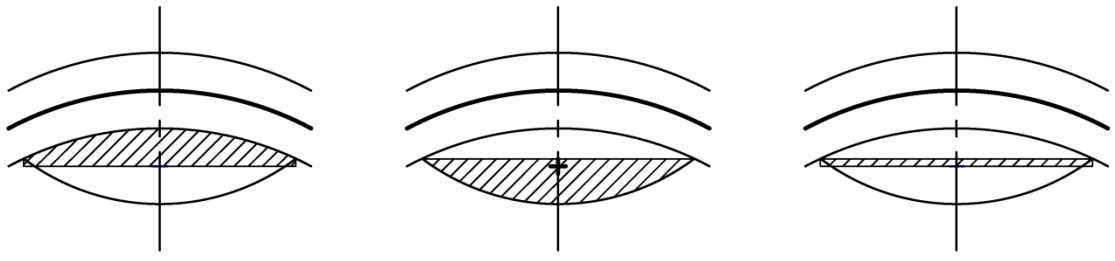

$$\int_{-\frac{w_{1,2}}{2}}^{\frac{w_{1,2}}{2}} A_{2,1} cos\left(\frac{\pi x_{2,1}}{l_{2,1}}\right) dx_{2,1} \qquad \int_{-\frac{w_{1,2}}{2}}^{\frac{w_{1,2}}{2}} a_{1,2} cos\left(\frac{\pi x_{2,1}}{w_{1,2}}\right) dx_{2,1} \qquad A_{2,1} w_{1,2} cos\left(\frac{\pi w_{1,2}}{2 l_{2,1}}\right)$$

Figure 4.11 Expressions for calculating the yarn cross sectional area with corresponding illustrations of the areas derived by each

$$AREA_{1,2} = \int_{-\frac{w_{1,2}}{2}}^{\frac{w_{1,2}}{2}} a_{1,2} cos\left(\frac{\pi x_{2,1}}{w_{1,2}}\right) dx_{2,1} + \int_{-\frac{w_{1,2}}{2}}^{\frac{w_{1,2}}{2}} A_{2,1} cos\left(\frac{\pi x_{2,1}}{l_{2,1}}\right) dx_{2,1}$$

$$- A_{2,1} w_{1,2} cos\left(\frac{\pi w_{1,2}}{2l_{2,1}}\right)$$

$$= \frac{2a_{1,2} w_{1,2} sin\left(\frac{\pi w_{1,2}}{2l_{2,1}}\right)}{\pi} + \frac{2A_{2,1} l_{2,1} sin\left(\frac{\pi w_{1,2}}{2l_{2,1}}\right)}{\pi} - A_{2,1} w_{1,2} cos\left(\frac{\pi w_{1,2}}{2l_{2,1}}\right)$$

$$= \frac{2w_{1,2}\left(t_{1,2} - A_{2,1}\left(1 - cos\left(\frac{\pi w_{1,2}}{2l_{2,1}}\right)\right)\right) sin\left(\frac{\pi w_{1,2}}{2l_{2,1}}\right)}{\pi} + \frac{2A_{2,1} l_{2,1} sin\left(\frac{\pi w_{1,2}}{2l_{2,1}}\right)}{\pi}$$

$$- A_{2,1} w_{1,2} cos\left(\frac{\pi w_{1,2}}{2l_{2,1}}\right)$$

$$= \frac{-A_{2,1} w_{1,2} \pi cos\left(\frac{\pi w_{1,2}}{2l_{2,1}}\right)}{\pi} + \frac{2A_{2,1} w_{1,2} cos\left(\frac{\pi w_{1,2}}{2l_{2,1}}\right)}{\pi} + \frac{2A_{2,1} l_{2,1} sin\left(\frac{\pi w_{1,2}}{2l_{2,1}}\right)}{\pi}$$

$$- \frac{2w_{1,2}(A_{2,1} - t_{1,2})}{\pi}$$

$$= \frac{-A_{2,1} w_{1,2}(\pi - 2) cos\left(\frac{\pi w_{1,2}}{2l_{2,1}}\right) + 2A_{2,1} l_{2,1} sin\left(\frac{\pi w_{1,2}}{2l_{2,1}}\right) - 2w_{1,2}(A_{2,1} - t_{1,2})}{\pi}$$

Equation 4.39

4.3.3 Yarn behaviour

Yarns will strain axially when load is applied in the plane of a woven fabric. However, strain of the unit cell, and the fabric as a whole, will be the sum of the crimp interchange and the axial extension of the yarns. The significantly lower stiffnesses of the coatings compared to the yarns means that a coating will not limit the maximum biaxial strain of the fabric. Yarn extension was initially incorporated into the predictive model by assuming yarn behaviour to be linearly elastic (Equation 4.40). This relationship calculates yarn length, $s_{1,2}$, as the original yarn, $s_{0\,1,2}$, length plus the strain in the yarn as a function of a constant value of the yarn's elasticity, $E_{1,2}$. Therefore, the predicted yarn strain was initial a linear function. However, an objective of this project was to improve the model proposed by Bridgens (2005) which assumed linear or multi-linear elasticity of the yarns.

$$s_{1,2} = s_{0\,1,2}\left[1 + \frac{fy_{1,2}}{l_{2,1}\,E_{1,2}}\right] \qquad \textbf{Equation 4.40}$$

Owing to the non-linear behaviour exhibited by architectural fabrics (§2.1), it was proposed that uniaxial test results could be used to create a 'look-up function' that would determine yarn strain from applied stress, i.e. a non-linear expression relating yarn stress and yarn strain from empirical data. Bi-linear and multi-linear approaches were briefly considered, but were dismissed in favour of a novel look-up approach that could incorporate the complex non-linear, elastic load response and hysteresis. A look-up function also held the benefit that it could remove judgment on the part of the model's user, i.e. there would be no need for a user to define linear approximations of stiffness.

The model must be capable of predicting stress-strain behaviour for any maximum stress value up to the values used in biaxial testing. Furthermore, multiple values of maximum stress may be required to match biaxial test profiles which comprise multiple cycles to different values of maximum stress. In order to achieve this using a look-up of uniaxial test data, the uniaxial data must match the load path of the biaxial test data/profile. This would require a complex and possibly long uniaxial test profile or, alternatively, a series of uniaxial tests to different maximum stresses. To avoid these complex requirements, it was proposed to scale a single uniaxial profile to match its maximum loads to the maximum loads of the biaxial cycles. The model would be able to scale the test results to match the desired stress profile, i.e. loading curve to be predicted, as the maximum stresses for any loading curve change.

This approach of scaling uniaxial cycles is demonstrated by comparing experimentally obtained data obtained from a uniaxial test profile with stress-strain cycles of increasing maximum stress (Figure 4.12) against a series of cycles which have scaled from a uniaxial test having set of stress-strain cycles at a single maximum stress. A warp specimen of Ferrari 702 (PVC/PES) was used for the tests. The stress-strain response was recorded for three load cycles between a maximum 30kN/m stress (50% UTS) and zero displacement.

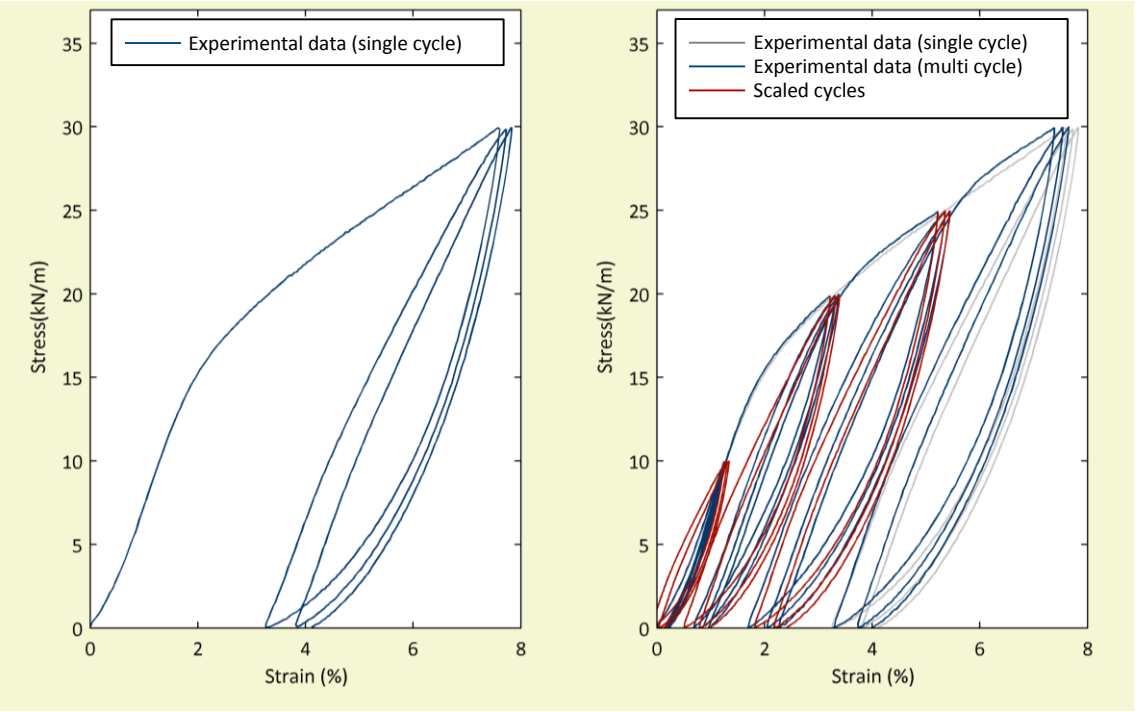

Figure 4.12 Comparison of experimental data and adjusted cycles, specimen used was Ferrari 702 (PVC/PES) cut in the warp direction

The scaling factor is the ratio between the maximum stress of the test data and the desired value of maximum stress, i.e. 25kN/m, 20kN/m and 10kN/m. The scaling is applied to both the stresses and strains. The adjusted cycles were then compared to experimental data from the profile with load cycles of increasing maximum stress (the "complex" test).

Comparing the test results to the scaled cycles shows that the 30kN/m stress-strain cycles appear largely unaffected by the preceding cycles at lower maximum stress values. The shape of the cycles is unaltered with subsequent cycles at increasing maximum stress values, thus the shape of the curves at lower stress values, including residual strain, is reflected by the scaled cycles. It is the shape of the curves that is important, as it is the gradient which determines the stiffness. The shapes of the cycles capture the nonlinearity, hysteresis and residual strain. This approach is more accurate than a linear approximation i.e. a secant modus.

By using the look-up approach, predictions of strain at a given biaxial stress ratio are no longer made independently of a materials' strain history. The model attempts to characterise the nonlinear stress-strain behaviour that occurs during the increasing deformation until a prescribed stress state is achieved in a fabric. In other words, the model predicts the entire stress-strain history of a biaxial load profile up to a given load. This is a novel approach which has not been suggested or incorporated in existing modelling approaches. The use of MATLAB allowed for this process to be implemented, the first stage of which is the identification of the loading cycles in the biaxial profiles being predicted (Figure 4.13).

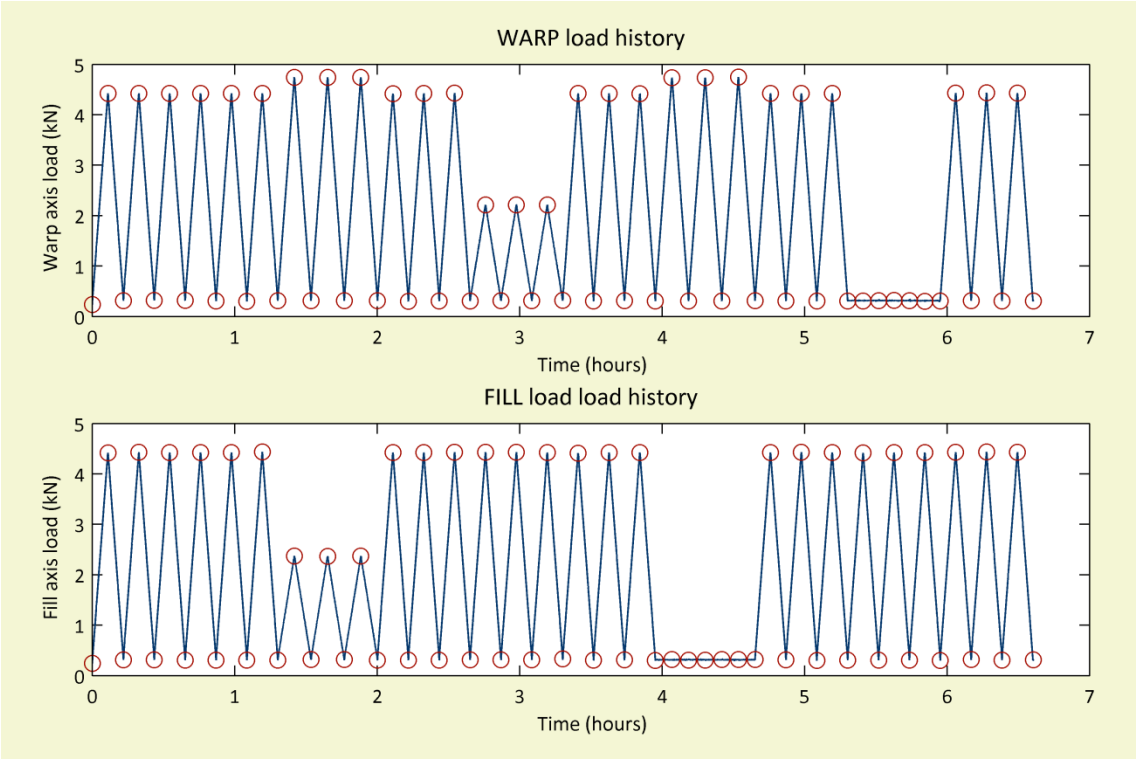

Figure 4.13 Automated biaxial load cycle identification, the MATLAB script generates an array of the locations of the turning points in the biaxial load profile, shown in red circles.

To enable scaling of the stress-strain curves, the model first requires the user to import a biaxial load (stress) profile so it can determine the range of stresses it will be required make stain predictions. The biaxial profile is either a user generated profile, i.e. a profile of interest, for which the model will predict the strains, or the recorded loads of a real biaxial test. The code then searches for minima and maxima in both the warp and fill load profiles by evaluating data points within a moving search window. This identifies minimum and maximum values of stress within a portion of the test data. Once the turning points have been found for each of the warp and fill profiles, the two lists of points (one for each yarn direction) are merged to remove coincident points in the two lists and to locate cycle start/end points in data where there is no turning point, i.e. when no load is applied in one yarn direction.

With the turning points in the biaxial load profile identified, the model now has a series of cycles for which strain predictions will be made. The first cycle includes the initial loading curve. There is no need to scale the initial uniaxial loading curve to determine the stress-strain relationship of the yarns for the loading portion of the first biaxial load cycle. This is because the initial uniaxial loading curve is representative of the behaviour of the yarns in a yet to be tested biaxial sample. Therefore, a curve is fitted to the initial uniaxial loading curve (Figure 4.14-A) and the non-linear equation of the fitted curve is used by the model to determine the yarn strains for the initial loading of the biaxial sample. The curve fit is performed using MATLAB's build in *curveFit* function.

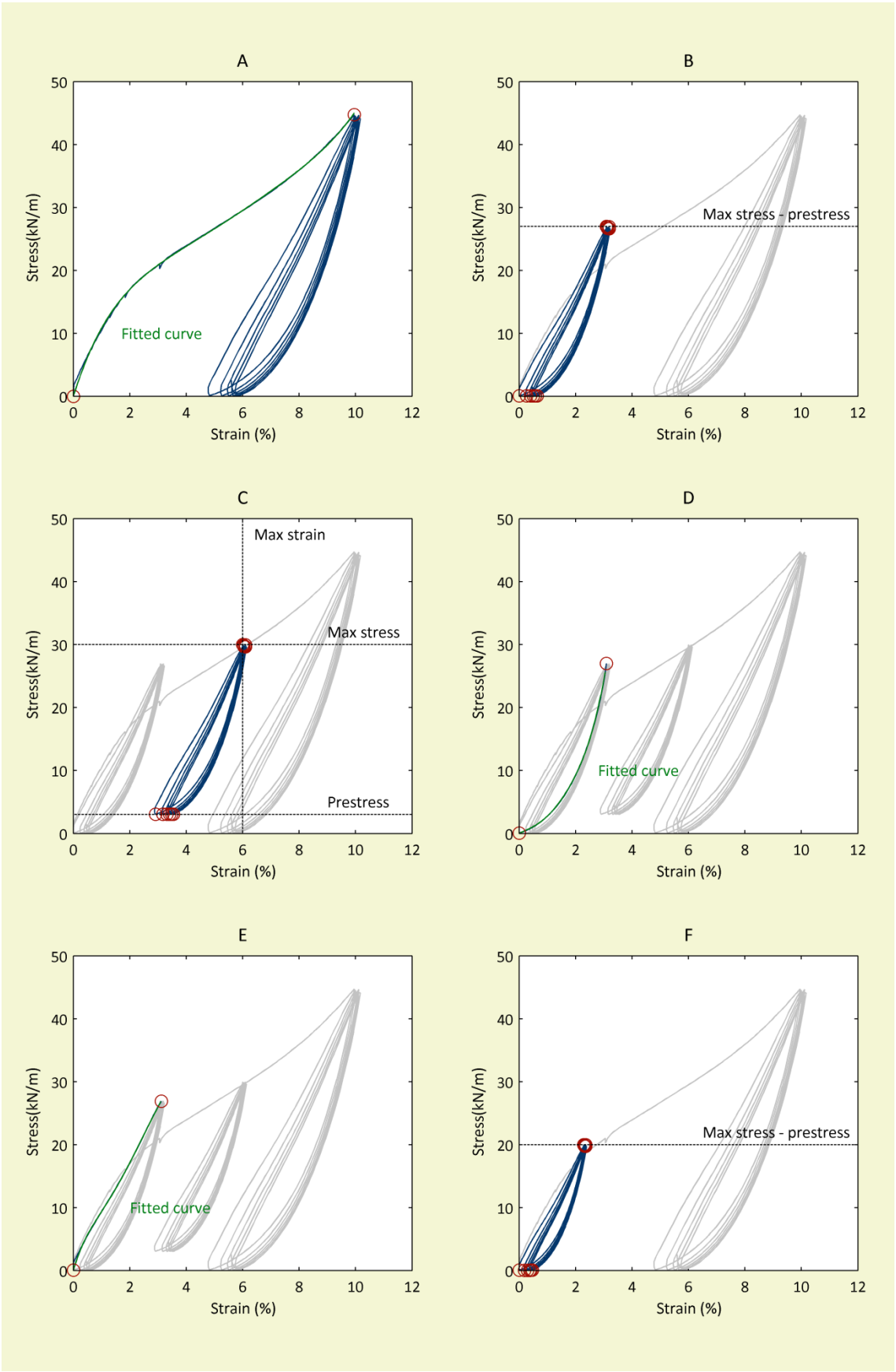

Figure 4.14 Stages of the uniaxial look-up depicting how the model adjusts uniaxial load cycles to predict yarn stress-strain behaviour

For the subsequent biaxial load cycles there is a maximum and minimum value of stress. These stress values correspond to the turning points identified in the biaxial load profile (the red circles shown in Figure 4.13). To use the uniaxial stress-strain data in determining yarn strain for any biaxial profile, the uniaxial data is scaled such that the maximum value of uniaxial stress is equal to difference between the maximum stress and the minimum desired biaxial stress for a given cycle, i.e. the difference between the maximum turning point and the minimum turning point (Figure 4.14-B). The scaled data is assumed to represent the stress-strain relationship exhibited by the yarns of the biaxial sample for after the initial loading curve.

Following the scaling of the uniaxial data, the maximum stress/strain value for the scaled uniaxial test data need matching to the maximum stress/strain value of the initial loading curve, otherwise there will be jumps in the predicted data between adjacent cycles. When the uniaxial data is scaled the maximum stress/strain value for the scaled uniaxial test data will <u>not</u> correspond to the maximum stress/strain value of the initial loading because the minimum stress/strain value is set to zero/zero to enable subsequent curve fitting. Therefore, the differences in stress/strain values are calculated and stored by the model as variables "$stressAdjustment_{1,2}$" and "$strainAdjustment_{1,2}$". These adjustment values have the effect of correctly "locating" the scaled uniaxial data in relation to the initial loading curve (Figure 4.14-C).

A further curve is then fitted to the unloading portion of the first cycle of the scaled uniaxial data (Figure 4.14-D). This curve fit determines a non-linear equation relating the stresses and strains for the first unloading curve. This equation can then be used to determine the yarn strains for the unloading portion of the first biaxial load cycle. Yarn strains are then used to update the yarn lengths in two of the model's equilibrium and compatibility equations (Equation 4.41 and Equation 4.42). *wfun* and *ffun* are the equations determined by the curve fitting for the warp and fill yarns, respectively.

$$s_1 = s_{0\,1}\left[1 + wfun\left(\frac{f_1}{l_2} - stressAdjustment_1\right) + strainAdjustment_1\right] \qquad \textbf{Equation 4.41}$$

$$s_2 = s_{0\,2}\left[1 + ffun\left(\frac{f_2}{l_1} - stressAdjustment_2\right) + strainAdjustment_2\right] \qquad \textbf{Equation 4.42}$$

The model then works though the loading and unloading portions of each cycle of the biaxial test profile, matching subsequent biaxial cycles to corresponding uniaxial cycles and fitting curves to each of the loading and unloading parts of the uniaxial data (Figure 4.14-E shows fitting of the next loading curve). Any residual strain between subsequent cycles is added to the $strainAdjustment_{1,2}$ variable. The model will continue to use the last cycle of the uniaxial test data when the number of biaxial cycles exceeds the number of uniaxial cycles.

However, if a given cycle has a different maximum stress value compared to the previous cycle, for example the first cycle in a set of 1:2 load ratio cycles following a set of 1:1 cycles, the maximum stress value of the uniaxial data will no longer be equal to the difference between the maximum

stress and the minimum stress for that given cycle as observed in the biaxial test profile (Figure 4.13). Therefore, the scaled uniaxial data will no longer be appropriate for determining the relationship between stresses and strains. Consequently, the stress differences between the maximum turning point and the minimum turning point must recalculated and uniaxial test data re-scaled (Figure 14.4-F) before the model can continue with it predictions.

Decrimping of the yarns has also been considered. Decrimping is the straightening of yarns (a reduction in crimp amplitude) resulting in positive strain of the fabric in the decrimped yarn direction. "Decrimping strain" occurs without tensile extension of the decrimped yarns. Simultaneously, orthogonal yarns will increase in crimp to accommodate the straightening yarns, thus causing the high levels of lateral contraction exhibited by woven fabrics. Decrimping will be present in the uniaxial data obtained to generate the look-up functions. Consequently, a value of decrimping strain should be removed from the uniaxial test data if it is to be used to determine yarn elongation in the predictive model because the model explicably includes decrimping.

It is extremely difficult to determine decrimping strains experimentally as decrimping will occur simultaneously with uniaxial extension. However, the predictive model may be used to calculate theoretical maximum values of decrimping strains, and respective negative strains due to crimp interchange, from changes in the yarn geometry. This is achieved by imposing the straightening of a yarn in one direction. This was performed for all fabrics used in validating the model (Table 4.4). These values of strain, if determined, could then be removed from the uniaxial test data in order to remove decrimping strain from the measured values of uniaxial extension of the test specimens. The proposed approach replies on the assumption that the yarns in uniaxial specimens achieve maximum decrimping, i.e. become totally straight, during a uniaxial test. However, the maximum possible values (total straightening) might not be achieved in practice, at least not for all fabrics.

Plotting the theoretical decrimping strains against uniaxial data (the data obtained in chapter 5) shows that the maximum value of theoretical decrimping strain is not always achieved by the fabric (Figure 4.15 to Figure 4.17). It is not possible to determine a value of decrimping strain to be removed from the test data or where in the initial cycle to remove it from. It was posited that decrimping strains may be limited by a maximum value of crimp that occurs in the orthogonal yarn direction. A limiting value might then be calculated and removed from the initial cycle.

Table 4.4 Theoretical decrimping and respective negative strains due to crimp interchange

		702	1202	B18089	B18059	ATEX3000	ATEX5000
Decrimped warp yarn	Warp strains (%):	0.7	0.7	3.4	5.1	2.4	5.1
	Fill strains (%):	-0.5	-0.3	-0.1	-0.4	-0.3	-0.2
Decrimped fill yarn	Warp strains (%):	-0.5	0.0	-0.7	-0.6	-0.6	-0.5
	Fill strains (%):	1.2	2.3	7.3	9.0	2.3	3.8

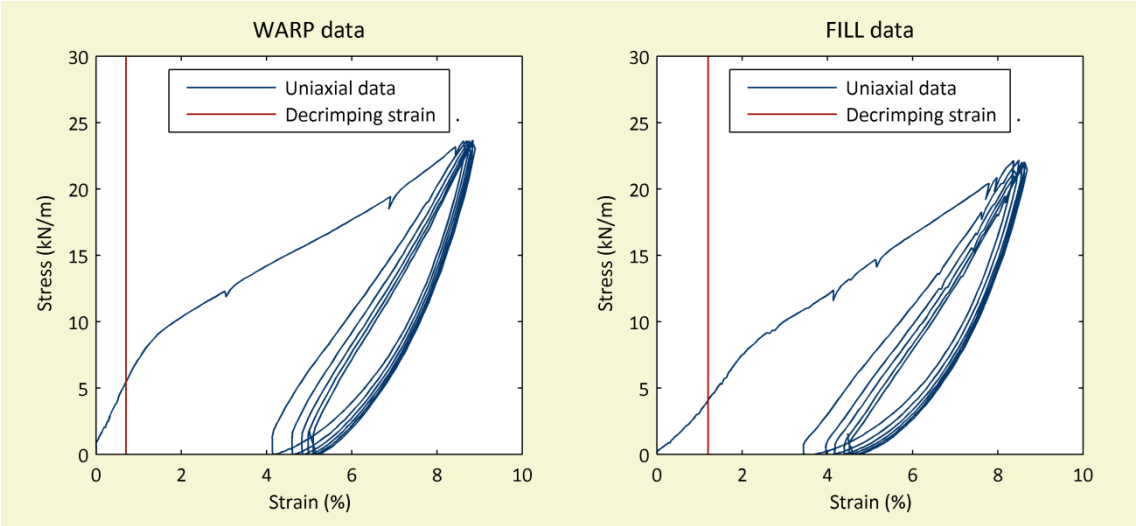

Figure 4.15 Uniaxial test data for F702 (PVC/PES) shown with maximum theoretical values of decrimping strain

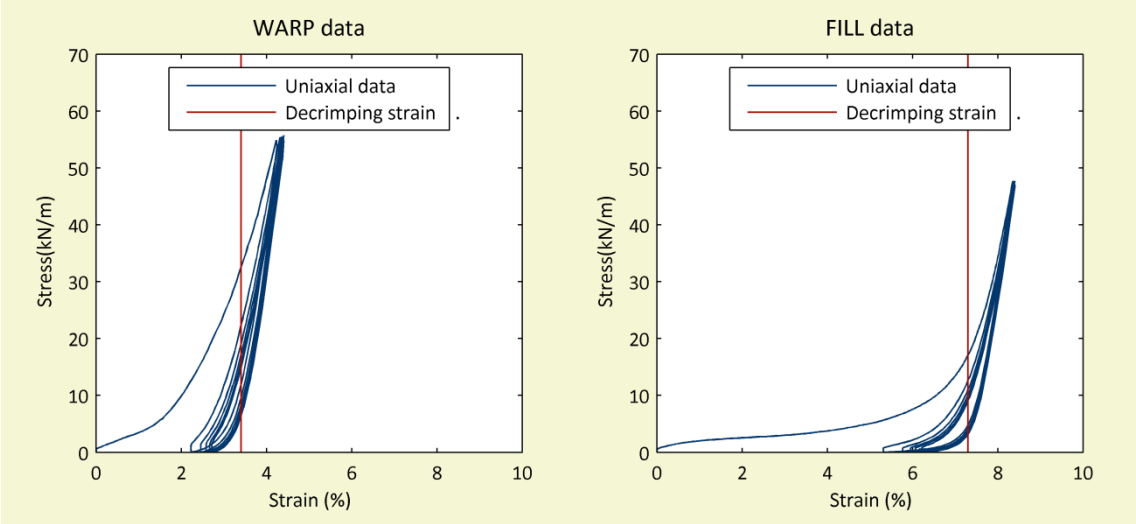

Figure 4.16 Uniaxial data for B18089 (PTFE/glass) shown with maximum theoretical values of decrimping strain

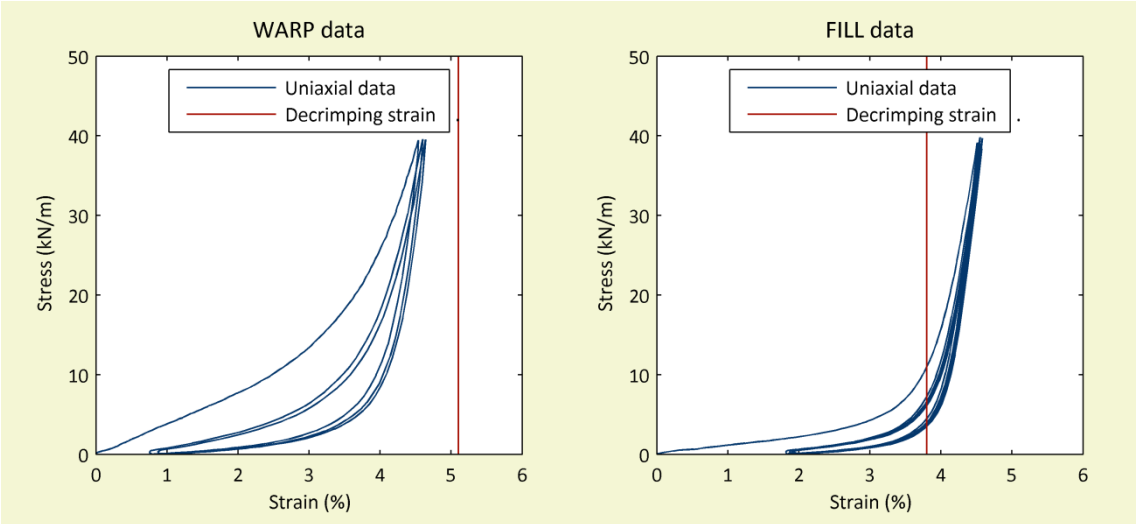

Figure 4.17 Uniaxial data for ATEX5000 (silicone/glass) shown with maximum theoretical values of decrimping strain

A series of uniaxial tests with digital image correlation were performed to explore the possible limit of maximum crimp, as measuring the transverse strain which arises due to crimp interchange is not straightforward by conventional means. The narrow width of the sample makes instrumenting the specimen difficult. However, DIC makes the tests possible, though such tests would not be a suitable requirement to provide input of the predictive model. A common factor, e.g. a limit of 70% maximum theoretical decrimp, that was consistent for all fabrics or a group of fabrics would need to be deduced from the range of fabrics tested.

If a relationship could be established, it was anticipated that negative strains due to crimp interchange would be smaller than those which were theoretically calculated by the model (Table 4.4). However, the results did not show this and were instead larger across all fabrics (Table 4.5). The results are inconclusive and it is not apparent how best to incorporate/remove a value of decrimping strain from the test data. A solution may be to remove the first cycle from the uniaxial data.

Table 4.5 Measured crimping strains, decrimp values are not possible to obtain from these test as values will include axial yarn strain

		702	1202	B18089	B18059	ATEX3000	ATEX5000
Decrimped warp yarn	Warp strains (%):	4.9	1.6	2.1	1.8	0.5	1.3
	Fill strains (%):	-0.8	-0.4	-2.6	-3.3	-0.9	-2.4
Decrimped fill yarn	Warp strains (%):	-0.8	-1.0	-3.8	-5.1	-0.8	-1.7
	Fill strains (%):	5.6	1.7	5.8	7.5	0.7	1.5

4.3.4 Coating behaviour

The previous model by Bridgens (2005) adopted the approach of Menges and Meffert (1976) by including coating resistance as a spring between the peaks of the sawtooth wave forms. An alternative approach has been developed for the improved model that sought to encompass both direct and shear stiffness of the coating, as shear deformation of the coating is likely to occur with biaxial deformation. In the proposed approach, the coating is modelled as a thin plate using the finite element method. A four noded quadrilateral isoparametric finite element (Figure 4.18) was selected as in future developments, i.e. for modelling whole structures, it may be desirable to incorporate curved sides to the element.

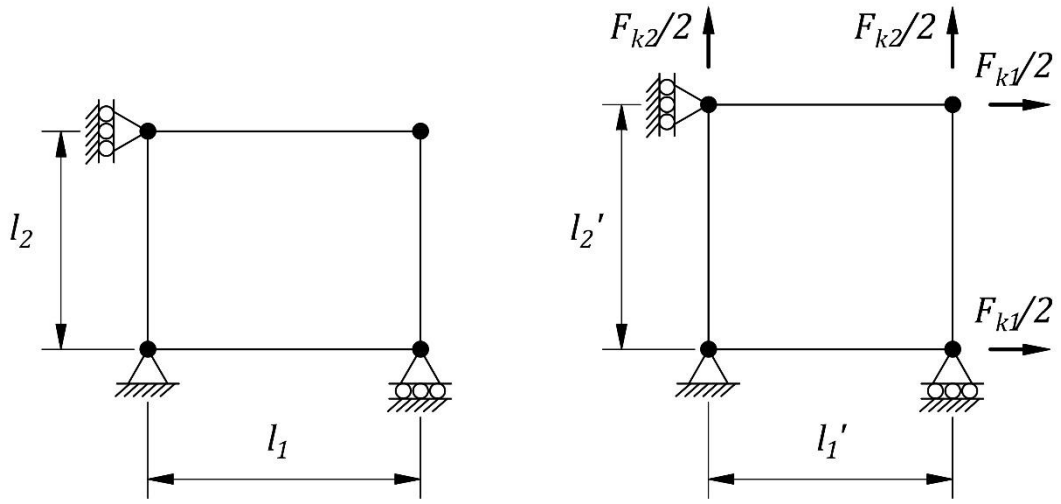

Figure 4.18 Deformation of the coating in the unit cell, represented as four noded quadrilateral isoparametric finite element showing (left) load applied prior to deformation and (right) load applied with deformation

This work was conducted prior to the look-up function being developed which accounts for strain in the coating and strain in the yarn. Therefore, it is not used in the final model formulation but is used in the sawtooth and linear model approaches that were modelled for comparison with the final formulation).

The model calculates load applied to the yarn being equal to load applied to the unit cell minus any load that is resisted by the coating. Prior to the model's initial iteration for predicting strain at a given load ratio it is assumed that no load is resisted by the coating. With each subsequent iteration the parametric element provides a force in the coating for the strain in the unit cell. This coating force is removed from the force applied to yarn in the next iteration where an updated strain in the cell is calculated and subsequently an updated coating force. This process will continue until a split of the load between the yarn and coating yields a strain of the cell that is consistent with the force in the coating.

4.3.5 Shear behaviour

Shear behaviour has not been incorporated in the predictive model. However, a possible approach to predicting the shear response of the architecture fabrics is proposed on the basis of existing work. A suitable approach has to be compatible with the biaxial unit cell model and its underlying description of the yarn geometry (§4.2.1). The proposed formulation adopts some assumptions of other investigators (Mack and Taylor, 1956; McGuinness and ÓBrádaigh, 1998; Nguyen *et al.*, 1999; Liu *et al.*, 2004; Liu *et al.*, 2005), namely assuming yarns to be:

- ridged beam elements;
- pin-jointed at every yarn intersection (allowing rotation between the yarns); and
- inextensible during shearing (no change in amplitude or length occurs).

Consequently, the resistance to shear deformation is limited to friction arising from contact of interwoven yarns at the yarn intersections and lateral compaction of adjacent yarns. When shearing a coated fabric, compaction of the coating will also occur. This approach fails to account for the three dimensional deformation of the woven yarns.

The works of Liu *et al.* (2004) and Liu *et al.* (2005) have been used as the starting point in developing a predictive unit cell shear model for architectural fabrics. Liu *et al.* (2004) and Liu *et al.* (2005) propose modelling approaches for predicting frictional resistance and lateral compaction, respectively (§2.3.3). The limitation of these models is that they have identical warp and fill yarn geometries. Therefore, the formulations were revised for different geometries in the orthogonal yarn directions and combined in a single model. The revised formulations consider moment equilibrium of the forces acting about the centre of each yarn intersection (Figure 4.19). In combining the two formulations, the moment due to shear force, M_s, must equal the sum of the moment due to friction, M_f, and the moment due to compaction, M_c (Equation 4.43).

$$M_s = M_c + M_f$$ **Equation 4.43**

In the revised formulation a new dimension, the contact length, $c_{1,2}$, is used to allow for non-equal yarn lengths and yarns widths in orthogonal yarn directions (Figure 4.20). The contact length is a measurement across the width of the yarn and is the smallest measurement between a yarn's parallel sides. This dimension defines how much of one yarn is in contact with the other in the orthogonal direction. When the intersecting yarns are orthogonal the contact length equals the width of the yarn and decreases with increasing shear deformation. Moment due to yarn compact is then derived considered dissimilar orthogonal yarn dimensions (Equation 4.44).

$$M_c = 2\int_{\frac{1}{2}(c_1 sin(\gamma/2) - l_1)}^{\frac{1}{2}(c_1 sin(\gamma/2) + l_1)} F_{c1}\ x_1\ dx_1\ +\ 2\int_{\frac{1}{2}(c_2 sin(\gamma/2) - l_2)}^{\frac{1}{2}(c_2 sin(\gamma/2) + l_2)} F_{c2}\ x_2\ dx_2$$

$$= F_{c1}\left[\left(\frac{1}{2}c_1 sin\left(\frac{\gamma}{2}\right) + \frac{1}{2}l_1\right)^2 - \left(\frac{1}{2}c_1 sin\left(\frac{\gamma}{2}\right) - \frac{1}{2}l_1\right)^2\right]$$

$$+\ F_{c2}\left[\left(\frac{1}{2}c_2 sin\left(\frac{\gamma}{2}\right) + \frac{1}{2}l_2\right)^2 - \left(\frac{1}{2}c_2 sin\left(\frac{\gamma}{2}\right) - \frac{1}{2}l_2\right)^2\right]$$

$$= F_{c1}\ c_1\ l_1\ sin\left(\frac{\gamma}{2}\right) +\ F_{c2}\ c_2\ l_2\ sin\left(\frac{\gamma}{2}\right) \qquad \textbf{Equation 4.44}$$

The earlier approach to predicting moment due to friction requires that the yarn intersection has four equal side lengths (Liu *et al.*, 2004). In the revised formulation a value of frictional force, F_f, is integrated over the area of a triangle that forms one quarter of the yarn intersection (Figure 4.21 and Equation 4.35 - Equation 4.39).

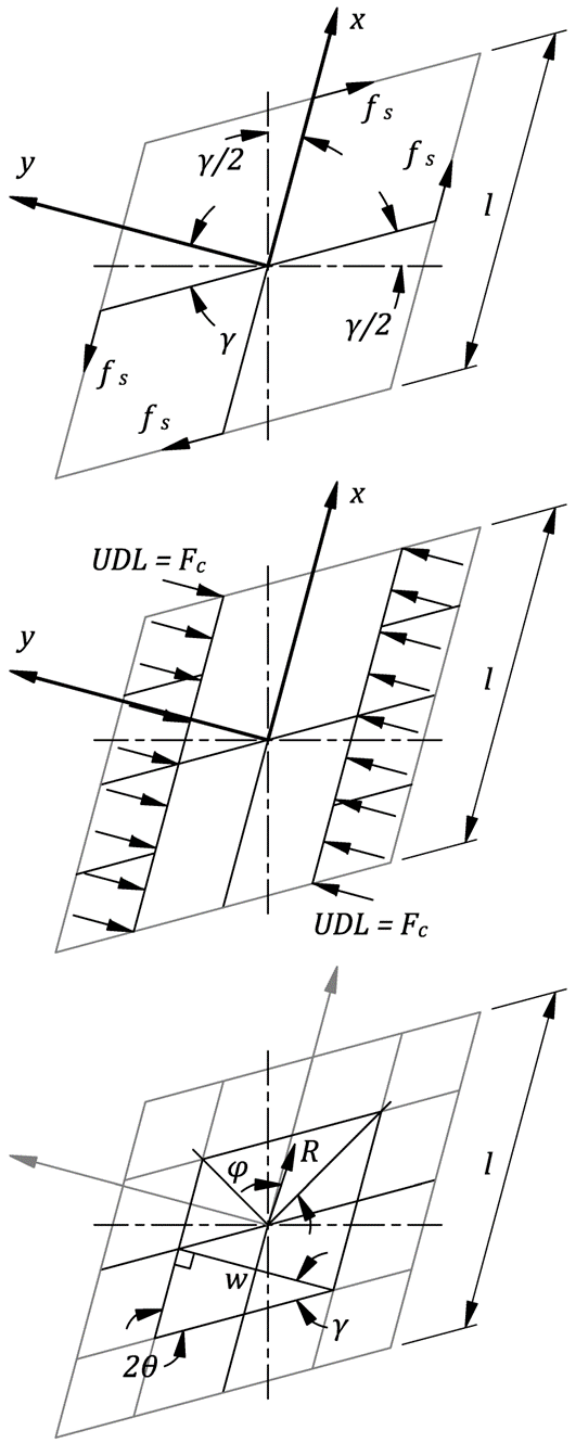

Figure 4.19 Forces acting about the centre unit cell, plan views of moment due to (top) shear resistance, (middle) lateral yarn compaction (adapted from Liu *et al.* (2004)), and (bottom) friction at yarn intersection (adapted from Liu *et al.* (2005)), N.B yarns have identical geometric properties in the warp and fill

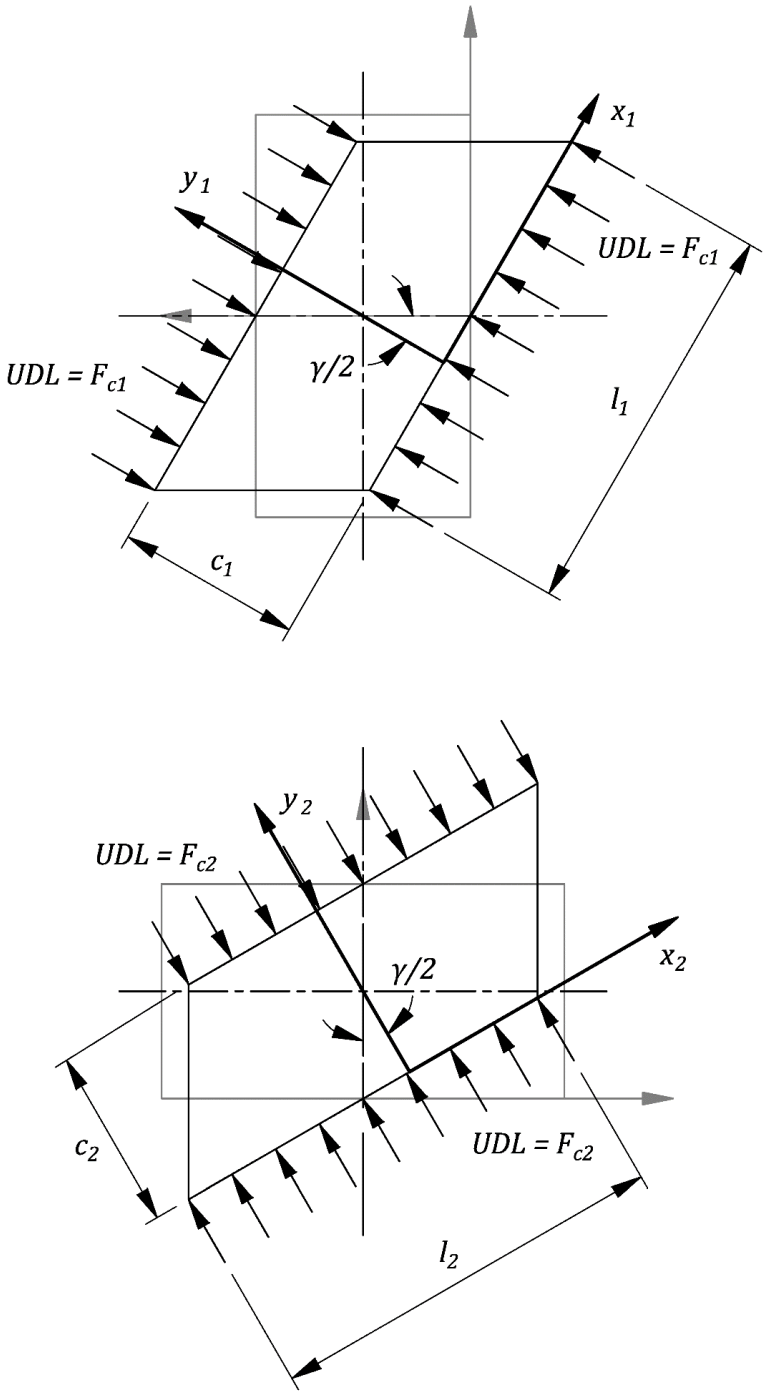

Figure 4.20 Moment in the shear model due to lateral compaction, showing forces acting about the centre of the unit cell in both (top) warp and (bottom) fill directions allowing for different yarn geometry in each the directions

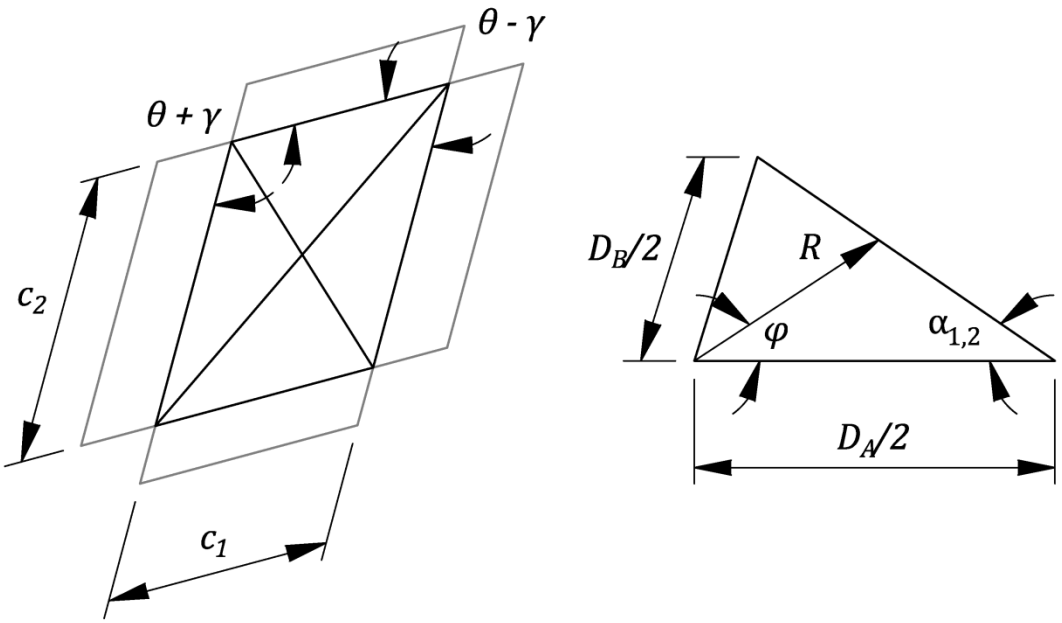

Figure 4.21 Determining the frictional force acting at the yarn intersection for non-square intersections, showing (left) the yarn intersection made up of four triangles and (right) one of the triangles over which the friction force is integrated

$$M_F = 2\int_0^{\phi_A}\int_0^{\frac{D_A sin(\alpha_A)}{2sin(\alpha_A+\phi)}} F_f R^2 dR\ d\phi + 2\int_0^{\phi_B}\int_0^{\frac{D_A sin(\alpha_B)}{2sin(\alpha_B+\phi)}} F_f R^2 dR\ d\phi$$

$$= 2\int_0^{\phi_A} F_f \left[\frac{1}{3}R^3\right]_0^{\frac{D_A sin(\alpha_A)}{2sin(\alpha_A+\phi)}} d\phi + 2\int_0^{\phi_B} F_f \left[\frac{1}{3}R^3\right]_0^{\frac{D_A sin(\alpha_B)}{2sin(\alpha_B+\phi)}} d\phi$$

$$= 2\int_0^{\phi_A} \frac{1}{3}F_f \left[\frac{D_A sin(\alpha_A)}{2sin(\alpha_A+\phi)}\right]^3 d\phi + 2\int_0^{\phi_B} \frac{1}{3}F_f \left[\frac{D_A sin(\alpha_B)}{2sin(\alpha_B+\phi)}\right]^3 d\phi$$

$$= \frac{1}{12}F_f {D_A}^3 sin^3(\alpha_A)\int_0^{\phi_A}\frac{d\phi}{sin^3(\alpha_A+\phi)}$$

$$+\frac{1}{12}F_f {D_A}^3 sin^3(\alpha_B)\int_0^{\phi_B}\frac{d\phi}{sin(\alpha_B+\phi)} \qquad \textbf{Equation 4.45}$$

where,

$$\phi_{A,B} = cos^{-1}\left(\frac{{D_A}^2 + {D_B}^2 - 4{c_{1,2}}^2}{2D_A D_B}\right) \qquad \textbf{Equation 4.46}$$

$$\alpha_{A,B} = cos^{-1}\left(\frac{{c_{1,2}}^2 + {D_A}^2 - 2{c_{2,1}}^2}{2c_{1,2}D_A}\right)$$ **Equation 4.47**

$$D_A = \sqrt{{c_1}^2 + {c_2}^2 - 2c_1c_2cos(\theta + \gamma)}$$ **Equation 4.48**

$$D_B = \sqrt{{c_1}^2 + {c_2}^2 - 2c_1c_2cos(\theta - \gamma)}$$ **Equation 4.49**

The friction force, $Ff_{1,2}$, is calculated by integrating the normal force multiplied by the yarn width and a coefficient of friction, μ, over the cross section (Equation 4.50).

$$Ff_{1,2} = \int \mu\, N_{1,2}(x) w_{1,2}\, ds$$

$$= \int_{-\frac{w_{2,1}}{2}}^{\frac{w_{2,1}}{2}} \mu\, \frac{-f_{1,2}}{w}\, \frac{y''_{1,2}}{\sqrt{\left(1 + {y_{1,2}}'(x)^2\right)^3}}\, w \sqrt{1 + {y_{1,2}}'(x)^2}\, dx$$

$$= -f_{1,2}\mu \int_{-\frac{w_{1,2}}{2}}^{\frac{w_{1,2}}{2}} \frac{y''_{1,2}}{\left(1 + {y_{1,2}}'(x)^2\right)^{\frac{3}{2}}} \sqrt{1 + {y_{1,2}}'(x)^2}\, dx$$

$$= -f_{1,2}\mu \int_{y'\left(-\frac{w_{2,1}}{2}\right)}^{y'\left(\frac{w_{2,1}}{2}\right)} \frac{d\left({y_{1,2}}'\right)}{1 + {y_{1,2}}'(x)^2}$$

$$= -f_{1,2}\mu \left[tan^{-1}\left(y'_{1,2}\right)\right]_{y'\left(-\frac{w_{2,1}}{2}\right)}^{y'\left(\frac{w_{2,1}}{2}\right)}$$

$$= -f_{1,2}\mu \left[tan^{-1}\left(y'_{1,2}\right)\right]_{+\frac{A_{1,2}\pi}{l_{1,2}} sin\left(\frac{\pi w_{2,1}}{2l_{1,2}}\right)}^{-\frac{A_{1,2}\pi}{l_{1,2}} sin\left(\frac{\pi w_{2,1}}{2l_{1,2}}\right)}$$

$$= -f_{1,2}\mu \left[tan^{-1}\left(-\frac{A_{1,2}\pi}{l_{1,2}} sin\left(\frac{\pi w_{2,1}}{2l_{1,2}}\right)\right) - tan^{-1}\left(\frac{A_{1,2}\pi}{l_{1,2}} sin\left(\frac{\pi w_{2,1}}{2l_{1,2}}\right)\right)\right]$$ **Equation 4.50**

where,

$$y'' = \frac{d}{dx}(d(y'))$$

$$\therefore y''dx = (d(y'))$$ **Equation 4.51**

$$\int \frac{1}{1 + x^2} = tan^{-1}(x)$$ **Equation 4.52**

4.4 Programming the model

The unit cell model is a non-linear system of equilibrium and compatibility equations that must be solved to predict biaxial strains. To solve the system of equations, the unit cell model was developed in MATLAB, a computing environment for numerical computation, visualisation and programming. The use of MATLAB to develop the model allows for ease of future adaptations and expansion of the model's capabilities, interfacing with other applications created by different researchers and to make use of MATLAB's built in functions, i.e. solvers.

4.4.1 The predictive model in MATLAB

The model comprises a number of MATLAB program files (sequences of executable commands) which take the form of either scripts or functions. Scripts are used for sequences of commands that occur only once following each execution of the model and functions are used where the model must perform the same sequence of commands with different variables and/or at different stages of the modelling process. The architecture of the principal program files (Figure 4.22) has evolved as the predictive model has developed to maintain the most efficient arrangement of commands, i.e. repeated commands were programed as functions. The following sections define the principal program files and relate them to the model's formulation.

The arrangement of the program files and the order of steps constitutes the methodology employed by the model in arriving at a prediction. The steps and their order form a novel modelling approach in addition to the formulations described in the forgoing sections.

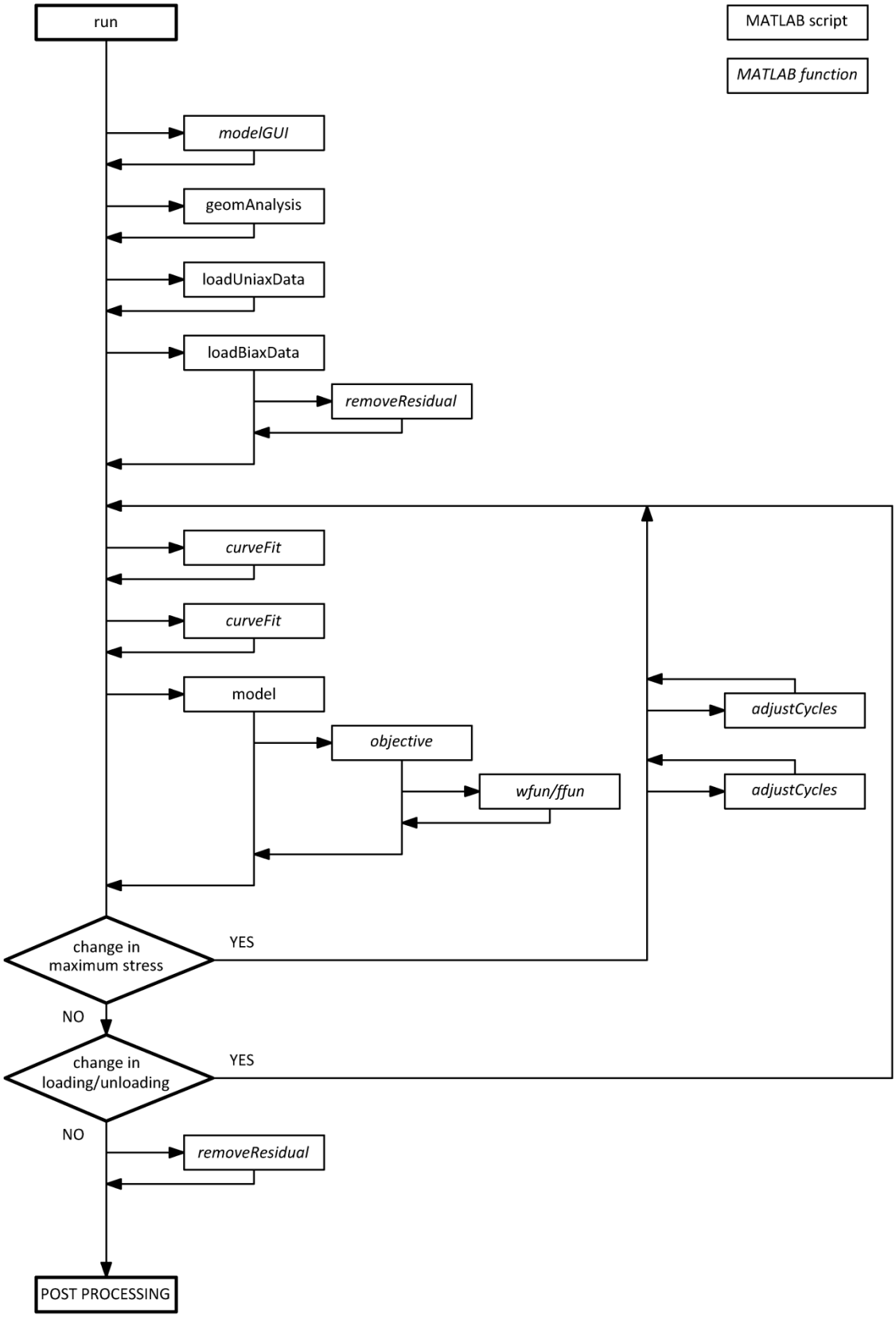

Figure 4.22 Process flow diagram of the model's principal programme files. A short description of each function/script illustrated is provided overleaf

adjustCycles Identifies each load cycle in the uniaxial input data and scales the cycles in both the stress and strain axes. The scale factor is determined as the ratio of the maximum stress of the biaxial load cycle to be predicted (in the yarn direction in question), minus the value of prestress to be applied in the prediction, to the maximum stress of the uniaxial data.

curveFit Calls MATLAB's built in curve fitting toolbox to fit a smoothing spline curve to uniaxial load data in order to define the look-up functions. Plots of the curve fits can be shown to the user when running the model, so the user can ensure that the turning points are being found.

modelGUI The model's graphical user interface (GUI).

objective The model's objective function. MATLAB's built in solver, *fsolve,* calls *objective* to solve the system of equilibrium and compatibly equations that define the model for each load ratio for which strain are to be predicted. This is performed iteratively until a solution is found (or until the solver fails to find a solution for a given load ratio). The objective function for the model's final formulation is shown in Box 4.1.

removeResidual Calculates the strain difference (residual strain) between the beginning and end of each cycle and removes the strain difference calculated.

loadBiaxData From data supplied by the user through the model's GUI, *loadBiaxData* imports the biaxial input data (load profile) for which predictions are to be made and identifies each load cycle. When test data is used, to prevent a large number of data points being predicted *loadBiaxData* will sample the data.

model Calculates data required to pass to MATLAB's solver, *fsolve*, and calls the objective function. This script also calls the different model formulations. *fsolve* is MATLAB's only solver for systems of non-linear equations.

run The model's core script, *run* initiates the predictive model, loads the GUI and loads the input data into MATLAB. *run* performs initial calculations before calling *model* to make strain predictions at every load case (data point in the test data) of interest. It generates the look-up function for the initial loading curves and calls *curvefit. Run* also handles post processing and plots results for the model's user.

wfun/ffun Determines the strain the in the respective yarns using the novel look up function.

4.5 Model test cases: checking the model formulation

A series of special case model runs have been executed to check for errors in the formulation of the model and in its implementation within MATLAB. These runs are special cases as they do not concern data relating to real architectural fabrics. Instead they use input parameters for 'pseudo fabrics' with prescribed yarn properties such that the fabric has identical properties in the warp and fill or different properties which can swapped between the two yarn directions. By prescribing yarn properties in this way it is possible to check that the model can:

- obtain symmetrical results in the warp and fill yarn directions for a fabric with identical warp and fill properties and cross sectional geometries, i.e. identical strain behaviour in the warp and fill (Case 1); and
- produce opposing results for two separate model runs with different warp and fill yarn properties and cross sectional geometries interchanged between the two yarn directions, i.e. identical strain behaviour in the warp and fill when comparing warp and fill between the two separate model runs (Cases 2 and 3).

These special cases are of course not intended to provide evidence that the model is suitable for predicting the behaviour of specific architectural fabrics. Instead the special cases check for typographical errors in the code and for any differences in the predicted behaviour between yarn directions due to the order of the calculations performed. The special cases ensure the model's formulation is correct and that it produces anticipated fabric behaviours. Observing the anticipated behaviours from execution of the special cases means the model is fit for subsequent validation against experimentally obtained data from real fabrics (Chapter 5). The pseudo fabrics' properties and yarn geometries (Table 4.6) are based upon those for a Ferrari 702 PVC/PES fabric. For the test case with identical yarn behaviours, warp uniaxial behaviour will be used for both yarn directions. The choice of the 702 fabric and warp uniaxial behaviour is inconsequential, any fabric or data from the fill yarn direction would be equally acceptable for the creating the special cases. Plots of the model results for the special cases (Figure 4.23) show that the model is correctly formulated. RMSE values of zero were obtained and are shown on each plot against the respective data.

Table 4.6 Pseudo fabric yarn geometries used for test cases

	A_1	A_2	l_1	l_2	w_1	w_2	t_1	t_2
Case 1	0.100	0.100	1.200	1.200	1.000	1.000	0.100	0.100
Case 2*	0.063	0.078	1.250	1.221	0.911	1.129	0.183	0.146
Case 3	0.078	0.063	1.221	1.250	1.129	0.911	0.146	0.183

*Ferrari 702 yarn geometry

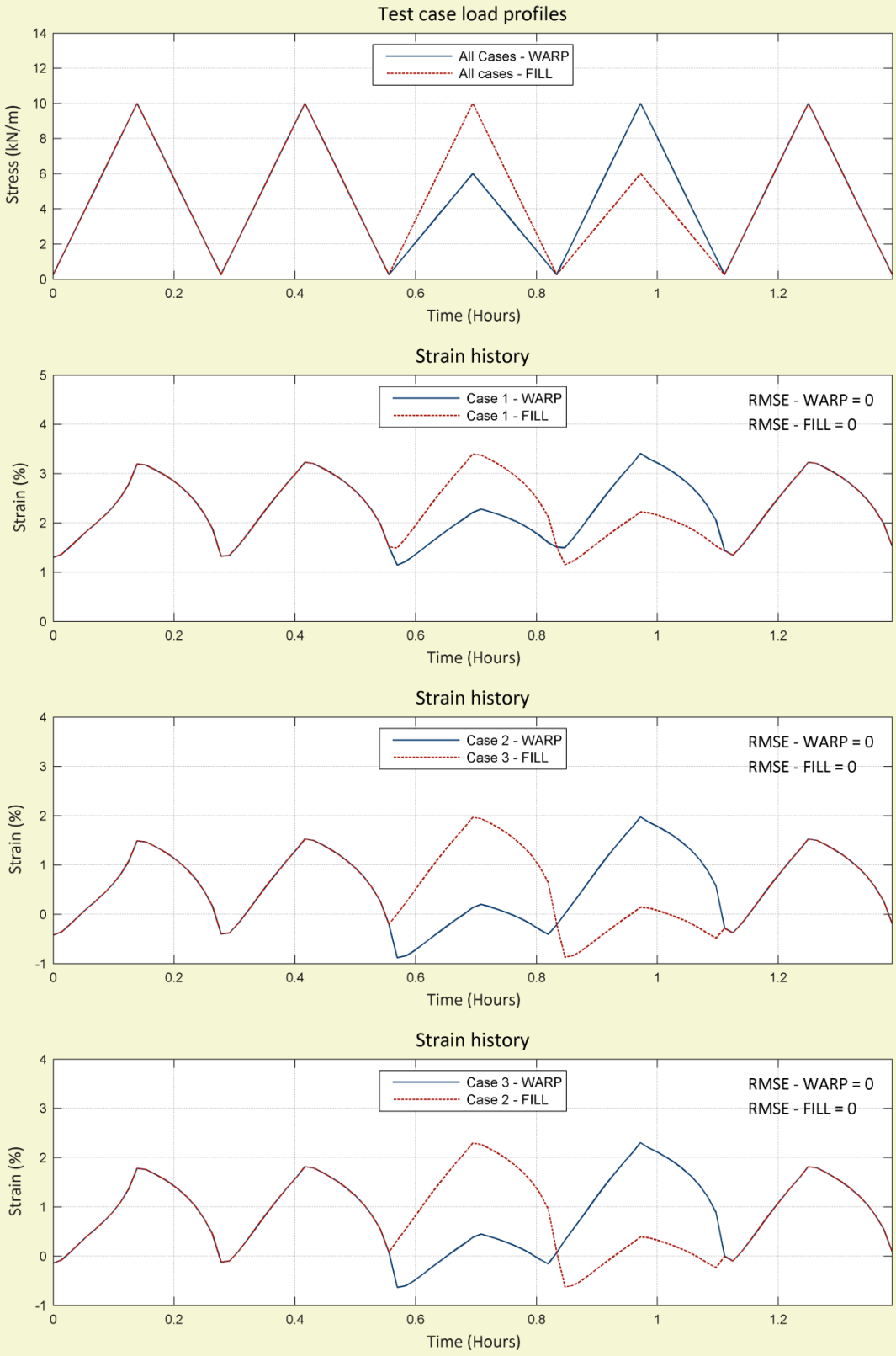

N.B. 3rd warp cycles and 4th fill cycles (and visa versa) are compared when calculating RMSE values

Figure 4.23 Results plots of special cases for checking implementation model's formulation

4.6 Summary

Predictive fabric models are not used in the design and analysis of tensile fabric structures and design engineers rely on specialist testing methodologies to provide material properties for use in design. A model which accurately predicts the results of these specialist tests would reduce the time and cost associated with experimentally obtaining the necessary material properties.

A predictive unit cell model has been developed for determining the biaxial behaviour of architectural fabrics without requiring input from biaxial testing. The model is a development of existing sawtooth models and builds upon the earlier model of Bridgens (2005). A realistic description of the yarn geometry has been implemented within the model following a quantitative assessment demonstrating the accuracy of using a sinusoidal representation of the undulating yarns. Goodness of fit measures show a strong correlation between the shape of the yarns of the architectural fabrics used and the approximating sine curves. It is hypothesised that a more realistic yarn description will allow for more accurate representation of the deformation mechanisms when load is applied to the fabric.

A series of sine curves, each with a single sine term, has been used to define the yarn waveforms and the cross sections of the orthogonal intersecting yarns, thus providing consistent geometry between each of the yarns. A more accurate representation may be achieved by increasing the number of sine terms used, but for the fabrics of interest here it was deemed unnecessary. Equilibrium and compatibility equations have been derived based upon the sinusoidal yarn description to model the key interactions of crimp interchange and yarn elongation. Changes in the yarn cross section are assumed to occur by rearrangement of the yarn fibres so that yarn crushing stiffnesses do not need to be determined. Unlike previous sinusoidal models, the improved unit cell utilises the shape of the yarn by applying the normal force over the length of yarn in contact with the orthogonal yarn to more accuracy replicate the real fabrics. While here the normal force is uniformly distributed, in future developments of the model the normal force could be varied over the yarn cross section. Importantly, no calibration factors are used in the proposed model.

A significant development of the proposed model is the inclusion of a novel look-up function which enables prediction of a fabric's non-linear, inelastic load response and hysteresis. The look up function dispenses with the requirement to subjectively determine constant yarn moduli. Further, each prediction at a given biaxial stress ratio is not made independently of the materials stress-strain history. Consequently, the intention of the model is to exactly replicate a biaxial test. A revised set of equations has been presented for modelling shear of woven fabrics with asymmetric base cloths.

Chapter 5:
Validating the predictive model

Contents

Figures

Tables

5.1 Introduction

This chapter first details the methodologies developed for obtaining input data as well as for obtaining data needed for the validation of the predictive model. Subsequently, the validation of the model is described. This involves comparing predicted fabric behaviour to experimentally obtained test data.

Results from the final model formulation, which incorporates the look-up function, are presented in contrast with experimental results. Additionally, results obtained using a sawtooth model formulation (Bridgens, 2005) and the sinusoidal formulation with isotropic coating element (§4.2.4) are also presented. These latter two models require a linear stiffness for the yarns and coating as they do not use the look-up function.

5.2 Model input data

A range of fabrics were tested to provide data required for validation of the predictive model. The fabrics tested (Table 5.1) represent a range of constituent materials, weights, thicknesses, tensile strengths and manufacturing methods used in tensile fabric structures. Uniaxial test results and images of the fabric cross section are required for the predictive model and the methodologies for obtaining these inputs are presented in this section.

Table 5.1 Summary of architectural fabrics used for model implementation

Fabric	Manufacturer	Material		Weight (g/m^2)	Thickness (mm)	Tensile strength†	
		Base cloth	Coating			(kN/m)	(N/5cm)
702‡	Serge Ferrari, France	PES	PVC	750	0.56	60/56	3000/2800
1202‡	Serge Ferrari, France	PES	PVC	1050	0.78	112/112	5600/5600
B18089	Verseidag, Germany	Glass fibre	PTFE	1150	0.70	140/160	7000/6000
B18059	Verseidag, Germany	Glass fibre	PTFE	1550	1.00	160/180	8000/7000
ATEX3000	P-D Interglas, UK	Glass fibre	Silicone	340	0.45	60/60	3000/3000
ATEX5000	P-D Interglas, UK	Glass fibre	Silicone	685	0.90	100/100	5000/5000

†as specified by the manufacturer (warp direction/fill direction)
‡Précontraint®
PES = Polyester, PVC = Polyvinylchloride, PTFE = Polytetrafluoroethylene

5.2.1 Uniaxial testing

Uniaxial testing of coated woven fabrics is described in BS EN ISO 1421:1998 'Rubber- or plastics-coated fabrics – Determination of tensile strength and elongations at break' (BSI, 1998). The standard specifies test specimen dimensions of 200 x 50mm, a rate of displacement of 100mm/min and that cross head displacement and load are to be recorded for the calculation of elongation and strength at failure. BS 3424-21:1993 'Testing coated fabrics – Part 21: Method 24. Method for determination of elongation and tension set' also details the uniaxial testing of coated fabrics (BSI, 1993). The latter standard describes a method that can be used to quantify residual strain. The specimen dimensions are the same as for BS EN ISO 1421:1998, the displacement rate specified is 5mm/min and crosshead displacement and load are recorded.

As the predictive model requires cyclic uniaxial test data in the warp and fill yarn directions, adhering to either of the aforementioned test standards would not provide the required information. Therefore, an alternative procedure was developed, based upon the two standards. The standard 200x50mm specimen dimensions were used to prepare uniaxial specimens. Further, the uniaxial test specimens were removed from the fabric roll directly adjacent to the biaxial specimen that was used to obtain the comparative results (Figure 5.1).

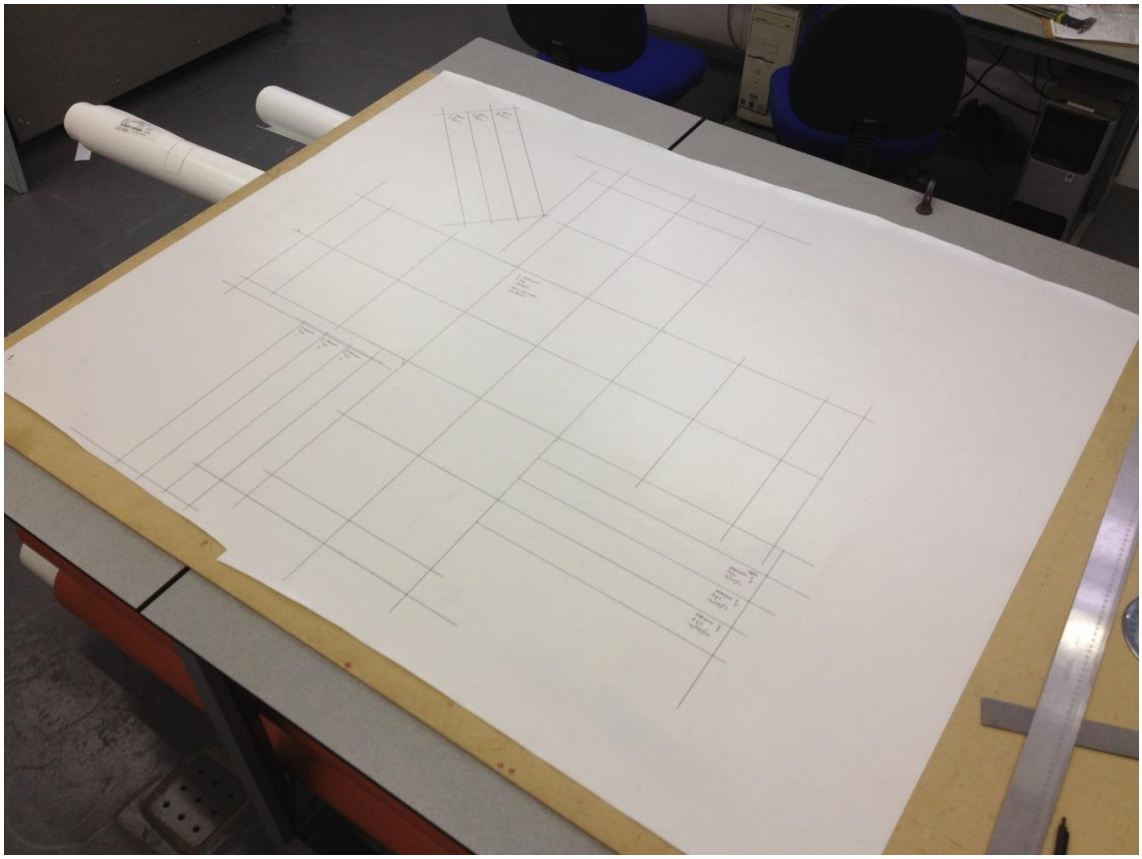

Figure 5.1 Biaxial and uniaxial test specimens to be removed from the fabric roll, showing the proximity of uniaxial specimens for input data to the biaxial specimen for comparative data

The rate of displacement was set at 10mm/min. While the standards mentioned above set a rate of 100mm/min, uniaxial testing on PVC/PES and PTFE/glass fibre fabrics has indicted that extension rates above 50mm/min result in a variable stress-strain response (Bridgens, 2005). A consistent stress-strain response exhibited by all specimens tested is necessary for uniaxial data to be used to predict biaxial behaviour. As extension rates in the warp and fill directions during a biaxial test will differ (§5.3.2), an extension rate lower than 50mm/min was necessary.

Capstans (cylinders around which a flexible material can be wound) were used to secure the uniaxial test specimens into a uniaxial test machine. The use of capstans is preferred to conventional clamping fixtures as yarn fibres will be damaged if clamped or loaded over an edge, thus becoming crushed or broken. Such damage will have the effect of reducing the ultimate tensile strength of the fabric and design loads may not be achieved during testing. Each end of a fabric specimen was secured in a respective capstan by winding the end of the specimen no fewer than two times around the cylinder of the capstan, the end having been first placed through a slot in the cylinder and folded back on itself (Figure 5.2).

The capstans were positioned approximately 200mm apart (Figure 5.3), in line with the specimen dimensions, and specimens were cut with a total length of 900mm to provide the material required to wrap around the capstans. However, the capstans cannot provide an accurate specimen length and slippage of the specimen was encountered when testing, notably with the PVC/PES fabrics. Measured displacement of the test machine crosshead will include any slippage of the specimen that may occur, and will appear as fabric strain. Therefore, displacement was measured using a linear extensometer affixed to the surface of the specimen with aluminium mounts, as this will not measure only strain in the fabric and not slippage of specimen. The use of a linear extensometer will avoid the influence of end effects in the stress strain response. The mounts have a threaded pin which penetrates the fabric and screws through a backing disc. This arrangement sandwiches the specimen between the mount and the backing disc and ensures the axis of the mount remains perpendicular to the plane of the specimen. The gauge length of the extensometer used was 110mm. Excessive slippage is still undesirable when using a surface mounted extensometer, as slippage will cause a reduction in applied load and a reduction in the strain rate.

When testing a non-PTFE coated specimen, it is desirable to wrap a strip of PTFE coated fabric around the capstan along with the specimen. The coated PTFE fabric reduces friction between the layers of non-PTFE material and the capstan, which ensures that the specimen is pulled tight about the capstan when setting up the test. Consequently, this reduces slippage during testing.

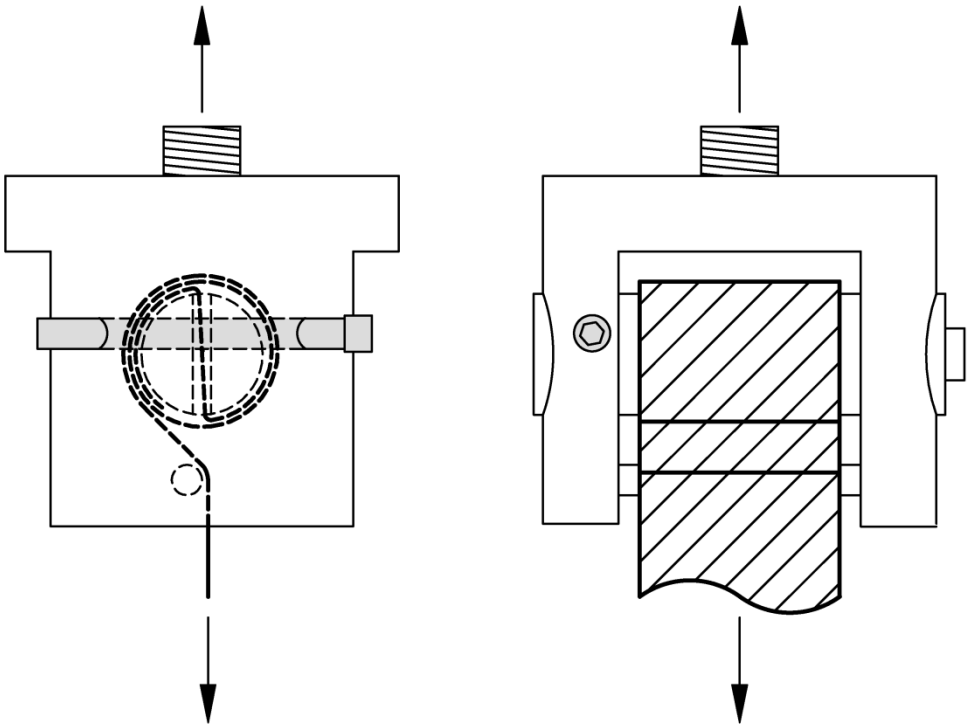

Figure 5.2 Uniaxial testing apparatus showing the fabric wound around the capstans, viewed from both the side (left) and the front (right)

The final model formulation requires experimentally obtained stress-strain behaviour in both yarn directions, which incorporates both yarn and coating behaviour. However, the sawtooth and linear sinusoidal formulations require a constant values of Young's modulus for each of the warp and fill directions, $E_{y1,2}$, and coating stiffness, E_k. The test methodology differed slightly between that for determining yarn behaviour and values of stiffness in the yarn directions and that for determining coating stiffness, as will now be described.

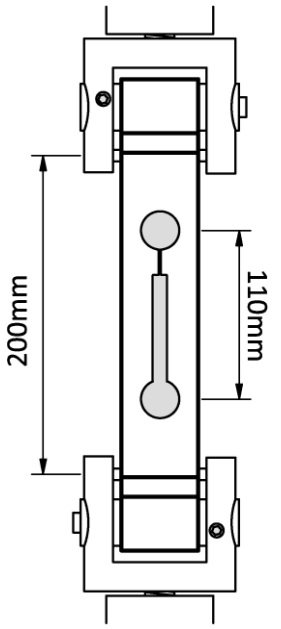

Figure 5.3 Uniaxial test apparatus set up, surface mounted linear extensometer are shown attached to specimen which is mounted in capstans

Uniaxial testing in the yarn directions was performed to a predetermined maximum stress greater than was applied during biaxial testing but less than the material's ultimate tensile strength (UTS). This ensured that stress-strain behaviour was captured for a sufficiently large envelope of values but that the fabric was prevented from being loaded to failure, which was undesirable as failure of the specimen would damage the extensometer. A maximum load of 40% of the UTS was applied to the uniaxial specimen for the testing in the yarn directions. As biaxial testing was performed to 25% of a material's UTS (§5.3.2), loads to 40% UTS provided a large enough stress-strain response for comparison of predicted behaviour with recorded behaviour, as well as scope for predictions to be made at higher values of biaxial stress (i.e. up to 40% UTS).

The look-up function has been implemented within the predictive model so as to allow a user to input an unlimited number of uniaxial test cycles. However, the number of cycles was limited to six for the fabrics tested for validation of the predictive model. This was because six cycles was observed to be a sufficient number of cycles for the residual strain, i.e. the non-recoverable strain at zero load, between each cycle to reduce to negligible amount. While further cycles would have been possible, limiting the number of cycles to six was also a practical consideration to limit the duration of the testing.

The standard approach for determining constant values of Young's moduli from uniaxial test results (required for the linear and sawtooth model formulations) is that adopted by previous researchers (Menges and Meffert, 1976; Testa *et al.*, 1978; Bridgens, 2005). The approach, although the application of standardised method, requires judgment when interpreting the results. Coating

stiffness is approximated using an initial shallow gradient of an initial loading curve for a fill test specimen and a subsequent, steeper gradient at higher stress to determine yarn stiffness. The difficulty of this approach is observed by comparing uniaxial test data for a PTFE/glass fabric with that of a PVC/PES fabric (Figure 5.4). As is typical, the glass fibre fabric exhibits the shallow initial gradient and subsequent steeper gradient, making it is possible to determine approximations for both yarn and coating. However, the polyester fabric does not exhibit the initial shallower gradient. A constant stiffness value is an approximation of fabric behaviour, so determining the most appropriate value is essential if the results of the predictive model are to be accurate.

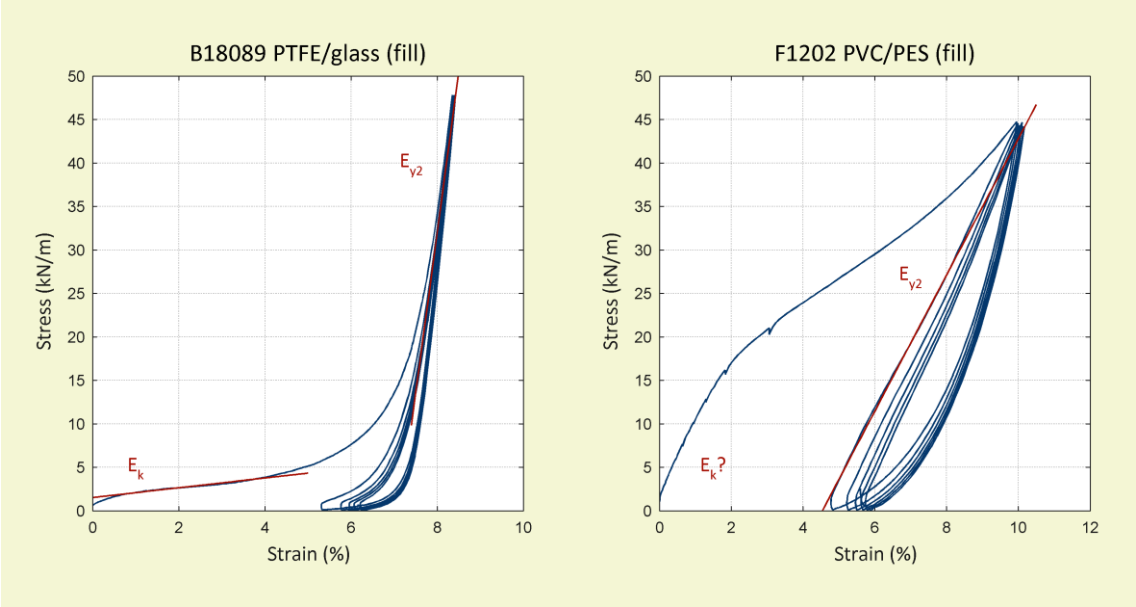

Figure 5.4 Best fit elastic constants determined from uniaxial test data where testing has been carried out in the direction of the yarns, note that for the PVC/PES specimen it is not readily apparent what part of the stress-strain response represents the coating stiffness

Uniaxial bias shear tests were proposed as an alternative approach for determining values of coating stiffnesses. This novel approach assumes the shear resistance of the specimen is governed by the axial coating stiffness at low angles of shear (i.e. shear resistance mechanisms of the yarns, such as friction and compaction have not yet active). Axial deformation of the bias specimen during testing was measured over the portion of the specimen subject to pure shear (§2.2.2) (Figure 5.5) and the initial loading curve used to determine the value of Young's modulus. This alternative approach was proposed to make identifying an accurate value easier for all fabrics.

Values obtained for all uniaxial tests are shown in Table 5.2. Values for coating were also obtained for the glass fibre fabrics using the aforementioned standard approach and this method can be seen to produce higher values of coating stiffness. Another deformation mechanism is supplementing the coating stiffness. Further, the results of the ATEX fabric is counter intuitive as the thinner of the two fabrics appears to have the higher coating stiffness. It is not clear why this is the case, though the results make the novel approach for determining coating stiffness the preferred choice over the typical approach.

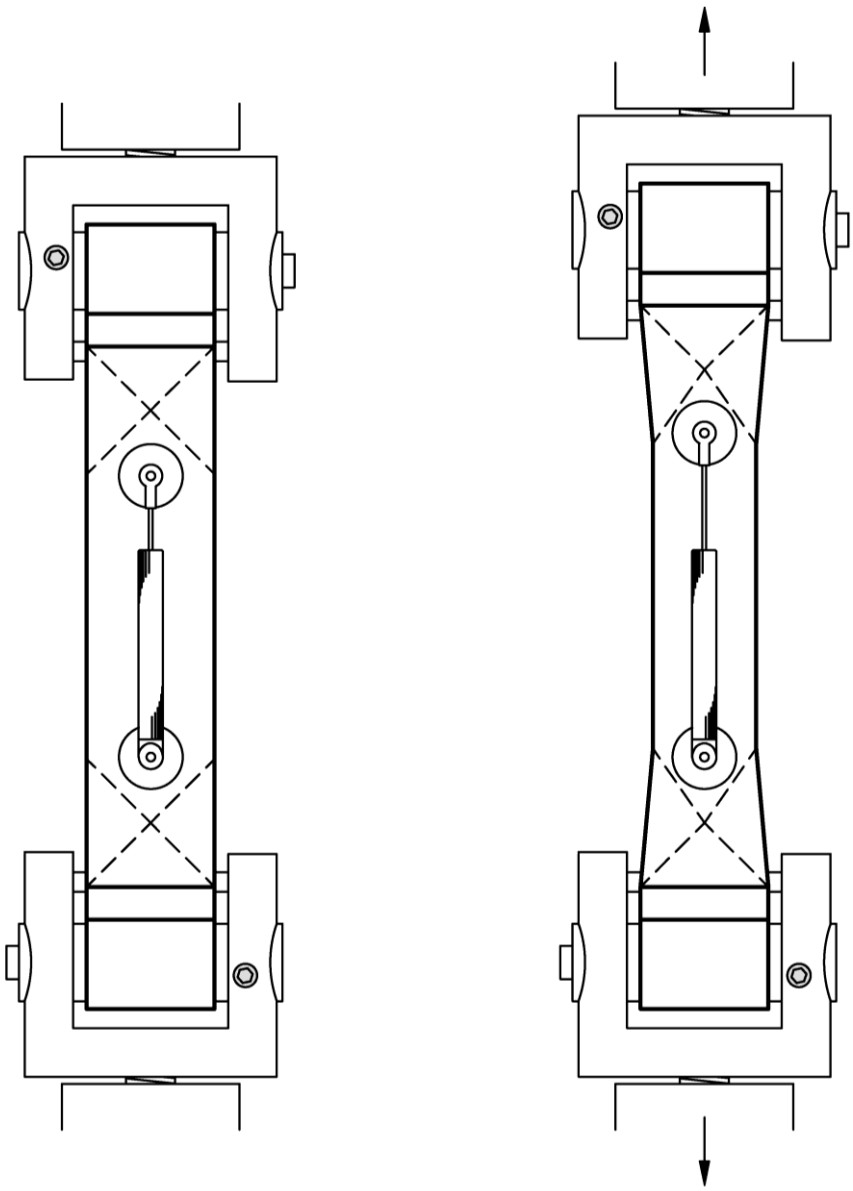

Figure 5.5 Bias testing of specimen to determine coating stiffness, illustrating an untested specimen (left) and an elongated specimen (right)

Table 5.2 Stiffness values determined from uniaxial tests

Fabric	Warp yarn stiffness, E1 (kN/m)	Fill Yarn stiffness, E2 (kN/m)	Coating, E_k from bias cut specimen (kN/m)	Coating, E_k (kN/m) from fill specimen
702	485	425	33	-
1202	880	810	37	-
B18089	4270	3970	36	60
B18059	4610	4770	54	86
ATEX3000	3120	3190	12	194
ATEX5000	4109	6302	21	112

5.2.2 Fabric imaging and measurement

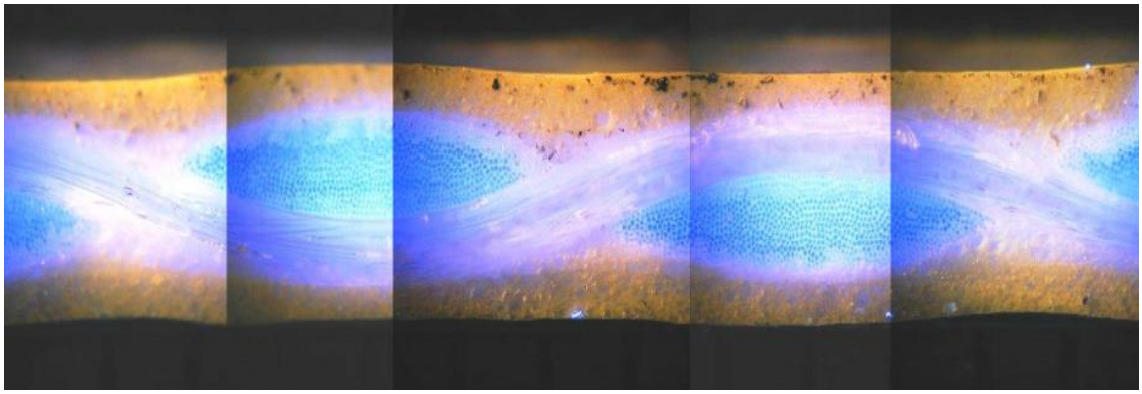

Figure 5.6 Example of an image of a Ferrari 1502 fabric cross section obtained by assembling multiple photomicrographs, reproduced from (Eddleston, 2007)

For the model to be used in the design of fabric structures, the methodology for collecting images of fabric cross sections must be easy to implement, without the need for prohibitively expensive specialist equipment and must be repeatable. Macrophotography has been used previously to provide images for predictive modelling where the same requirement existed (Bridgens, 2005). However, a subsequent study (Mellor, 2006) failed to capture images with adequate contrast and sharpness when following the macrophotography methodology. Sophisticated imaging technologies, synchrotron radiation X-ray imaging (Gong *et al.*, 2009) and X-ray micro-computed tomography (X-ray micro CT) (Desplentere *et al.*, 2005), have been shown to produce highly detailed images of a woven fabric's yarn cross section. However, such methodologies are not available to design engineers when designing tensile fabric structures, owing to the expense of the X-ray equipment, thus despite their advantages these methods are unsuitable for use here.

Photomicroscopy has also been used to obtain images (photomicrographs) of sufficient quality to obtain measurements of architectural fabric yarn geometry (Eddleston, 2007) (Figure 5.6). Consequently, the development of a photomicroscopy methodology was initially used for producing images required for the predictive model. However, such an approach was employed only briefly as it was immediately apparent that obtaining a photomicrograph of reasonable quality was difficult and time consuming. Furthermore, multiple photomicrographs were required to construct an image containing a complete yarn wavelength (as shown in Figure 5.6). Such processing of images has additional, undesirable, time costs. For the predictive model to meet its requirements, an easier more rapid means to capture images of the yarn cross section was required. The appropriate method will need to provide a field of view, at sufficient magnification, large enough capture a complete yarn wavelength, i.e. up to 2mm.

An alternative was to develop a macrophotography methodology that addressed possible causes of poor image quality. Causes of poor image quality include:

- insufficient depth of field;
- inappropriate selection of exposure (aperture size and shutter speed) and sensitivity (ISO);
- insufficient illumination of the fabric specimen; and
- movement of the camera (camera shake).

Capturing very high quality images was made possible by following some general photographic principles and complementing the camera and lens with some inexpensive additional equipment. The macrophotographs were readily and easily obtained using a *Canon EOS 50D* digital SLR camera coupled with a *Canon MP-E* 65mm 1-5x extreme macro lens, a LED ring light, a copy stand and a computer which was used to control the camera (Figure 5.7 and Figure 5.8).

Small aperture settings (higher f-stop values) were selected to maximise the depth of field. The depth of field is the distance, parallel to the axis of the lens, between the nearest and farthest feature within an image that is in focus. Maximising the depth of field is important when taking such close up macrophotographs where the depth of field will be extremely small. The depth of field of the *Canon MP-E* 65mm lens ranges from 2.240mm (1x, f/16) to only 0.048mm (5x, f/2.8). If the macrophotography set up fails to ensure a sufficient depth of field then parts of the captured images of the fabric cross sections may not be in focus, making it difficult to obtain reliable measurements. However, a small aperture setting reduces the amount of light that passes through the aperture to the camera's image sensor, thus degrading the clarity of the image. The shutter speeds and ISO settings were subsequently chosen to compensate for the use of smaller aperture sizes. However, selecting a slow shutter speed allows more light to pass through the lens to the image sensor, but can result in image blur where the camera or the subject moves when the shutter is open. Further, a higher ISO setting will increase the sensitivity of the digital light sensor, but will increase image noise and reduce contrast and sharpness (Garrett and Harris, 2008). A suitable balance between the ISO setting and the exposure was determined for the fabrics photographed.

The **camera settings** that were used to produce the macrophotographs were:

- Focal length: **f/9**
- Exposure/shutter speed: **1/13 sec**
- ISO setting: **ISO-1000**
- White balance: **Auto**

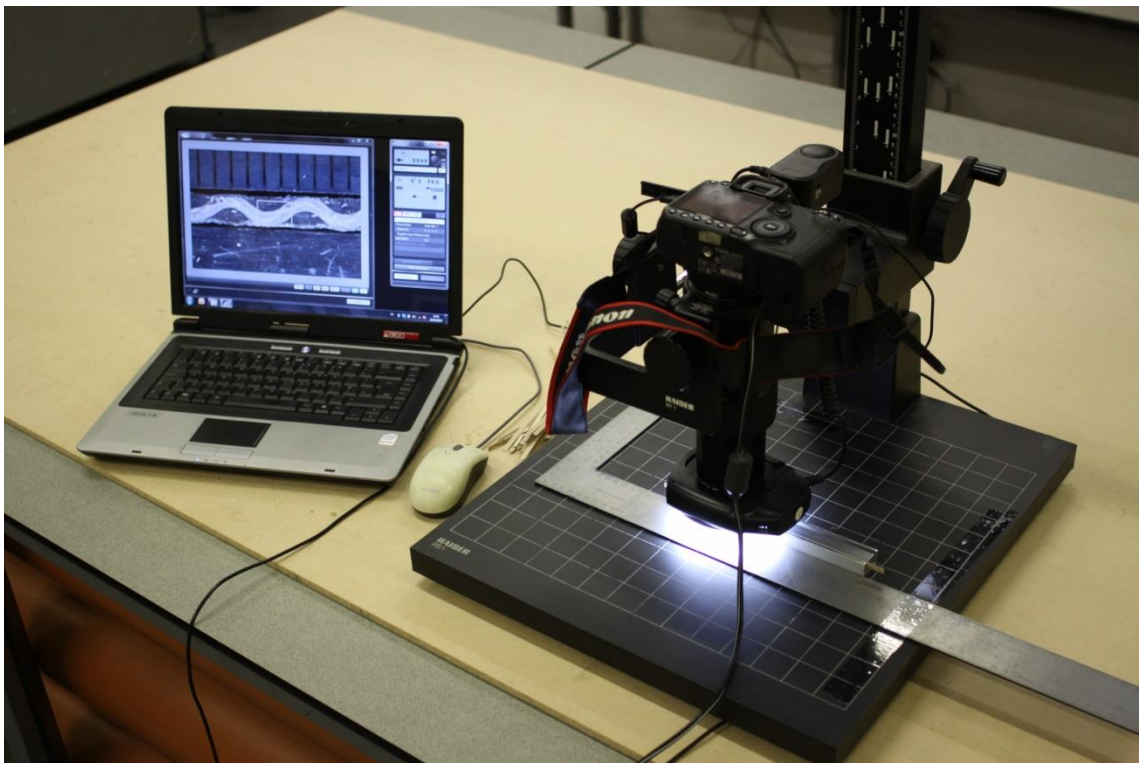

Figure 5.7 Macrophotography setup, a steel edge has been secured to the copy stand allowing the sample mount to be quickly positioned

Figure 5.8 Canon EOS 50D digital SLR camera coupled with a Canon MP-E 65mm 1-5x extreme macro lens, a LED ring light is shown mounted on the front of the lens

Providing a sufficient light source and the use of a copy stand dramatically improved the ease at which images could be obtained. At 5x magnification the distance of the fabric specimen from the front of the lens when focused is approximately 40mm. A LED ring light was mounted onto the front of the lens to improve the illumination of the fabric specimens. The use of a copy stand coupled with a computer to control the camera eliminated camera shake, enabling slower shutter speeds, as the camera is not touched when capturing the images.

The setup also allows for rapid and easy focusing of the lens. As the *Canon* MP-E 65mm lens is manual focus lens, it is possible to focus the lens by adjusting the focus ring, though this will alter the magnification. Alternatively, selecting the required magnification and adjusting the distance to the fabric specimen will also bring the image into focus. It was found to be easier to focus the lens using the focus ring, though this sacrifices the choice of magnification. Therefore, a combined approach is advisable. Images were roughly focused by adjusting the distance of the lens from the specimen using the copy stand and then fine-tuned using the focus ring, resulting in very small changes to the magnification of the image. This allows the magnification to be approximately selected whilst ensuring the lens can be successfully focused for every image with ease.

Comparing the images obtained using the macrophotography approach (Figure 5.9 – Figure 5.11) with an image constructed from multiple microphotographs (Figure 5.6) illustrate that the former offers a suitable means to readily obtain cross sectional images of the types of fabric used in this research. The macrophotographs are sharp with good contrast.

With a suitable methodology for obtaining images established, the dimensions required to define the yarn's internal architecture were determined from measurements taken from captured images. Previously, only a small number of images have been measured due to limitations regarding image processing. Obtaining representative dimensions of the fabric cross sections was important to ensure accurate representations of the materials in the predictive model. Therefore, many images were required to be measured. To make the measurement of many images of fabric cross sections practicable, an automated tool with a graphical user interface (GUI) was implemented in MATLAB (Figure 5.12). The tool enables rapid and precise on-screen selection of a series of 14 predefined points (x,y coordinates), from which fabric geometry is determined. A warp cross sectional image shows the warp yarn cross section and the undulating fill yarn; a fill cross sectional image shows the fill yarn cross section and the undulating warp yarn. The tool also allows a user to rotate the image so the centreline of the undulating yarn is horizontal by performing a coordinate transformation.

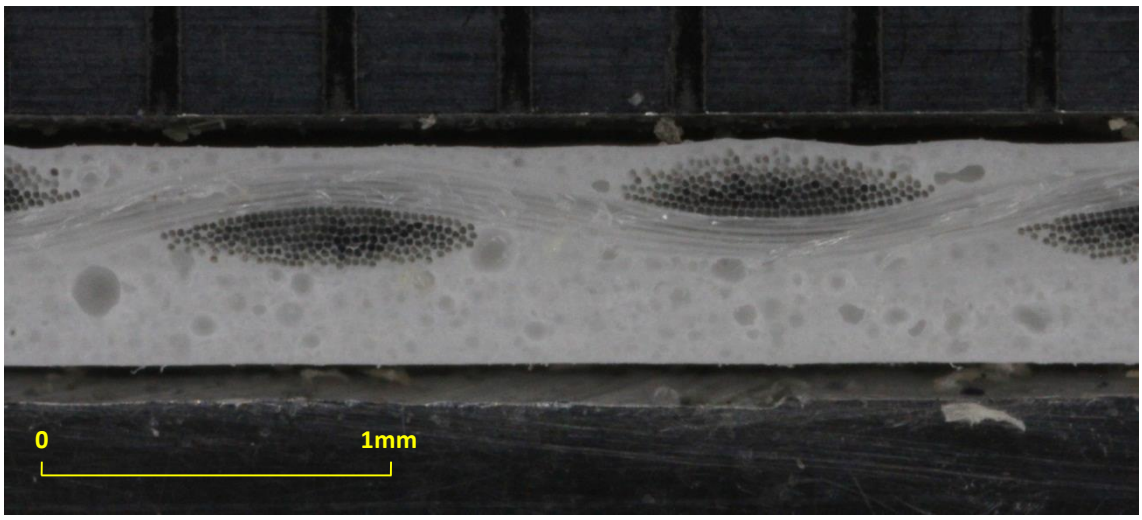

Figure 5.9 Example macrophotograph of PVC/PES fabric cross section, Ferrari 702

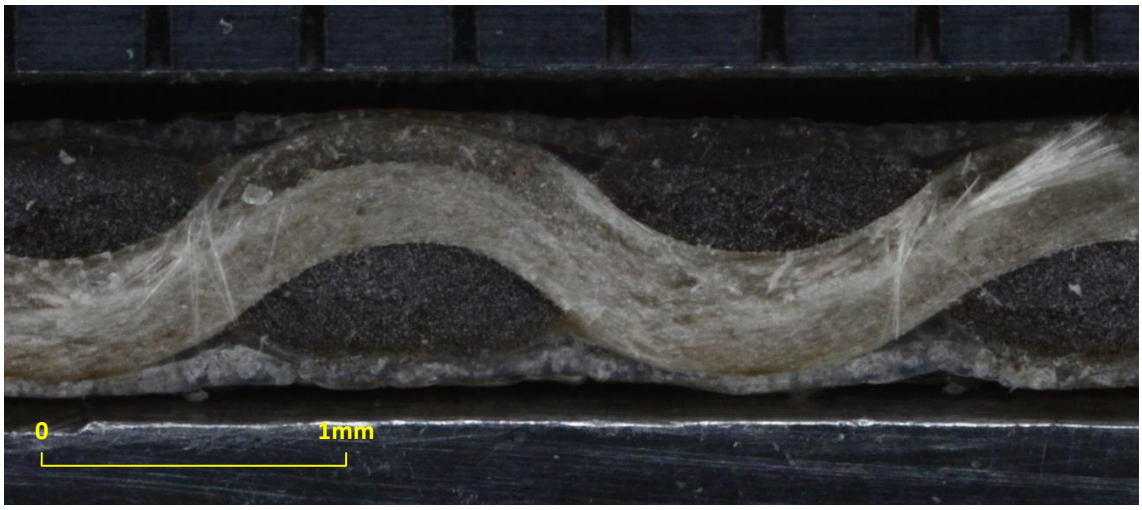

Figure 5.10 Example macrophotograph of PTFE/glass fabric cross section, Verseidag B18059

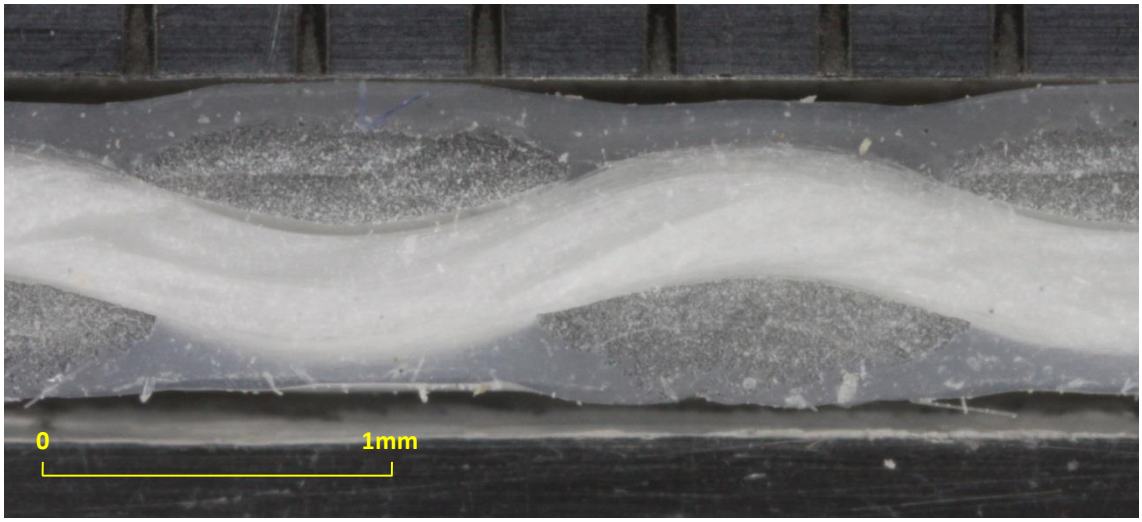

Figure 5.11 Example macrophotograph of silicone/glass fabric cross section, Interglas ATEX5000

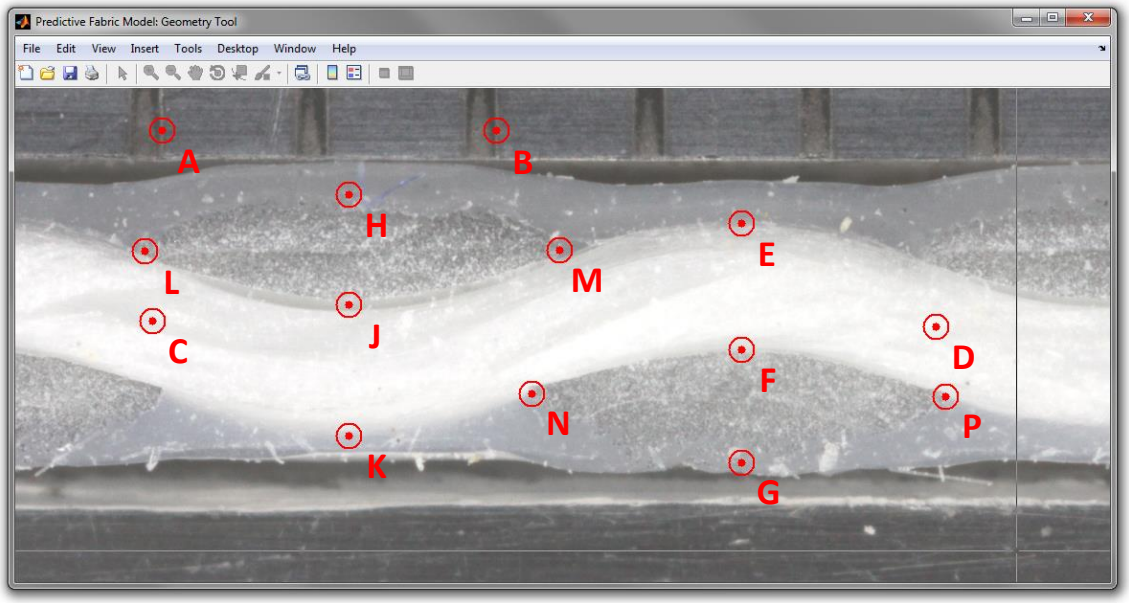

Figure 5.12 Geometry tool GUI with points that are selected to define a fabric's cross section, crosshairs (visible in the screenshot) aid point selection, note: brightness of original fabric image has been increased to aim clarity of the points

The units of the image measurements are pixels, requiring a scale factor to establish the correct dimensions in mm. A graduated steel rule forms part of the specimen mount and is visible in each image and this allows the calculation of the required factor (Equation 5.1). Crimp amplitudes are calculated from the inflection points on the undulating yarn (Equation 5.2). Points on the yarn cross sections for calculating thickness (Equation 5.3) could also be used in determining the cross section. However, the yarn cross sections visible in each image do not form part a single yarn and so they have not been used. With many images being processed, enough data will be obtained to determine the necessary dimensions. Unit cell lengths are defined by selecting the start and end of single yarn wavelength (Equation 5.4) and yarn width is taken from the visible cross sections (Equation 5.5).

$$imageScale_{1,2} = 1/(\boldsymbol{B}(x)_{1,2} - \boldsymbol{A}(x)_{1,2})$$ **Equation 5.1 (Bridgens, 2005)**

Crimp amplitude, $A_{2,1} = (\boldsymbol{J}(y)_{2,1} - \boldsymbol{E}(y)_{2,1} + \boldsymbol{K}(y)_{2,1} - \boldsymbol{F}(y)_{2,1}) / 4 * imageScale_{1,2}$ **Equation 5.2**

Yarn thickness, $t_{1,2} = (\boldsymbol{G}(y)_{1,2} - \boldsymbol{F}(y)_{1,2} + \boldsymbol{J}(y)_{1,2} - \boldsymbol{H}(y)_{1,2}) / 2 * imageScale_{1,2}$ **Equation 5.3**

Unit cell length, $l_{2,1} = (\boldsymbol{D}(x)_{2,1} - \boldsymbol{C}(x)_{2,1}) / 2 * imageScale_{1,2}$ **Equation 5.4**

Yarn width, $w_{1,2} = (\boldsymbol{M}(x)_{1,2} - \boldsymbol{L}(x)_{1,2} + \boldsymbol{P}(x)_{1,2} - \boldsymbol{N}(x)_{1,2}) / 2 * imageScale_{1,2}$ **Equation 5.5 (Bridgens, 2005)**

N.B. Bold letters denote points shown in Figure 5.12 and should not be confused with the model's nomenclature. (x) and (y) denote coordinate axes, and subscripts 1 and 2 denote warp cross sectional and fill cross sectional images, respectively.

Using the macrophotography setup and the image processing tool developed in MATLAB, 50 cross sectional images of each of the fabrics used for validation were analysed. Images were obtained in sets of five from ten specimens cut from each of the fabrics, five in the warp direction and five in the fill. The 50 measurements for each of the principal dimensions have been summarised and plotted (Table 5.3 and Figure 5.13). Boxplots of the data show the spread of the measurements for the fabrics analysed and highlight which dimensions of each fabric's weave geometry vary more widely. For example, yarn widths were observed to vary more than other dimensions and amplitudes are largely consistent. Examination of the raw data revealed that the outliers for the unit cell length, *l2,* measurements for ATEX5000 are from one of the five fabric samples, indicating that the sample may not have been representative of the fabric. This indicates, more than a single set of measurements should be used to provide the model with dimensions of the fabric geometry. Owing to skew and outliers observed in the measurements for some of the dimensions, the median values were chosen to be used when running the model, as they are more representative of the measurements than mean values.

An alternative could be to perfect a cutting methodology to provide a single representative image of the fabric cross section. However, it would be unrealistic to expect such an approach to yield repeatable results. While care can be taken when preparing a specimen to be photographed, some variation is to be expected and is likely to occur due to human error during measurement and disturbance of the yarn when the sample is cut.

Table 5.3 Summary of fabric measurements for all fabrics obtained from macrophotography

Fabric type		A_1	A_2	l_1	l_2	w_1	w_2	t_1	t_2
Ferrari 702 (PVC/PES)	*Mean*	0.064	0.077	1.249	1.222	0.911	1.128	0.183	0.149
	Median	0.063	0.078	1.250	1.221	0.911	1.129	0.183	0.146
	S.D.	0.008	0.007	0.025	0.023	0.032	0.051	0.010	0.011
Ferrari 1202 (PVC/PES)	*Mean*	0.066	0.197	1.289	2.163	1.568	1.344	0.338	0.237
	Median	0.066	0.199	1.290	2.163	1.571	1.345	0.337	0.237
	S.D.	0.009	0.011	0.016	0.039	0.040	0.033	0.016	0.014
Verseidag B18089 (PTFE/glass)	*Mean*	0.116	0.144	1.000	0.847	0.827	0.733	0.264	0.276
	Median	0.115	0.143	0.996	0.843	0.828	0.731	0.263	0.273
	S.D.	0.010	0.009	0.018	0.017	0.018	0.025	0.013	0.014
Verseidag B18059 (PTFE/glass)	*Mean*	0.210	0.219	1.447	1.150	1.040	1.031	0.407	0.459
	Median	0.207	0.219	1.452	1.149	1.033	1.024	0.403	0.455
	S.D.	0.024	0.015	0.028	0.022	0.035	0.058	0.026	0.040
Interglas ATEX3000 (Silicone/glass)	*Mean*	0.083	0.073	0.902	0.782	0.728	0.672	0.172	0.179
	Median	0.083	0.070	0.899	0.778	0.731	0.669	0.171	0.180
	S.D.	0.014	0.013	0.018	0.021	0.031	0.026	0.016	0.011
Interglas ATEX5000 (Silicone/glass)	*Mean*	0.182	0.141	1.363	1.191	1.133	1.033	0.357	0.366
	Median	0.183	0.137	1.359	1.169	1.127	1.035	0.362	0.365
	S.D.	0.010	0.023	0.020	0.069	0.055	0.031	0.028	0.013

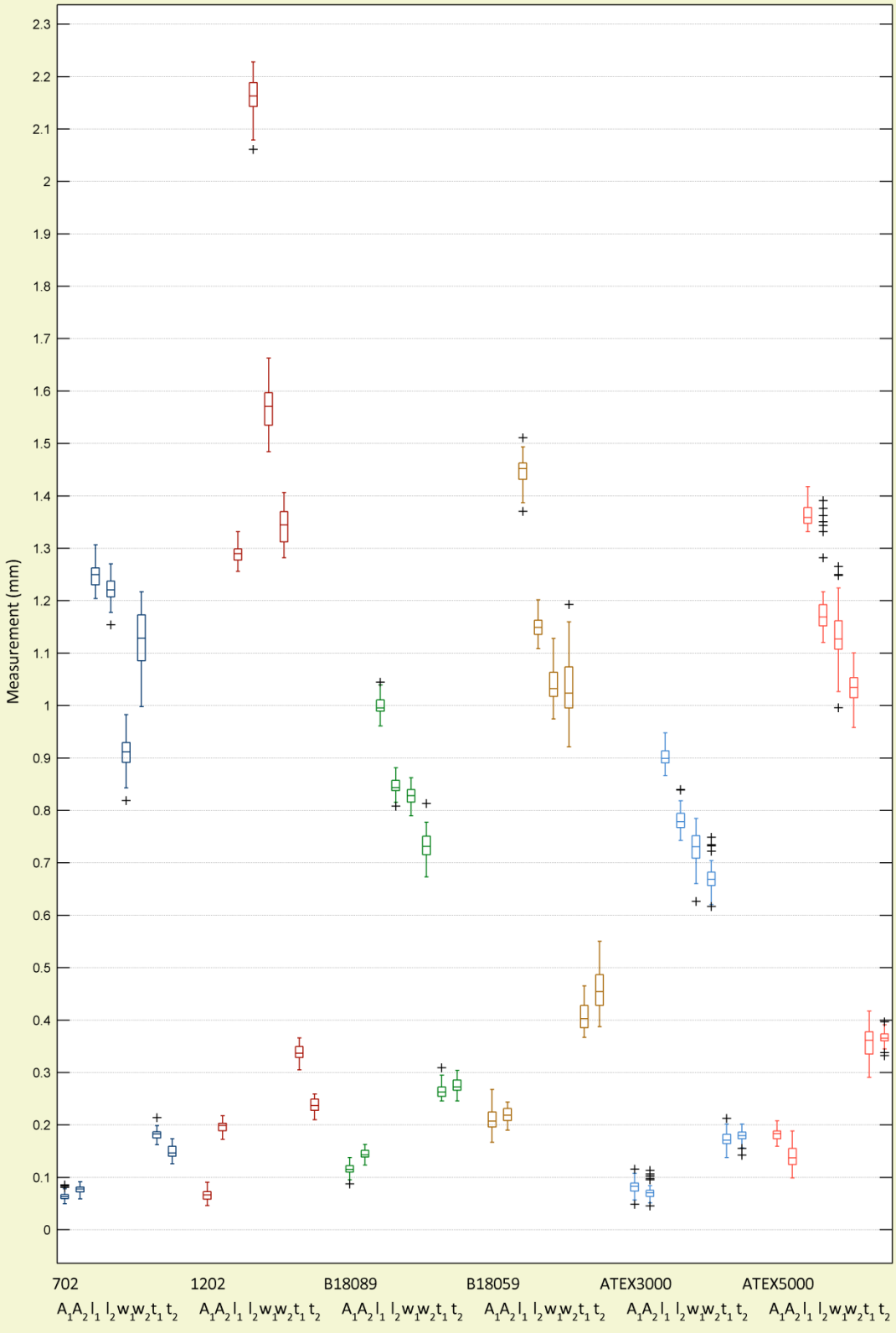

Figure 5.13 Boxplots of fabric measurements for all fabrics obtained using macrophotography, boxes indicate the upper and lower quartiles of the measurements with the mean value indicated by a horizontal bar, variability outside the upper and lower quartiles is illustrated by the vertical lines ("whiskers") and outliers are shown in black

5.3 Comparative test data

The predictive model has been developed to provide information to designers that would otherwise be obtained through experimental testing. Model predictions were compared to experimentally obtained results produced by following a test protocol that a designer may specify to determine design values. Biaxial tensile testing is conducted for the purpose of determining design values, namely elastic constants and Poisson's ratios. As no British or European standards exist for the biaxial testing of architectural fabrics, the biaxial testing conducted to provide comparative test data is based upon a single available international standard MSAJ (1995) and previously published work (Blum and Bögner, 2001; Blum *et al.*, 2004; Bridgens and Gosling, 2004; Bridgens, 2005).

5.3.1 Biaxial test rig and specimen preparation

A 'floating' biaxial test rig (§2.2.1) has been used to perform all the biaxial testing undertaken in the course of this research project. The design of the rig used allows each of the loading axes of the rig to be aligned with the warp and fill axes of a specimen where the angle between the warp and fill yarn directions is not necessarily orthogonal (Skelton and Freeston, 1971). As load is applied to the specimen, the axes of the floating upper frame will both translate and rotate, to provide balanced loading of the specimen, relative to the lower frame. This ensures the axis of the applied loads coincide with the warp and fill yarn directions (Figure 5.14). The purpose of this approach is to not introduce shear effects. The test rig can be load controlled or displacement controlled. Applied loads are measured with load cells positioned at the ends of the actuators. Strains were calculated from displacements measured be extensometers mounted on the surface of the fabric, in the same way as for the shear testing (§3.3.2). Loads and displacements are recorded every two seconds.

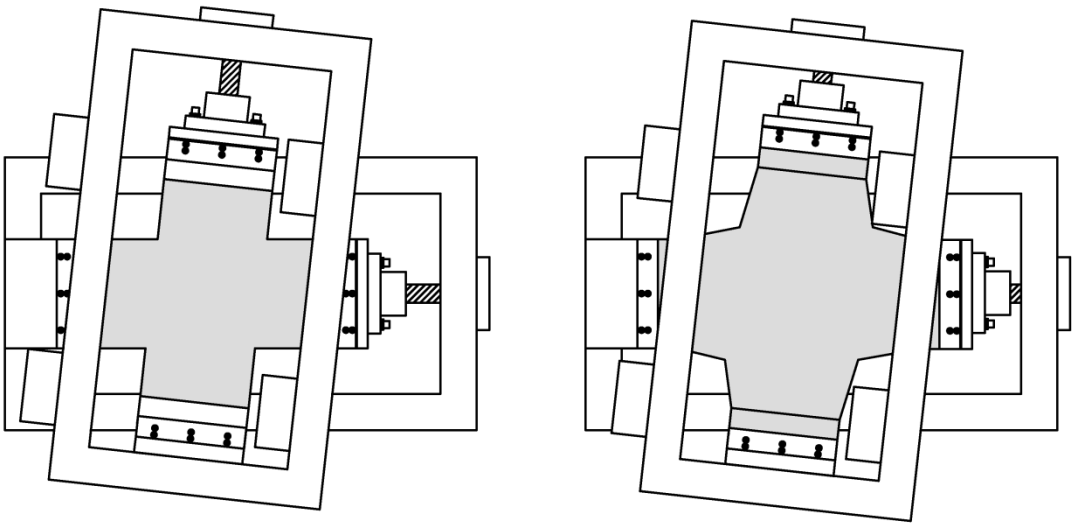

Figure 5.14 Biaxial test rig with frame aligned with yarn direction, (left) before application of load and (right) with load applied to the specimen

5.3.2 Biaxial load profile

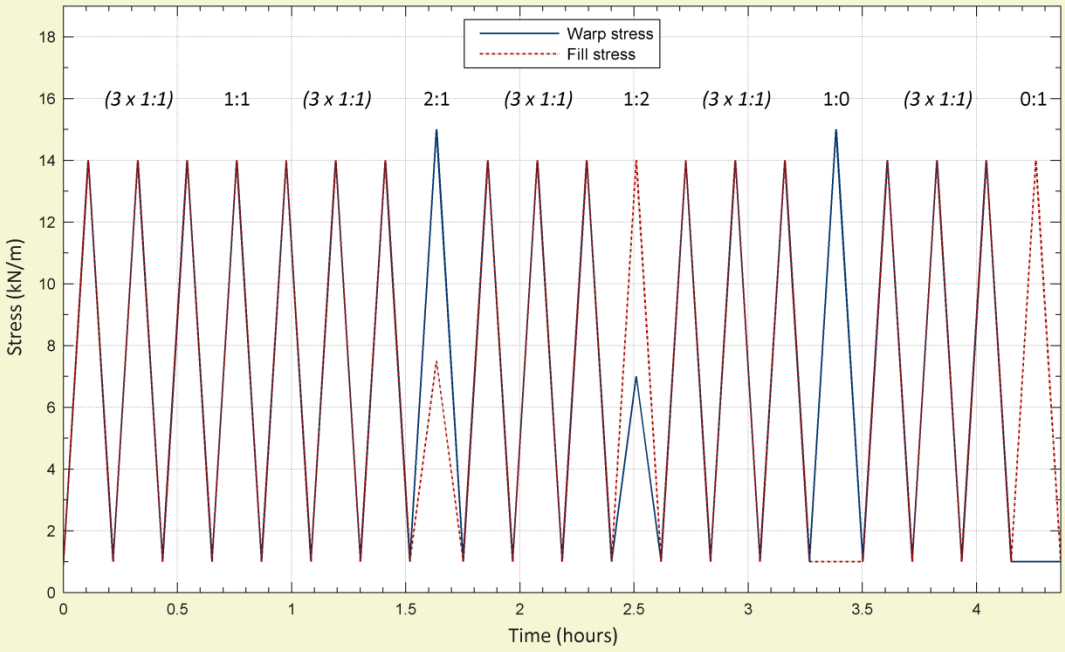

Figure 5.15 Membrane Structures Association of Japan (MSAJ) biaxial test profile showing load cycles, profile shown is for Ferrari 702 (PVC/PES) fabric, conditioning cycles in italics, minimum load is equal to prestress

The load profile used was intended to reflect those which are currently used in industry, such as the profile described in the Membrane Structures Association of Japan (MSAJ) test standard for determining elastic constants of membrane materials (MSAJ, 1995). The standard presents a method for applying load to a biaxial cruciform specimen in both axes for multiple sets of cycles at different load ratios/stress states: 1:1, 2:1, 1:2, 1:0 and 0:1 (Figure 5.15). The stress-strain relationship at each different load ratio is then used to determine elastic constants for the test specimen. Similar methodologies used in industry also exist (Blum *et al.*, 2004).

A revised version of the MSAJ biaxial test profile was used to obtain comparative test data for the validation of the predictive model (Figure 5.16). Cycling the applied load for each of the different stress states was included in the profile in order to mechanically condition the specimen (Bridgens, 2005). Conditioning results in the same strains being exhibited in the fabric for repeated cycles a given stress state. This process ensures that the behaviour used to calculate an elastic constant is not the initial behaviour, but the behaviour that more closely represents the medium to long term response of a fabric in service, e.g. wind and snow acting on a fabric structure. This is important as it is medium to long term behaviour that is considered when a designing fabric structure.

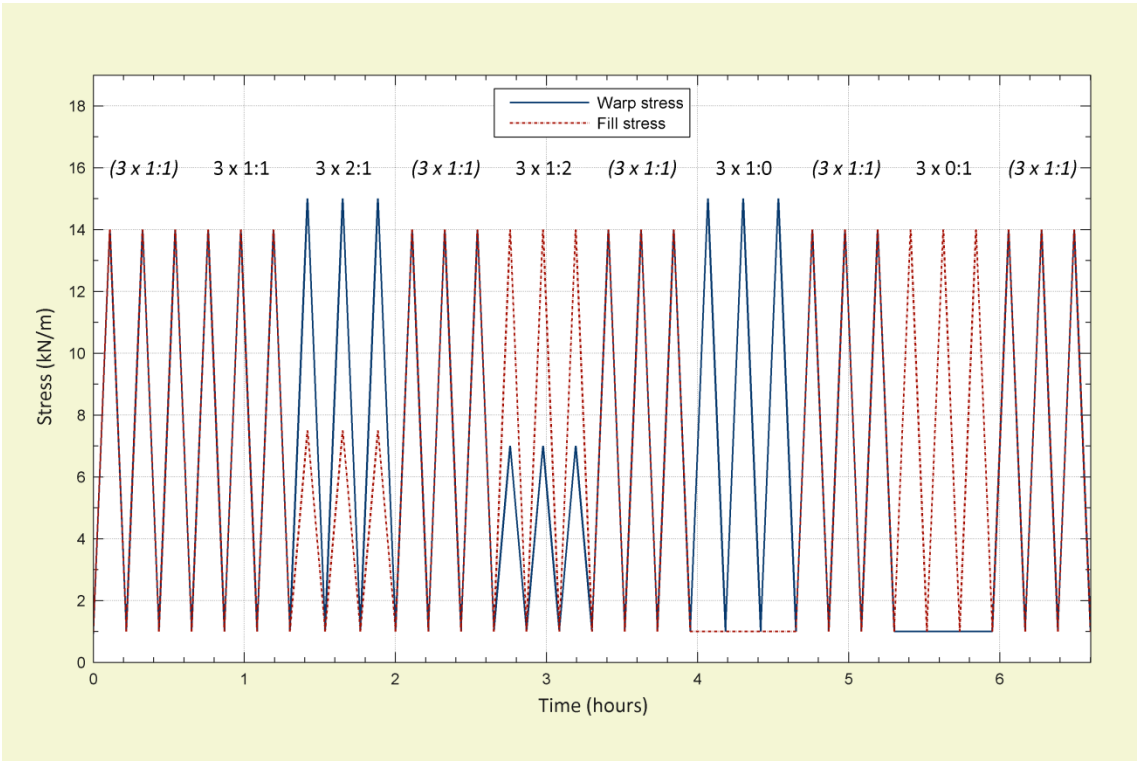

Figure 5.16 Modified Membrane Structures Association of Japan (MSAJ) biaxial test profile showing load cycles, profile shown is for Ferrari 702 (PVC/PES) fabric, conditioning cycles in italics

Sets of cycles at the 1:1 load ratio are repeated between each of the non 1:1 load ratios. By performing the tests in this way, the stress-strain behaviour for one set of non 1:1 cycles are not influenced by a preceding set of non 1:1 cycles (Bridgens, 2005). This allows for multiple biaxial stress ratios to be applied to a single test specimen.

Load is controlled during a biaxial test because the ranges of stress are known and the ranges of strains are unknown. Minimum and maximum loads in both yarn directions for each fabric were determined to create the load profile for each of the fabrics tested (Table 5.4). Typically, biaxial tests are performed to a maximum stress of 25% of the ultimate tensile strength (UTS) of the material being tested, as this is approximately the level of stress at which tear propagation occurs (Happold *et al.*, 1987) and is therefore the maximum value that would be allowed in design. This criterion was applied to the testing performed and the profile increases the stress to a value not exceeding 25% of the UTS in either the warp or fill directions. Note that the maximum stress can vary between load ratios when a fabric has different UTSs in the warp and fill.

The load is then returned to the minimum stress, which is no less than 1% of the UTS in the weaker of the warp or fill directions, or a minimum stress of 1kN/m. The 1kN/m limit upon the minimum stress was imposed by the capabilities of the test rig used. The minimum load the test rig is capable of maintaining in each axis is 0.25kN which, owing to the dimensions of the specimens, is equivalent to a stress 0.83kN/m. This value was rounded to 1kN/m to ensure that the applied load stayed in the range of values that could be stabilised by the test rig.

Table 5.4 Determining minimum and maximum biaxial loading for load ratios

Fabric	Yarn direction	UTS (kN/m)	1% UTS (kN/m)	25% UTS (kN/m)	Min. load (kN/m)	Max. load (kN/m)	Duration (Hours)
702	Warp	60	0.60	15	**1.00**	**15**	6.6
	Fill	56	0.56	14		**14**	
1202	Warp	112	1.12	28	**1.12**	**28**	13.4
	Fill	112	1.12	28		**28**	
B18089	Warp	140	1.40	35	**1.20**	**35**	14.8
	Fill	120	1.20	30		**30**	
B18059	Warp	160	1.60	40	**1.40**	**40**	17.2
	Fill	140	1.40	35		**35**	
ATEX3000	Warp	60	0.60	15	**1.00**	**15**	7.0
	Fill	60	0.60	15		**15**	
ATEX5000	Warp	100	1.00	25	**1.00**	**25**	12.0
	Fill	100	1.00	25		**25**	

Load rates in each yarn direction will differ as the maximum load applied to each axis in a single cycle can differ. To ensure a consistent stress strain response at different rates (§5.2.1), a load rate of 2kN/m per min in the axis undergoing loading to 25% UTS was applied to all tests. This loading rate was chosen as it results in a low displacement rate (i.e. below 50mm/min) for all fabrics tested. This loading rate resulted in individual cycle times of between 7 and 15 minutes, depending on the fabric.

Careful manual loading of the test specimen was required up to the 1kN/m value. However, by performing this procedure, strain is not zero at the start of the test profile, as a small amount of strain will occur at 1kN/m of stress. As the data is to be used for comparison with the model, the magnitudes of the strains are important and it is not appropriate to use an arbitrary value of strain which can be used when it is only the gradient that is of interest. Therefore, it was necessary to record a value of displacement which corresponded to zero strain at zero load before the loading of the specimen up to 1kN/m. This value of displacement was then used in calculating the strains during the test.

A load factor of 0.95 was required to adjust the applied load to ensure the level of stress in the centre of the specimen is as expected (Bridgens, 2005). This factor is required to account for higher biaxial stress around the periphery of the specimen, i.e. a variation over the surface of the specimen, which is caused by the arms of the specimen. While slits cut in the arms of specimen reduce this variation of stress, the load applied during testing must be adjusted to account for any variation, which is determined using an FE model for each specimen size (Bridgens, 2005).

Three biaxial tests were performed on each of the six different fabrics to ensure that the data was representative of the materials, i.e. did not contain experimental error. Testing was conducted at 23°C ± 0.5°C and 50% ± 1% relative humidity in a room with environmental controls. Results of all of the tests are included in the Appendices.

5.4 Model output

5.4.1 Evaluating model output

The model was run for data points over all cycles recorded during a biaxial test performed on each of the six fabrics. Comparative time-strain plots for the test data and the model output provide a good visual assessment of the quality of the models (Figure 5.17 – Figure 5.24). Time-strain, as opposed to stress-strain plots, help to draw visual comparisons between the model results and test data. Comparisons have been made both with and without residual strain included in consecutive cycles. Residual strains have been removed by a process of 1) subtracting the value of strain observed or predicted at the first point in a given load cycle from every point in the cycle, and 2) subtracting a proportion of the difference between the strains at the start and end of each load cycle from every point in the cycle. Therefore, the first and last point of each cycle is set to zero strain.

The time-strain plots provide an overview of the results for all model formulations, allowing comparison between the formulations by comparing the magnitude of the strains for given stress ratios. The magnitude of the strains at any point in the profile can be compared between the test data and model outputs. It is these plots that will allow the success of the look-up function to be observed, as hysteresis is present in the plots of test results and model output. Presenting the results in this manner also allows the relative magnitude of the strains between different load ratios to be compared, determining whether increases seen in test data are comparable to increases in model predictions.

A numerical assessment has also been performed which provides a quantitative means to examine the models' predictions of stress-strain behaviour by comparing the magnitude of strains. A numerical comparison of the results obtained using the different formulations allows for assessment of the quality of the model between cycles at different load ratios, yarn directions, fabrics tested and results overall. This is particularly useful should results include good and poor predictions at different load ratios as it can help identify particular load conditions where model performance is more accurate compared to others. Root mean square error (RMSE) values (Equation 5.6) have been calculated to provide a measure of quality of the model's output and to compare the predictions between the different model formulations. Normalised root mean square error (NRMSE) allows for comparison between the results of different fabric types and yarn directions as results are normalised over the range of strains exhibited by the tested material in each yarn direction.

$$RMSE = \sqrt{\frac{\sum_1^n (\varepsilon_{test} - \varepsilon_{model})^2}{n}} \qquad \textbf{Equation 5.6}$$

where n = total number of strain values being compared, ε_{test} = measured strains obtained from test data, and ε_{model} = predicted strains

Response surfaces (Figure 5.25 – Figure 5.30) have also been used to visualise the predicted data. As the models generate stress-strain response at a number of different load ratios, response surfaces offer a means to visualise the data in a single plot. However, when viewing the surfaces, it is important to note that values of strain corresponding to stresses between the ratios actually recorded during testing are derived by interpolating between the recorded strains. This approximation may not be representative of the true fabric behaviour and the surface may be misleading. Calculating differences in strains from interpolated values would not provide a reliable means of comparison, thus the time-strain plots used for this purpose. However, response surfaces are useful for comparing the relative error of the stress-stress-strain interaction between test data and predicted data.

Surfaces presented here have been generated using the loading half of the third cycle in each cycle set at the five different load ratios: 1:1, 2:1, 1:1, 1:0 and 0:1. Mean values of the loading and unloading predictions and test data have been used to compare results in this way (Bridgens, 2005). However, an approach using mean values was not used as the novel non-linear (look-up) formulation predicts loading and unloading differently unlike the linear model formulations. Comparison of loading data was chosen over unloading (or both) as it is loading data that is typically used in design.

5.4.2 Comparison with test data and previous predictive models

The predicted strain histories for the Ferrari 702 and 1202 PVC/PES fabrics (Figure 5.17 and Figure 5.18) appear very well correlated with test data for all model formulations. The correlation that is observed between the test data and predictions made by the final (look-up model) formulation is extremely good for both of the PVC/PES fabrics tested. The model is performing the novel function of predicting the non-linear load response and hysteresis of the materials. The 702 fill and 1202 warp strains are especially well correlated with test data, where the model has performed well in predicting the initial loading curve.

The accuracy of the look up model in predicting the residual strain must be emphasised. Comparisons of the initial 1:1 cycles show that the magnitude of the residual strains occurring during biaxial testing is replicated in the model's predictions for the Ferrari PVC/PES fabrics (Figure 5.19 and Figure 5.20). Existing linear models cannot do this. However, if the look-up model is unable to replicate the residual strain in the first cycle then the accuracy of the model in subsequent cycles is reduced. With accurate prediction of the initial load cycle, agreement of residual strains for subsequent cycles is highly accurate. This is demonstrated by matching the observed and predicted strains at the end of the first cycle and then comparing the residuals for the subsequent cycles (Table 5.7). Values of strain are small, ranging from 0.7% to 7.4% of the maximum strain recorded during testing for the initial cycles compared. Note that these values are absolute error expressed as a percentage of the range, not NRMSE values.

Comparing the calculated RMSE values confirms the observation made of the visual results for the PVC/PES fabrics (Table 5.5 and Table 5.6). Without removing the residual strain from the model predictions and test results, the final model formulation is more accurate than the two linear formulations. For example, NRMSE values for the entire fill strain history for Ferrari 702 is only 6.8% compared to 39.7% and 38.2% for the linear sinusoidal and sawtooth representations, respectively. Note that the two linear yarn stiffness models cannot predict the large strain encountered in the initial loading cycle. The RMSE/NRMSE values for the final look-up model formulation are influenced by the model's accuracy in predicting the initial loading curve.

An alternative comparison of the different formulations can be made with the residual strain removed. This assesses model accuracy at different load ratios and for all cycles after the first cycle. This will improve the observed accuracy of linear model formulations.

The NRMSE values calculated for the entire test profile indicate that the sawtooth and linear sinusoidal model formulations are more accurate when compared to the final formulation *if residual strains are removed*. For both the PVC/PES fabrics, the predictions are well correlated with the experimentally obtained data for the load ratios other than the 1:0 and 0:1 in both the warp and fill yarn directions. The inaccuracy of the final formulation overall can be attributed to its predictions of negative strains at 1:0 and 0:1 load ratios, where the NRSME values can be seen to be high for the final model (see highlighted values in Table 5.5 and Table 5.6). The result indicates that the final formulation is not replicating the mechanisms that resists compression in the yarn directions, but that is represented in the liner formulations, for example compression of the coating or compression of the yarns.

It should be noted that the linear formulations also make good strain predictions despite the best fit input data they rely upon. NRMSE values for the linear yarn stiffness models range between 9.3% and 11.1%. The linear formulations more accurately predict negative strains during the 1:0 and 0:1 load ratios in three of the four instances such strains occur for the two materials.

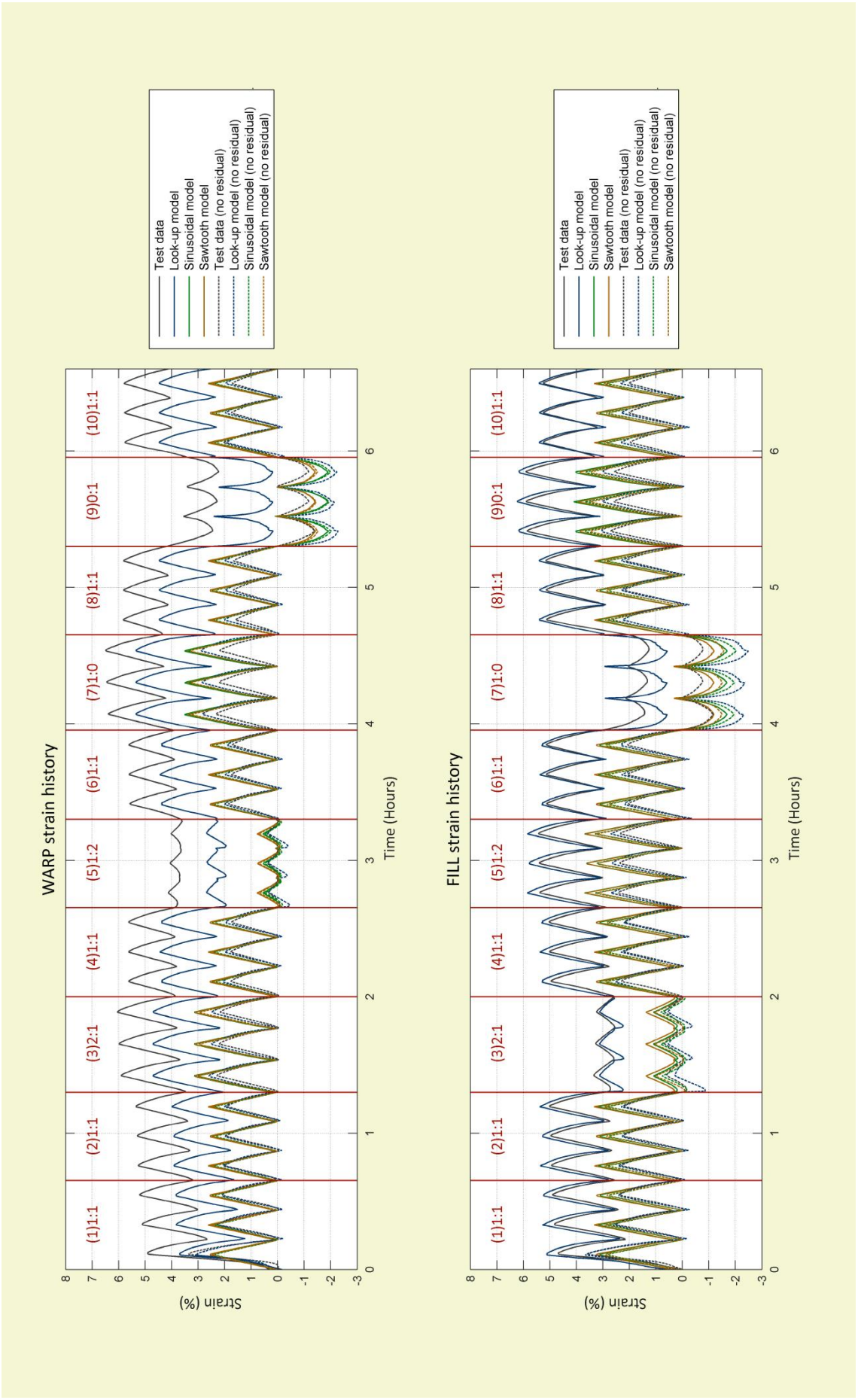

Figure 5.17 Comparison with test and model data for Ferrari 702 (PVC/PES)

Table 5.5 Comparison of test and model data for Ferrari 702 (PVC/PES), Root Mean Square Error (RMSE) (percentage strain) and Root Mean Square Error Normalised over the range of strains (NRMSE) (percentage of range)

	Load cycle →	*1*	2	3	*4*	5	*6*	7	*8*	9	*10*	All	All'[†]
	Load ratio (w:f) →	*1:1*	1:1	2:1	*1:1*	1:2	*1:1*	1:0	*1:1*	0:1	*1:1*	-	-
LOOK-UP MODEL													
1) Raw data													
Warp	RMSE	*1.2*	1.3	1.3	*1.3*	1.5	*1.2*	1.2	*1.5*	2.1	*1.4*	**1.4**	1.3
	NRMSE	*18.7*	21.7	20.3	*20.6*	23.8	*20.0*	18.6	*23.9*	33.6	*21.8*	**22.6**	21.4
Fill	RMSE	*0.5*	0.4	0.2	*0.4*	0.4	*0.2*	0.7	*0.4*	0.4	*0.2*	**0.4**	0.4
	NRMSE	*8.5*	6.8	3.7	*6.8*	7.4	*3.7*	11.1	*6.0*	6.5	*2.8*	**6.8**	6.0
2) Residual strain removed (No residual)													
Warp	RMSE	*0.2*	0.1	0.3	*0.2*	0.2	*0.2*	0.6	*0.3*	0.9	*0.2*	**0.4**	0.2
	NRMSE	*3.5*	2.4	7.0	*4.9*	3.4	*4.0*	12.7	*5.8*	19.2	*3.9*	**8.4**	4.6
Fill	RMSE	*0.2*	0.1	0.3	*0.2*	0.3	*0.2*	1.3	*0.2*	0.5	*0.3*	**0.5**	0.2
	NRMSE	*3.9*	3.0	5.8	*4.9*	6.8	*4.9*	27.1	*4.6*	10.0	*5.8*	**10.5**	5.1
SINUSOIDAL MODEL													
1) Raw data													
Warp	RMSE	*2.6*	3.1	3.2	*3.5*	3.7	*3.5*	3.4	*3.7*	4.1	*3.6*	**3.4**	3.4
	NRMSE	*41.9*	49.5	51.2	*56.2*	59.3	*55.7*	54.5	*60.0*	66.3	*58.1*	**55.5**	54.2
Fill	RMSE	*1.8*	2.2	2.4	*2.2*	2.2	*2.4*	2.8	*2.3*	2.3	*2.6*	**2.3**	2.3
	NRMSE	*31.3*	36.9	40.7	*37.7*	37.2	*41.2*	47.5	*39.7*	38.8	*43.6*	**39.7**	38.7
2) Residual strain removed (No residual)													
Warp	RMSE	*0.5*	0.3	0.5	*0.4*	0.1	*0.4*	0.8	*0.4*	0.6	*0.3*	**0.5**	0.4
	NRMSE	*10.9*	6.2	10.9	*7.4*	2.0	*7.3*	16.0	*9.0*	13.6	*6.4*	**9.9**	8.1
Fill	RMSE	*0.5*	0.4	0.1	*0.4*	0.6	*0.4*	0.9	*0.3*	0.7	*0.5*	**0.5**	0.4
	NRMSE	*10.2*	7.8	2.8	*8.3*	12.1	*9.3*	18.8	*7.1*	15.2	*10.3*	**11.1**	8.9
SAWTOOTH MODEL													
1) Raw data													
Warp	RMSE	2.6	3.0	3.2	3.4	3.5	3.4	3.5	3.7	3.8	3.6	**3.4**	3.3
	NRMSE	41.3	49.0	51.9	55.7	57.1	55.2	56.1	59.4	61.3	57.5	**54.7**	53.6
Fill	RMSE	1.8	2.1	2.2	2.1	2.2	2.3	2.4	2.3	2.4	2.5	**2.2**	2.2
	NRMSE	30.1	35.6	37.3	36.4	37.9	39.8	41.5	38.4	41.1	42.2	**38.2**	37.3
2) Residual strain removed (No residual)													
Warp	RMSE	0.5	0.3	0.5	0.4	0.2	0.4	0.7	0.5	0.3	0.4	**0.4**	0.4
	NRMSE	10.8	7.1	10.4	8.5	3.5	8.4	14.4	10.1	6.8	7.5	**9.3**	8.6
Fill	RMSE	0.5	0.4	0.2	0.4	0.5	0.5	0.6	0.4	0.6	0.5	**0.5**	0.4
	NRMSE	10.2	8.8	4.3	9.2	10.9	10.5	12.1	7.9	11.9	11.3	**10.0**	9.4

All'[†] = All strain data modified so not to include 1:0 and 0:1 load ratio data

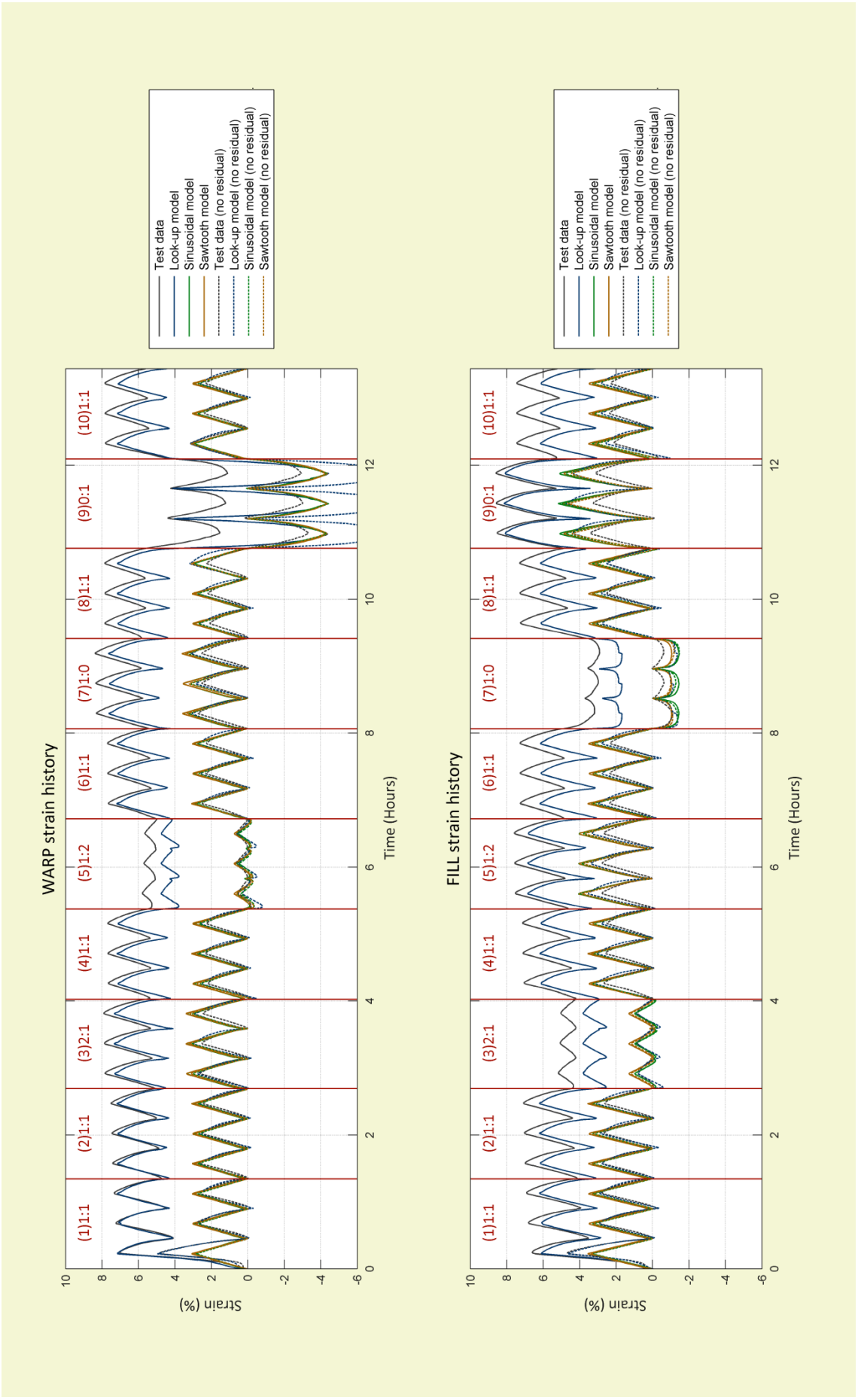

Figure 5.18 Comparison with test and model data for Ferrari 1202 (PVC/PES)

Table 5.6 Comparison of test and model data for Ferrari 1202 (PVC/PES), Root Mean Square Error (RMSE) (percentage strain) and Root Mean Square Error Normalised over the range of strains (NRMSE) (percentage of range)

Load cycle →		*1*	2	3	*4*	5	*6*	7	*8*	9	*10*	All	All'†
Load ratio (w:f) →		*1:1*	**1:1**	**2:1**	*1:1*	**1:2**	*1:1*	**1:0**	*1:1*	**0:1**	*1:1*	-	-
LOOK-UP MODEL													
1) Raw data													
Warp	RMSE	*0.2*	0.3	0.6	*0.6*	1.1	*0.6*	0.8	*0.9*	4.6	*0.7*	**1.6**	0.7
	NRMSE	*2.5*	3.9	7.0	*7.7*	12.6	*7.4*	9.2	*10.5*	55.2	*8.7*	**19.1**	8.1
Fill	RMSE	*0.6*	0.9	1.4	*1.0*	0.8	*1.3*	1.4	*1.1*	0.6	*1.5*	**1.1**	1.1
	NRMSE	*6.8*	10.3	16.4	*11.7*	9.8	*14.9*	16.5	*13.5*	7.1	*17.4*	**13.0**	13.0
2) Residual strain removed (No residual)													
Warp	RMSE	*0.2*	0.2	0.4	*0.3*	0.3	*0.3*	0.4	*0.6*	4.2	*0.3*	**1.4**	0.3
	NRMSE	*2.1*	2.4	4.8	*3.5*	3.4	*3.9*	5.1	*7.4*	51.0	*3.1*	**16.6**	4.1
Fill	RMSE	*0.2*	0.3	0.2	*0.4*	0.6	*0.4*	0.6	*0.2*	1.2	*0.4*	**0.5**	0.4
	NRMSE	*3.0*	4.9	2.8	*7.1*	10.9	*7.1*	9.8	*4.0*	20.8	*7.0*	**9.3**	6.4
SINUSOIDAL MODEL													
1) Raw data													
Warp	RMSE	*4.1*	4.7	4.8	*5.0*	5.2	*5.0*	5.0	*5.2*	5.2	*5.1*	**4.9**	4.9
	NRMSE	*48.7*	56.2	57.0	*59.9*	62.5	*59.7*	60.5	*62.6*	62.0	*60.9*	**59.1**	58.6
Fill	RMSE	*3.6*	4.1	4.4	*4.2*	4.1	*4.5*	4.5	*4.4*	4.1	*4.7*	**4.3**	4.2
	NRMSE	*41.8*	48.5	51.4	*49.6*	47.8	*52.8*	52.9	*51.5*	48.6	*55.4*	**50.1**	50.0
2) Residual strain removed (No residual)													
Warp	RMSE	*0.8*	0.3	0.4	*0.3*	0.3	*0.3*	0.5	*0.4*	0.9	*0.3*	**0.5**	0.4
	NRMSE	*10.1*	3.7	5.1	*3.6*	3.1	*3.5*	5.8	*4.9*	10.7	*3.6*	**6.0**	5.2
Fill	RMSE	*0.7*	0.4	0.2	*0.4*	0.7	*0.5*	0.6	*0.4*	1.0	*0.5*	**0.6**	0.5
	NRMSE	*12.8*	6.9	3.3	*7.6*	12.7	*8.5*	11.1	*6.4*	17.8	*8.7*	**10.4**	8.9
SAWTOOTH MODEL													
1) Raw data													
Warp	RMSE	*4.1*	4.7	4.8	*5.0*	5.2	*5.0*	5.1	*5.2*	5.4	*5.1*	**5.0**	4.9
	NRMSE	*48.8*	56.3	57.5	*60.1*	62.1	*59.9*	61.1	*62.8*	64.2	*61.0*	**59.5**	58.7
Fill	RMSE	*3.4*	3.9	4.1	*4.0*	4.0	*4.3*	4.2	*4.2*	4.2	*4.5*	**4.1**	4.1
	NRMSE	*39.9*	46.5	48.1	*47.5*	47.7	*50.8*	48.9	*49.5*	49.8	*53.4*	**48.3**	48.0
2) Residual strain removed (No residual)													
Warp	RMSE	*0.8*	0.3	0.5	*0.4*	0.2	*0.4*	0.5	*0.5*	1.0	*0.3*	**0.5**	0.4
	NRMSE	*9.7*	4.1	5.5	*4.5*	2.2	*4.3*	6.2	*5.9*	11.7	*3.9*	**6.4**	5.4
Fill	RMSE	*0.7*	0.4	0.2	*0.5*	0.7	*0.6*	0.4	*0.4*	0.8	*0.6*	**0.6**	0.5
	NRMSE	*12.5*	7.6	3.4	*8.3*	11.3	*9.5*	7.4	*6.8*	14.2	*9.9*	**9.6**	9.1

All'† = All strain data modified so not to include 1:0 and 0:1 load ratio data

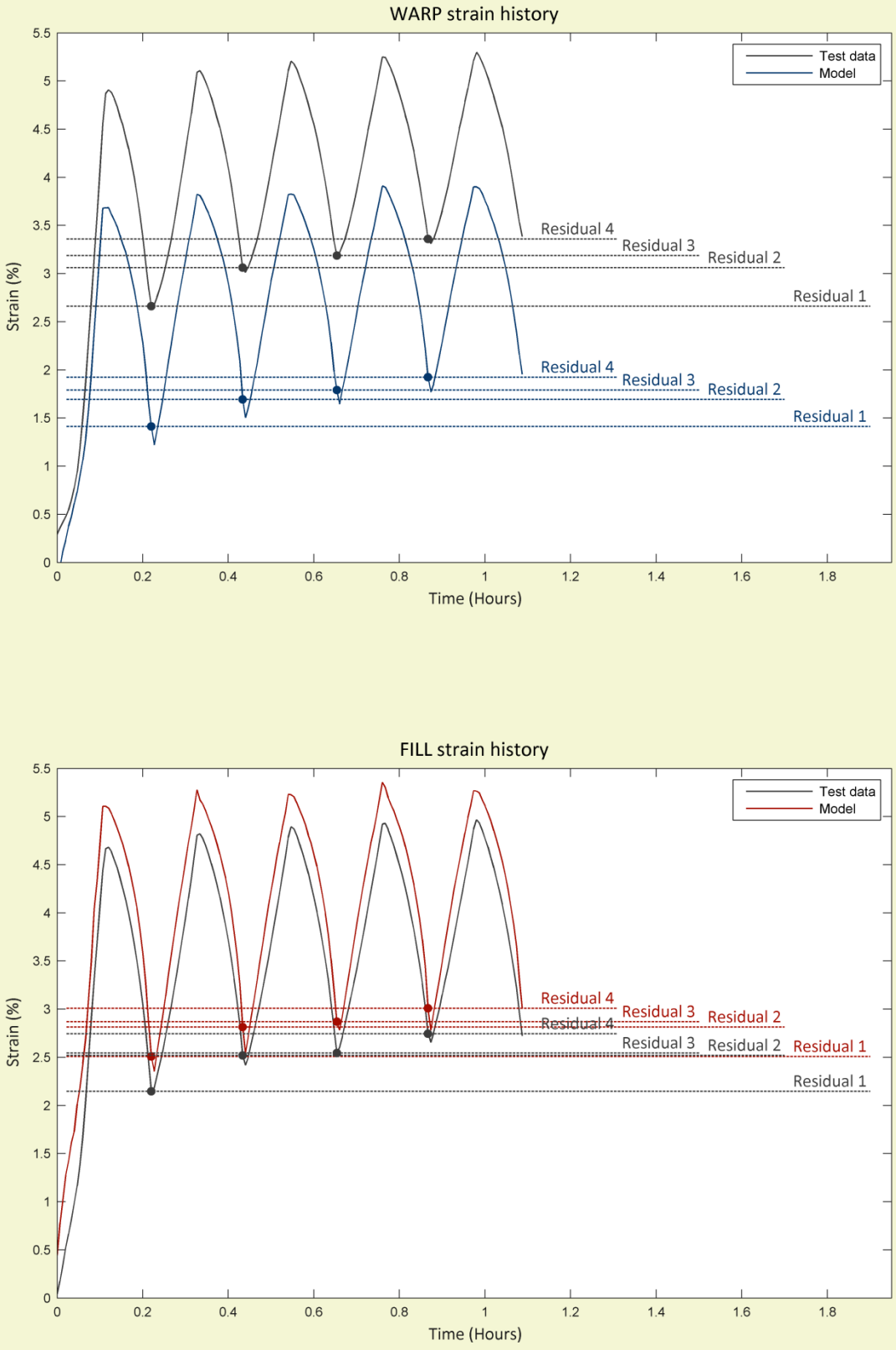

Figure 5.19 Initial load cycles for 702 (PVC/PES) indicating increasing residual strain

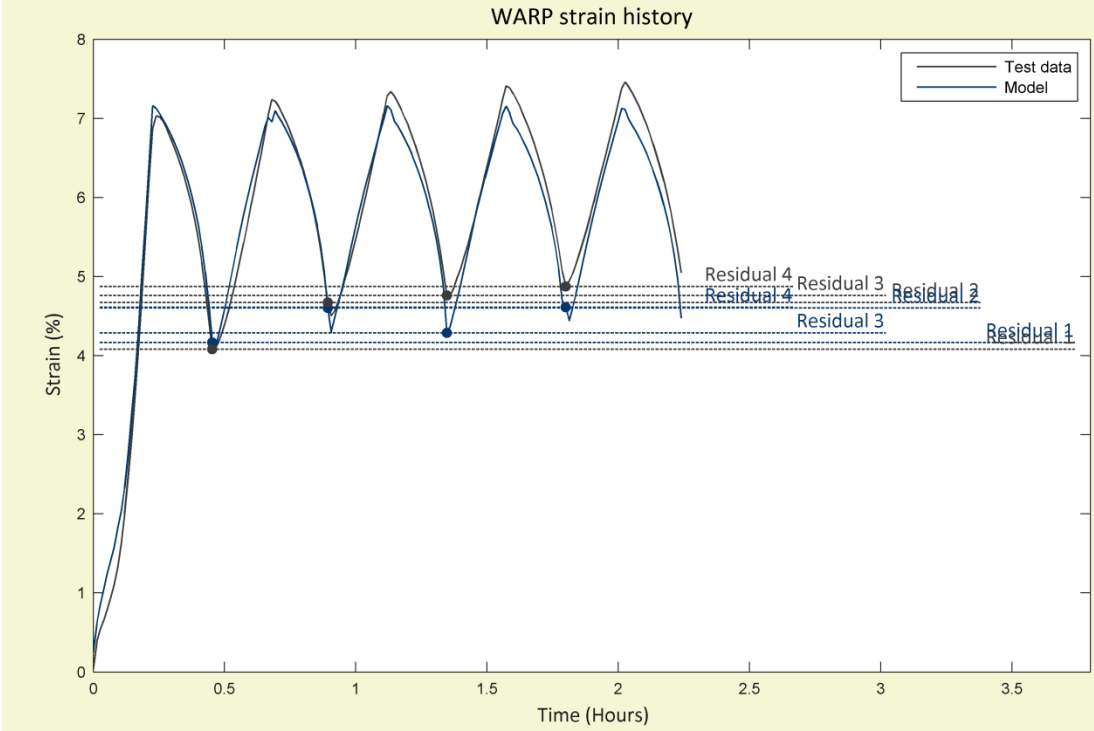

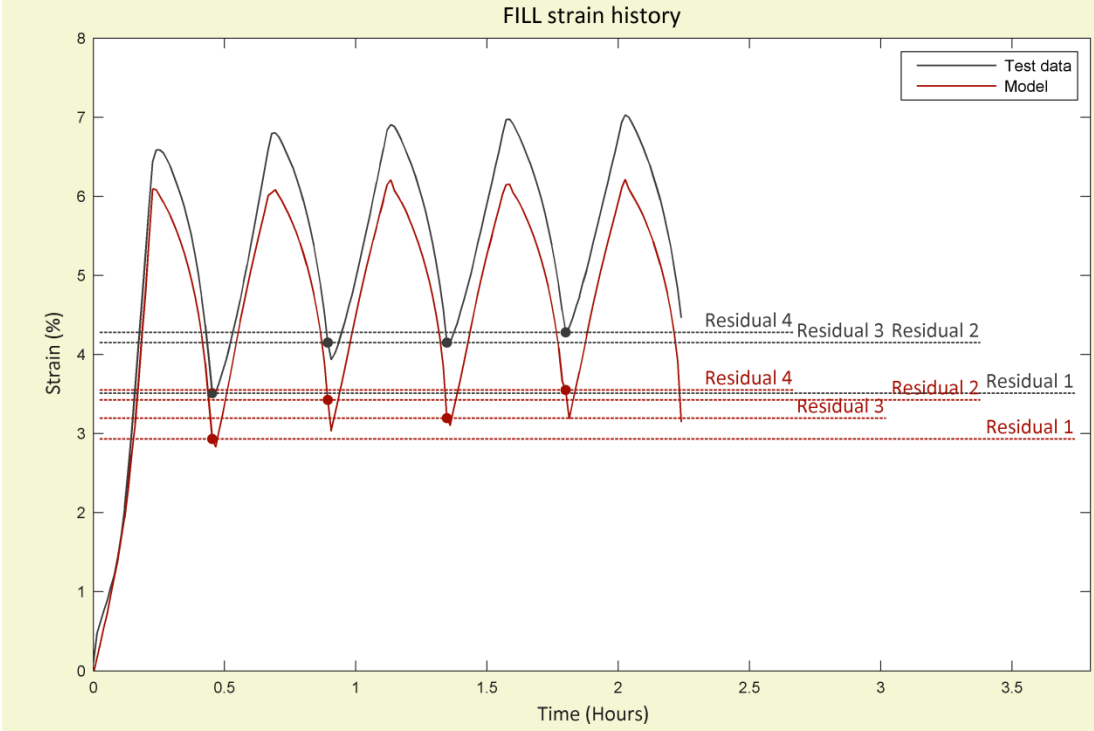

Figure 5.20 Initial load cycles for 1202 (PVC/PES) indicating increasing residual strain

Table 5.7 Difference in minimum strain between of initial cycles

Fabric	End of cycle No.	Difference in strain (%)		Difference strain as % of maximum test strain (%)	
		Warp	Fill	Warp	Fill
702	1	0.00	0.00	-	-
	2	0.12	0.07	2.3	1.4
	3	0.15	0.04	2.8	0.7
	4	0.19	0.10	3.6	2.0
1202	1	0.00	0.00	-	-
	2	0.15	0.15	2.0	2.2
	3	0.55	0.38	7.5	5.4
	4	0.35	0.15	4.7	2.2

Observing the results of the Verseidag B18089 and B18059 PTFE/glass fabrics (Figure 5.21 and Figure 5.22) it appears that all model formulations have reduced accuracy when compared to that achieved in predicting the behaviour of PVC/PES fabrics. For the B18059, the final formulation is failing to find a solution for the 1:0 cycles, resulting in spikes in the predicted strains at this load ratio. However, the 1:1 fill cycles predicted by the final model formulation for both the B18089 and B18059 fabrics show very similar magnitude of strains when compared to test data. NRMSE values (Table 5.8 and Table 5.9) for these 1:1 fill cycles, where test fill strains are positive and warp strains are negative or small, are more accurate than the linear models by a margin exceeding that of the PVC/PES comparisons.

The NRMSE values are best overall for the sawtooth model, 13.7% and 13.8%, for the warp and fill, respectively, excluding the 1:0 fill data and 0:1 warp data. However, poor accuracy when predicting negative fabric strain is exhibited by all model formulations for the PTFE/glass fabrics tested. A coating compressive stiffness factor was used by Bridgens (2005) to improve the prediction at negative strains. However, factors calibrated against comparative data are not being used to compare model formulations here. Better understanding of the compressive mechanisms and the ability to determine them through simple tests is needed to incorporate such mechanisms in a truly predictive model.

The magnitude of the strains PD Interglas ATEX3000 and ATEX5000 silicone/glass fabrics (Figure 5.23 and Figure 5.24) is also more accurately predicted by the linear model formulations when compared to the final look-up model formulation. Again, for the 1:1 cycles the RMSE/NRMSE values show that the look-up model is more accurate when small or negative strains are not occurring.

While the final model formulation does not need biaxial test data in order to make predictions, results of the PTFE- and silicone glass fabrics indicate that negative stains are not always adequately predicted and, therefore, the underlying mechanisms need to be modelled more accurately.

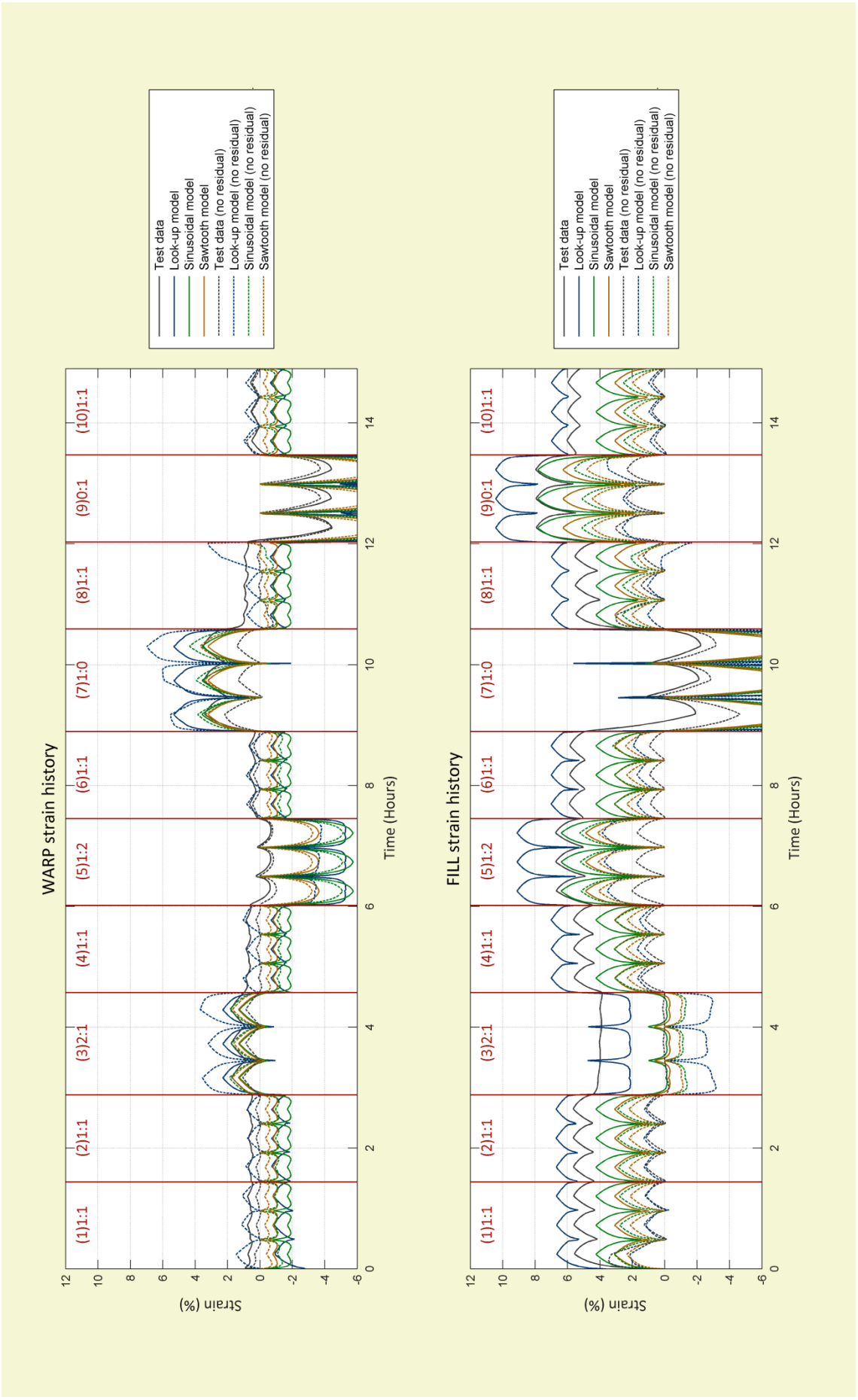

Figure 5.21 Comparison with test and model data for Verseidag B18089 (PTFE/glass)

Table 5.8 Comparison of test and model data for Verseidag B18089 (PTFE/glass), Root Mean Square Error (RMSE) (percentage strain) and Root Mean Square Error Normalised over the range of strains (NRMSE) (percentage of range)

Load cycle →		*1*	2	3	*4*	5	*6*	7	*8*	9	*10*	All	All'†
Load ratio (w:f) →		*1:1*	1:1	2:1	*1:1*	1:2	*1:1*	1:0	*1:1*	0:1	*1:1*	-	-
LOOK-UP MODEL													
1) Raw data													
Warp	RMSE	*2.0*	1.7	0.6	*1.8*	4.6	*1.5*	1.8	*2.1*	12.0	*1.3*	**4.3**	2.2
	NRMSE	*25.0*	22.0	7.7	*23.3*	58.0	*19.3*	22.6	*26.0*	151.2	*16.9*	**53.9**	28.0
Fill	RMSE	*0.7*	0.4	2.3	*0.6*	2.7	*0.2*	4.3	*1.4*	8.2	*0.2*	**3.2**	1.4
	NRMSE	*10.6*	5.7	34.7	*8.7*	40.8	*3.6*	65.1	*21.6*	122.8	*3.7*	**48.3**	21.6
2) Residual strain removed (No residual)													
Warp	RMSE	*0.7*	0.4	2.3	*0.6*	2.7	*0.2*	4.3	*1.4*	8.2	*0.2*	**3.2**	1.4
	NRMSE	*10.6*	5.7	34.7	*8.7*	40.8	*3.6*	65.1	*21.6*	122.8	*3.7*	**48.3**	21.6
Fill	RMSE	*0.6*	0.2	2.6	*0.4*	2.0	*0.8*	22.8	*1.2*	0.8	*0.2*	**7.8**	1.3
	NRMSE	*7.3*	2.4	31.8	*5.6*	24.2	*10.5*	282.2	*14.6*	9.6	*2.3*	**96.7**	16.4
SINUSOIDAL MODEL													
1) Raw data													
Warp	RMSE	*2.4*	2.3	0.8	*2.5*	4.4	*2.2*	0.8	*2.6*	6.9	*2.0*	**3.1**	2.6
	NRMSE	*29.8*	29.3	9.7	*31.0*	55.7	*27.5*	9.6	*33.5*	87.6	*25.7*	**39.7**	32.3
Fill	RMSE	*1.6*	1.8	4.0	*1.7*	1.1	*2.1*	6.9	*1.5*	1.0	*2.3*	**3.1**	2.2
	NRMSE	*15.7*	17.3	39.0	*16.9*	10.9	*20.7*	67.6	*14.7*	9.7	*22.2*	**30.1**	21.7
2) Residual strain removed (No residual)													
Warp	RMSE	*1.2*	1.1	0.7	*1.2*	3.6	*1.4*	2.0	*0.6*	5.7	*1.2*	**2.4**	1.6
	NRMSE	*17.5*	16.8	10.8	*17.6*	53.6	*20.7*	30.3	*9.3*	86.1	*17.6*	**35.9**	24.1
Fill	RMSE	*1.1*	1.5	1.1	*1.5*	3.0	*1.9*	6.3	*0.8*	2.4	*1.4*	**2.7**	1.7
	NRMSE	*13.8*	18.1	13.4	*18.8*	37.2	*23.1*	78.2	*9.4*	29.4	*17.9*	**33.4**	20.5
SAWTOOTH MODEL													
1) Raw data													
Warp	RMSE	*1.6*	1.5	0.7	*1.7*	2.6	*1.4*	0.8	*1.9*	3.5	*1.2*	**1.8**	1.6
	NRMSE	*19.7*	19.3	8.4	*21.0*	33.4	*17.5*	10.4	*23.5*	44.5	*15.6*	**23.3**	20.7
Fill	RMSE	*2.6*	2.8	4.2	*2.7*	2.2	*3.1*	5.4	*2.5*	2.2	*3.3*	**3.3**	3.0
	NRMSE	*25.5*	27.2	41.1	*26.7*	22.1	*30.5*	52.9	*24.7*	21.4	*32.1*	**32.4**	29.5
2) Residual strain removed (No residual)													
Warp	RMSE	*0.6*	0.6	0.6	*0.6*	2.0	*0.8*	1.6	*0.3*	2.9	*0.7*	**1.3**	0.9
	NRMSE	*9.6*	8.8	8.9	*9.0*	30.3	*11.8*	23.7	*4.3*	43.4	*10.8*	**19.9**	13.7
Fill	RMSE	*0.9*	0.9	0.9	*0.9*	2.0	*1.2*	4.5	*0.6*	1.7	*1.0*	**1.9**	1.1
	NRMSE	*10.6*	11.0	11.0	*10.8*	24.8	*14.8*	55.5	*8.0*	21.4	*12.1*	**23.4**	13.8

All'† = All strain data modified so not to include 1:0 and 0:1 load ratio data

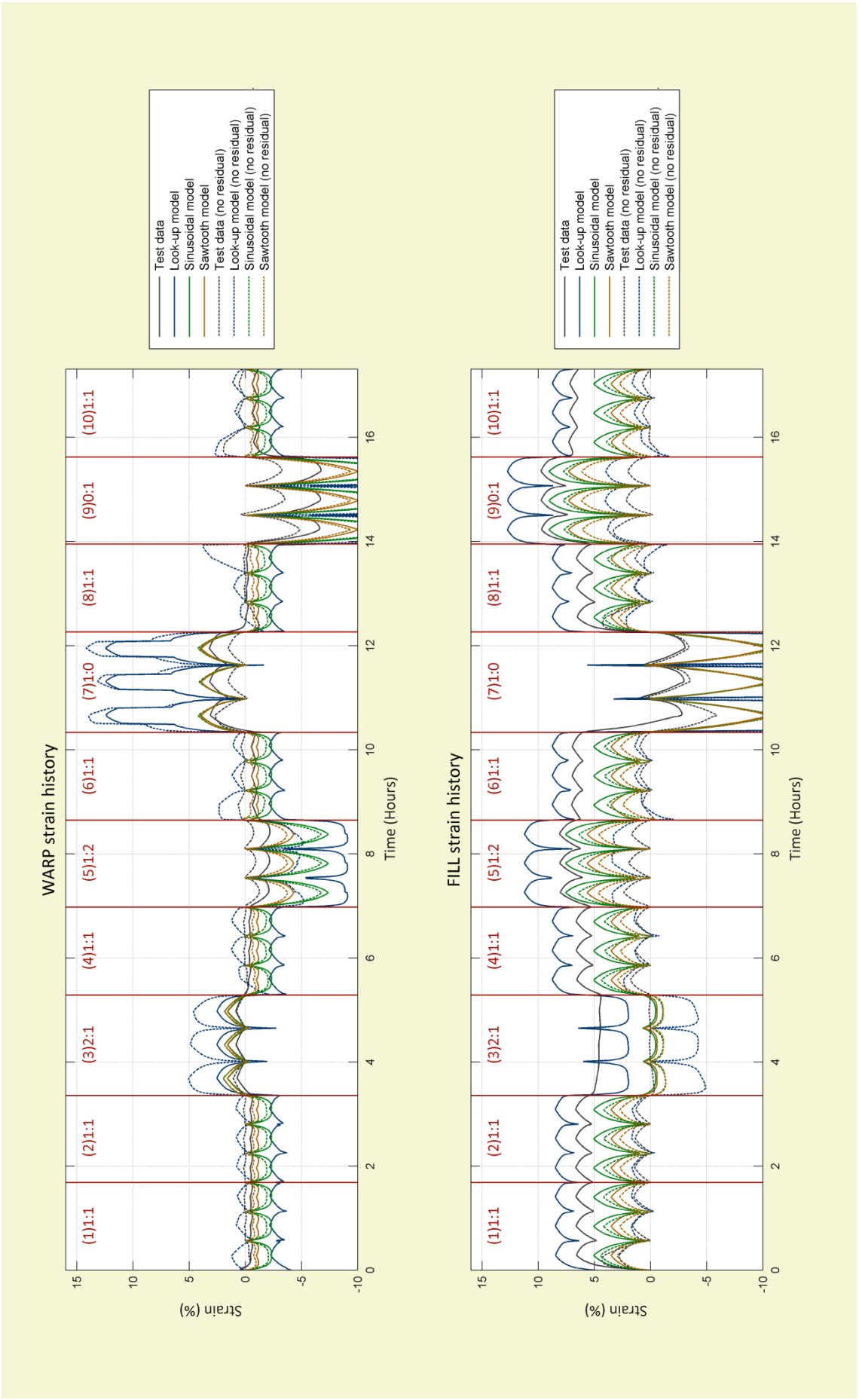

Figure 5.22 Comparison with test and model data for Verseidag B18059 (PTFE/glass)

Table 5.9 Comparison of test and model data for Verseidag B18059 (PTFE/glass), Root Mean Square Error (RMSE) (percentage strain) and Root Mean Square Error Normalised over the range of strains (NRMSE) (percentage of range)

Load cycle →		***1***	**2**	**3**	***4***	**5**	***6***	**7**	***8***	**9**	***10***	**All**	**All'†**
Load ratio (w:f) →		*1:1*	**1:1**	**2:1**	*1:1*	**1:2**	*1:1*	**1:0**	*1:1*	**0:1**	*1:1*	**-**	**-**
LOOK-UP MODEL													
1) Raw data													
Warp	RMSE	*2.3*	2.1	1.5	*2.3*	6.7	*1.8*	6.6	*2.6*	19.9	*1.6*	**7.1**	3.0
	NRMSE	*22.9*	21.3	14.9	*22.7*	67.7	*18.5*	65.9	*26.1*	200.3	*16.5*	**71.6**	30.6
Fill	RMSE	*2.1*	1.9	2.3	*2.2*	3.3	*1.7*	19.3	*2.5*	3.1	*1.4*	**6.8**	2.2
	NRMSE	*16.7*	14.6	18.1	*17.5*	25.4	*13.1*	150.7	*19.4*	24.1	*10.7*	**53.3**	17.5
2) Residual strain removed (No residual)													
Warp	RMSE	*0.7*	0.5	3.6	*0.8*	3.6	*1.0*	8.8	*1.6*	16.8	*0.4*	**6.3**	2.0
	NRMSE	*9.5*	6.2	47.1	*10.3*	47.4	*13.3*	116.9	*21.6*	222.5	*5.8*	**83.2**	26.5
Fill	RMSE	*0.7*	0.4	3.9	*0.5*	1.5	*0.4*	22.7	*1.0*	1.6	*0.7*	**7.8**	1.7
	NRMSE	*7.0*	4.0	38.0	*5.2*	15.1	*4.3*	222.0	*10.1*	15.9	*6.8*	**75.9**	16.2
SINUSOIDAL MODEL													
1) Raw data													
Warp	RMSE	*1.5*	1.5	0.5	*1.6*	3.8	*1.3*	0.8	*1.9*	5.6	*1.2*	**2.4**	1.9
	NRMSE	*15.2*	15.0	5.1	*16.4*	38.6	*12.9*	7.6	*19.0*	56.5	*12.5*	**24.5**	19.0
Fill	RMSE	*2.2*	2.5	4.8	*2.4*	1.9	*3.0*	5.6	*2.2*	2.2	*3.3*	**3.3**	3.0
	NRMSE	*17.5*	19.3	37.6	*18.6*	15.0	*23.4*	43.7	*17.4*	17.1	*26.0*	**25.8**	23.2
2) Residual strain removed (No residual)													
Warp	RMSE	*1.5*	1.6	0.7	*1.6*	4.3	*1.8*	1.7	*1.3*	7.4	*2.3*	**3.0**	2.1
	NRMSE	*20.3*	21.6	9.1	*20.7*	57.3	*23.3*	22.6	*17.5*	97.8	*30.2*	**40.2**	28.2
Fill	RMSE	*1.7*	2.2	0.9	*2.1*	3.6	*2.4*	4.7	*1.7*	4.5	*2.8*	**2.9**	2.3
	NRMSE	*16.7*	21.4	9.1	*20.7*	35.6	*23.3*	46.0	*16.2*	43.7	*27.1*	**28.7**	22.4
SAWTOOTH MODEL													
1) Raw data													
Warp	RMSE	*0.6*	0.5	0.6	*0.7*	1.7	*0.4*	0.7	*1.0*	2.3	*0.5*	**1.1**	0.8
	NRMSE	*6.0*	5.4	5.5	*7.0*	17.0	*3.7*	7.3	*9.9*	22.9	*5.2*	**10.6**	8.4
Fill	RMSE	*3.3*	3.5	5.0	*3.4*	3.1	*4.0*	5.5	*3.3*	3.3	*4.3*	**4.0**	3.8
	NRMSE	*25.5*	27.3	38.9	*26.5*	23.9	*31.2*	42.9	*25.4*	25.9	*33.8*	**31.0**	29.6
2) Residual strain removed (No residual)													
Warp	RMSE	*0.6*	0.7	0.7	*0.7*	2.2	*0.9*	1.7	*0.5*	3.9	*1.4*	**1.7**	1.1
	NRMSE	*8.5*	9.6	9.4	*8.8*	29.5	*11.4*	22.2	*6.9*	51.8	*18.7*	**22.1**	14.6
Fill	RMSE	*1.0*	1.1	1.0	*1.0*	2.2	*1.3*	4.5	*1.1*	3.1	*1.7*	**2.2**	1.4
	NRMSE	*10.2*	10.9	9.7	*10.2*	21.7	*12.9*	44.2	*10.3*	30.0	*16.6*	**21.2**	13.4

All'† = All strain data modified so not to include 1:0 and 0:1 load ratio data

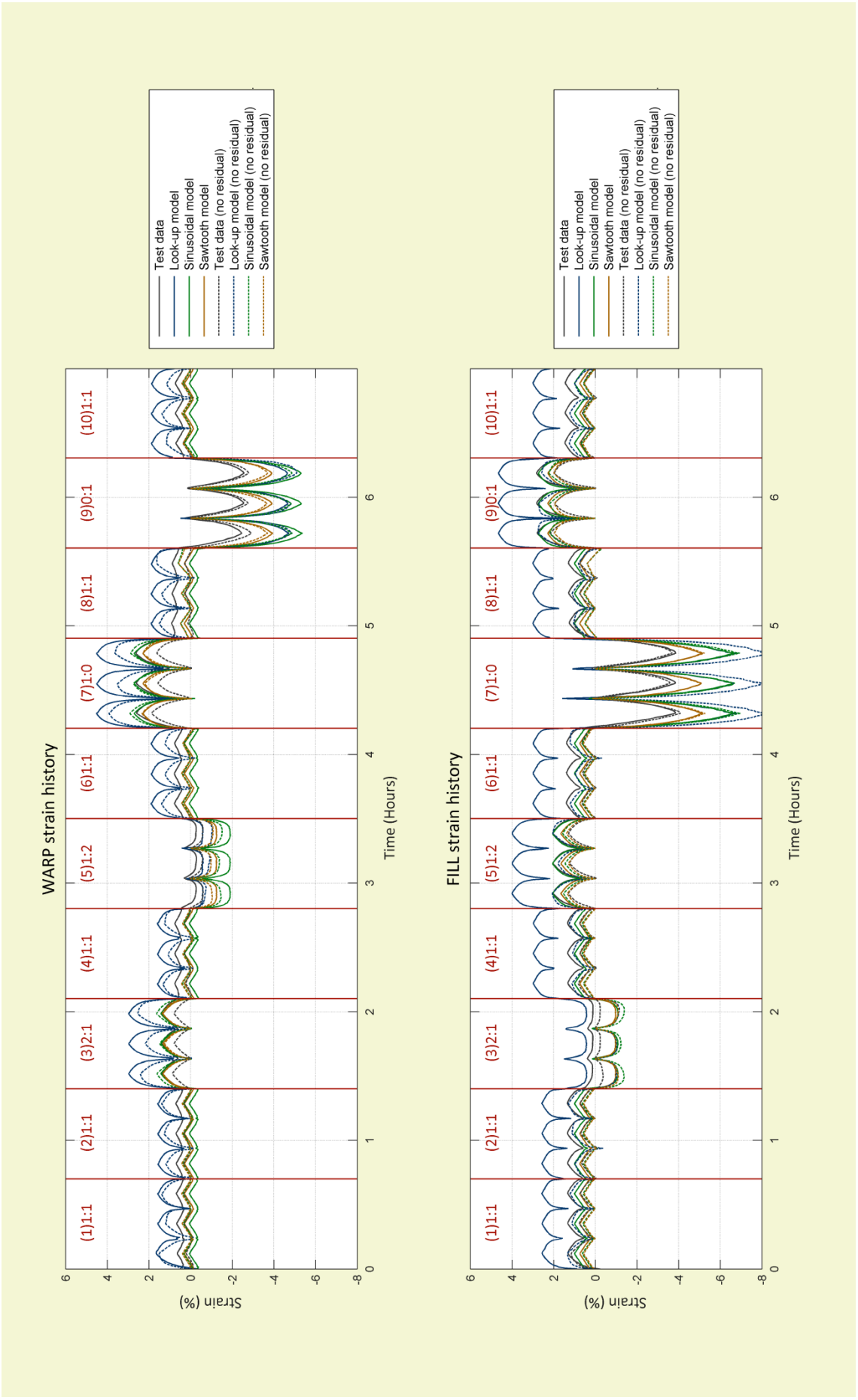

Figure 5.23 Comparison with test and model data for Interglas ATEX3000 (silicone/glass)

Table 5.10 Comparison of test and model data for PD Interglas ATEX3000 (silicone/glass), Root Mean Square Error (RMSE) (percentage strain) and Root Mean Square Error Normalised over the range of strains (NRMSE) (percentage of range)

Load cycle →		*1*	2	3	*4*	5	*6*	7	*8*	9	*10*	All	All'†
Load ratio (w:f) →		*1:1*	**1:1**	**2:1**	*1:1*	**1:2**	*1:1*	**1:0**	*1:1*	**0:1**	*1:1*	-	-
LOOK-UP MODEL													
1) Raw data													
Warp	RMSE	*0.8*	0.7	1.4	*0.7*	0.4	*1.0*	1.8	*0.8*	2.1	*1.0*	**1.2**	0.9
	NRMSE	*15.5*	14.3	27.4	*13.5*	6.9	*18.9*	35.4	*16.2*	39.9	*20.0*	**23.1**	17.5
Fill	RMSE	*1.2*	1.2	0.5	*1.6*	2.0	*1.6*	2.2	*1.8*	2.0	*1.5*	**1.6**	1.5
	NRMSE	*18.5*	18.1	7.2	*24.7*	29.5	*23.5*	32.5	*26.2*	29.5	*22.5*	**24.3**	22.2
2) Residual strain removed (No residual)													
Warp	RMSE	*0.9*	0.8	1.4	*0.8*	0.3	*0.8*	1.9	*1.1*	2.0	*0.8*	**1.2**	0.9
	NRMSE	*19.6*	17.2	29.5	*17.1*	7.2	*16.5*	40.3	*23.4*	42.2	*15.9*	**25.4**	19.3
Fill	RMSE	*0.4*	0.5	0.7	*0.4*	0.7	*0.5*	3.6	*0.3*	0.8	*0.5*	**1.3**	0.5
	NRMSE	*6.0*	7.4	10.9	*6.5*	11.8	*8.0*	57.3	*4.3*	13.2	*8.3*	**20.1**	8.3
SINUSOIDAL MODEL													
1) Raw data													
Warp	RMSE	*0.6*	0.7	0.2	*0.8*	1.5	*0.7*	0.3	*0.9*	2.6	*0.7*	**1.1**	0.9
	NRMSE	*12.5*	13.2	4.1	*14.7*	29.7	*14.4*	5.9	*17.9*	49.4	*13.2*	**21.5**	16.4
Fill	RMSE	*0.3*	0.3	1.1	*0.3*	0.1	*0.4*	2.1	*0.3*	0.2	*0.5*	**0.8**	0.5
	NRMSE	*4.7*	4.9	15.8	*4.7*	1.7	*5.8*	31.9	*4.0*	2.7	*7.0*	**12.1**	7.2
2) Residual strain removed (No residual)													
Warp	RMSE	*0.1*	0.0	0.7	*0.1*	0.8	*0.1*	1.1	*0.2*	1.8	*0.1*	**0.8**	0.4
	NRMSE	*1.3*	0.8	13.7	*1.6*	16.4	*1.1*	22.8	*4.8*	37.7	*1.4*	**15.7**	7.8
Fill	RMSE	*0.3*	0.1	0.9	*0.2*	0.3	*0.1*	2.4	*0.4*	0.3	*0.1*	**0.8**	0.4
	NRMSE	*4.8*	1.6	14.4	*2.6*	4.3	*1.2*	38.3	*5.7*	5.5	*1.1*	**13.5**	6.1
SAWTOOTH MODEL													
1) Raw data													
Warp	RMSE	*0.4*	0.4	0.2	*0.5*	1.0	*0.5*	0.4	*0.7*	1.4	*0.4*	**0.7**	0.6
	NRMSE	*7.9*	8.6	3.7	*10.1*	18.5	*9.8*	7.2	*13.3*	27.3	*8.6*	**13.2**	10.8
Fill	RMSE	*0.5*	0.6	1.0	*0.5*	0.4	*0.6*	1.2	*0.5*	0.4	*0.7*	**0.7**	0.6
	NRMSE	*8.1*	8.5	14.9	*8.2*	5.5	*9.5*	17.6	*7.3*	6.6	*10.6*	**10.4**	9.4
2) Residual strain removed (No residual)													
Warp	RMSE	*0.1*	0.1	0.4	*0.1*	0.4	*0.0*	0.6	*0.2*	0.9	*0.0*	**0.4**	0.2
	NRMSE	*2.0*	1.1	9.3	*1.9*	9.1	*0.7*	13.1	*4.7*	18.7	*0.7*	**8.5**	5.0
Fill	RMSE	*0.3*	0.1	0.7	*0.2*	0.1	*0.1*	1.3	*0.4*	0.2	*0.1*	**0.5**	0.3
	NRMSE	*5.4*	2.2	10.8	*3.2*	2.2	*1.7*	20.4	*5.9*	3.1	*1.5*	**8.0**	5.1

All'† = All strain data modified so not to include 1:0 and 0:1 load ratio data

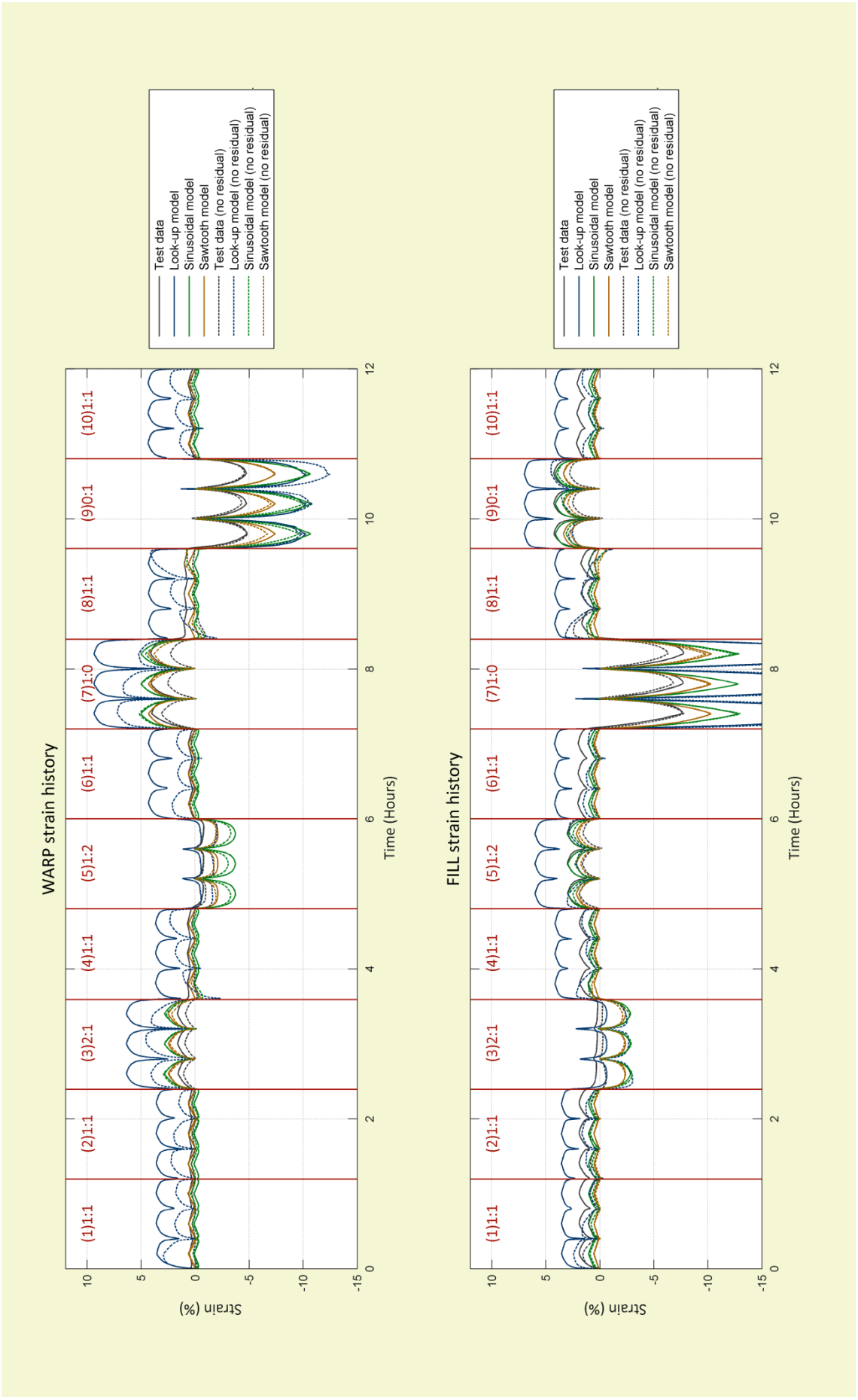

Figure 5.24 Comparison with test and model data for Interglas ATEX5000 (silicone/glass)

Table 5.11 Comparison of test and model data for PD Interglas ATEX5000 (silicone/glass), Root Mean Square Error (RMSE) (percentage strain) and Root Mean Square Error Normalised over the range of strains (NRMSE) (percentage of range)

Load cycle →		*1*	2	3	*4*	5	*6*	7	*8*	9	*10*	All	All'[+]
Load ratio (w:f) →		*1:1*	**1:1**	**2:1**	*1:1*	**1:2**	*1:1*	**1:0**	*1:1*	**0:1**	*1:1*	-	-
LOOK-UP MODEL													
1) Raw data													
Warp	RMSE	*2.7*	2.7	4.4	*2.7*	0.4	*3.5*	5.3	*3.0*	4.8	*3.5*	**3.6**	3.1
	NRMSE	*30.7*	30.9	50.0	*30.2*	4.6	*39.0*	59.4	*33.8*	54.1	*39.6*	**40.1**	34.6
Fill	RMSE	*1.7*	1.7	0.8	*2.3*	3.0	*2.2*	14.7	*2.6*	2.9	*2.0*	**5.1**	2.1
	NRMSE	*14.0*	13.9	6.6	*19.2*	25.4	*18.0*	122.2	*21.5*	24.4	*16.9*	**42.6**	17.8
2) Residual strain removed (No residual)													
Warp	RMSE	*1.7*	1.4	2.9	*1.4*	0.9	*1.2*	3.8	*2.2*	5.8	*1.3*	**2.7**	1.8
	NRMSE	*21.9*	17.8	36.9	*17.2*	11.8	*15.7*	47.3	*28.0*	73.3	*15.9*	**34.0**	22.1
Fill	RMSE	*0.7*	0.6	2.1	*0.8*	1.1	*0.6*	17.0	*0.6*	1.3	*0.8*	**5.5**	1.0
	NRMSE	*6.1*	5.4	19.4	*7.2*	10.2	*5.8*	158.6	*5.8*	11.7	*7.1*	**51.2**	9.5
SINUSOIDAL MODEL													
1) Raw data													
Warp	RMSE	*0.6*	0.6	0.9	*0.7*	2.5	*0.6*	0.8	*1.1*	4.5	*0.6*	**1.8**	1.1
	NRMSE	*6.4*	6.8	10.1	*8.2*	28.5	*6.5*	9.2	*12.0*	50.4	*6.3*	**19.8**	12.8
Fill	RMSE	*0.8*	0.9	2.6	*0.8*	0.3	*1.0*	3.4	*0.6*	0.3	*1.1*	**1.5**	1.2
	NRMSE	*6.8*	7.1	21.3	*6.5*	2.3	*8.2*	28.0	*5.1*	2.9	*9.1*	**12.5**	9.8
2) Residual strain removed (No residual)													
Warp	RMSE	*0.1*	0.2	1.5	*0.2*	2.0	*0.2*	1.9	*0.3*	4.1	*0.3*	**1.6**	0.9
	NRMSE	*1.4*	1.9	18.4	*2.4*	24.7	*2.4*	24.1	*3.8*	51.0	*3.3*	**20.5**	11.1
Fill	RMSE	*0.4*	0.1	2.0	*0.1*	0.7	*0.1*	3.9	*0.7*	0.8	*0.1*	**1.4**	0.8
	NRMSE	*3.5*	1.1	18.8	*1.3*	6.4	*0.9*	36.2	*6.3*	7.5	*1.3*	**13.5**	7.5
SAWTOOTH MODEL													
1) Raw data													
Warp	RMSE	*0.2*	0.2	0.7	*0.3*	1.2	*0.1*	0.5	*0.6*	2.1	*0.1*	**0.8**	0.6
	NRMSE	*1.7*	2.0	7.5	*3.3*	13.7	*1.6*	5.4	*7.2*	23.6	*1.5*	**9.5**	6.3
Fill	RMSE	*1.3*	1.3	2.3	*1.2*	0.8	*1.4*	2.0	*1.0*	0.9	*1.5*	**1.5**	1.4
	NRMSE	*10.5*	10.8	19.1	*10.2*	6.9	*11.9*	16.7	*8.6*	7.5	*12.8*	**12.1**	11.8
2) Residual strain removed (No residual)													
Warp	RMSE	*0.2*	0.2	1.1	*0.2*	0.9	*0.1*	1.3	*0.5*	2.0	*0.1*	**0.9**	0.5
	NRMSE	*2.8*	2.0	13.6	*2.1*	11.4	*1.3*	16.1	*5.9*	24.5	*1.1*	**11.1**	6.8
Fill	RMSE	*0.6*	0.3	1.6	*0.3*	0.3	*0.2*	2.3	*0.9*	0.4	*0.2*	**1.0**	0.7
	NRMSE	*5.8*	3.1	14.6	*2.9*	2.7	*1.9*	21.6	*8.5*	4.1	*1.5*	**9.2**	6.6

All'[+] = All strain data modified so not to include 1:0 and 0:1 load ratio data

Response surfaces (Figure 5.25 – Figure 5.30) compare the accuracy achieved by the final model formulation at different load ratios, as well as the relative accuracy in the warp and fill yarn directions. The impact of the 1:0 and 0:1 load ratios on the overall accuracy of the model is disproportionately large. Therefore, if the biaxial test profiles had contained more load ratios, i.e. 1:3, 2:3 etc., the 1:0 and 0:1 ratios would not account for such a large proportion of the data and the accuracy of the overall accuracy of the final model might have been higher.

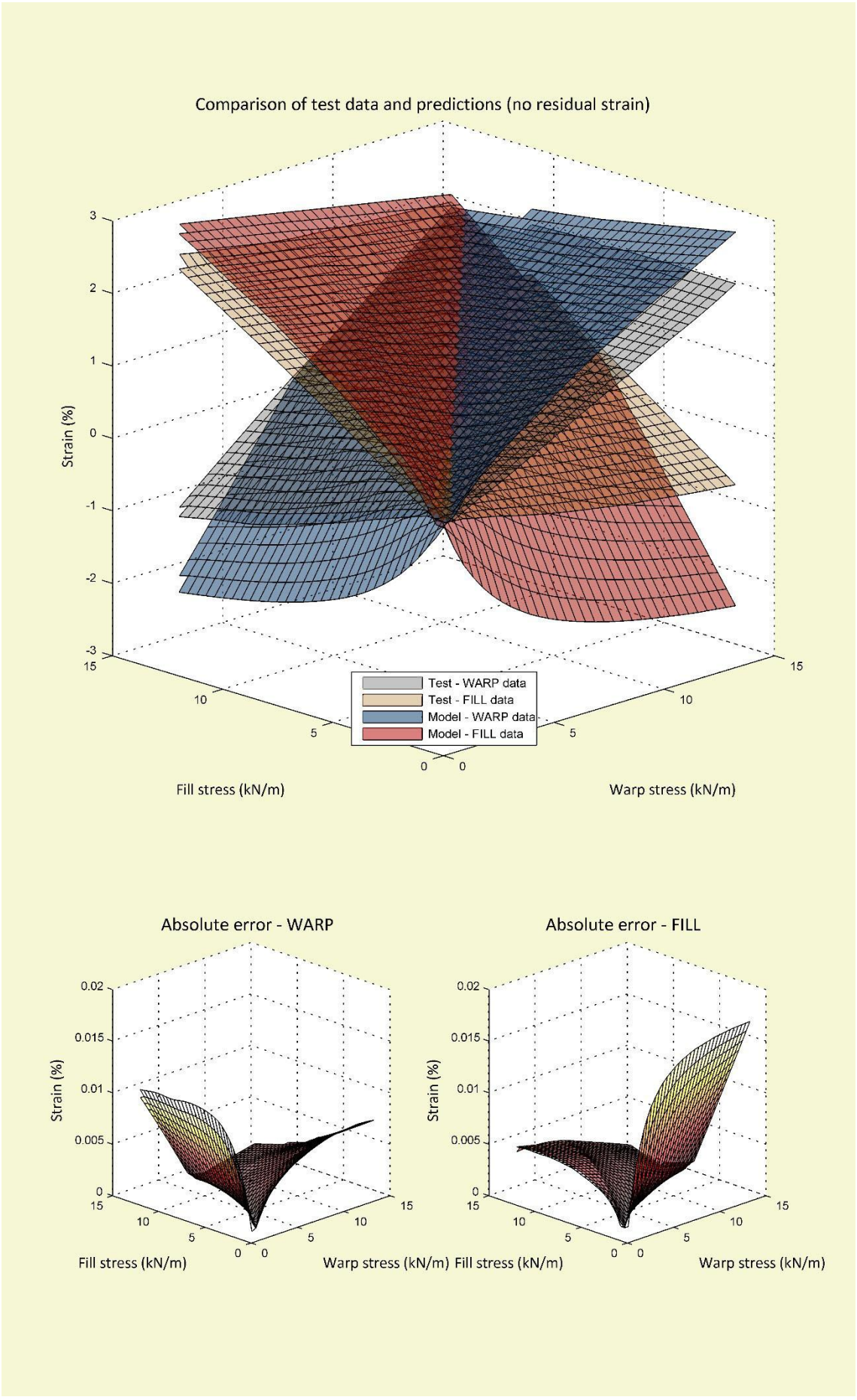

Figure 5.25 Response surfaces for Ferrari 702 (PVC/PES), model, test data and error

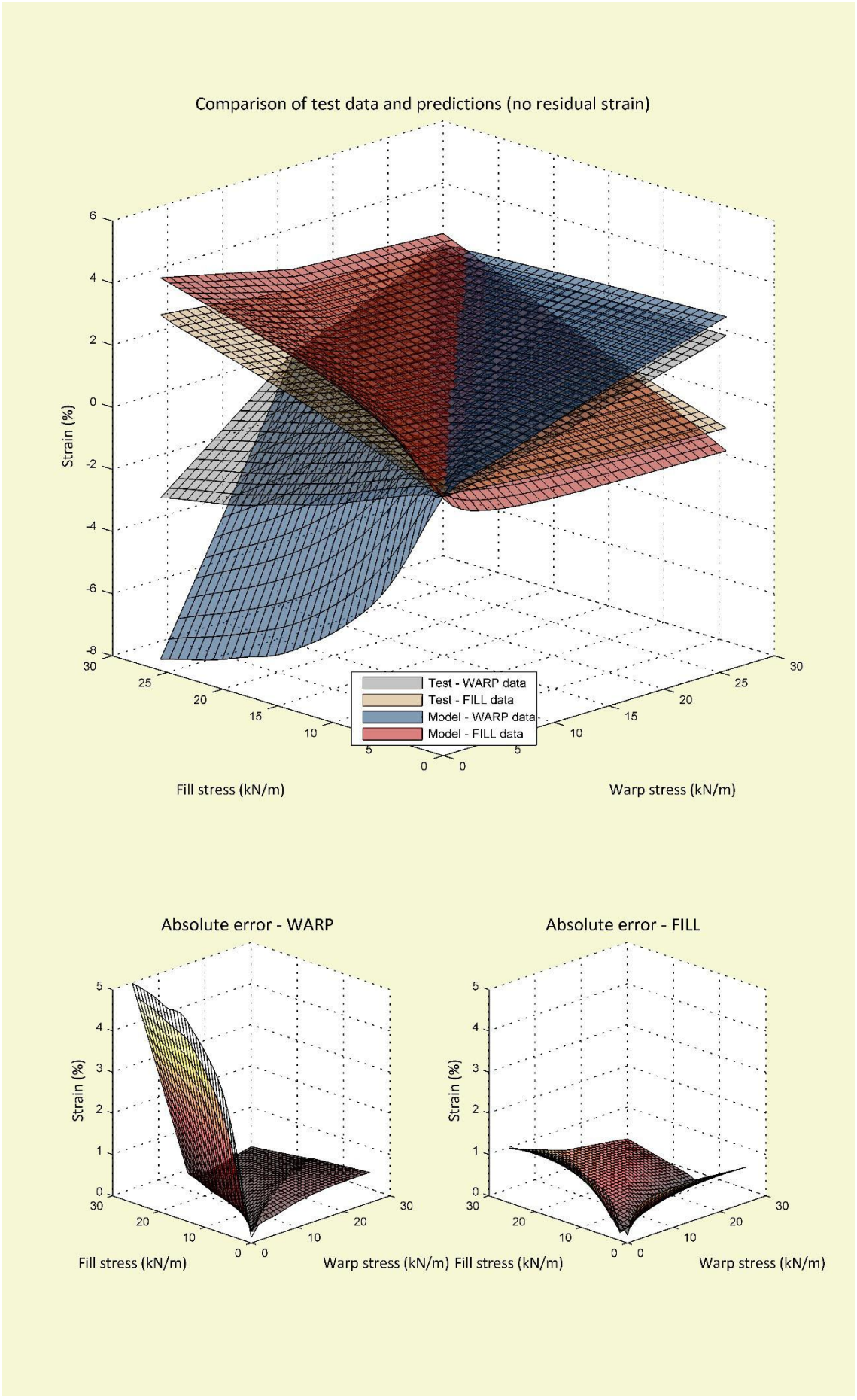

Figure 5.26 Response surfaces for Ferrari 1202 (PVC/PES), model, data and error

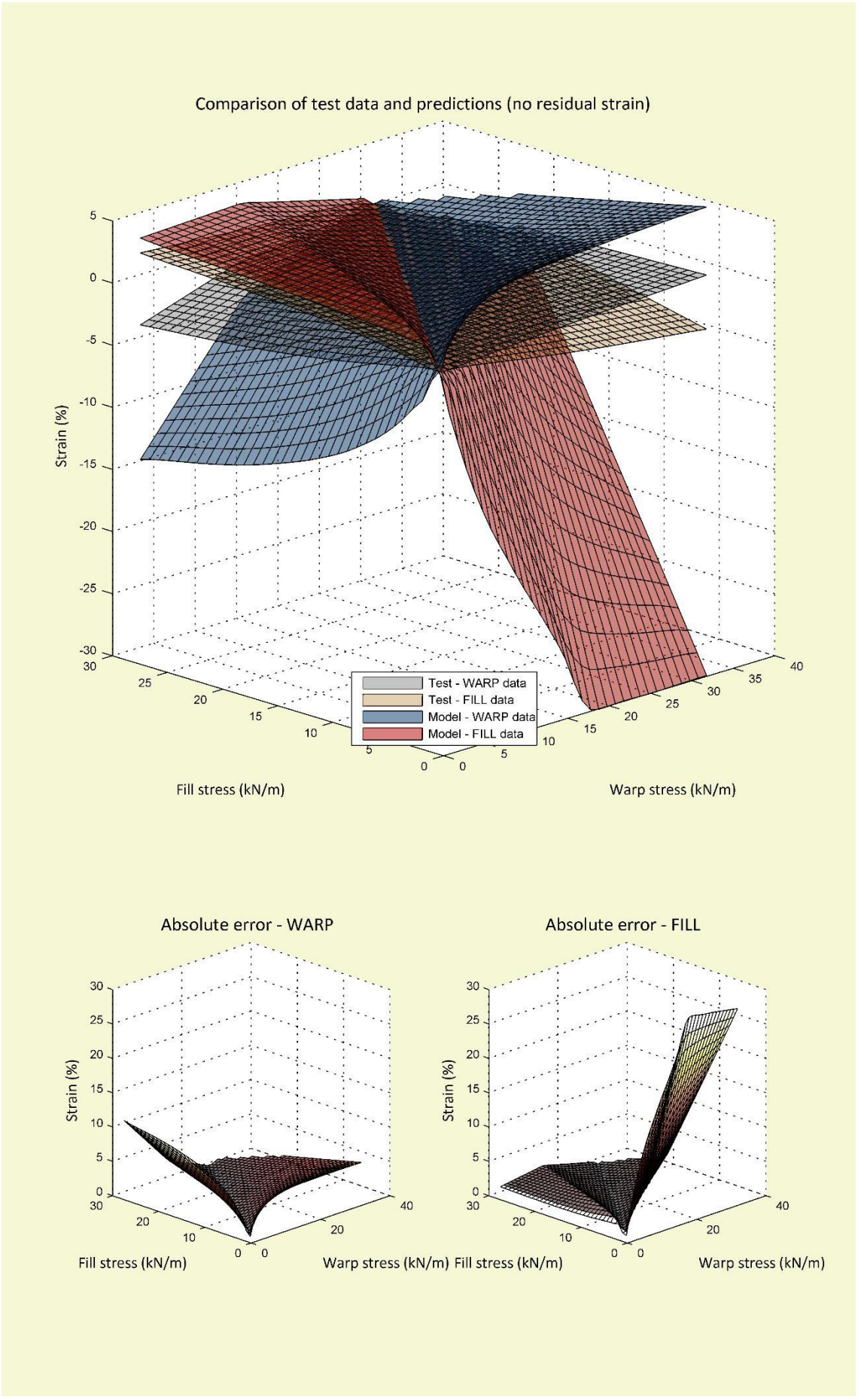

Figure 5.27 Response surfaces for Verseidag B18089 (PTFE/glass), model, data and error

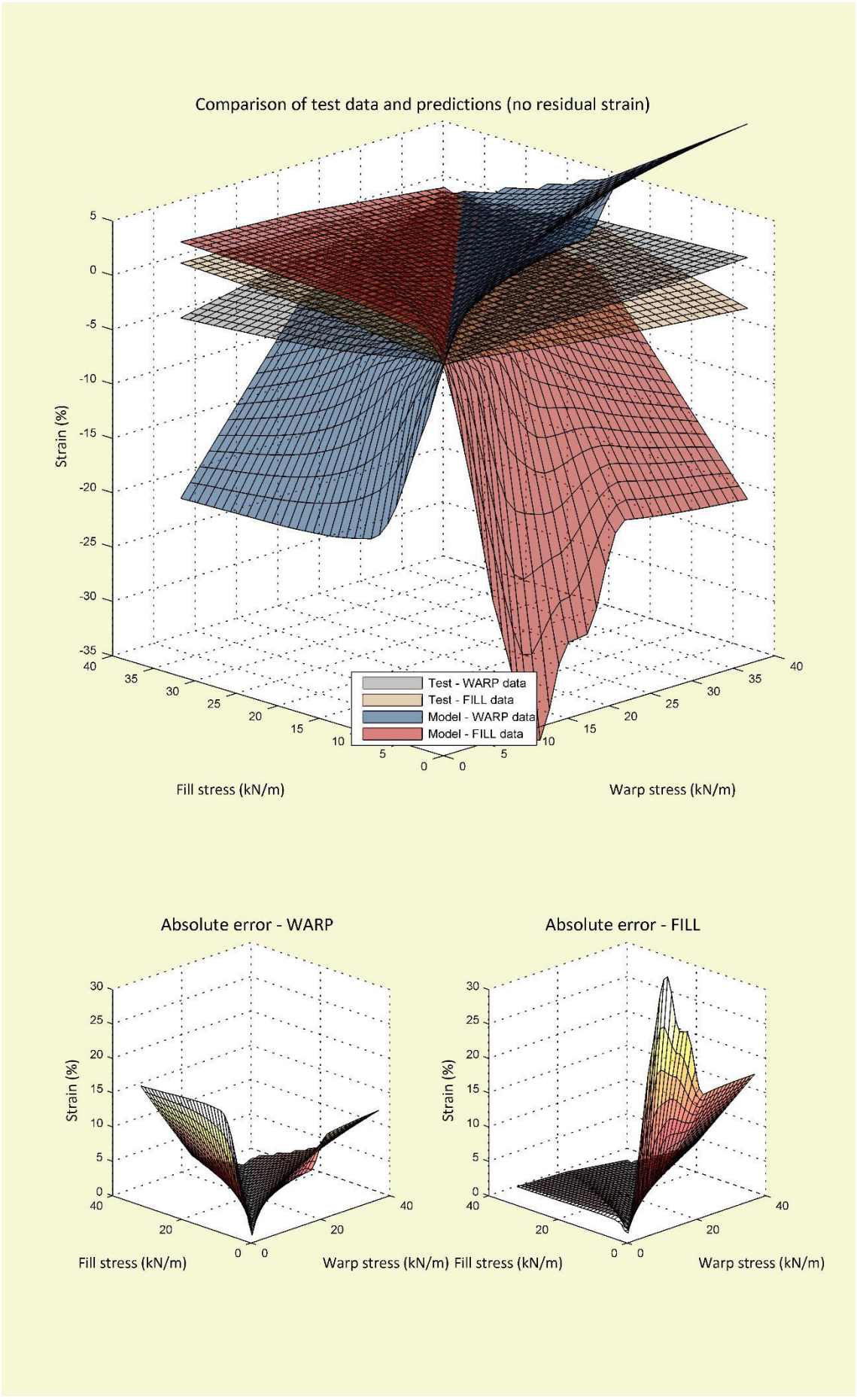

Figure 5.28 Response surfaces for Verseidag B18059 (PTFE/glass), model, test and error

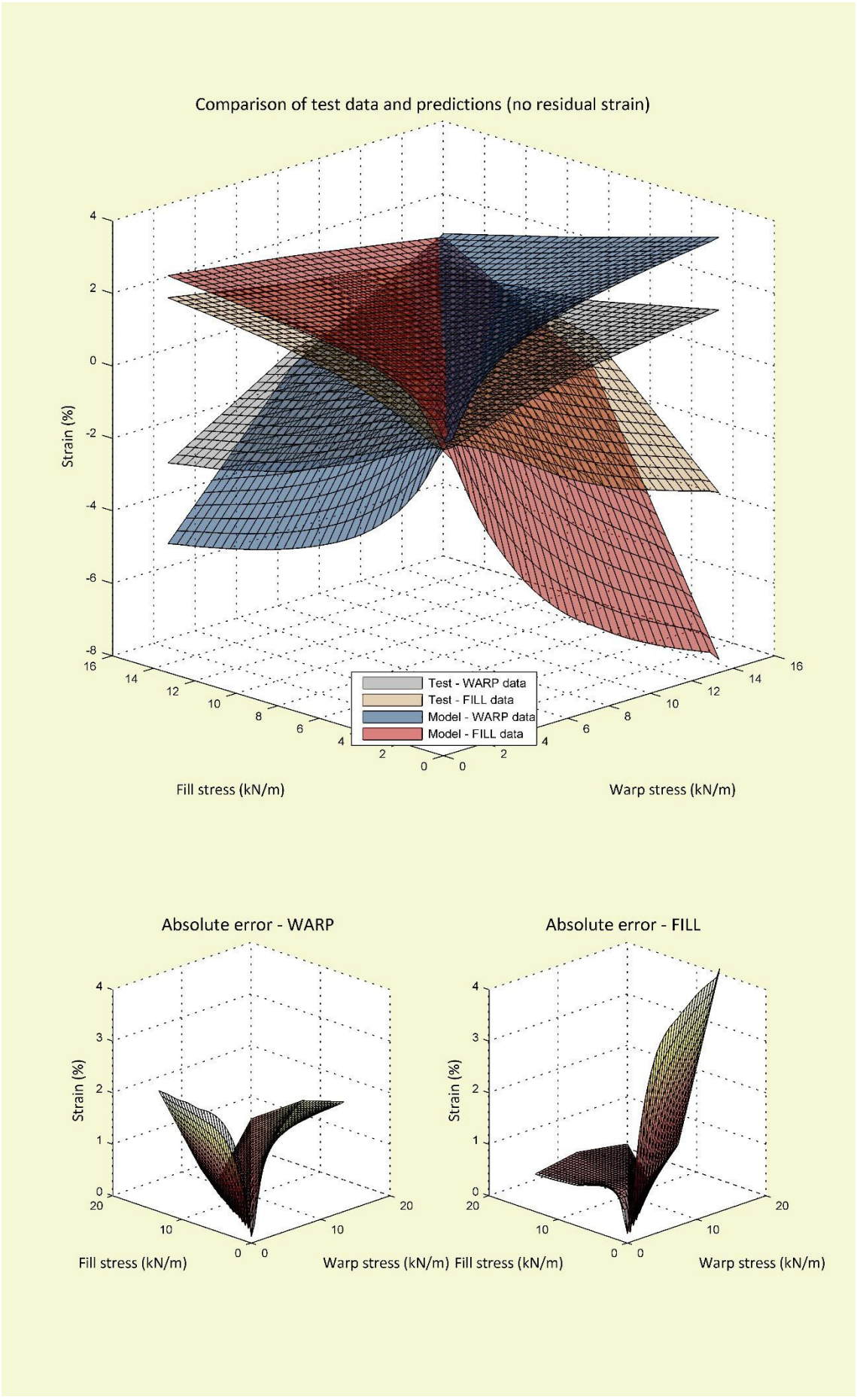

Figure 5.29 Response surfaces for PD Interglas ATEX3000 (silicone/glass), model, test and error

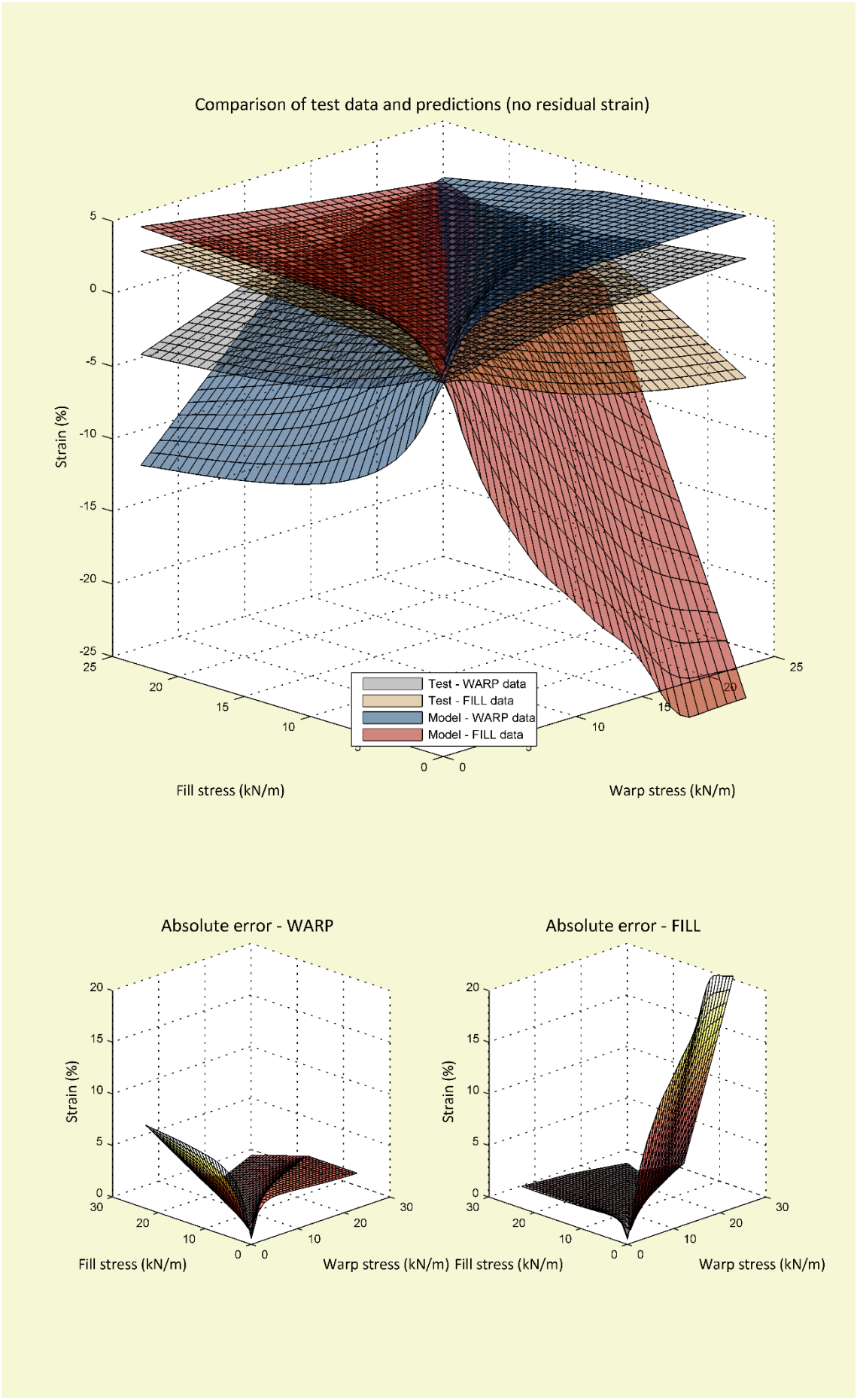

Figure 5.30 Response surfaces for PD Interglas ATEX3000 (silicone/glass), model, test and error

5.4.3 Comparisons with plane stress approximations

Stress-strains plots have been prepared for the third cycle in each cycles set (Figure 5.31 – Figure 5.36). The RMSE/NRMSE values and the strain history plots only compare the magnitude of the strains at each point. This is useful for comparing the different model formulations and to give a measure of the overall success of the models. However, calculating average differences in the magnitude of the strains over sets of cycles does not provide an indication of model accuracy in predicting a single cycle, which could be better or worse over a single cycle. A high average deviation of the magnitude of the strains between the test data and the predictions could result from poor predictive capabilities at initial/low stress values, i.e. inaccurate predictions at low stress values could affect the magnitude of the strains at higher stress values. The stress-strain plots allow for comparison of single cycles to be made between test data and model predictions. These plots have also been used to compare the model against data fitted to a plane stress framework, i.e. comparison with best fit data (§5.4.3).

Typically, design engineers will use biaxial test results in design and analysis within a plane stress framework defined by elastic moduli and Poisson's ratios. A plane stress framework is used to approximate the non-linear hysteretic fabric behaviour with two 'best fit' surfaces determined by four elastic constants (Equation 5.7). Note that while a linear elastic orthotropic material under biaxial load conditions satisfies the reciprocal relationship (Equation 5.8) between stiffnesses and Poisson's ratios, thereby having only three interdependent elastic constants, plane stress theory is arguably inappropriate of accurately represent in the material behaviour of architectural fabrics (§3.4.3). As coated woven materials are not homogeneous materials and behave more like a mechanism (§4.3.2), values of Young's' moduli and Poisson's ratios determined for architectural fabrics do not satisfy reciprocal relationship (Gosling and Bridgens, 2008). Therefore, while stiffness values and Poisson's ratios are used for approximating best fit surfaces they are essentially four arbitrary parameters which are useful to determine planes of best fit to allow design engineers to model fabric structure behaviour in analysis software.

$$\begin{Bmatrix} \varepsilon_w \\ \varepsilon_f \end{Bmatrix} = \begin{bmatrix} \frac{1}{E_w} & \frac{-v_{fw}}{E_f} \\ \frac{-v_{wf}}{E_w} & \frac{1}{E_f} \end{bmatrix} \cdot \begin{Bmatrix} \sigma_w \\ \sigma_f \end{Bmatrix} \qquad \textbf{Equation 5.7}$$

where ε = strain; σ = stress; E = Young's modulus; subscripts w and f denote warp and fill respectively; Poisson's ratios v_{wf} = fill direction strain caused by unit strain in the warp direction and v_{fw} = warp direction strain caused by unit strain in the fill direction.

$$\frac{v_{wf}}{E_w} = \frac{v_{fw}}{E_f} \qquad \textbf{Equation 5.8}$$

Stress-strain plots have been used to compare test data, predictions made by the final formulation and the best fit approximations of the test data (Figure 5.31 – Figure 5.36). Presenting the data in this way allows for better visual comparison of the gradients at each of the stress ratios when compared to surface plots. In order for the comparisons to be made, and for the best fit approximations to be computed for the test data, residual strain is removed from the data and model predictions. Best fit constant were calculated using a methodology described by the Membrane Structures Association of Japan (MSAJ, 1995) (Table 5.12 – Table 5.17). Lines representing the constant value of stiffness can be seen on the stress-strain plots. The best fit elastic constants of the predicted test data are lower than for the experiential data.

Across all the fabrics tested, the linear approximations of plane stress more accurately represent the architectural fabrics' response to load than the predictive model by visual comparison of the data. Generally, gradients of the predicted data are well aligned with those of the test data at higher values of stress. However, inaccuracies are present in the predictions at low values of stress, indicating that while the uniaxial look up function is replicating yarn elongation, the model is failing to accurately replicate crimp interchange. As above, the inclusion of a mechanism that resists contraction in the yarn direction is missing from the model.

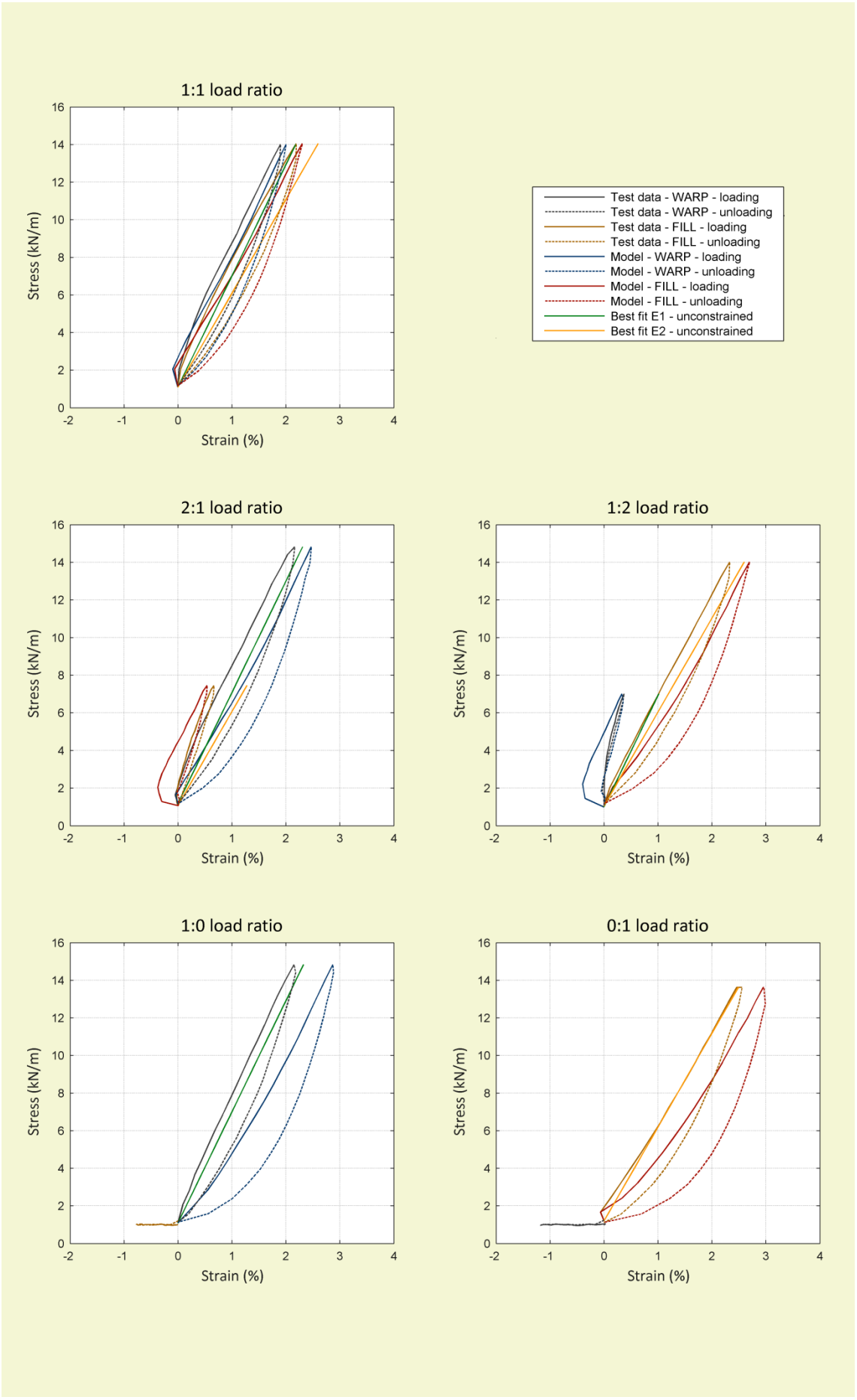

Figure 5.31 Stress-strain loading curves used in determining stiffnesses for Ferrari 702 (PVC/PES)

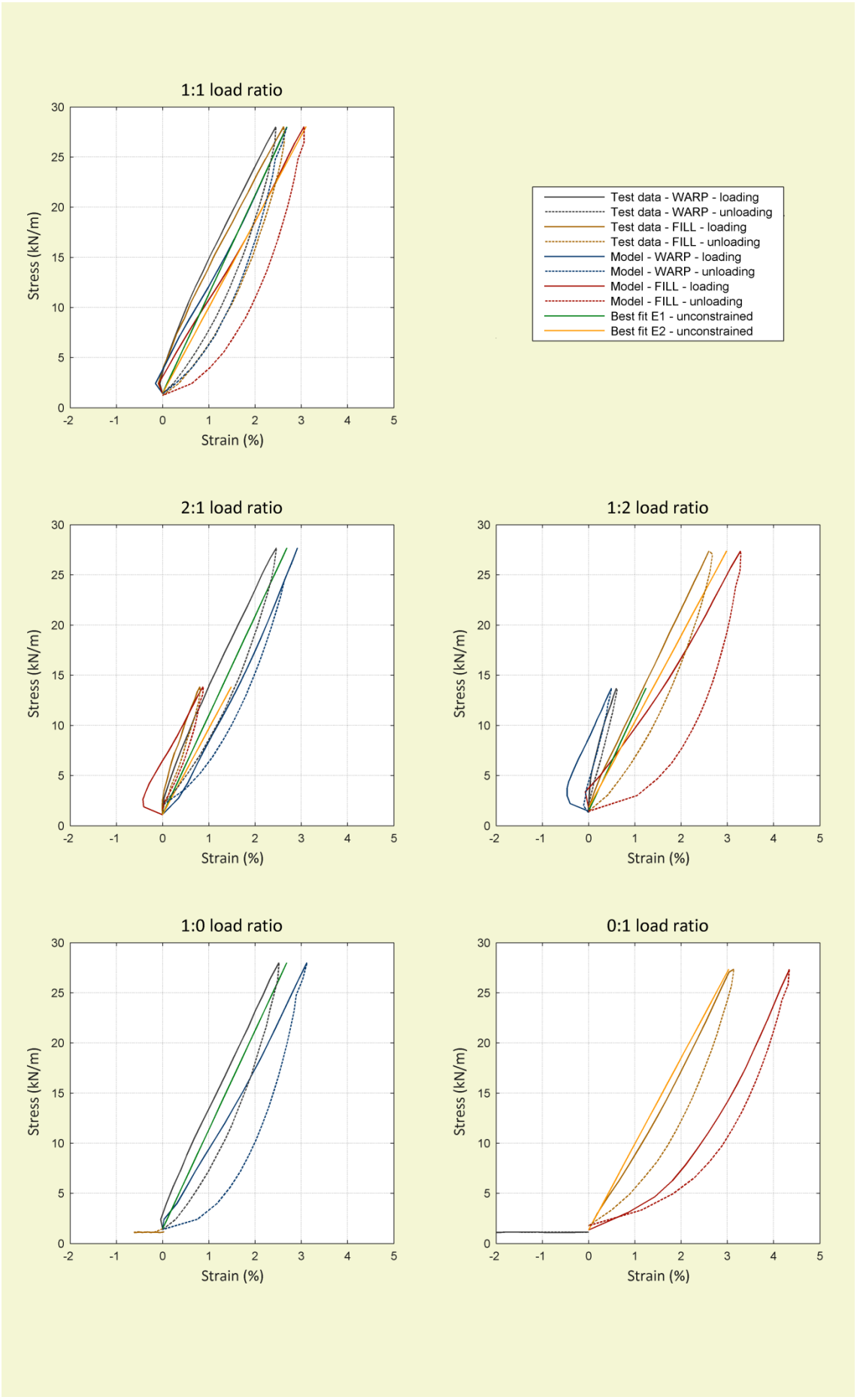

Figure 5.32 Stress-strain loading curves used in determining stiffnesses for Ferrari 1202 (PVC/PES)

Table 5.12 Best fit elastic moduli for Ferrari 702 (PVC/PES), loading data only

Load ratios used to determine elastic constants	Source of data	Reciprocal constraint applied?	Warp stiffness, E_1, (kN/m)	Fill stiffness, E_2, (kN/m)	Warp-fill Poisson's ratio, ν_{12}	Fill-warp Poisson's ratio, ν_{21}	Sum of strain differences squared, s, (% strain)
All load ratios	Test	Y	614	515	0.42	0.35	0.0630
		N	602	524	0.38	0.39	0.0618
	Model	Y	392	354	0.65	0.59	0.4116
		N	398	350	0.68	0.56	0.4101
All load ratios minus 0 loading curves	Test	Y	591	499	0.32	0.27	0.0580
		N	586	502	0.31	0.28	0.0580
	Model	Y	419	376	0.40	0.36	0.1768
		N	423	374	0.41	0.35	0.1767

Table 5.13 Best fit elastic moduli for Ferrari 1202 (PVC/PES), loading data only

Load ratios used to determine elastic constants	Source of data	Reciprocal constraint applied?	Warp stiffness, E_1, (kN/m)	Fill stiffness, E_2, (kN/m)	Warp-fill Poisson's ratio, ν_{12}	Fill-warp Poisson's ratio, ν_{21}	Sum of strain differences squared, s
All load ratios	Test	Y	916	792	0.48	0.42	0.3750
		N	815	887	0.26	0.65	0.2931
	Model	Y	538	450	0.80	0.66	4.3879
		N	427	575	0.31	1.28	3.3438
All load ratios minus 0 loading curves	Test	Y	988	858	0.25	0.22	0.0795
		N	975	868	0.24	0.24	0.0794
	Model	Y	695	574	0.35	0.29	0.3641
		N	662	599	0.28	0.35	0.3613

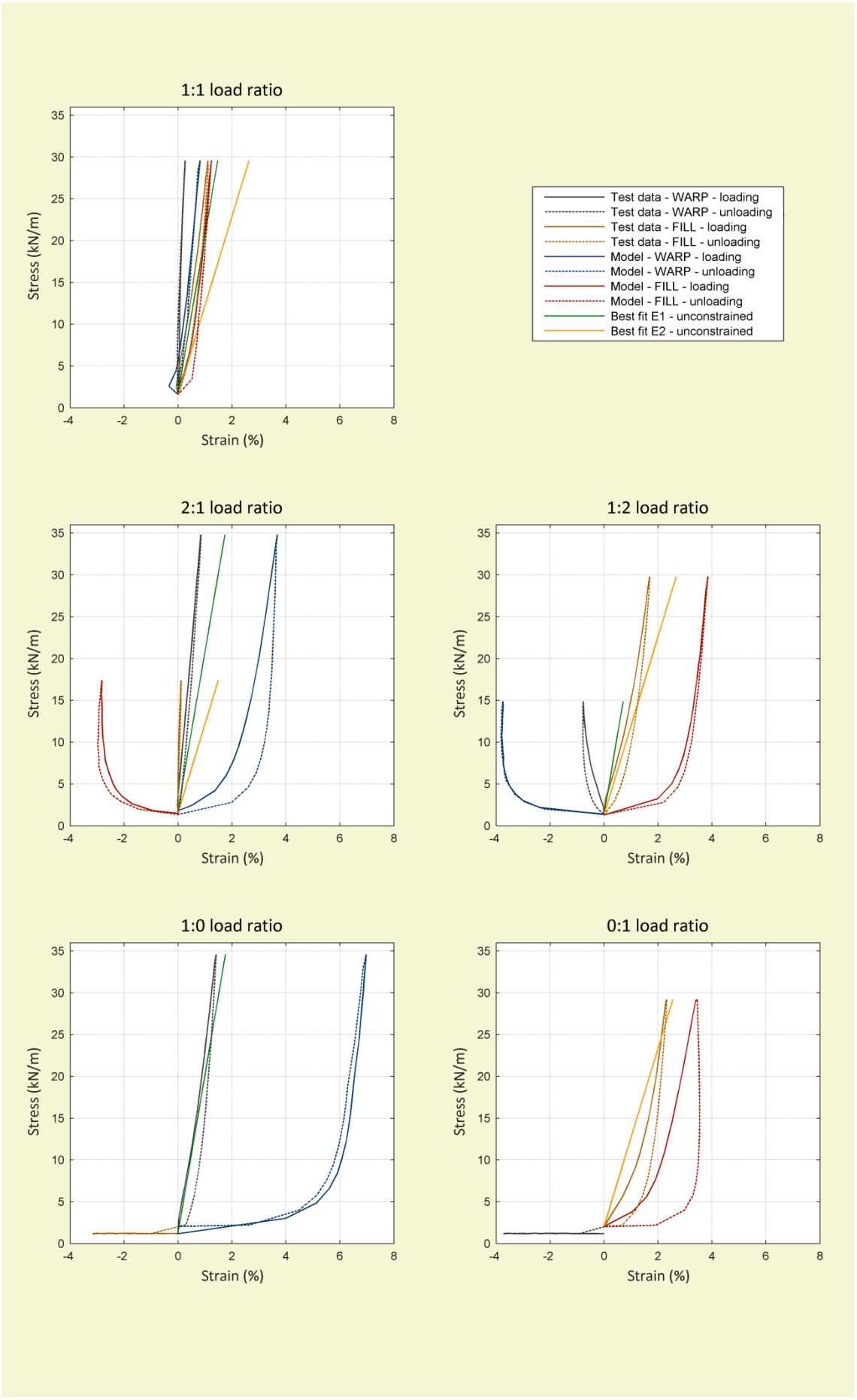

Figure 5.33 Stress-strain loading curves in determining stiffnesses for Verseidag B18089 (PTFE/glass)

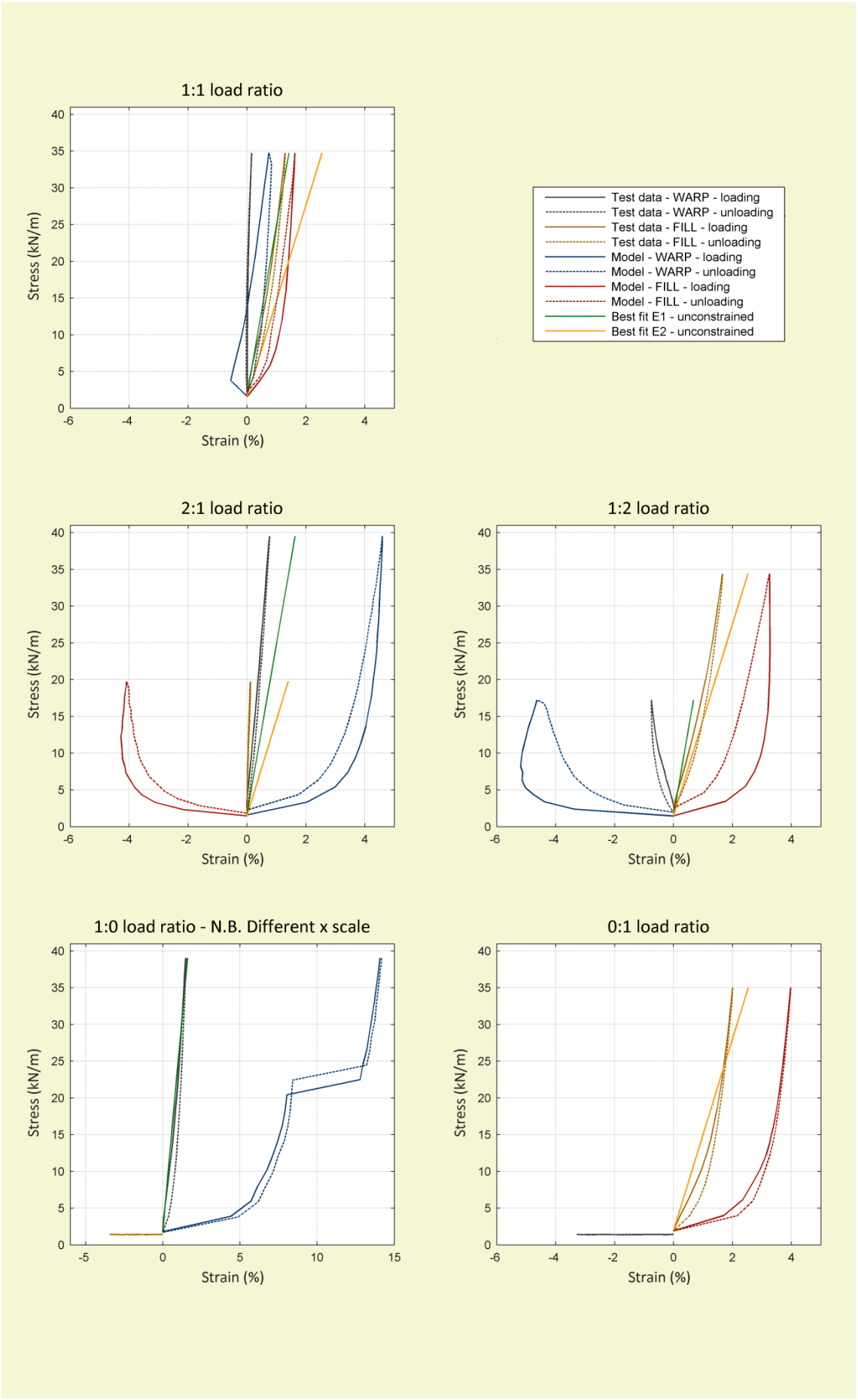

Figure 5.34 Stress-strain loading curves in determining stiffnesses for Verseidag B18059 (PTFE/glass)

Table 5.14 Best fit elastic moduli for Verseidag B18089, loading data only

Load ratios used to determine elastic constants	Source of data	Reciprocal constraint applied?	Warp stiffness, E_1, (kN/m)	Fill stiffness, E_2, (kN/m)	Warp-fill Poisson's ratio, ν_{12}	Fill-warp Poisson's ratio, ν_{21}	Sum of strain differences squared, s, (% strain)
All load ratios	Test	Y	1537	892	1.27	0.73	0.4334
		N	1418	937	1.06	0.87	0.4128
	Model	Y	212	202	1.35	1.29	65.2178
		N	268	169	2.09	0.77	58.4740
All load ratios minus 0 loading curves	Test	Y	1897	1065	0.74	0.41	0.1863
		N	1866	1075	0.71	0.43	0.1863
	Model	Y	306	325	0.73	0.78	6.3883
		N	332	300	0.88	0.63	6.3379

Table 5.15 Best fit elastic moduli for Verseidag B18059, loading data only

Load ratios used to determine elastic constants	Source of data	Reciprocal constraint applied?	Warp stiffness, E_1, (kN/m)	Fill stiffness, E_2, (kN/m)	Warp-fill Poisson's ratio, ν_{12}	Fill-warp Poisson's ratio, ν_{21}	Sum of strain differences squared, s, (% strain)
All load ratios	Test	Y	1758	1061	1.21	0.73	0.3868
		N	1671	1095	1.08	0.81	0.3796
	Model	Y	~~192~~	~~210~~	~~1.17~~	~~1.29~~	~~90.1665~~
		N	~~185~~	~~220~~	~~1.08~~	~~1.42~~	~~89.8264~~
All load ratios minus 0 loading curves	Test	Y	2320	1303	0.71	0.40	0.1502
		N	2308	1307	0.70	0.40	0.1502
	Model	Y	~~256~~	~~313~~	~~0.67~~	~~0.82~~	~~15.9462~~
		N	~~269~~	~~294~~	~~0.76~~	~~0.70~~	~~15.9074~~

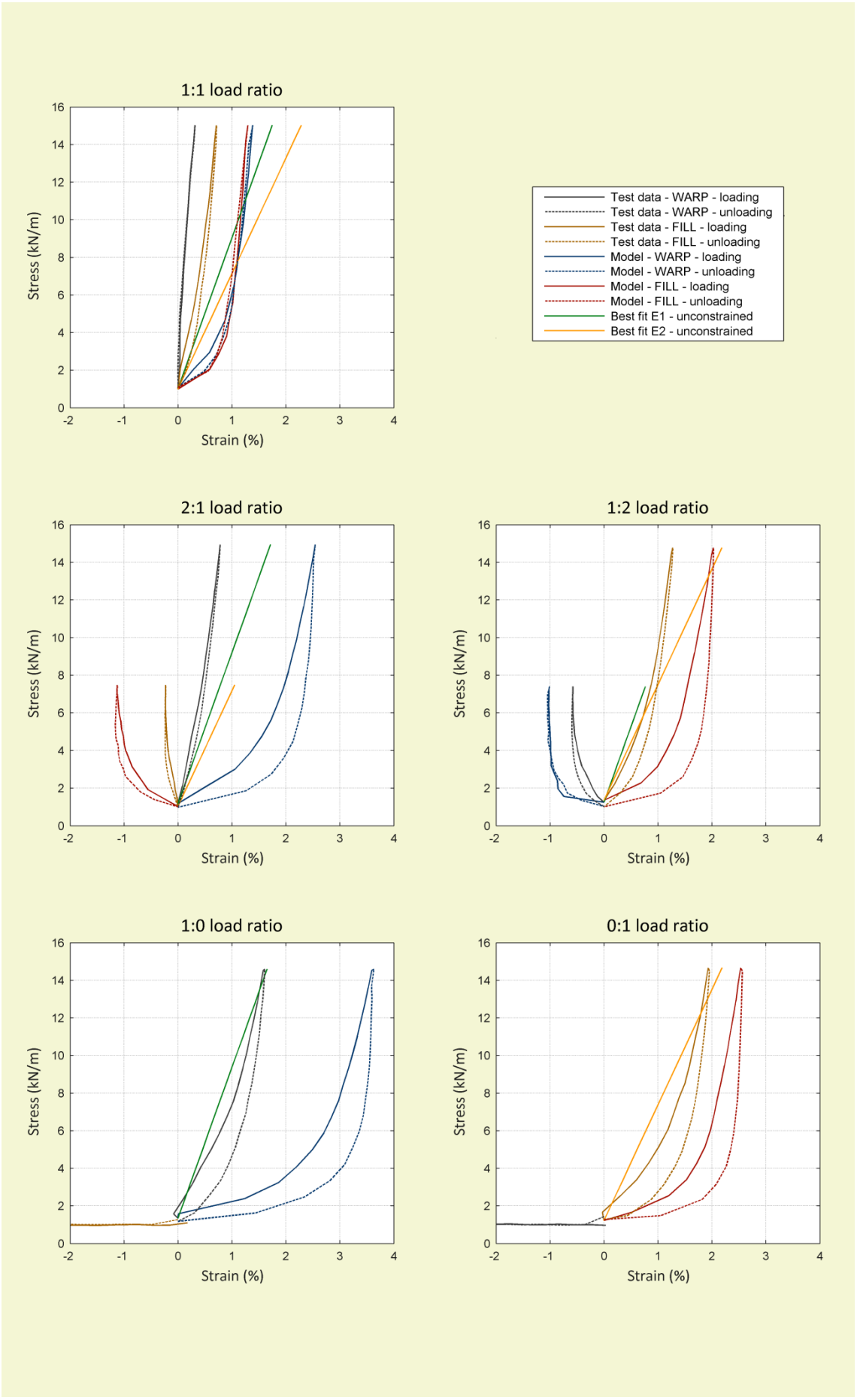

Figure 5.35 Stress-strain loading curves for PD Interglas ATEX3000 (silicone/glass)

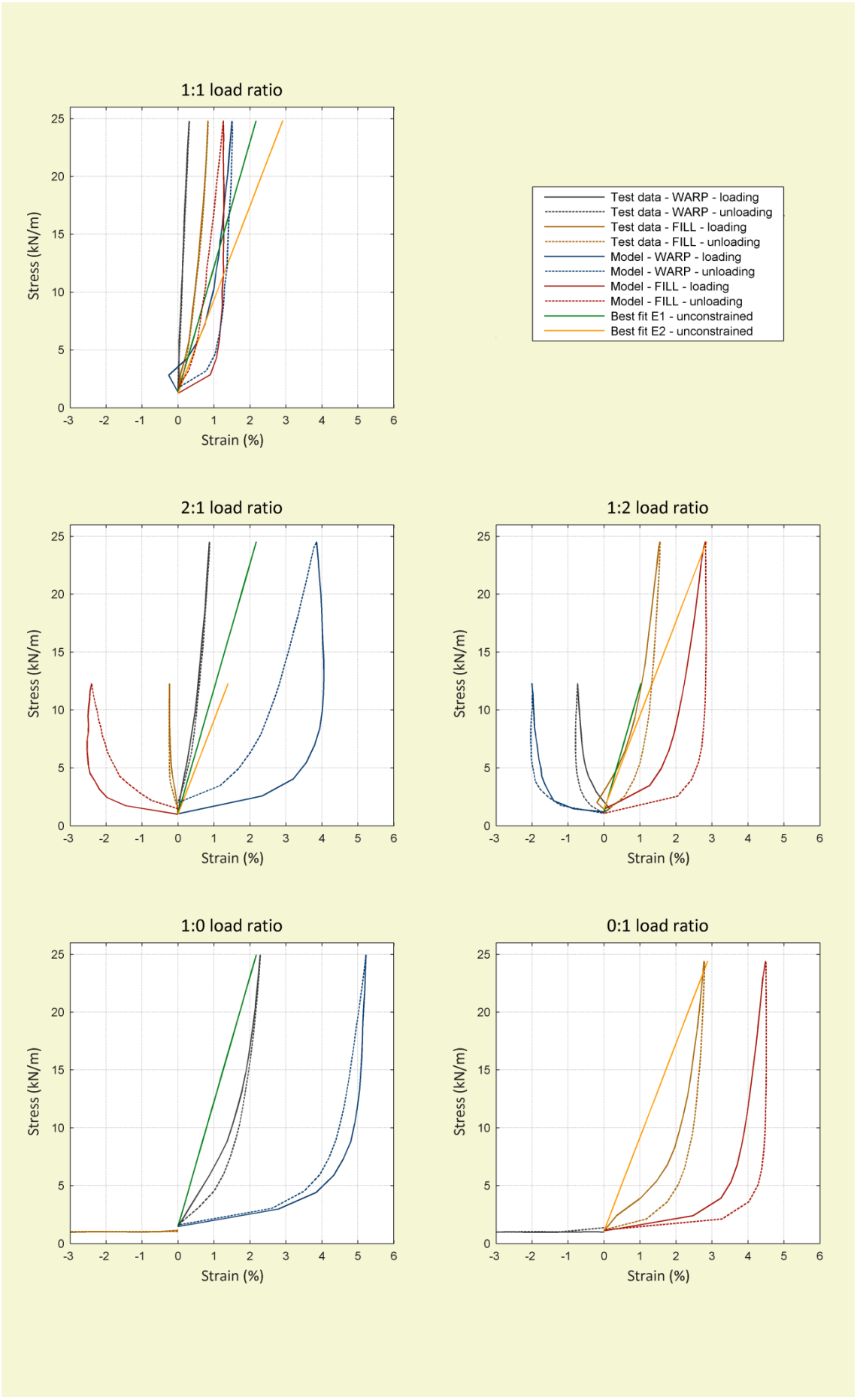

Figure 5.36 Stress-strain loading curves for PD Interglas ATEX5000 (silicone/glass)

Table 5.16 Best fit elastic moduli for PD Interglas ATEX3000, loading data only

Load ratios used to determine elastic constants	Source of data	Reciprocal constraint applied?	Warp stiffness, E_1, (kN/m)	Fill stiffness, E_2, (kN/m)	Warp-fill Poisson's ratio, ν_{12}	Fill-warp Poisson's ratio, ν_{21}	Sum of strain differences squared, s, (% strain)
All load ratios	Test	Y	602	489	1.08	0.88	0.3286
		N	643	465	1.26	0.76	0.3165
	Model	Y	230	254	0.93	1.03	3.0414
		N	252	232	1.16	0.81	2.8847
All load ratios minus 0 loading curves	Test	Y	802	614	0.66	0.50	0.2179
		N	791	620	0.64	0.52	0.2179
	Model	Y	266	300	0.58	0.65	0.9053
		N	262	305	0.55	0.68	0.9047

Table 5.17 Best fit elastic moduli for PD Interglas ATEX5000, loading data only

Load ratios used to determine elastic constants	Source of data	Reciprocal constraint applied?	Warp stiffness, E_1, (kN/m)	Fill stiffness, E_2, (kN/m)	Warp-fill Poisson's ratio, ν_{12}	Fill-warp Poisson's ratio, ν_{21}	Sum of strain differences squared, s, (% strain)
All load ratios	Test	Y	632	533	1.14	0.96	1.3928
		N	686	500	1.36	0.80	1.3420
	Model	Y	168	188	1.13	1.26	42.6615
		N	218	150	1.92	0.70	36.7183
All load ratios minus 0 loading curves	Test	Y	1079	809	0.57	0.43	0.6316
		N	962	891	0.39	0.58	0.6262
	Model	Y	252	285	0.64	0.72	4.0259
		N	232	315	0.50	0.91	3.9779

5.5 Summary

Input parameters for the predictive fabric model have been obtained through test methods available in typical material testing laboratories. Biaxial testing has been performed on a range of fabrics which represent the most common materials used in the construction of tensile fabric structures to generate test data for validation of the model.

The model has been implemented with no modification factors or calibration against biaxial test data. The test data has been compared to stress-strain predictions made by different model formulations: the improved unit cell model including the novel look-up function; a sinusoidal linear stiffness model; and a sawtooth linear stiffness model. For the PVC/PES fabrics, the improved model is more accurate than the linear models overall. The improved model replicates the non-linear, hysteric behaviour of real fabric behaviour. With residual strains removed, the improved model achieves greater accuracy than then linear stiffness models across all fabrics tested for 1:1 load ratios. However, at load ratios other than 1:1 the model fails to replicate a mechanism which resists contraction in the yarn directions. Further work is needed to identify the mechanisms which limit contraction of the fabric and to incorporate them into the predictive model.

Chapter 6:
Conclusions and recommendations for future work

6.1 Research summary

This project has focused on the determination and prediction of the material behaviour of architectural fabrics. **Detailed summaries are provided at the end of the preceding chapters** and this chapter provides a concise overview of the project's main conclusions.

The **literature review** described the existing level of knowledge regarding architectural fabrics and relevant associated testing and modelling practices. Key areas of limited knowledge are:

1. Although a number of fabric models exist, the majority concern uncoated fabrics and fabric deformation for rigid composite forming. There is a lack of models which accurately predict the non-linear stiffness characteristics of coated architectural fabrics. Further, many existing models require experimental determination of yarn properties, for example transverse yarn stiffness, or calibration against test data.
2. There is a lack of understanding of shear behaviour of architectural fabrics and the influence of biaxial tension on shear stiffness.
3. While shear testing has been performed on woven materials for decades, many shear test methodologies are unsuitable for testing of architectural fabrics as they cannot simultaneously apply biaxial deformation and shear to a test specimen. Of the methods which are suitable for shear testing of architectural fabrics, achieving homogeneity of the strain field is an issue.

6.2 Conclusions

The aim of this research was to develop an analytical/numerical tool to enable the accurate prediction of the non-linear stiffness characteristics of architectural fabrics for analysis of tensile fabric structures. A predictive fabric model has been developed using a unit cell modelling approach and experimental testing has been carried out to provide model input data and data for validation of the model. The conclusions related to the research objectives presented in Chapter 1 are outlined below.

Design and fabricate a shear test apparatus suitable for architectural fabrics:

Comparison of available shear methods demonstrated the suitability of the picture frame shear test for characterising shear behaviour of architectural fabrics. A novel picture frame design has been fabricated which avoids crushing of the fabric in the corners of the frame and which applies a homogenous strain field during testing. The shear angle experienced by a test specimen is less than the angle applied by the frame, so instrumentation mounted to the surface of the test specimen is required to measure strains. Friction of the corners of the frame should be accounted for when determining shear stiffness.

Investigate the in-plane shear behaviour of architectural fabrics:

An improved understanding of shear behaviour has been established. Shear behaviour is shown to change with increasing biaxial stress, with greater strain energy required to mobilise shear deformation in a highly tensioned fabric. Whether biaxial pretension affects constant values of the shear stiffness of the fabric depends on how the stiffness is evaluated from the non-linear, hysteretic shear response. The use linear approximations may be problematic for designers as consensus is needed on how shear test results should be interpreted.

Improve the accuracy of the predictive model unit cell model proposed by Bridgens (2005):

A significant development of the proposed model is the development of a novel look up function which uses cyclic uniaxial stress-strain data to enable the model to predict biaxial non-linear, inelastic load response and hysteresis. The look up function disposes with the requirement to subjectively determine a representation of the yarn moduli, such as linear or multi linear representation. Further, each prediction at a given biaxial stress ratio is not made independently of a material's stress-strain history.

Develop the model to include shear response:

A shear model was not fully implemented. At the project's outset, it was not envisaged that development of a suitable shear test apparatus would be required. Initial shear testing, and the literature review, demonstrated that the existing shear test equipment at Newcastle University was unsuitable for use in this project. Following the development of a reliable shear frame, there was not time to fully develop a shear model. However, an initial approach has been identified from existing shear models.

Develop suitable testing to provide the model with input parameters:

Uniaxial testing is used to provide the model with input data and a macrophotography methodology has been developed for obtaining measurements of yarn cross sections. Where values of coating stiffness are required, bias testing achieves more accurate values than interpretation of uniaxial test results.

Demonstrate the accuracy of the predictive model through a series of comparative tests:

The predictive unit cell model can replicate the non-linear load response and hysteresis of the PVC/PES fabrics tested. Although, without the inclusion of a coating or yarn compression factor, such as that used in the earlier model by Bridgens (2005), the model cannot accurately predict strains at non 1:1 load ratios.

6.3 Recommendations for future work

There are several ways in which the work presented in this thesis can be taken forward:

- **Further development of the predictive unit cell model**. Further developments should include accounting for resistance to negative strains, i.e. a mechanism which replicates coating and/or yarn compression stiffnesses. This may require development of methods to accurately determine yarn and coating compressive properties. The shear model should also be fully implemented.
- **Assessment of fabric variability**. The predictive model could be used to investigate the variability of woven materials by accounting for variability in the properties of the yarns and the coating. Values for use in design could then be specified as an envelope of values accounting for variation in the materials. The measurements of fabric cross sections collected in this study could be used to undertake such an assessment.
- **Reverse engineering of architectural fabrics**. The model could be further developed to design architectural fabrics with specified material properties, i.e. for given stiffness values the model would determine required yarn and coating properties. A project is underway at Newcastle University to develop such a model.
- **Interpretation of shear test data**. Uncertainty over a choice of a single stiffness value should be addressed. This could be achieved with the use of a statistical approach.
- **Comparative shear testing studies**. A comparative study of the various shear test apparatuses and protocols used in multiple laboratories would quantify the level of consistency achieved by the various methods. The studies could also include interpretation of shear test results.
- **Picture frame modifications**. To reduce or remove friction in the hinges of the frame, modification to the frame could include replacement of the self-lubricating bushes with needle roller bearings.

References

Ansar, M., Xinwei, W., Chouwei, Z., (2011) 'Modeling strategies of 3D woven composites: A review', Composite Structures, 93(8), pp. 1947-1963.

ASCE/SEI (2010) 55-10: Tensile Membrane Structures.

Ayranci, C., Carey, J., (2008) '2D braided composites: A review for stiffness critical applications', Composite Structures, 85(1) 2008, pp. 43-58.

Badel, P., Vidal-Sallé, E. and Boisse, P. (2007) 'Computational determination of in-plane shear mechanical behaviour of textile composite reinforcements', Computational Materials Science, 40(4), pp. 439-448.

Balz, M. and Dencher, M. (2004) 'Design Loading Conditions', in Foster, B. and Mollaert, M. (eds.) European Design Guide for Tensile Surface Structrues. Brussels: TensiNet, pp. 191-204.

Barnes, M., Foster, B. and Dencher, M. (2004a) 'Structural design basis and safety criterea', in Foster, B. and Mollaert, M. (eds.) European design guide for tensile surface structrues. TensiNet, pp. 177-190.

Barnes, M., Grundig, L. and Moncrieff, E. (2004b) 'Form-finding, load analysis and patterning', in Foster, B. and Mollaert, M. (eds.) European design guide for tensile surface structures. TensiNet, pp. 205-218.

Bartle, N.J., Gosling, P.D. and Bridgens, B.N. (2013) 'A Neural Network Material Model for the Analysis of Fabric Structures', TensiNet Symposium Mimar Sinan Fine-Art University, Istanbul, 8 May 2013.

Bassett, R.J., Postle, R. and Pan, N. (1999) 'Experimental Methods for Measuring Fabric Mechanical Properties: A Review and Analysis', Textile Research Journal, 69(11), pp. 866-875.

Berger, H. (1999) 'Form and function of tensile structures for permanent buildings', Engineering Structures, 21(8), pp. 669-679.

Birchall, M. (2013) 'Pneumatic structures and the state of the art: learning from the past, looking forward to the future', TensiNet Symposium: [Re]Thinking lightweight structures. Istanbul, Turkey. TensiNet.

Blacketter, D.M., Walrath, D. E., and Hansen, A. C., (1995) 'Modeling damage in plain weave reinforced composite material', J. Composite materials, 29 pp. 233-2363.

Blum, R. and Bögner, H. (2001) 'A new class of biaxial machine', Internet publication http://www.tensinet.com Tensinews Newslett, 1, p. 4.

Blum, R., Bögner, H. and Némoz, G. (2004a) 'Material Properties and Testing', in Foster, B. and Mollaert, M. (eds.) European Design Guide for Tensile Surface Structures. Bussels: TensiNet, pp. 219-242.

Blum, R., Bögner, H. and Némoz, G. (2004b) 'Testing Methods and Standards', in Foster, B. and Mollaert, M. (eds.) European Design Guide for Tensile Surface Structures. Brussels: TensiNet, pp. 293-322.

Boisse, P., Gasser, A. and Hivet, G. (2001) 'Analyses of fabric tensile behaviour: determination of the biaxial tension–strain surfaces and their use in forming simulations', Composites Part A: Applied Science and Manufacturing, 32(10), pp. 1395-1414.

Boisse, P., Zouari, B. and Gasser, A. (2005) 'A mesoscopic approach for the simulation of woven fibre composite forming', Composites Science and Technology, 65(3-4), pp. 429-436.

Bridgens, B.N. (2005) Architectural fabric properties: Determination, representation and prediction. PhD thesis. Newcastle University.

Bridgens, B. and Birchall, M. (2012) 'Form and function: The significance of material properties in the design of tensile fabric structures', Engineering Structures, 44(0), pp. 1-12.

Bridgens, B.N. and Gosling, P.D. (2004) 'A New Biaxial Test Protocol for Architectural Fabrics', Journal of the International Association for Shell and Spatial Structures (J. IASS), 45(3), pp. 175-181.

Bridgens, B.N., Gosling, P.D. and Birchall, M.J.S. (2004a) 'Membrane material behaviour: concepts, practice and developments', The Structural Engineer, 82(14), pp. 28-33.

Bridgens, B.N., Gosling, P.D. and Birchall, M.J.S. (2004b) 'Tensile fabric structures: concepts, practice and developments', The Structural Engineer, 82(14), pp. 21-27.

Bridgens, B., Gosling, P., Jou, G.T. and Hsu, X.Y. (2011) 'Inter-laboratory comparison of biaxial tests for architectural textiles', Journal of the Textile Institute, 103(7), pp. 706-718.

BSI (1993) Testing coated fabrics – Part 21: Method 24. Method for determination of elongation and tension set. British Standards Institute (BSI).

BSI (1998) Rubber- or plastics-coated fabrics – Determination of tensile strength and elongations at break. British Standards Institute (BSI).

Bögner-Balz, H. and Blum, R. (2008) 'The Mechanical Behaviour of Coated Fabrics Used in Prestressing Textile Engineering Structures: Theory, Simulation and Numerical Analysis to Be Used in a FEM-Model', Journal of the International Association for Shell and Spatial Structures (J. IASS), 49(1), pp. 39-47.

Cai, Z. and Gutowski, T. (1992) 'The 3-D Deformation Behavior of a Lubricated Fiber Bundle', Journal of Composite Materials, 26(8), pp. 1207-1237.

Cao, J., Akkerman, R., Boisse, P., Chen, J., Cheng, H.S., de Graaf, E.F., Gorczyca, J.L., Harrison, P., Hivet, G., Launay, J., Lee, W., Liu, L., Lomov, S.V., Long, A., de Luycker, E., Morestin, F., Padvoiskis, J., Peng, X.Q., Sherwood, J., Stoilova, T., Tao, X.M., Verpoest, I., Willems, A., Wiggers, J., Yu, T.X. and Zhu, B. (2008) 'Characterization of mechanical behavior of woven fabrics: Experimental methods and benchmark results', Composites Part A: Applied Science and Manufacturing, 39(6), pp. 1037-1053.

Cavallaro, P.V., Sadegh, A.M. and Quigley, C.J. (2007) 'Decrimping Behavior of Uncoated Plain-woven Fabrics Subjected to Combined Biaxial Tension and Shear Stresses', Textile Research Journal, 77(6), pp. 403-416.

Chapman, C. and Whitcomb J. D., (1995) Effect of assumed tow architecture on predicted moduli and stress in plain weave composites. Journal composite materials, 29 pp. 214-2159.

Colman, A.G., Bridgens, B.N., Gosling, P.D., Jou, G.T. and Hsu, X.Y. (2014) 'Shear behaviour of architectural fabrics subjected to biaxial tensile loads', Composites Part A: Applied Science and Manufacturing, 66(0), pp. 163-174.

Clulow, E.E. and Taylor, H.M. (1963) 'An experimental and theoretical investigation of biaxial stress–strain relations in a plain-weave cloth', Journal of the Textile Institute Transactions, 54(8), pp. T323-T347.

Crookston, J.J., Long, A.C., Jones, I.A., (2005) 'A summary review of mechanical properties prediction methods for textile reinforced polymer composites' Proceedings of the Institution of Mechanical Engineers, Part L: Journal of Materials Design and Applications, 219, pp. 91-109.

Culpin, M.F. (1979) 'The shearing of fabrics: A novel approach', Journal of the Textile Institute, 70(3), pp. 81-88.

Cusick, G.E. (1965) 'The dependence of fabric drape on bending and shear stiffness', Journal of the Textile Institute Transactions, 56(11), pp. T596-T606.

Durville, D. (2008) 'Finite Element Simulation of the Mechanical Behaviour of Textile Composites at the Mesoscopic Scale of Individual Fibers', in Oñate, E. and Kröplin, B. (eds.) Textile Composites and Inflatable Structures II. Springer Netherlands, pp. 15-34.

Desplentere, F., Lomov, S.V., Woerdeman, D.L., Verpoest, I., Wevers, M. and Bogdanovich, A. (2005) 'Micro-CT characterization of variability in 3D textile architecture', Composites Science and Technology, 65(13), pp. 1920-1930.

Dolatabadi, M.K. and Kovař, R. (2009a) 'Geometry of plain weave fabric under shear deformation. Part II: 3D model of plain weave fabric before deformation', Journal of the Textile Institute, 100(5), pp. 381 - 386.

Dolatabadi, M.K. and Kovař, R. (2009b) 'Geometry of plain weave fabric under shear deformation. Part III: 3D model of plain weave fabric under shear deformation', Journal of the Textile Institute, 100(5), pp. 387 - 399.

Dreby, E.C. (1941) 'The Planoflex, a simple device for the evaluating the pliability of fabrics', Journal of Research of the National Bureau of Standards, 27, pp. 469-477.

Drew, P. (2008) New Tent Architecture. London, UK: Thames and Hudson.

Eddleston, P. (2007) Accurately measuring architectural fabric weave geometry. MEng thesis. Newcastle Univesity.

Eeg-Olofsson, T. (1955) 'Relation between Fabric Deformation and Fabric Structure', Ann. Sei. Textiles Beiges NR, 4, p. 7.

Farboodmanesh, S., Chen, J., Mead, J.L., White, K.D., Yesilalan, H.E., Laoulache, R. and Warner, S.B. (2005) 'Effect of Coating Thickness and Penetration on Shear Behavior of Coated Fabrics', Journal of Elastomers and Plastics, 37(3), pp. 197-227.

Fournier, F. (2013) 'LCA of PRECONTRAINT composite membranes & TEXYLOOP recycling case studies', TensiNet Symposium: [Re]Thinking lightweight structures. Istanbul, Turkey. TensiNet.

Freeston, W.D., Platt, M.M. and Schoppee, M.M. (1967) 'Mechanics of Elastic Performance of Textile Materials: Part XVIII. Stress-Strain Response of Fabrics Under Two-Dimensional Loading1', Textile Research Journal, 37(11), pp. 948-975.

Galliot, C. and Luchsinger, R.H. (2010a) 'The shear ramp: A new test method for the investigation of coated fabric shear behaviour – Part I: Theory', Composites Part A: Applied Science and Manufacturing, 41(12), pp. 1743-1749.

Galliot, C. and Luchsinger, R.H. (2010b) 'The shear ramp: A new test method for the investigation of coated fabric shear behaviour – Part II: Experimental validation', Composites Part A: Applied Science and Manufacturing, 41(12), pp. 1750-1759.

Garrett, J. and Harris, G. (2008) Complete photography course. London, UK: HarperCollins.

Glaessgen, E.H., Pastore, C.M., Griffin, O.H. and Birger, A. (1996) 'Geometrical and finite element modelling of textile composites', Composites Part B: Engineering, 27(1), pp. 43-50.

Gong, R.H., Ozgen, B. and Soleimani, M. (2009) 'Modeling of Yarn Cross-Section in Plain Woven Fabric', Textile Research Journal, 79(11), pp. 1014-1020.

Gosling, P.D. and Bridgens, B.N. (2008) 'Material Testing & Computational Mechanics - A New Philosophy For Architectural Fabrics', International Journal of Space Structures, 23(4), pp. 215-232.

Gosling, P.D., Bridgens, B.N., Albrecht, A., Alpermann, H., Angeleri, A., Barnes, M., Bartle, N., Canobbio, R., Dieringer, F., Gellin, S., Lewis, W.J., Mageau, N., Mahadevan, R., Marion, J.M., Marsden, P., Milligan, E., Phang, Y.P., Sahlin, K., Stimpfle, B., Suire, O. and Uhlemann, J. (2013) 'Analysis and design of membrane structures: Results of a round robin exercise', Engineering Structures, 48(0), pp. 313-328.

Gosling, P.D., Bridgens, B.N. and Zhang, L. (2013b) 'Adoption of a reliability approach for membrane structure analysis', Structural Safety, 40(0), pp. 39-50.

Green, S.D., Matveev, M.Y., Long, A.C., Ivanov, D., Hallett, S.R., (2014) Mechanical modelling of 3D woven composites considering realistic unit cell geometry. Composite Structures, 118, pp. 284-293

Grosberg, P., Leaf, G.A.V. and Park, B.J. (1968) 'The Mechanical Properties of Woven Fabrics Part VI: The Elastic Shear Modulus of Plain-Weave Fabrics', Textile Research Journal, 38(11), pp. 1085-1100.

Grosberg, P. and Park, B.J. (1966) 'Part V: The initial modulus and the frictional restraint in shearing of plain weave fabrics', Textile Research Journal, 36, pp. 420-31.

Grujicic, M., Bell, W.C., Arakere, G., He, T. and Cheeseman, B.A. (2009) 'A meso-scale unit-cell based material model for the single-ply flexible-fabric armor', Materials & Design, 30(9), pp. 3690-3704.

Haas, R. and Dietzius, H. (1917) 'The stretching of the fabric and the shape of the envelope in non-rigid balloons', National Advisory Council on Aeronautics, Report, (16).

Harrison, P., Abdiwi, F., Guo, Z., Potluri, P. and Yu, W.R. (2012) 'Characterising the shear–tension coupling and wrinkling behaviour of woven engineering fabrics', Composites Part A: Applied Science and Manufacturing, 43(6), pp. 903-914.

Harrison, P., Clifford, M.J. and Long, A.C. (2002) 'Shear charcterisation of woven textile composites', 10th European conference on composite materials. Bruges, Belgium.

Harrison, P., Clifford, M.J. and Long, A.C. (2004) 'Shear characterisation of viscous woven textile composites: a comparison between picture frame and bias extension experiments', Composites Science and Technology, 64(10-11), pp. 1453-1465.

Hearle, J.W.S., Konopasek, M. and Newton, A. (1972) 'On some general features of a computer-based system for calculation of the mechanics of textile structure', Textile Research Journal, 42(10), pp. 613-626.

Hearle, J.W.S. and Shanahan, W.J. (1978) 'An energy method for calculations in fabric mechanics part i: principles of the method', Journal of the Textile Institute, 69(4), pp. 81-91.

Hivet, G. and Duong, A.V. (2011) 'A contribution to the analysis of the intrinsic shear behavior of fabrics', Journal of Composite Materials, 45(6), pp. 695-716.

Hu, J.-L. and Zhang, Y.-T. (1997) 'The KES shear test for fabrics', Textile research journal, 67(9), pp. 654-664.

Ivanov, S.D., Ivanov, S.G., Lomov, S.V., Verpoest, I., (2011) 'Unit cell modelling of textile laminates with arbitrary inter-ply shifts', Composites Science and Technology, 72(1), pp. 14-20.

Jackson, A.L., Bridgens, B.N. and Gosling, P.D. (2009) Evolution and Trends in Design, Analysis and Construction of Shell and Spatial Structures. Valencia. International Association for Shell and Spatial Structures (IASS).

Kato, S., Yoshino, T. and Minami, H. (1999) 'Formulation of constitutive equations for fabric membranes based on the concept of fabric lattice model', Engineering Structures, 21(8), pp. 691-708.

Kawabata, S. (1980) 'Examination of Effect of Basic Mechanical Properties of Fabrics on Fabric Hand, in" Mechanics of Flexible Fiber Assemblies,"', NATO Advanced Study Institute Series.(Eds JWS Hearle, JJ Thwaites, J Amirbayat) pp, pp. 405-417.

Kawabata, S. (1989) 'Nonlinear mechanics of woven and knitted materials', in Chou, T.-W. and Ko, F.K. (eds.) Textile structural composites. Amsterdam: Elsevier, pp. 67-116.

Kawabata, S., Niwa, M. and Kawai, H. (1973a) 'The finite-deformation theory of plain-weave fabrics. Part I: The biaxial deformation theory', Journal of the Textile Institute, 64(1), pp. 21-46.

Kawabata, S., Niwa, M. and Kawai, H. (1973b) 'The finite-deformation theory of plain-weave fabrics. Part III: The shear deformation theory', Journal of the Textile Institute, 64(2), pp. 42-85.

Kemp, A. (1958) 'An extension of Peirce's cloth geometry to the treatment of non-circular threads', Journal of the Textile Institute, 49, pp. T44-48.

King, M.J., Jearanaisilawong, P. and Socrate, S. (2005) 'A continuum constitutive model for the mechanical behavior of woven fabrics', International Journal of Solids and Structures, 42(13), pp. 3867-3896.

Klein, W.G. (1959) 'Stress-Strain Response of Fabrics Under Two-Dimensional Loading Part I: The RL Biaxial Tester', Textile Research Journal, 29(10), pp. 816-821.

Launay, J., Hivet, G., Duong, A.V. and Boisse, P. (2008) 'Experimental analysis of the influence of tensions on in plane shear behaviour of woven composite reinforcements', Composites Science and Technology, 68(2), pp. 506-515.

Leaf, G.A.V. and Sheta, A.M.F. (1984) 'The initial shear modulus of plain woven fabrics', Journal of the Textile Institute, 75(3), pp. 157-163.

Lebrun, G., Bureau, M.N. and Denault, J. (2003) 'Evaluation of bias-extension and picture-frame test methods for the measurement of intraply shear properties of PP/glass commingled fabrics', Composite Structures, 61(4), pp. 341-352.

Liu, L., Chen, J., Gorczyca, J.L. and Sherwood, J.A. (2004) 'Modeling of Friction and Shear in Thermostamping of Composites - Part II', Journal of Composite Materials, 38(21), pp. 1931-1947.

Liu, L., Chen, J., Li, X. and Sherwood, J. (2005) 'Two-dimensional macro-mechanics shear models of woven fabrics', Composites Part A: Applied Science and Manufacturing, 36(1), pp. 105-114.

Lo, W.M. and Hu, J.L. (2002) 'Shear properties of woven fabrics in various directions', Textile research journal, 72(5), pp. 383-390.

Lomov, S.V., Boisse, P., Deluycker, E., Morestin, F., Vanclooster, K., Vandepitte, D., Verpoest, I. and Willems, A. (2008) 'Full-field strain measurements in textile deformability studies', Composites Part A: Applied Science and Manufacturing, 39(8), pp. 1232-1244.

Lomov, S.V., Huysmans, G., Luo, Y., Parnas, R.S., Prodromou, A., Verpoest, I. and Phelan, F.R. (2001) 'Textile composites: modelling strategies', Composites Part A: Applied Science and Manufacturing, 32(10), pp. 1379-1394.

Lomov, S.V., Truong Chi, T., Verpoest, I., Peeters, T., Roose, D., Boisse, P. and Gasser, A. (2003a) 'Mathematical modelling of internal geometry and deformability of woven preforms', International Journal of Forming Processes, 6, pp. 413-442.

Lomov, S.V. and Verpoest, I. (2006) 'Model of shear of woven fabric and parametric description of shear resistance of glass woven reinforcements', Composites Science and Technology, 66(7-8), pp. 919-933.

Lomov, S.V., Verpoest, I., Barburski, M. and Laperre, J. (2003b) 'Carbon composites based on multiaxial multiply stitched preforms. Part 2. KES-F characterisation of the deformability of the preforms at low loads', Composites Part A: Applied Science and Manufacturing, 34(4), pp. 359-370.

Mack, C. and Taylor, H.M. (1956) 'The fitting of woven cloth to surfaces', Journal of the Textile Institute, 47, pp. 477-89.

MacRory, B.M. and McNamara, A.B. (1967) 'Knitted Fabrics Subjected to Biaxial Stress—An Experimental Study', Textile Research Journal, 37(10), pp. 908-911.

Matsudaira, M., Kawabata, S. and Niwa, M. (1985) 'Measurement of Mechanical Properties of Thin-Dress Fabrics for Hand Evaluation', Journal of the Textile Machinery Society of Japan, 31(3), pp. 53-60.

McBride, T.M. and Chen, J. (1997) 'Unit-cell geometry in plain-weave fabrics during shear deformations', Composites Science and Technology, 57(3), pp. 345-351.

McGuinness, G.B. and ÓBrádaigh, C.M. (1998) 'Characterisation of thermoplastic composite melts in rhombus-shear: the picture-frame experiment', Composites Part A: Applied Science and Manufacturing, 29(1), pp. 115-132.

Mellor, T. (2006) Reliability-based determination of the strength and stiffness of PVC-coated polyester architectural fabrics. MEng thesis. Newcastle University.

Menges, G. and Meffert, B. (1976) 'Mechanical behaviour of PVC-coated polyester fabrics under biaxial stress', Kunststoffe German plastic, 66(11), pp. 12-14/741-745.

Mohammed, U., Lekakou, C., Dong, L. and Bader, M.G. (2000) 'Shear deformation and micromechanics of woven fabrics', Composites Part A: Applied Science and Manufacturing, 31(4), pp. 299-308.

Mollaert, M. and Foster, B. (eds.) (2004) European Design Guide for Tensile Surface Structures. TensiNet.

Mott, R., Huber, G. and Leewood, A. (1985) 'Biaxial test method for characterization of fabric materials used in permanent fabric roof structures', Journal of testing and evaluation, 13(1), pp. 9-16.

MSAJ (1993) Standard of the Membrane Structures Association of Japan. Testing method for in-plane shear stiffness of membrane materials. Membrane Structures Association of Japan.

MSAJ (1995) Standard of the Membrane Structures Association of Japan. Testing method for elastic constants of membrane materials. Membrane Structures Association of Japan.

Naik, N.K. and Madhavan, V. (2000) 'Twisted impregnated yarns: Elastic properties', The Journal of Strain Analysis for Engineering Design, 35(2), pp. 83-91.

Nguyen, M., Herszberg, I. and Paton, R. (1999) 'The shear properties of woven carbon fabric', Composite Structures, 47(1-4), pp. 767-779.

Nguyen, Q.T., Vidal-Sallé, E., Boisse, P., Park, C.H., Saouab, A., Bréard, J. and Hivet, G. (2013) 'Mesoscopic scale analyses of textile composite reinforcement compaction', Composites Part B: Engineering, 44(1), pp. 231-241.

Olofsson, B. (1964) 'General model of a fabric as a geometric-mechanical structure', Journal of the Textile Institute Transactions, 55(11), pp. T541-T557.

Otto, F. (ed.) (1967) Tensile Structures. Cambridge, MA: M.I.T. Press.

Otto, F. (2004) 'Forward', in Foster, B. and Mollaert, M. (eds.) European Design Guide for Tensile Surface Structures. TensiNet, pp. 5-7.

Page, J. and Wang, J. (2000) 'Prediction of shear force and an analysis of yarn slippage for a plain-weave carbon fabric in a bias extension state', Composites Science and Technology, 60(7), pp. 977-986.

Pargana, J.B., Lloyd Smith, D. and Izzuddin, B.A. (2000) 'Advanced material model for the analysis of tensioned fabric structures', Computational Methods for Shell and Spatial Structures, IASS-IACM 2000.

Pargana, J.B., Lloyd-Smith, D. and Izzuddin, B.A. (2007) 'Advanced material model for coated fabrics used in tensioned fabric structures', Engineering Structures, 29(7), pp. 1323-1336.

Peirce, F.D. (1937) 'The geometry of cloth structures', Journal of the Textile Institute, 28, pp. T45-96.

Peng, X.Q. and Cao, J. (2005) 'A continuum mechanics-based non-orthogonal constitutive model for woven composite fabrics', Composites Part A: Applied Science and Manufacturing, 36(6), pp. 859-874.

Peng, X.Q., Cao, J., Chen, J., Xue, P., Lussier, D.S. and Liu, L. (2004) 'Experimental and numerical analysis on normalization of picture frame tests for composite materials', Composites Science and Technology, 64(1), pp. 11-21.

Potluri, P. and Sagar, T.V. (2008) 'Compaction modelling of textile preforms for composite structures', Composite Structures, 86(1-3), pp. 177-185.

Potter, K. (2002) 'Bias extension measurements on cross-plied unidirectional prepreg', Composites Part A: Applied Science and Manufacturing, 33(1), pp. 63-73.

Potter, K.D. (1979) 'The influence of accurate stretch data for reinforcements on the production of complex structural mouldings: Part 1. Deformation of aligned sheets and fabrics', Composites, 10(3), pp. 161-167.

Prodromou, A.G. and Chen, J. (1997) 'On the relationship between shear angle and wrinkling of textile composite preforms', Composites Part A: Applied Science and Manufacturing, 28(5), pp. 491-503.

Ramgulam, R., Potluri, P. and Ciurezu, D. (2008) 'Tensile and Shear Deformation Modelling of Woven Fabrics', International Journal of Material Forming, 1(0), pp. 945-948.

Reichardt, C.H., Woo, H.K. and Montgomery, D.J. (1953) 'A two-dimensional load-extension tester for woven fabrics', Textile Research Journal, 23(6), pp. 424-428.

Reinhardt, H.W. (1976) 'On the biaxial testing and strength of coated fabrics', Experimental Mechanics, 16(2), pp. 71-74.

Sasai, T. and Kawabata, S. (1985) 'Biaxial tensile properties of textured yarn fabrics', Journal of the Textile Machinery Society of Japan, 31(2), pp. 29-34.

Schock, H.J. (1991) 'On The Structural Behavior and Material Characteristics of PTFE-Coated Glass-Fiber Fabric', Journal of Industrial Textiles, 20(4), pp. 277-288.

Šejnoha, M., Zeman, J., (2008) 'Micromechanical modelling of imperfect textile composites', International Journal of Engineering Science, 46(6) pp. 513-526.

Sharma, S.B., Sutcliffe, M.P.F. and Chang, S.H. (2003) 'Characterisation of material properties for draping of dry woven composite material', Composites Part A: Applied Science and Manufacturing, 34(12), pp. 1167-1175.

Skelton, J. (1976) 'Fundamentals of Fabric Shear', Textile Research Journal, pp. 862-869.

Skelton, J. (1980) 'Shear of woven fabrics', NATO Advanced Study Institute on Mechanics of fiberous assemblies. Netherlands. Sijthoff & Noordhoff, pp. 212-226.

Skelton, J. and Freeston, J.W.D. (1971) 'Mechanics of elastic performance of textile materials. Part XIX: The shear behavior of fabrics under biaxial loads', Textile Research Journal, 41(11), pp. 871-880.

Spivak, S.M. and Treloar, L.R.G. (1968) 'The Behavior of Fabrics in Shear Part III: The Relation Between Bias Extension and Simple Shear', Textile research journal, 38(9), pp. 963-971.

Stroud, K.A. (1996) Further Engineering Mathematics. Third edn. Hampshire: Palgrave Macmillan.

Stroud, K.A. (2011) Advanced Engineering Mathematics. Fifth edn. Hampshire, UK: Palgrave Macmillan.

Stubbs, N. and Fluss, H. (1980) 'A space-truss model for plain-weave coated fabrics', Applied Mathematical Modelling, 4(1), pp. 51-58.

Sun, H. and Pan, N. (2005) 'Shear deformation analysis for woven fabrics', Composite Structures, 67(3), pp. 317-322.

Tanov, R.R. and Brueggert, M. (2003) 'Finite element modeling of non-orthogonal loosely woven fabrics in advanced occupant restraint systems', Finite elements in analysis and design, 39(5), pp. 357-367.

Testa, R.B., Spillers, W.R. and Stubbs, N. (1978) 'Bilinear Model for Coated Square Fabrics', Journal of the Engineering Mechanics Division, 104(5), pp. 1027-1042.

Turner, A.W., Kabche, J.P., Peterson, M.L. and Davids, W.G. (2008) 'Tension/torsion testing of inflatable fabric tubes', Experimental Techniques, 32(2), pp. 47-52.

Vysochina, K., Gabor, A., Bigaud, D. and Ronel-Idrissi, S. (2005) 'Identification of Shear Stiffness of Soft Orthotropic Textile Composites: Part I – Development of a Mixed Method for Shear Elastic Constant Identification', Journal of Industrial Textiles, 35(2), pp. 137-155.

Wang, F. (2002) 'Prediction method for tensile property of woven fabrics in lower loads', Journal of Dong Hua University (Eng. Ed.), 19(2), pp. 6-14.

Willems, A., Lomov, S.V., Verpoest, I. and Vandepitte, D. (2007) 'Picture frame shear tests on woven textile composite reinforcements with controlled pretension', AIP Conference Proceedings, 907(1), pp. 999-1004.

Willems, A., Lomov, S.V., Verpoest, I. and Vandepitte, D. (2008) 'Optical strain fields in shear and tensile testing of textile reinforcements', Composites Science and Technology, 68(3), pp. 807-819.

Woo, K., and Whitcomb, J. D., (1996) Three-Dimensional Failure Analysis of Plain Weave Textile Composites Using a Global/Local Finite Element Method, Journal of Composite Materials, 30, pp. 984-1003.

Xue, P., Peng, X. and Cao, J. (2003) 'A non-orthogonal constitutive model for characterizing woven composites', Composites Part A: Applied Science and Manufacturing, 34(2), pp. 183-193.

Yu, J.Z., Cai, Z. and Ko, F.K. (1994) 'Formability of textile preforms for composite applications. Part 1: Characterization experiments', Composites Manufacturing, 5(2), pp. 113-122.

Zhu, B., Yu, T.X. and Tao, X.M. (2007) 'Large deformation and slippage mechanism of plain woven composite in bias extension', Composites Part A: Applied Science and Manufacturing, 38(8), pp. 1821-1828.

Appendix A:
Workshop drawings

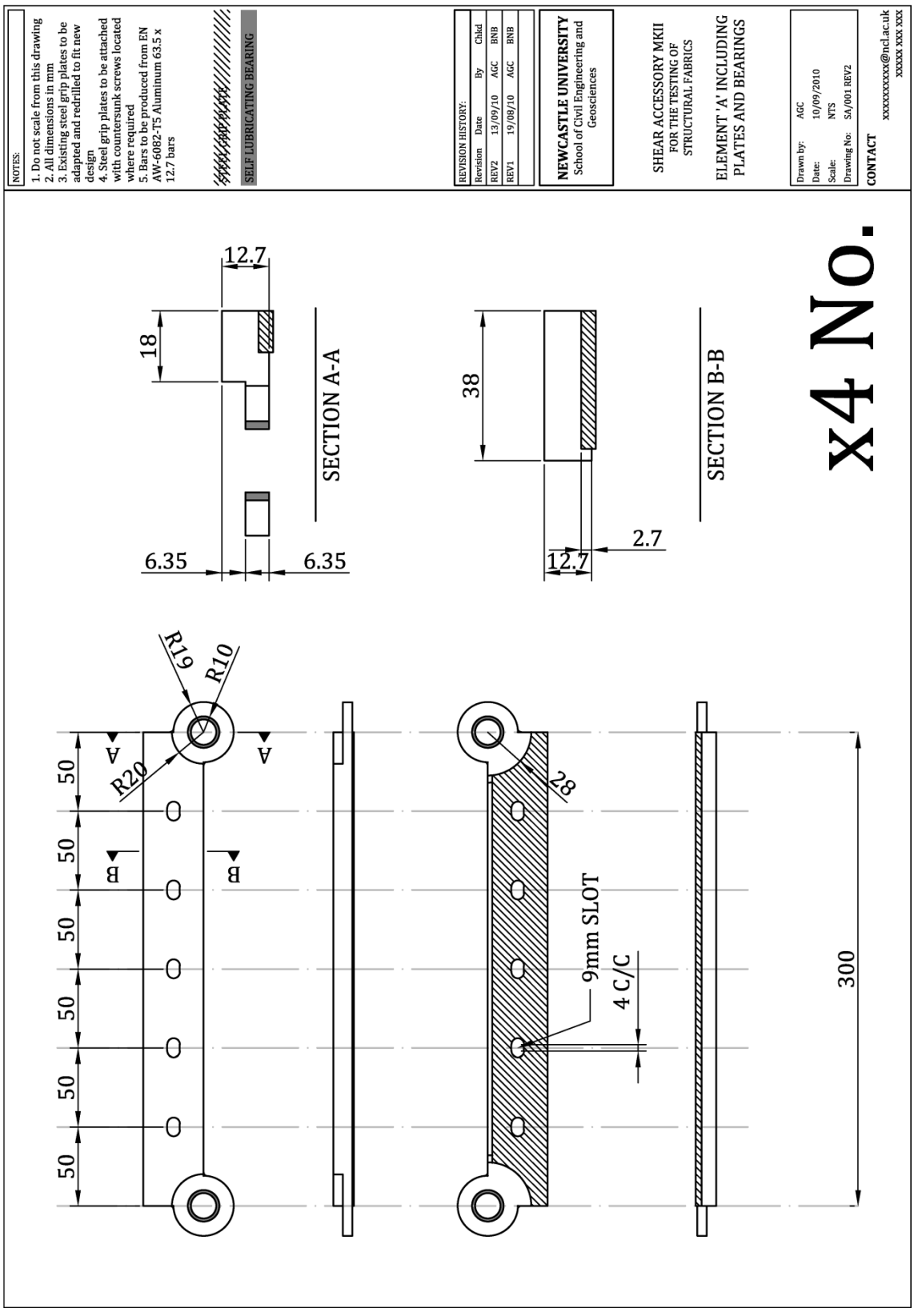
NOTES:
1. Do not scale from this drawing
2. All dimensions in mm
3. Existing steel grip plates to be adapted and redrilled to fit new design
4. Steel grip plates to be attached with countersunk screws located where required
5. Bars to be produced from EN AW-6082-T5 Aluminum 63.5 x 12.7 bars
SELF LUBRICATING BEARING
REVISION HISTORY:
Revision Date By Chkd
REV2 13/09/10 AGC BNB
REV1 19/08/10 AGC BNB
NEWCASTLE UNIVERSITY
School of Civil Engineering and Geosciences
SHEAR ACCESSORY MKII
FOR THE TESTING OF
STRUCTURAL FABRICS
ELEMENT 'A' INCLUDING
PLATES AND BEARINGS
Drawn by: AGC
Date: 10/09/2010
Scale: NTS
Drawing No: SA/001 REV2
CONTACT
xxxxxxxxxx@ncl.ac.uk
xxxxx xxx xxx
12.7
18
SECTION A-A
6.35
6.35
38
SECTION B-B
2.7
12.7
x4 No.
R19
R10
R20
A
A
B
B
50
50
50
50
50
50
28
9mm SLOT
4 C/C
300

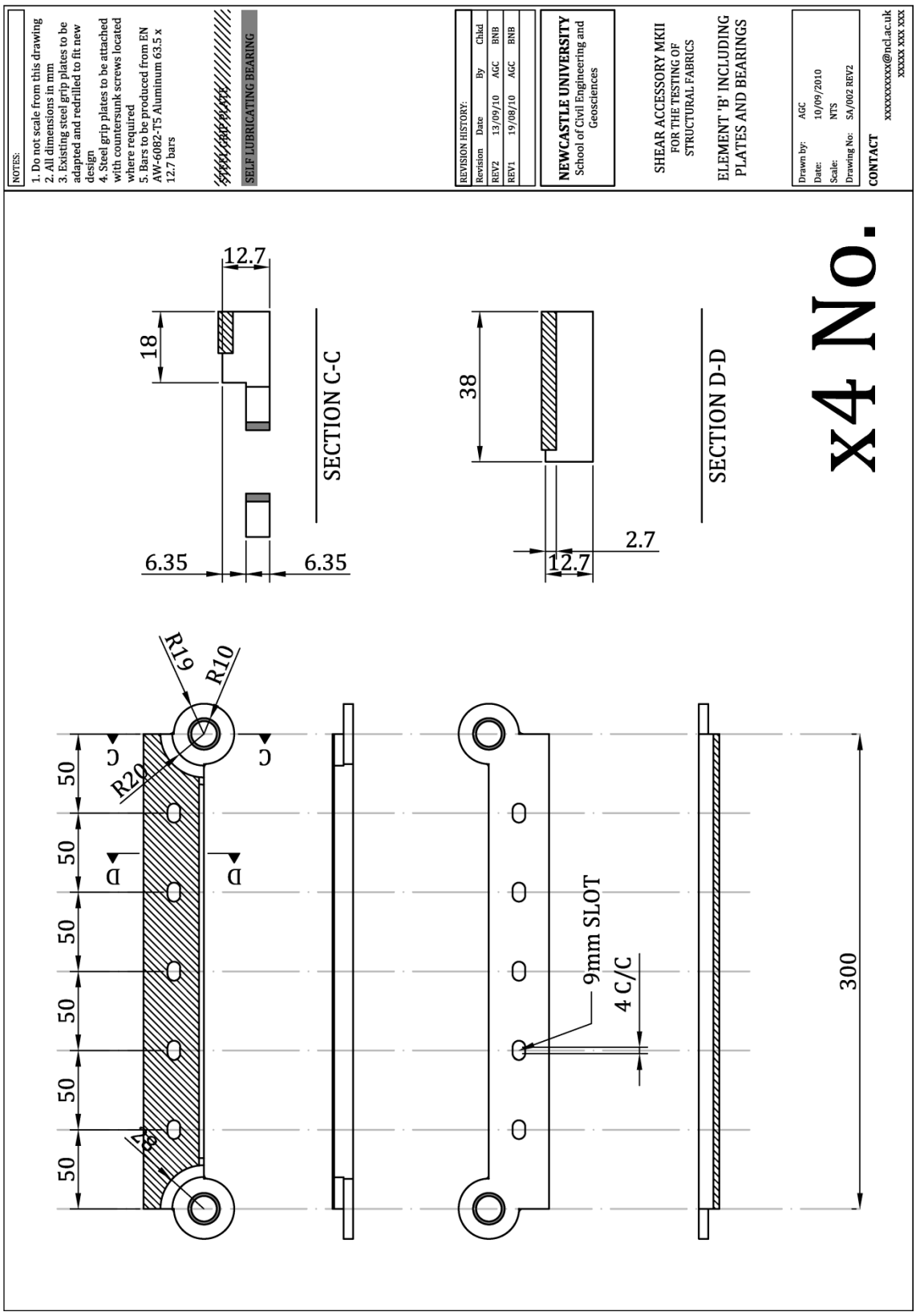
NOTES:
1. Do not scale from this drawing
2. All dimensions in mm
3. Existing steel grip plates to be adapted and redrilled to fit new design
4. Steel grip plates to be attached with countersunk screws located where required
5. Bars to be produced from EN AW-6082-T5 Aluminum 63.5 x 12.7 bars
SELF LUBRICATING BEARING
REVISION HISTORY:
Revision Date By Chkd
REV2 13/09/10 AGC BNB
REV1 19/08/10 AGC BNB
NEWCASTLE UNIVERSITY
School of Civil Engineering and Geosciences
SHEAR ACCESSORY MKII
FOR THE TESTING OF
STRUCTURAL FABRICS
ELEMENT 'B' INCLUDING
PLATES AND BEARINGS
Drawn by: AGC
Date: 10/09/2010
Scale: NTS
Drawing No: SA/002 REV2
CONTACT
xxxxxxxxxx@ncl.ac.uk
xxxxx xxx xxx
x4 No.
12.7
18
6.35
6.35
SECTION C-C
38
2.7
12.7
SECTION D-D
R19
R10
R20
C
C
D
D
50
50
50
50
50
50
18
9mm SLOT
4 C/C
300

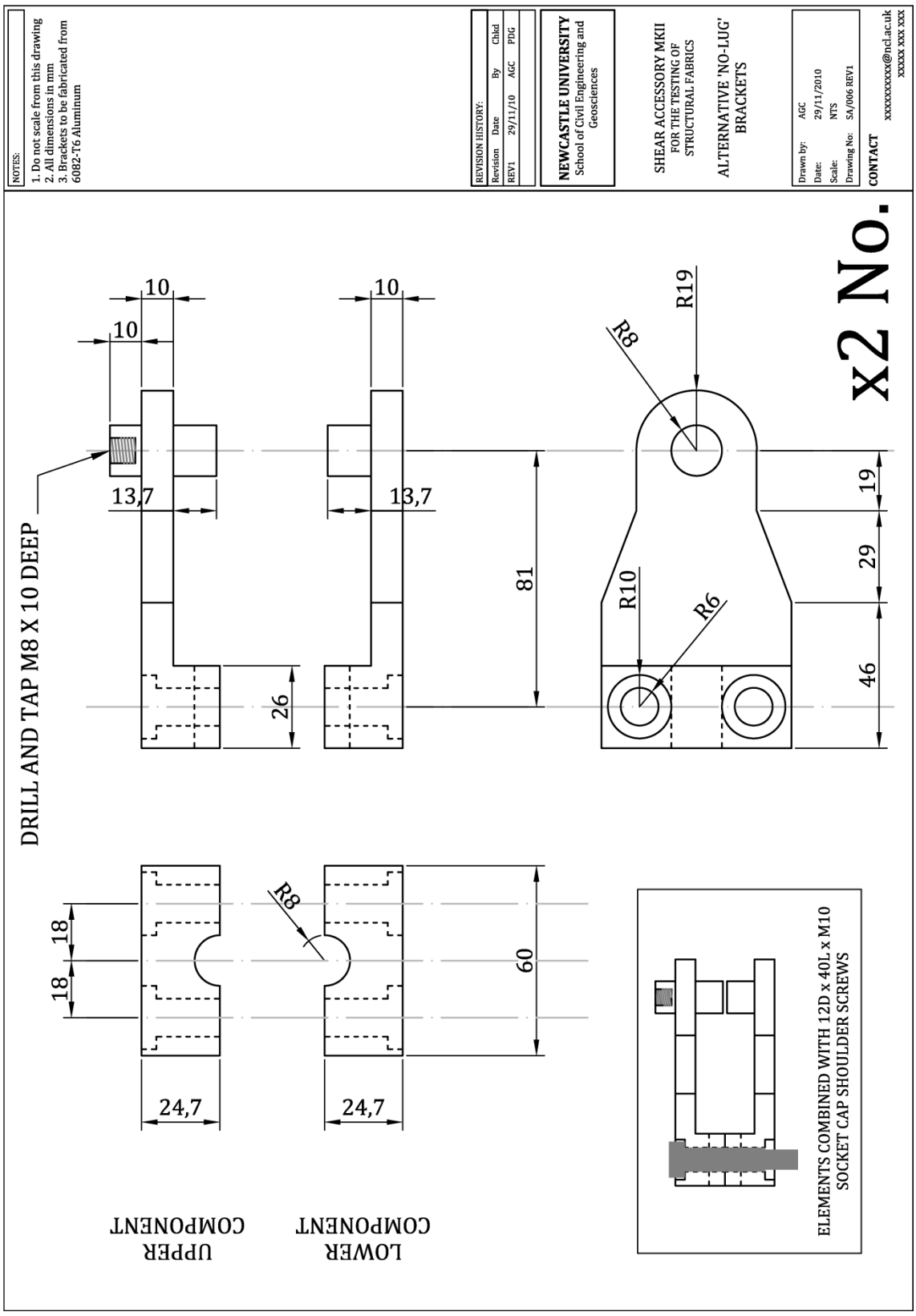
NOTES:
1. Do not scale from this drawing
2. All dimensions in mm
3. Brackets to be fabricated from 6082-T6 Aluminum
REVISION HISTORY:
Revision Date By Chkd
REV1 29/11/10 AGC PDG
NEWCASTLE UNIVERSITY
School of Civil Engineering and Geosciences
SHEAR ACCESSORY MKII
FOR THE TESTING OF
STRUCTURAL FABRICS
ALTERNATIVE 'NO-LUG'
BRACKETS
Drawn by: AGC
Date: 29/11/2010
Scale: NTS
Drawing No: SA/006 REV1
CONTACT
xxxxxxxxxx@ncl.ac.uk
xxxxx xxx xxx
x2 No.
DRILL AND TAP M8 X 10 DEEP
10
10
13,7
26
10
10
13,7
81
R8
R19
R10
R6
19
29
46
18
18
24,7
R8
24,7
60
LOWER COMPONENT
UPPER COMPONENT
ELEMENTS COMBINED WITH 12D x 40L x M10
SOCKET CAP SHOULDER SCREWS

NOTES:
1. Do not scale from this drawing
2. All dimensions in mm
3. Existing steel grip plates to be adapted and redrilled to fit design
4. Steel grip plates to be attached with countersunk screws located where required
REVISION HISTORY:
Revision Date By Chkd
NEWCASTLE UNIVERSITY
School of Civil Engineering and Geosciences
UNIAXIAL TEST CLAMPS
FOR TEXTILES
1/3
Drawn by: AGC
Date: 26/03/2012
Scale: NTS
Drawing No: BC/001
CONTACT
xxxxxxxxxx@ncl.ac.uk
xxxxx xxx xxx
x2 No.
144.0
10.0
Ø16.0
Ø10.0
10.0
20.0
30.0
25.0
25.0
30.0
150.0
13.0
10.0
52.0
BACK VIEW SHOWING
EXTERIOR PLATE
35.0
Ø15.0
35.0
150.0
5.0
24.0
5.0
FRONT VIEW SHOWING
INTERIOR OF PLATE
(INCLUDING GRIPS)
3.0
21.0
19.0
6.0
SIDE VIEW

NOTES:
1. Do not scale from this drawing
2. All dimensions in mm
3. Existing steel grip plates to be adapted and redrilled to fit design
4. Steel grip plates to be attached with countersunk screws located where required
REVISION HISTORY:
Revision Date By Chkd
NEWCASTLE UNIVERSITY
School of Civil Engineering and Geosciences
UNIAXIAL TEST CLAMPS
FOR TEXTILES
2/3
Drawn by: AGC
Date: 26/03/2012
Scale: NTS
Drawing No: BC/002
CONTACT
xxxxxxxxxx@ncl.ac.uk
xxxxx xxx xxx
x2 No.
102.0
10.0
Ø10.0
30.0
25.0
25.0
30.0
150.0
13.0
52.0
BACK VIEW SHOWING
EXTERIOR PLATE
35.0
Ø15.0
35.0
150.0
5.0
24.0
5.0
FRONT VIEW SHOWING
INTERIOR OF PLATE
(INCLUDING GRIPS)
6.0
18.0
SIDE VIEW

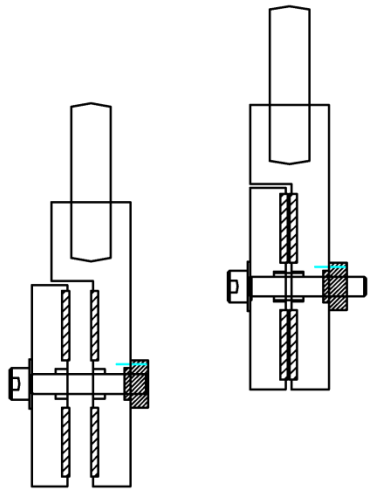

ASSEMBLED COMPONENTS SHOWING CLOSED CONFIGURATION (RIGHT) AND OPEN CONFIGURATION (LEFT)

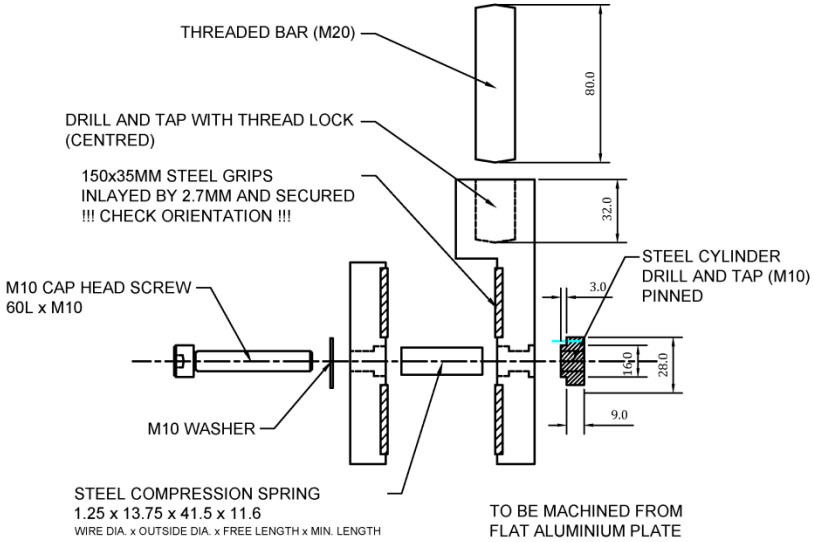

EXPLODED VIEW OF COMPONENTS WITH ASSEMBLY INSTRUCTIONS

x2 No.

NOTES:

1. Do not scale from this drawing
2. All dimensions in mm
3. Existing steel grip plates to be adapted and redrilled to fit design
4. Steel grip plates to be attached with countersunk screws located where required

STEEL GRIP PLATE

REVISION HISTORY:

Revision	Date	By	Chkd

NEWCASTLE UNIVERSITY
School of Civil Engineering and Geosciences

UNIAXIAL TEST CLAMPS FOR TEXTILES
3/3

Drawn by:	AGC
Date:	26/03/2012
Scale:	NTS
Drawing No:	BC/003

CONTACT
xxxxxxxxxx@ncl.ac.uk
xxxxx xxx xxx